Modelling and Characterization of Down-Conversion and Down-Shifting Processes for Photovoltaic Applications

by

Ahmed Gabr

Thesis submitted to the
Faculty of Graduate and Postdoctoral Studies
in partial fulfillment of the requirements
for the Doctorate of Philosophy degree in Electrical and Computer Engineering

School of Electrical Engineering and Computer Science
Faculty of Engineering
University of Ottawa

Abstract

Down-conversion (DC) and down-shifting (DS) layers are optical layers mounted on the top surface of a solar cell that can potentially increase the solar cell efficiency. The effect of DC and DS layers to enhance the performance of single-junction solar cells has been studied by means of simulation and experimental work. In this thesis a model is developed to study the effects of DC and DS layers by modifying the incident spectrum. The effect of the layers on ideal cells as well as commercial grade silicon and CIGS solar cells that are modeled in a device simulator is examined.

Silicon nanocrystals (Si-nC) embedded in a silicon dioxide matrix to act as a DS layer were fabricated and characterized at McMaster University as part of this project. The measured optical properties as well as the photoluminescence measurements are used as input parameters to the optical model. The enhancement due to the Si-nC when coupled to silicon and CIGS solar cells is explored. Beside the DC and DS effects, there is also disturbance to the surface reflections due to the addition of a new layer to the top surface and is referred to as antireflection coating (ARC) effect. For the simulated silicon solar cell under the standard AM1.5G spectrum (1000W/m^2), a maximum increase in J_{sc} of 8.4% is achieved for a perfect DS layer as compared to a reference cell, where 7.2% is due to ARC effect and only 1.2% is due to DS effect. On the other hand, there is an increase in J_{sc} of 19.5% for the CIGS solar cell when coupled to a perfect DS layer. The DS effect is dominant with 18%, while the ARC effect contributes only 1.5% to the total J_{sc} enhancement.

Accurately characterizing DS layers coupled to solar cell requires knowledge of optical properties of the complete structure. Internal quantum efficiency is an important tool for characterizing DS systems, nevertheless, it is rarely reported. In addition, the ARC effect is not experimentally decoupled from the DS effect. In this work, a straightforward method for calculating the active layer contribution that minimizes error by subtracting optically-modeled electrode absorption from experimentally measured total absorption.

Statement of Originality

The author declares that results presented in this thesis were obtained during the period of his PhD research project and under the supervision of Dr. Karin Hinzer. To the best of the author‘s knowledge, these results are original.

Some parts of the work described here were carried out by individuals other than the author. In particular, all silicon nanocrystals were fabricated and characterized at McMaster University by Justin Sack. The silicon solar cells were fabricated at Carleton University under the supervision of Dr. Garry Tarr. The SEM images of the silicon solar cells were carried out by Anthony Olivieri at the University of Ottawa. The optical properties of the titanium silica layer were measured by Kevin Boyed at McMaster University. The methodology for simulating CIGS solar cells is derived from earlier work by Alex Walker and Frédéric Bouchard from SUNLAB, University of Ottawa.

The work presented in this thesis has led to the following manuscripts and conference proceedings

Publications in refereed conference proceedings

A. M. Gabr, A. H. Trojnar, M. M. Wilkins, T. J. Hall, R. N. Kleiman, and K. Hinzer, "*Optimization of anti-reflection coatings for bifacial solar cells with upconversion layers",* Proceedings of the 40th IEEE Photovoltaic Specialist Conference (PVSC), pp.2230 – 2233 (2014).

A. M. Gabr, A. Walker, A. H. Trojnar, T. J. Hall, R. N. Kleiman, and K. Hinzer, "*Numerical Modeling of Silicon Nanocrystal Down-Shifting Layers for Enhanced Photovoltaic Efficiency"*, Proceedings of the 39th IEEE Photovoltaic Specialists Conference (PVSC), pp.1003,1007 USA, (2013).

A. M. Gabr, R. M. Beal, A. Walker, J. F. Wheeldon, J. Sacks, R. M. Savidge, T. J. Hall, R. N. Kleiman, and K. Hinzer, *Modeling Down-Conversion and Down-Shifting for Photovoltaic Applications,* Proceedings of the 38th IEEE Photovoltaic Specialists Conference (PVSC), pp 48-52 (2012).

J. Sacks , R. M. Savidge**, A. Gabr,** A. Walker, R. Beal, J. Wheeldon, A. P. Knights, P. Mascher, K. Hinzer, and R. N. Kleiman, *Quantum Efficiency Measurements of Down-Shifting Using Silicon Nanocrystals for Photovoltaic Applications,* Proceedings of the 38th IEEE Photovoltaic Specialists Conference (PVSC), pp 92-96 (2012).

Oral Presentations

A. M. Gabr, R. Cheriton, M. Wilkins, D. Frisina, A. Trojnar, R. N. Kleiman and K. Hinzer*, "Effect of Silicon Nanocrystals as a Down-Shifting Layer Coupled to a Silicon Solar Cell"*, 5th Canadian Photovoltaics Conference, Montreal, QC, May 14-16, 2014.

A. M. Gabr, A. Walker, R. N. Kleiman and K. Hinzer *"Challenges in realizing next generation spectral conversion for enhanced silicon solar cell performance"*, 4th Canadian Photovoltaics Conference, Hamilton, ON, May 8-10, 2013.

A. M. Gabr, R.M. Beal, A. Walker, J. F. Wheeldon, J. Sacks, R. M. Savidge, T. J. Hall, R. N. Kleiman and K. Hinzer*, Modeling down-conversion and down-shifter layers for enhanced silicon solar cell performance***,** 3rd Canadian Photovoltaics Conference, Montreal, QC, May 14-15, 2012.

Poster Presentations

A. M. Gabr, A. H. Trojnar, M. M. Wilkins, T. J. Hall, R. N. Kleiman, and K. Hinzer, "Optimization of anti-reflection coatings for bifacial solar cells with upconversion layers", Photovoltaic Specialist Conference (PVSC), 2014 IEEE 40th, pp.2230,2233, June 8-13, 2014.

A. M. Gabr, A. Walker, J. F. Wheeldon, T. J. Hall, R. N. Kleiman, and K. Hinzer, "Numerical Modeling of Silicon Nanocrystal Down-Shifting Layers for Enhanced Photovoltaic Efficiency", 2013 IEEE 39th Photovoltaic Specialists Conference, Tampa, FL, USA, June 16-21 2013.

A. M. Gabr, R.M. Beal, A. Walker, J. F. Wheeldon, J. Sacks, R. M. Savidge, T. J. Hall, R. N. Kleiman, and K. Hinzer, Modeling Down-Conversion and Down-Shifting for Photovoltaic Applications, 38th IEEE Photovoltaic Specialists Conference (PVSC), Austin, TX, June 2012.

A. M. Gabr, A. Walker, R. Beal, J. F. Wheeldon, J. Sacks, R. Savidge, T. J. Hall, R. N. Kleiman, and K. Hinzer, "Optimization of Down-Converters for Photovoltaics Applications", Nano Ontario Conference and Workshop 2011, Hamilton, ON, October 14, 2011.

Contributions not presented in this thesis

M. Wilkins, C. E. Valdivia, **A. M. Gabr**, D. Masson, S. Fafard, and K. Hinzer, "Luminescent coupling in planar opto-electronic devices," *J. Appl. Phys.*, vol. 118, no. 14, p. 143102, 2015.

M. M. Wilkins**, A. Gabr,** P. Sharma, H. Schriemer, and K. Hinzer**,** "*4-junction solar cells with dilute nitrides: Optimization with luminescent coupling",* Proceedings of the European Photovoltaic Solar Energy Conference, Amsterdam, The Netherlands September 22-26th, 2014.

M. M. Wilkins**, A. M. Gabr,** A. H. Trojnar, H. Schriemer, S. Farad, and K. Hinzer, "*Effects of Luminescent Coupling in Single- and 4-Junction Dilute Nitride Solar Cells",* Proceedings of the 40th IEEE Photovoltaic Specialist Conference (PVSC), pp.3601 – 3604 (2014).

Acknowledgments

I would like to express my sincere gratitude to my supervisor, Dr. Karin Hinzer for her continuous support during my Ph.D study and related research, for her patience, motivation, and immense knowledge. I could not have imagined having a better mentor or devoted supervisor. I cannot thank Karin enough for this research opportunity, which also allowed me to travel to several international conferences presenting my work and networking with colleagues within the field of photovoltaics.

I would like to thank the past and present members of SUNLAB for their support and useful discussions, particularly Alex Walker, Matthew Wilkins, Jeffrey Wheeldon, Richard Beal, Ross Cheriton, Joan Haysom, and Anna Trojnar. I would like to thank my collaborators in this project from McMaster University: Dr. Rafael Kleiman, Justin Sacks, Rachel Savidge and Daniel Frisina. I am grateful to the very useful discussions and the samples provided by the group.

Special thanks to Dr. Alex Walker for his support and useful discussion during the first two years of my program and for his excellent proofreading of my thesis with very valuable comments. I would like also to thank Matthew Wilkins for his valuable input and fruitful discussions.

This work has been supported by Natural Sciences and Engineering Research Council of Canada (NSERC), by Photovoltaic Innovation Network (PVIN), and Ontario Graduate Scholarship (OGS).

I would like to thank my parents for supporting me spiritually throughout my graduate studies and my life in general.

Last but not least, to my better half, Heba, thank you for all the sleepless nights and taking care of our four kids throughout the writing of this thesis and my graduate studies in general.

Table of Contents

List of Figures

List of Tables

List of Acronyms

AM	Air Mass
a-Si	amorphous silicon
ARC	Anti-reflection coating
c-Si	Crystalline silicon
CdTe	Cadmium telluride
CB	Conduction band
CO_2	Copper dioxide
CIGS	Copper indium gallium selenide ($Cu(In,Ga)Se_2$)
DUT	Device under test
DC	Down-conversion
DS	Down-shifting
EQE	External quantum efficiency
FC	Front-converter
FWHM	Full width at half maximum
GaAs	Gallium arsenide
Ge	Germanium
G8	Group of eight
HOMO	Highest occupied molecular orbital
IR	Infrared
IQE	Internal quantum efficiency
LUMO	Lowest unoccupied molecular orbital
mc-Si	Multicrystalline silicon
NIR	Near-infrared
NREL	National renewable energy laboratory
PL	Photoluminescence
PLQY	Photoluminescence quantum yield
PV	Photovoltaic
QD	Quantum dots
QE	Quantum efficiency
RC	Rear-converter

SEM	Scanning electron microscope
SRH	Shockley-Read-Hall
Si_3N_4	Silicon nitride
Si-nC	Silicon nanocrystals
SS	Solar simulator
SR	Spectral response
STC	Standard Test Condition
SRV	Surface recombination velocity
TCAD	Technology Computer-Aided Design
TE	Transverse electric
TM	Transverse magnetic
TMM	Transfer matrix method
TCO	Transparent conducting oxide
UC	Up-conversion
UV	Ultraviolet
VB	Valence band

List of Symbols

α	Absorption coefficient
Δ	Phase difference
ΔEQE_{DS}	*External quantum efficiency due to DS effects*
δ	Optical phase
ε	Electric permittivity of semiconductor
η	Efficiency
θ_z	Zenith angle
λ	Wavelength
μ	Carrier mobility
μ_n, μ_p	electron and hole mobilities
ρ	Free charge density
$\tau_{SRH,n}, \tau_{SRH,p}$	SRH carrier lifetimes for electrons and holes
φ	Electrical potential
Ψ	Amplitude ratio
A	Area of solar cell
A_p	Parasitic absorption
A_PV	Absorption in the active layer
B_{rad}	Radiative recombination rate
b	Photon flux
c	Speed of light
D_n, D_p	Diffusion constant for electrons and holes
E	Electric field
E_f	Final state
E_g	Bandgap energy
E_i	Intrinsic energy level
EQE_ARC	External quantum efficiency due to ARC effects
EQE_ref	External quantum efficiency of the reference cell
EQE_tot	External quantum efficiency of the DS layer coupled to the solar cell
E_p	Phonon energy

E_{ph}	Photon energy
E_t	Trap energy level
F	Spectral irradiance
FF	Fill factor
G_{OPT}	Net optical Generation rate
G_n, G_p	Generation rate of electrons and holes
h	Plank's constant
I_{in}	Incident spectral irradiance
I_o	Light intensity
J	Total current density
J_o	Saturation current density (or dark current density)
$\vec{J}_D$	Displacement current density
J_m	Current density of solar cell at maximum power point
$\vec{J}_n^{diff}, \vec{J}_p^{diff}$	Diffusion current density for electrons and holes
J_L	Light generated current density
J_{sc}	Short-circuit current density
k	Extinction coefficient (imaginary part of refractive index)
k_B	Boltzmann constant
N_A, N_D	Acceptor and donor concentrations
n	electron concentration; ideality factor; Refractive index
n_i	Intrinsic carrier concentration
n_t, p_t	electron and hole trap concentrations
q	Electronic charge
p	hole concentration
P_{in}	Total incident power
P_{max}	Maximum output power generated by solar cell
R	Reflectance
R_n, R_p	Recombination rate of electrons and holes
R_s	Series resistance
R_{sh}	Shunt resistance
S_n, S_p	Surface recombination velocity for electrons and holes

T	Temperature; Transmission
U	net recombination rate
υ_d	Drift velocity
V_m	Voltage of solar cell at maximum power point
V_{oc}	Open-circuit voltage

Chapter 1: Introduction

It is becoming more evident that greenhouse gas emissions have to be reduced in order to avoid dangerous repercussions from climate change. The threat has made our world more vulnerable and the Group of eight (G8) nations have agreed to reduce greenhouse gas emissions to mid-century by keeping atmospheric carbon dioxide (CO_2) concentrations in the "safe zone" – below 450 ppm [1]. Despite this restriction, global emissions of CO_2 from fossil fuel combustion and industrial processes, including but not limited to cement production, have reached a new massive high of 35.3 billion tonnes CO_2 in 2013, as shown in Figure 1.1. This is a 2.0% increase from 2012, which is a continuing trend over the past decade [2]. Now more than ever, there is pressure to use alternative sources of clean energy, more specifically renewable energy.

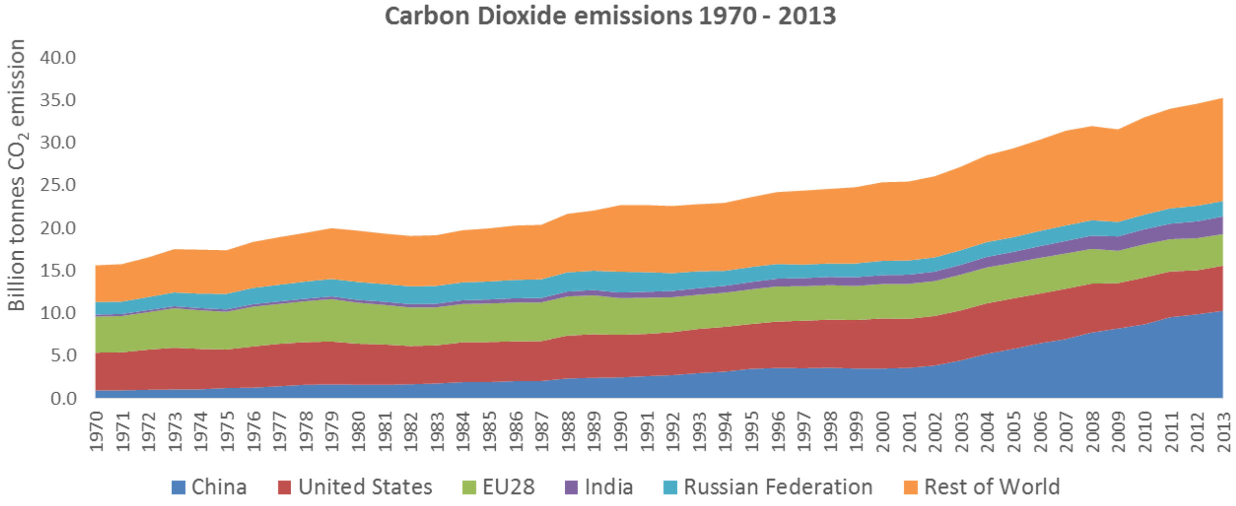

Figure 1.1. CO_2 emission totals of fossil fuel use and industrial processes per region/country for the time 1970-2013 [2].

Solar energy, a source of renewable energy, is the third source of renewable energy in terms of global power generation, after hydropower and wind energy. The cumulative global photovoltaic (PV) capacity installed as of the end of 2015 is 242 GW, up from 177 GW in 2014 [3]. While Europe represented a major part of all global installations, Asia's share grew rapidly in 2012 and this growth was confirmed in recent years. Figure 1.2 shows the relative share of cumulated PV installations in four regional market segments.

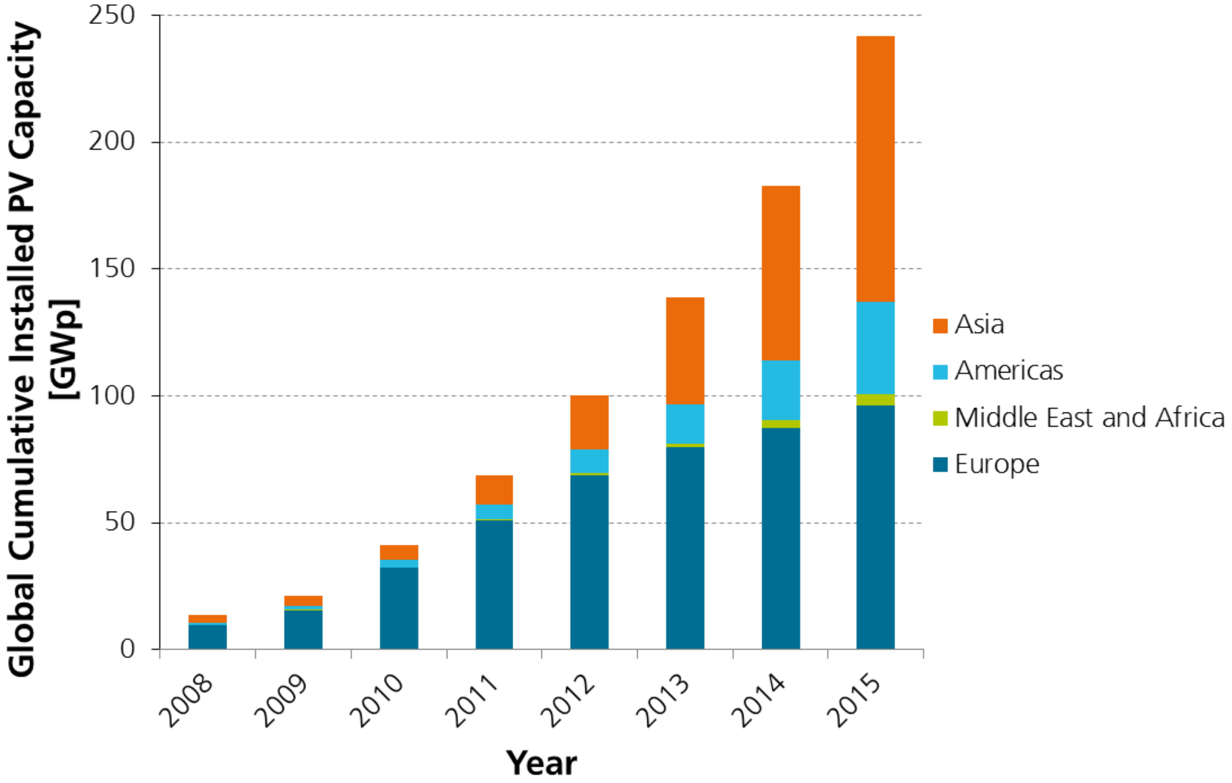

Figure 1.2. PV installation (MWpDC) from 2008 to 2015 by region, figure reproduced from [3].

1.1. Motivation

Silicon based solar cells and modules have dominated the market for a long time with more than 80% market share. Crystalline silicon (c-Si) is approaching its theoretical limit of 31% [4] with record efficiency of 25.6% for solar cells and 23.8% for modules [5]. Emerging thin film technologies such as copper indium gallium selenide (CIGS) and cadmium telluride (CdTe) are showing an increase in market share after remarkable increases in their respective efficiencies. Record thin film efficiencies are now 21.0% for solar cells and more than 15% for modules. Table 1.1 lists the record efficiencies of some of the common single-junction solar cells such as c-Si, multicrysalline silicon (mc-Si), gallium arsenide (GaAs), CIGS, and CdTe [5].

Table 1.1. Performance parameters for common single-junction solar cell materials measured under the global air mass (AM) 1.5 spectrum (1000 W/m^2) at 25 °C [5].

Cell type	**Area (cm^2)**	V_{oc} **(V)**	J_{sc} **(mA/cm^2)**	FF **(%)**	η**(%)**
c-Si	143.7	0.74	41.8	82.7	25.6
mc-Si	242.74	0.6678	39.80	80.0	21.3
GaAs	0.9927	1.122	29.68	86.5	28.8
CIGS	0.9927	0.757	35.70	77.6	21.0
CdTe	1.0623	0.8759	30.25	79.4	21.0

Single-junction semiconductor solar cells efficiently absorb photons with energy close to the semiconductor bandgap. Photons with energy smaller than the bandgap, also called sub-bandgap photons, are not absorbed by the solar cell and thus their energy is lost, which is known as transparency loss. Photons with energy larger than the bandgap are absorbed, but the excess energy is lost as heat due to nonradiative relaxation of the excited electrons towards the edge of the conduction band, which is known as thermalization loss. Transparency and thermalization losses are the two main loss mechanisms in single-junction solar cells and together they account for almost 50% of the incident power of the solar spectrum, as shown in Figure 1.3.

There have been many advances in photovoltaic technology that have led to the beginning of a so-called third generation. First generation technology was based on conventional silicon wafers. With the advances in thin film technology, the photovoltaic industry was ready to switch to a second generation based on thin-film solar-cell technology. It is interesting to note that the efficiency of second generation cells is lower than that of first generation cells, but the cost-effectiveness of second generation cells outweighs this drawback. To progress further, the photovoltaic industry was looking forward for a third generation technology. Third generation technology aims to achieve higher conversion efficiency than the theoretical limit of single-junction solar cells by minimizing transparency and thermalization losses, while maintaining cost-effective production. Different approaches have been proposed to utilize the broadband solar spectrum, such as multi-junction solar cells [6], intermediate band solar cells [7], multiple carrier excitation [8], hot carrier solar cells [9], and optical up- and down-conversion [10], [11]. While most approaches aim to modify the design of the solar cell to absorb the broadband solar spectrum, up- and down-conversion processes modifies the solar spectrum to be better absorbed by a single-junction solar cell. Up- and down-conversion processes aim to increase the solar cell efficiency beyond the theoretical limit without changing the design of the cells. As in other approaches, up- and down-conversion processes aim to mitigate surface recombination, thermalization and sub-bandgap losses.

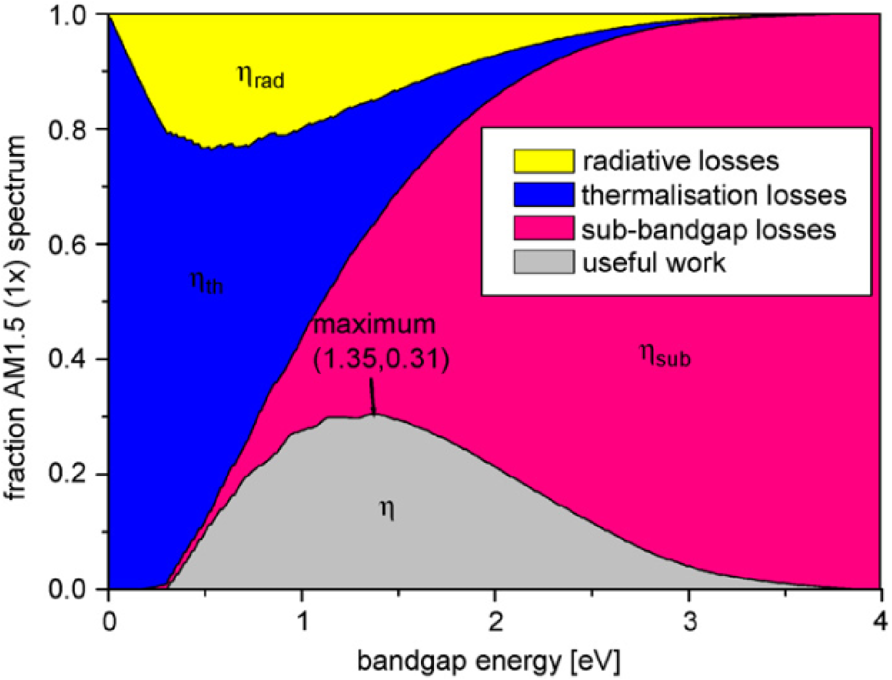

Figure 1.3. Theoretical losses and limiting efficiencies for single-junction bandgap devices. Both thermalization and sub-bandgap losses account for more than 50% incident intensity losses. Reproduced with permission from [12].

Down-conversion (DC) layers absorb high energy photons and convert them to two or more lower-energy photons that can be absorbed efficiently by the solar cell. Therefore DC layers located on the top surface of solar cells can be used to reduce surface recombination and thermalization losses. Unlike other third generation methods, there is no change in the solar cell design since the DC layers are only optically coupled to the front surface of a solar cell, as shown in Figure 1.4. Down-conversion was first introduced by Dexter in the 1950s followed by Hovel *et al* in the late 1970s to overcome the poor ultra-violet (UV) response of single-junction solar cells with bandgaps optimized for maximum efficiency, where UV is portion of spectrum from 100 nm to

400 nm [13], [14]. Despite the increase in solar cell efficiency since the 1970s, commercial solar cells with poor front passivation can suffer from poor UV response due to high surface recombination.

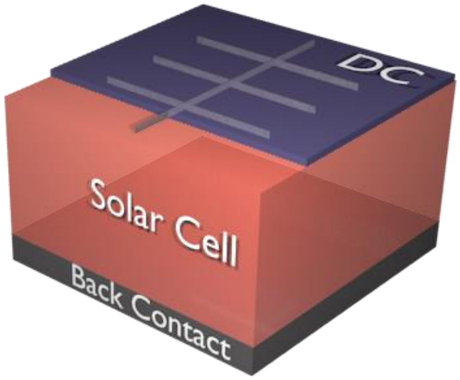

Figure 1.4. Schematic of a down-conversion layer located on front surface of a single-junction solar cell.

On the other hand, up-conversion (UC) is the conversion of two or more low-energy photons to one high-energy photon. UC layers located on the rear surface of a bifacial solar cell utilize sub-bandgap photons that are otherwise transmitted through the solar cell. A schematic of an UC layer located at the bottom of a bifacial solar cell with a back reflector is shown in Figure 1.5. Unlike down-conversion, up-conversion layers do not disturb the incident photons. The up-converted photons that are absorbed by the solar cell simply contribute to electron-hole generation and as a result increase the short-circuit current beyond that of a solar cell with no u-conversion layer. In addition, with a reflector placed behind the UC layer almost all up-converted photons are directed towards the solar cell for absorption. Detailed balance calculations show that the efficiency of silicon solar cells can increase from 30% to 40.2% when coupled to an UC layer [10]. However, UC involves the absorption of two or more photons sequentially, thus the intensity of converted photons scales quadratically with incident light intensity. Another challenge is to find efficient materials with wide absorption profiles in the long-wavelength range (1100 nm – 2500 nm) yet have rich electronic energy levels that can up-convert the absorbed photons to visible or near infra-red photons with a sufficient efficiency. Trivalent erbium, Er^{3+}, is ideally suited for the UC of near-infrared light due to its ladder of nearly equally spaced energy levels that are multiples of the $^4I_{15/2}$ to $^4I_{13/2}$

transition. The Er^{3+} ion is well suited for silicon solar cells as the absorption spectrum is centered at 1520 nm whereas it emits at 980 nm, 880 nm and 650 nm. Another common choice for UC are coupled Er^{3+}/Yb^{3+} ions, which are suitable for higher bandgap devices such as CdTe (1.5 eV) or amorphous silicon (1.7 eV) solar cells since the absorption profile of Yb^{3+} is centered at 980 nm. The hexagonal sodium yttrium fluoride (β-$NaYF_4$) is the prominent host material used in UC applications [15]–[17]. Experimental results show an increase in the short-circuit current density of a bifacial silicon solar cell of 13.1mA/cm² under concentration of 210 suns due to the presence of such a UC layer, which corresponds to 0.19% relative increase in solar cell efficiency [15].

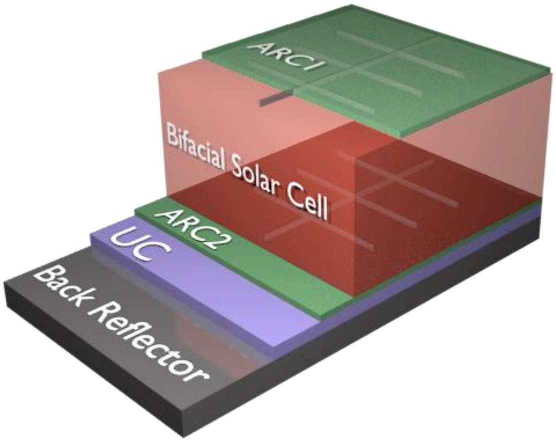

Figure 1.5. Schematic of up-conversion layer located on the rear surface of a bifacial solar cell with a back reflector.

For the standard AM1.5G spectrum, 27% of photons are in the 280 - 550 nm range and available for down-conversion, whereas 19% of the photons are in the range 1100 – 2500 nm (sub-bandgap photons for silicon) and therefore available for up-conversion, as shown in Figure 1.6.

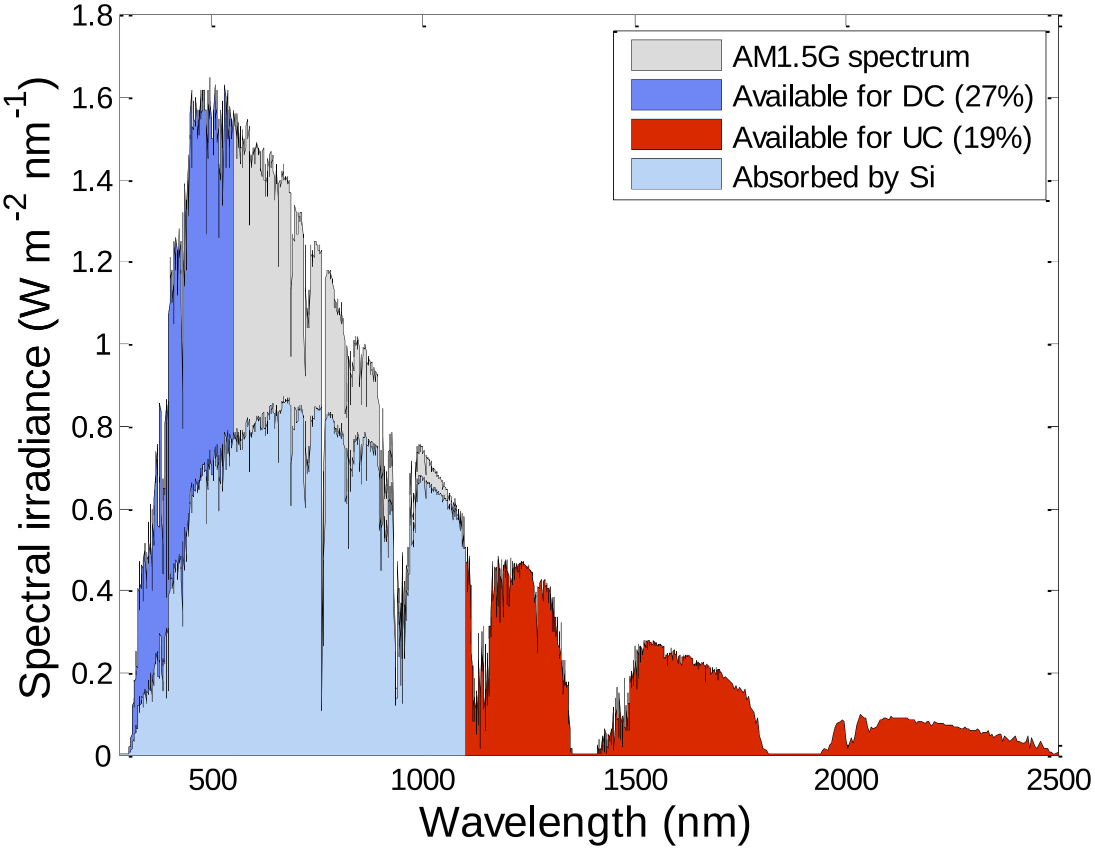

Figure 1.6. The standard AM1.5G spectrum showing the absorbed part that is used by the silicon solar cell and other parts that can contribute to up- and down- conversion processes.

1.2. Thesis Objective

The objective of this thesis is to model and characterize the enhancement in system conversion efficiency of single-junction solar cells when down-conversion and down-shifting layers are located on the top surface. The work in this thesis can be divided into two main parts, modelling and characterization. The modelling is the main part of the thesis where the focus is on simulating and modelling the effect of DC layers. Down-conversion and down-shifting effects are modeled by modifying the incident spectrum with respect to their absorption profiles, photoluminescence spectra, thickness of the layers, and photoluminescence quantum yield (PLQY). The incident spectrum is modified based on optical calculations using the transfer matrix method and is simulated in MATLAB. Although the DC model developed here is a general model, in this thesis the model is calibrated based on measured parameters of silicon nanocrystals. The effect of coupling down-conversion and down-shifting layers to solar cells is investigated by developing models of monocrystalline silicon and CIGS solar cells in the numerical device simulator TCAD Sentaurus by Synopsys (G-2012.06, Mountain View, California). The input parameters are based on values reported in the literature.

The second part of the thesis focuses on the characterization of silicon solar cells with and without silicon nanocrystals embedded in a silicon dioxide matrix. Silicon solar cells fabricated at Carleton University are characterized by measuring the current density-voltage curve (*J*-*V*) and the quantum efficiency of the cells. The internal and external quantum efficiencies of a system of the silicon nanocrystals mounted on top of the silicon solar cells is determined. Expressions are derived to decouple the DS effect from the enhancement due to surface reflections.

1.3. Thesis outline

This section summarizes the content of each chapter of this thesis. There are a total of seven chapters including this introductory chapter. An overview of fundamental concepts of solar cells and semiconductor equations is presented in **Chapter 2.** Moreover, an overview of how solar cells are characterized by means of *I*-*V* curves and quantum efficiency are explained. Finally, efficiency limits of single-junction solar cells are derived and presented.

A detailed literature review on down-conversion and down-shifting processes is presented in **Chapter 3**. First an overview of the efforts of modeling down-conversion process from detailed balance to more practical studies is discussed. Then experimental work using different materials such as rare earth ions, quantum dots and organic dyes to achieve down-conversion and down-shifting effects is summarized with most recent results. Finally, as silicon nanocrystals are the material used for DS process in this thesis, the principle theory of silicon nanocrystals is discussed.

Modelling of single-junction solar cells such as silicon and CIGS is discussed in detail in **Chapter 4**. A brief introduction to the semiconductor device simulation software package TCAD Sentaurus by Synopsys is given, while also illustrating how the basic theory introduced in Chapter 2 is incorporated in the software. The material parameters used in each model are summarized and simulation results such as J-V curves and quantum efficiency are presented. The effect of changing some parameters such as surface recombination velocity or minority carrier lifetime on the solar cell performance is discussed. The developed solar cell models will be used in the DC model discussed in chapter 5.

In **Chapter 5,** the model of down-conversion and down-shifting layers is discussed. Improvement to the basic model is presented by incorporating a model to calculate transmission, reflection and absorption of photons emitted from a medium stacked within a number of thin-film layers. The enhancement in solar cell conversion efficiency is explored when ideal down-conversion and down-shifting layers are located on the top surface. Then the effect of coupling a practical material for down-shifting layer such as silicon nanocrystals is examined where measured parameters are input to the model.

Chapter 6 focuses on the experimental work where the solar cells and down conversion layers are characterized. The silicon solar cells fabricated at Carleton University are characterized by measuring the quantum efficiency and plotting the I-V curves. The quantum efficiency of the silicon nanocrystals coupled to the silicon solar cells are measured and analyzed. Expressions are derived to decouple the ARC and DS effects using experimental results and optical modelling.

Finally, the thesis conclusion is discussed in **Chapter 7**.

Chapter 2: Physics of Solar Cells

A brief overview of the physics of semiconductors is presented throughout this chapter. It should be noted that in this chapter, an overview of the solar cells fundamentals are also discussed, and for more details the reader is referred to [18]–[20]. Light absorption as well as the main recombination losses in solar cells with their impacts on the conversion efficiency of sunlight are illustrated. Finally, the figures of merits of solar cells are presented and the limiting efficiency of the technology is discussed.

2.1. Light Absorption in Semiconductors

Light absorption is essential for the operation of solar cells where an election-hole pair is generated. If a beam of light characterized by a given intensity and wavelength is incident on an absorbing material, a portion of the incident power is reflected by the surface while the remainder is transmitted into the absorber material. The transmitted light into the absorber material is attenuated exponentially as it penetrates into the material. The entity of the attenuation of the light propagating through an absorbing material depends on the wavelength λ of the photons and on the material absorption characteristics. According to the Beer-Lambert law, the light intensity in an absorber material after a distance x is given by:

$$I(x) = I_0(0)e^{-\alpha(\lambda)x} \tag{2.1}$$

where I_o is the intensity of light at the interface where $x = 0$, λ is the wavelength in meters and α is the absorption coefficient in units of inverse meters. The absorption coefficient is a property of a material and is related to the imaginary part of the complex refractive index, k, according to:

$$\alpha(\lambda) = \frac{4\pi k}{\lambda} \tag{2.2}$$

Photogeneration is the excitation of an electron from the valence band (VB) to the conduction band (CB) after the absorption of a photon. Since the process depends on the electron density in the valence band as well as the density of available states in the conduction band, the absorption coefficient of a material is dependent on the band structure. Semiconductors can be categorized according to their bandgap structure to direct and indirect bandgap materials. In direct bandgap materials, like GaAs, the CB minimum and the VB maximum occur at the same wave vector value. Therefore a photon with energy equal to the bandgap of the material is sufficient to excite an electron from CB to VB. In indirect bandgap semiconductors, like silicon, the CB minimum and VB maximum have different wave vector values, then a photon on its own cannot excite an electron to the CB as a change in momentum is required and photons have very little momentum. A phonon, lattice vibration, is required to give up its momentum to the electron so that both energy and momentum are conserved. Thus the absorption of indirect bandgap materials tends to be weaker than direct bandgap materials.

In direct bandgap materials, the absorption of a photon with energy $E_{ph} = hc/\lambda$, where h is Plank constant, c is the speed of light and λ is the photon wavelength, excites an electron from initial state in the valence band to a final state in the conduction band. The higher the photon energy, the more the initial and final energies are away from the band edge. Since the probability of absorption depends on the density of electrons at the initial state and the density of empty states in the final state, and both increase with energy away from the band edge, the absorption coefficient increases rapidly with higher photon energies. An approximated theoretical model for the absorption relates the absorption coefficient for direct band-gap material to the photon energy according to [19]:

$$\alpha \propto \sqrt{E_{ph} - E_g} \qquad (2.3)$$

where E_g is the energy bandgap of the semiconductor.

In indirect bandgap semiconductors, the probability of light absorption in these semiconductors is significantly lower than that of direct bandgap materials due to momentum conservation. The theoretical value of the absorption coefficient for indirect bandgap materials can be approximated as

$$\alpha = \alpha_a + \alpha_e \tag{2.4}$$

where α_a and α_e are the absorption coefficients contributions for a transition involving phonon absorption and emission, respectively, and are given by:

$$\alpha_a \propto \frac{\left(E_{ph} - E_g + E_p\right)^2}{e^{\frac{E_p}{k_B T}} - 1} \tag{2.5}$$

and

$$\alpha_e \propto \frac{\left(E_{ph} - E_g - E_p\right)^2}{1 - e^{\frac{-E_p}{k_B T}}} \tag{2.6}$$

where E_p is the phonon energy, k_B is Boltzmann constant and T is the temperature in Kelvin.

Other absorption processes are possible, like that occurring when the photon energy is sufficiently large to allow a direct excitation across the forbidden bandgap of an indirect bandgap semiconductor or the two-step absorption in direct bandgap semiconductors, which involves the emission or the absorption of phonons.

Figure 2.1 shows the absorption coefficients for Si, GaAs, germanium (Ge), CIGS, and CdTe which are common semiconductors for photovoltaics [21]–[24]. As can be seen direct semiconductors such as GaAs and CIGS have a sharper edge than indirect semiconductors such as Si. Absorption coefficients are important characteristics of semiconductors when designing solar cells as we can determine the required thickness of each material in order to absorb > 99% of the incident sunlight.

In order to simulate an optoelectronic device such as a solar cell, the calculation of the optical generation rate, G_{OPT}, is required. The optical generation rate account for the number of photogenerated electron-hole pairs per unit volume per unit time inside the absorber material. When calculating the optical generation rate, reflection at the material surface must be considered as well as the transmittance. The optical generation rate at position x can be expressed in terms

$$g(\lambda, x) = \left(1 - R(\lambda)\right)\alpha(\lambda)b(\lambda) \cdot e^{-\alpha(\lambda,x)\cdot x} \tag{2.7}$$

where R is the reflectance and b is the incident photon flux. The total generation rate is computed by integrating over all photon wavelengths.

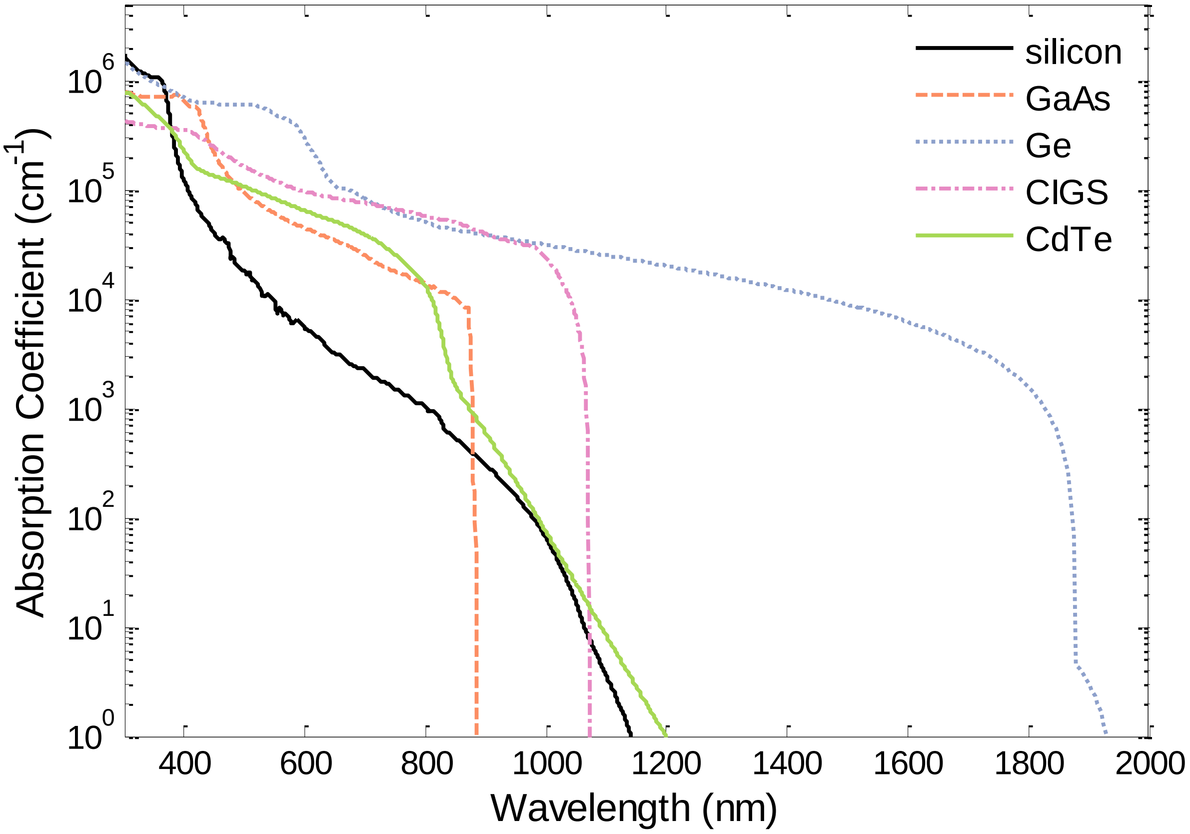

Figure 2.1. Absorption coefficients for some common semiconductor materials used for photovoltaics.

2.2. Semiconductor Model Equations

2.2.1. Drift-diffusion

Electrons and holes in semiconductors move from regions of high concentration to regions of low concentration, thus introducing a diffusion current. The flux of particles movement is in the negative direction of the concentration gradient. Thus the diffusion current densities for electrons and holes are given by Fick's law as:

$$\vec{J}_n^{diff} = qD_n \frac{\mathrm{dn}}{dx} \quad \text{and} \quad \vec{J}_p^{diff} = -qD_p \frac{\mathrm{dp}}{dx} \tag{2.8}$$

where D_n and D_p are the diffusion constants for electrons and holes, respectively, and n and p are the electrons and hole densities, respectively. In the presence of an electric field, E, electrons in the crystal structure will move in an opposite direction to the applied electric field, thereby introducing a drift current. In low electric fields (<10^4 V/cm), the drift velocity of carriers, v_d, is proportional to the applied electric field through the carrier mobility, μ. The drift current density for electrons and holes in the CB and VB, respectively, can be written as

$$\vec{J}_n^{drift} = qn\mu_n\mathrm{E} \quad \text{and} \quad \vec{J}_p^{drift} = qp\mu_p\mathrm{E} \tag{2.9}$$

where μ_n and μ_p are the electron and holes mobilities, respectively, E is the applied electric field. In sufficiently high electric fields, a saturation drift velocity is achieved, but such high electric fields are not typical in single junction solar cells. In nondegenerate materials, the Einstein relation links the diffusion coefficients to the carrier mobilities as:

$$D = \mu\frac{k_BT}{q} \tag{2.10}$$

The total hole and electron current densities are the sum of their drift and diffusion components; equations (2.9) and (2.10) become:

$$\vec{J}_n = qD_n\nabla\mathrm{n} + \mathrm{q}n\mu_n\mathrm{E} \quad \text{and} \quad \vec{J}_p = -\mathrm{q}D_p\nabla\mathrm{p} + \mathrm{q}p\mu_p\mathrm{E} \tag{2.11}$$

The total current is then

$$\vec{J} = \vec{J}_n + \vec{J}_p + \vec{J}_D \tag{2.12}$$

where $\vec{J}_D$ is the displacement current given by

$$\vec{J}_D = \varepsilon\frac{\partial\vec{E}}{\partial t} \tag{2.13}$$

and ε is the electric permittivity of the semiconductor. The displacement current can be neglected in solar cells since they are static devices.

2.2.2. Poisson’s Equation

Poisson’s equation relates the divergence of the electric field, E, to the free charge density, ρ, as:

$$\nabla \cdot (\varepsilon \mathrm{E}) = \rho \qquad (2.14)$$

The free charge density is the sum of electron and hole concentrations as well as the donor and acceptor impurity concentrations, hence:

$$\rho = q(p - n + N_D - N_A) \qquad (2.15)$$

where N_D and N_A are donor and acceptor concentrations (assumed 100% ionized), respectively. Combining equations (2.14) and (2.15), and expressing the electric field, E, in terms of the gradient of electrostatic potential field as $E = -\nabla\varphi$, we arrive at the definition of Poisson’s equation:

$$\nabla \cdot (\varepsilon \nabla \varphi) = -q(p - n + N_D - N_A) \qquad (2.16)$$

2.2.3. Continuity Equations

The electron and hole continuity equations are based on the fact that there is conservation of the number of carriers. Therefore, the continuity equation for electrons and holes are formulated as:

$$\nabla \cdot \overrightarrow{J_n} = q\left(R_n - G_n + \frac{\partial n}{\partial t}\right) \quad \text{and} \quad -\nabla \cdot \overrightarrow{J_p} = q\left(R_p - G_p + \frac{\partial p}{\partial t}\right) \qquad (2.17)$$

where $G_{n(p)}$ is the optical generation rate of electrons (holes), $R_{n(p)}$ is the recombination rate for electrons (holes). Under steady-state conditions the net rate is zero and therefore the continuity equations reduce to:

$$\nabla \cdot \overrightarrow{J_n} = q(R_n - G_n) \quad \text{and} \quad -\nabla \cdot \overrightarrow{J_p} = q\left(R_p - G_p\right) \qquad (2.18)$$

The continuity equations (2.18) along with the total current density for holes and electrons defined in (2.11) and Poisson‘s equation (2.16) form the coupled set of nonlinear differential equations for semiconductor devices that can be solved numerically.

2.3. Recombination Processes

Recombination processes in semiconductors represent the losses of free carriers due to recombination of holes and electrons. There are several recombination mechanisms important to the operation of solar cells – recombination through traps (defects) in the forbidden gap, radiative (band-to-band) recombination, and Auger recombination. These three processes are illustrated in Figure 2.2.

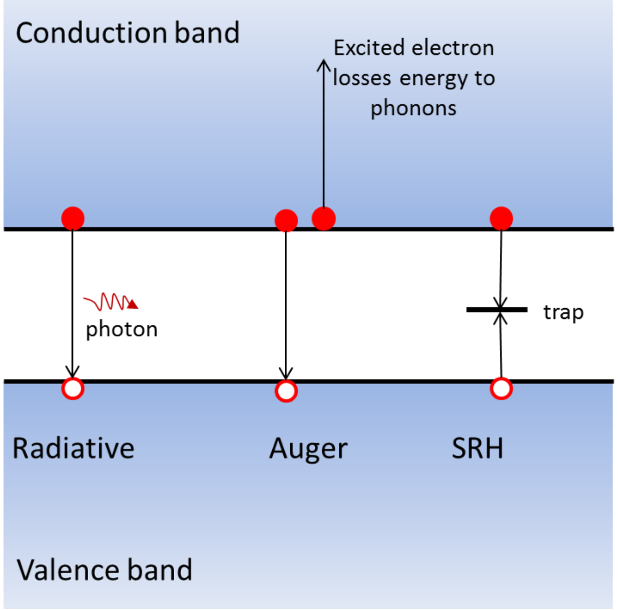

Figure 2.2. Schematic diagram showing the three main recombination processes: Radiative, Auger and SRH.

2.3.1. Radiative Recombination

Radiative recombination involves the transition of an excited electron in the conduction band to recombine with a hole in the valence band with the emission of a photon with energy equal to the energy difference between the electron excited state and ground state, or valence band. The net radiative recombination rate is given by:

$$U_{rad,net} = B_{rad} \cdot (np - n_i^2) \tag{2.19}$$

where B_{rad} is the radiative recombination coefficient and is a material property as it depends on the intrinsic carrier concentration, n_i, the bandgap of the material, its absorption as well as the optical properties of the structure. The radiative recombination is very small for indirect bandgap semiconductors such as silicon (10^{-15} cm^3s^{-1}) compared to direct bandgap semiconductors such as GaAs (10^{-10} cm^3s^{-1}). When the system is in thermodynamic equilibrium, no net emission takes place.

2.3.2.**Auger Recombination**

In Auger recombination, the collision of two similar carriers results in one carrier losing its energy and recombining with a carrier of opposite polarity while the second carrier gains the kinetic energy and is therefore excited to a higher state before losing its energy usually in the form of heat, and subsequently returning to its original energy state. The Auger recombination rate is expressed as:

$$U_{Aug} = (C_n n + C_p p)(np - n_{i,eff}^2) \tag{2.20}$$

where C_n and C_p are material specific coefficients. The coefficients can be extended to be temperature dependence such that:

$$C_n(T) = \left(A_{A,n} + B_{A,n}\left(\frac{T}{T_0}\right) + C_{A,n}\left(\frac{T}{T_0}\right)^2\right) \cdot \left[1 + H_n \cdot e^{-\frac{n}{N_{0,n}}}\right] \tag{2.21}$$

and

$$C_p(T) = \left(A_{A,p} + B_{A,p}\left(\frac{T}{T_0}\right) + C_{A,p}\left(\frac{T}{T_0}\right)^2\right) \cdot \left[1 + H_p \cdot e^{-\frac{p}{N_{0,p}}}\right] \tag{2.22}$$

where $T_o = 300\ K$. A_A, B_A, C_A, and H are fitting parameters for electrons and holes and are material specific parameters. At high injection levels, the Auger coefficient decreases and therefore H is used to empirically model this effect. This mechanism is usually important in highly doped materials or under high injection conditions.

2.3.3.**SRH Recombination**

Shockley-Read-Hall (SRH) recombination is the most important recombination process in semiconductors. SRH recombination accounts for non-radiative recombination through defects or traps states. The trap-assisted recombination process occurs when an electron relaxes down to the defect level from the conduction band and then from the defect level to the valence band by exploiting a two-step process. Defect states close to the band edge usually capture and release one type of carriers are referred to as trap states. While defect levels deep in the bandgap are referred to as recombination centers. The net SRH recombination rate per unit volume per second through a single level trap located at energy $E = E_t$ within the forbidden bandgap is given by:

$$U_{SRH,net} = \frac{np - n_i^2}{\tau_{SRH,p}(n + n_t) + \tau_{SRH,n}(p + p_t)} \tag{2.23}$$

where $\tau_{SRH,n}$ and $\tau_{SRH,p}$ are the SRH carrier lifetimes for electrons and holes, respectively, and n_t and p_t are the trap concentrations at the trap level and are given by

$$n_t = n_i e^{\frac{E_t - E_i}{K_B T}} \quad \text{and} \quad p_t = n_i e^{\frac{E_i - E_t}{K_B T}} \tag{2.24}$$

where E_t is the energy level associated with the defect, E_i is the intrinsic energy level. It is worth noting that the maximum value of $U_{SRH,net}$ occurs when E_t is exactly in the middle of the bandgap. For equal capture times, the maximum value of $U_{SRH,net}$ occurs when $n = p$, as shown in Figure 2.3.

Equation (2.23) further simplifies in the quasi-neutral region of a doped semiconductor where either $n \gg p, n_t, p_t$, or $p \gg n, n_t, p_t$. Under these conditions, the minority carrier recombination rate in n- or p-type material becomes

$$U_{SRH,n-type} = \frac{\Delta p}{\tau_{SRH,p}} \quad \text{and} \quad U_{SRH,p-type} = \frac{\Delta n}{\tau_{SRH,n}} \tag{2.25}$$

where Δn and Δp are the excess minority carrier concentrations.

Defects are more likely to occur at surfaces and interfaces between different materials. Surface recombination process is described in a very similar manner to bulk SRH theory but in this case surface recombination is a 2-dimensional recombination process. The net surface recombination rate per unit area can be expressed by:

$$U_{surf,net}^{SRH} = \frac{np - n_i^2}{\frac{(n + n_t)}{S_p} + \frac{(p + p_t)}{S_n}} \tag{2.26}$$

where S_p and S_n are the surface recombination velocities (SRV) for holes and electrons, respectively, and is expressed in units of cm/s.

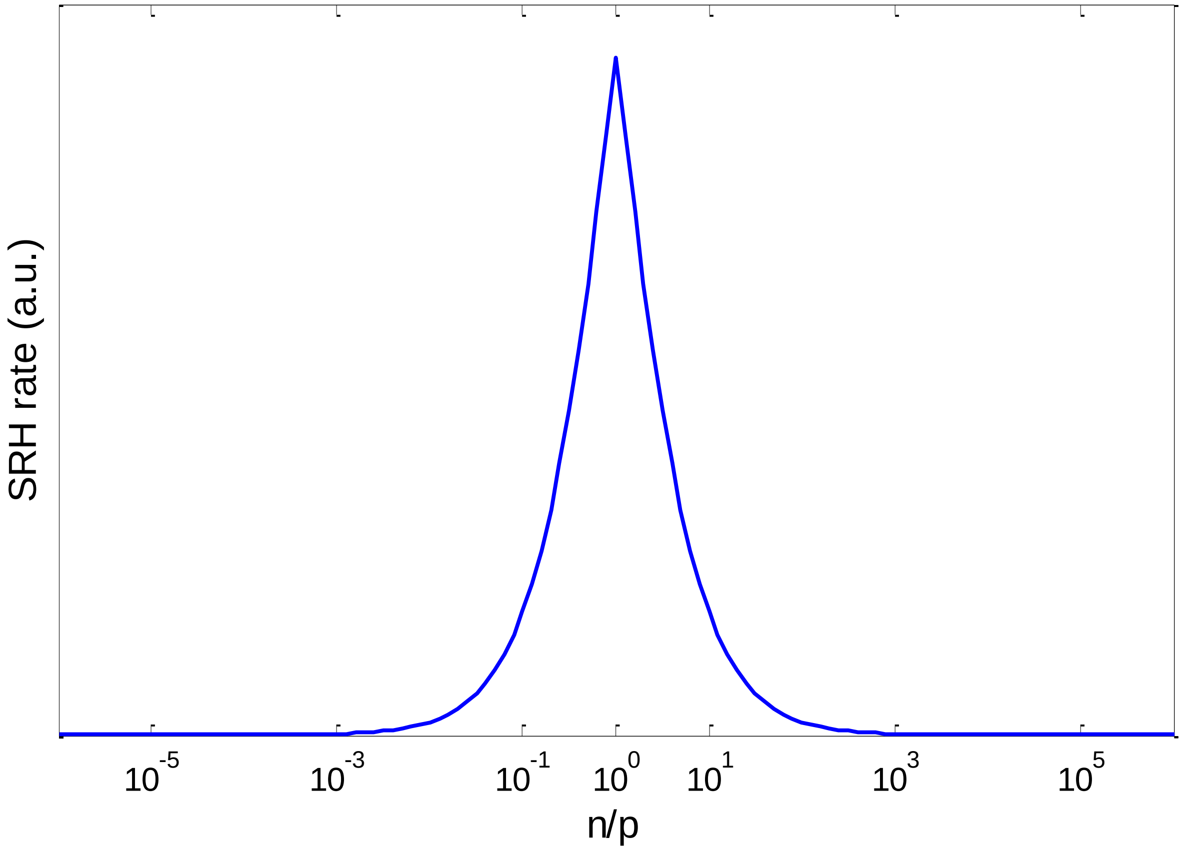

Figure 2.3. SRH recombination rate as a function of the ratio n/p for trap level at the middle of the bandgap and equal capture times for electrons and holes.

2.4. Effective Carrier Lifetime

An expression of lifetimes for each recombination mechanism can be derived:

$$\tau_{n,rad} = \frac{1}{B_{rad}N_A} \quad \text{and} \quad \tau_{p,rad} = \frac{1}{B_{rad}N_D} \tag{2.27}$$

The minority carrier lifetimes are modeled empirically based on doping dependent equation as follows:

$$\tau_{n,dop}(N_{A,0}) = \tau_{min} + \frac{\tau_{max} - \tau_{min}}{1 + \left(\frac{N_{A,0}}{N_{ref}}\right)^{\gamma}} \quad \text{and} \quad \tau_{p,dop}(N_{D,0}) = \tau_{min} + \frac{\tau_{max} - \tau_{min}}{1 + \left(\frac{N_{D,0}}{N_{ref}}\right)^{\gamma}} \tag{2.28}$$

where τ_{min}, τ_{max}, N_{ref} and γ are material constants.

In n-type doped material, the hole lifetime for a two electron collision followed by a recombination with a hole is given by:

$$\tau_{p,Aug} = \frac{1}{C_n N_D^2} \tag{2.29}$$

Similarly, in p-type doped material, the electron lifetime for a two hole collision followed by a recombination with an electron is given by:

$$\tau_{n,Aug} = \frac{1}{C_p N_A^2} \tag{2.30}$$

The effective lifetime is combination of all lifetimes and therefore can be expressed as

$$\frac{1}{\tau_{eff}} = \frac{1}{\tau_{rad}} + \frac{1}{\tau_{SRH}} + \frac{1}{\tau_{Aug}} \tag{2.31}$$

2.5. Solar Spectrum

Photovoltaics convert the incident solar spectrum into electricity. The incident solar spectrum that is emitted from the sun is composed of photons with a distribution of energies, or in other words, with different wavelengths. The surface of the sun is maintained at a temperature of approximately 5800 K and the sun radiation can be modeled as a black body emission according to Plank's law [25]

$$F(\lambda, T) = \frac{2\pi h c^3}{\lambda^5 (e^{hc/\lambda k_B T} - 1)} \tag{2.32}$$

where F(λ) is the spectral irradiance. Equation (2.32) represents the irradiance at the surface of the sun in W/m^2 per unit wavelength in m with a total power density of 63 MW/m^2. By the time this energy has traveled 150 million km to the earth, the total extraterritorial power density decreases to almost 1367 W/m^2, which is referred to as solar constant. Using equation (2.32) and considering the sun's radius and the distance from the sun to the earth, the black body radiation at T = 5800 K just outside the earth's atmosphere can be used to model the extraterrestrial spectrum, AM0, as shown in Figure 2.4.

It is important to distinguish between the irradiance at the top of the earth's atmosphere and the irradiance reaching the surface of the Earth. While the former is mostly constant, the latter is affected by many factors including latitude, time of day and year, cloud cover, and absorption/scattering in the atmosphere. For example the Ozone absorbs a significant amount of radiation in the ultraviolet region, while water vapor and carbon dioxide absorb primarily in the visible and infrared parts of the spectrum. The amount of sunlight either scattered or absorbed depends on the length of the path through the atmosphere, which is quantified using air mass (AM). The air mass is defined as

$$\text{AM} = \frac{1}{cos\theta_z} \tag{2.33}$$

where θ_z is the zenith angle or the angle between a line pointing at the sun and the normal to the earth's surface. At a zenith angle of zero degrees the sun is directly overhead and the air mass value is 1 (AM1). For altitudes higher than sea level the air mass is less than unity and hence AM0 represents the irradiance above the Earth's atmosphere (extraterrestrial spectrum). For zenith angles larger than zero, the air mass is larger than unity. For example, AM2.0 is when the Sun makes a 60° angle with the vertical (meaning light effectively travels through twice as much atmosphere).

Scattered sunlight that reach the earth's surface are called diffuse radiation, while parallel rays that reach the earth's surface are called direct radiation. Therefore at a given air mass the two components, direct and diffuse, make up the global spectrum. The AM1.5 ($\theta_z = 48.19°$) is the standard spectrum for characterizing solar cells because it represents "a reasonable average for the 48 contiguous states of the United States of America over a period of one year" as quoted by the national renewable energy laboratory (NREL) [26]. The direct component of the AM1.5 spectrum is usually used to characterize concentrated photovoltaic systems, and is denoted as AM1.5D. While for unconcentrated photovoltaic systems the total global AM1.5 spectrum is used as the standard spectrum and is denoted as AM1.5G.

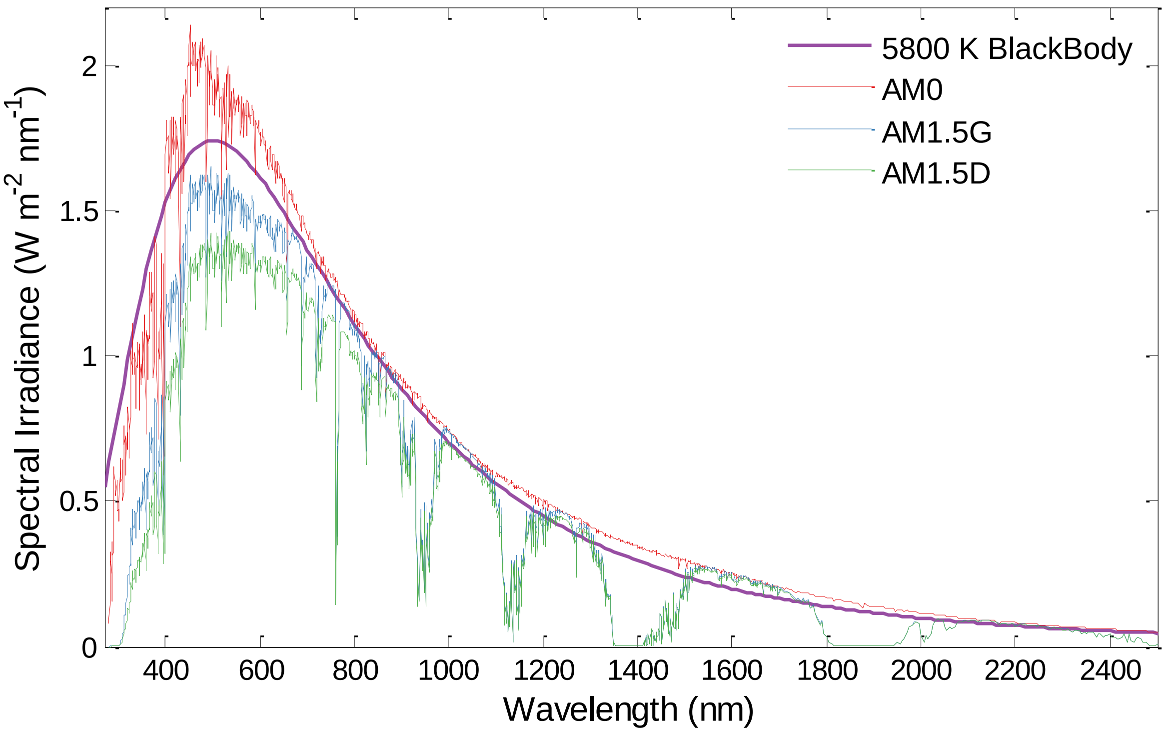

Figure 2.4. Comparison between extra-terrestrial (AM0) solar spectrum (red line) and black body radiation at temperature 5800 (purple). The standard spectrum AM1.5G (blue line) and AM1.5D spectrum (green line), where G and D stand for global and direct, respectively, are also shown.

2.6. Solar Cell *J*-*V* Characteristics

Semiconductor solar cells are *p*-*n* junctions where electrons and holes are excited within the semiconductor material, when the junction is illuminated. The junction separates these electrons and holes, and provides the electrical potential to drive them through an external circuit as current. The better the junction is at separating charge, the higher the voltage the solar cell can produce.

A typical planar *p*-*n* junction solar cell consists of a thick n- or p-type slab of semiconductor (substrate) with a thin p- or n-type layer (emitter). Current is extracted by electrical contacts to each region. When sunlight is incident from the top of the device, the current density-voltage (*J*–*V*) behavior of an ideal *p*-*n* junction solar cell is:

$$J(V) = J_L - J_0\left(e^{\frac{qV}{nk_BT}} - 1\right) \tag{2.34}$$

where J is the total current density of the solar cell, J_L is the light generated current density, J_o is the saturation current density, V is the voltage, and n is the ideality factor.

The light generated current density, J_L, is determined by how many photocarriers are excited and collected by the device. The dark current (or saturation current), J_o, describes how "leaky" the junction is. The larger the J_o, the worse the junction is at separating the photocarriers. The -1 term can usually be neglected since the exponential term is much greater than 1. The ideality factor is determined by the recombination mechanisms in the solar cell and will have an effect on the shape of the curvature of the *J*-*V* curve. For single junction solar cells, the ideality factor lies between n = 1 and n = 2. Figure 2.5 depicts a typical *J*–*V* curve of a single junction solar cell and is described by equation (2.34). Important parameters can be identified from the *J*-*V* curve and are the key descriptors of photovoltaic performance.

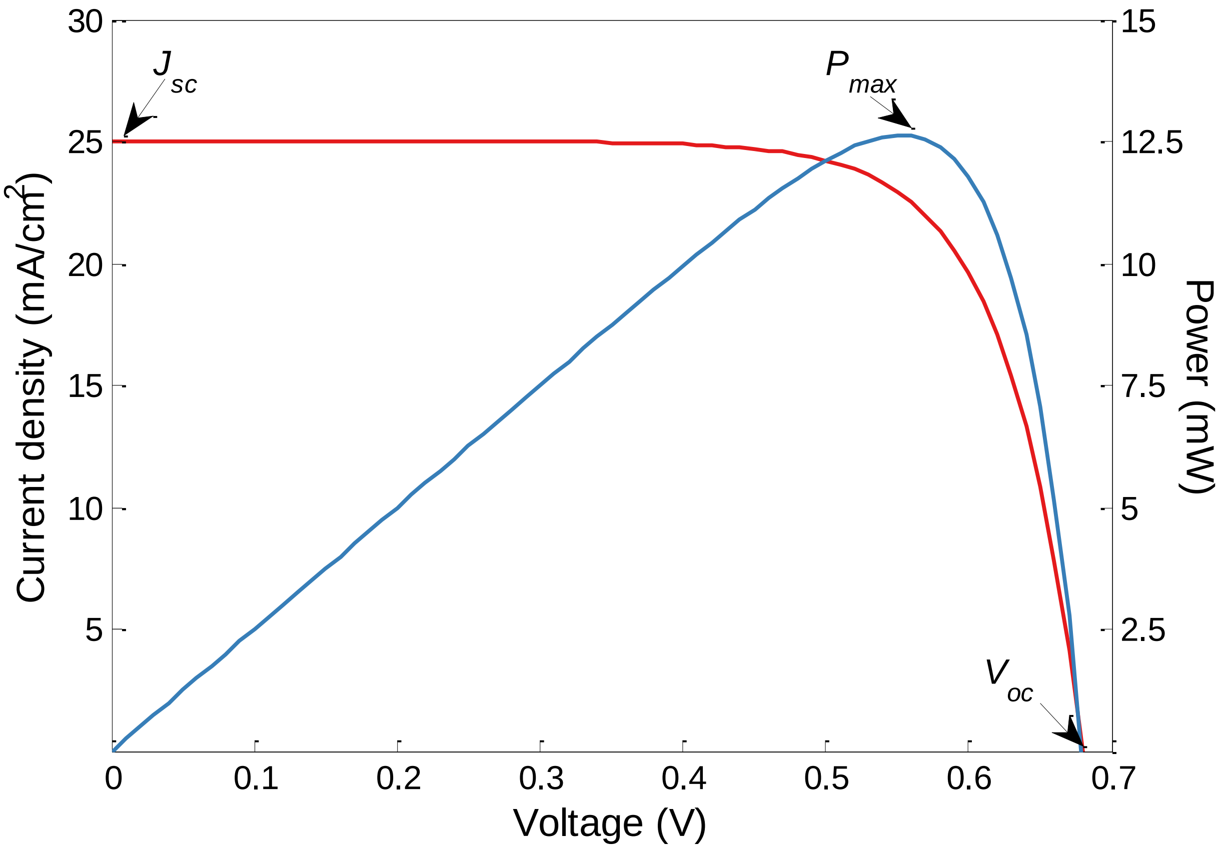

Figure 2.5. Typical *J*-*V* curve of a single junction solar cell calculated from equation 2.34.

The short-circuit current density (J_{sc}) is the current measured through the solar cell when the voltage across the solar cell is zero (V = 0). As can be seen from equation (2.34), at short-circuit condition J_{sc} is equal to J_L. However in the case of high series resistance, the measured short-circuit current, J_{sc}, is less than the light generated current, J_L.

The open-circuit voltage, V_{oc}, is the measured voltage at the solar cell output when the current is zero, and it is the maximum voltage available from a solar cell. It can be expressed as:

$$V_{oc} = \frac{nk_BT}{q}\ln\left(\frac{J_L}{J_0}+1\right) \tag{2.35}$$

The power generated by the solar cell is given by the product of the voltage and current, $P = JVA$, where A is the area of the solar cell. The maximum amount of power that the solar cell can produce, P_{max}, occurs at a maximum power point with certain voltage V_m and current density J_m. This determines the solar cell's conversion efficiency, η:

$$\eta = \frac{P_{max}}{P_{in}} = \frac{J_m \cdot V_m \cdot A}{P_{in}} = \frac{FF \cdot J_{sc} \cdot V_{oc} \cdot A}{P_{in}} \tag{2.36}$$

The quantity *FF* is the fill factor of the cell, which describes how closely the cell can operate to J_{sc} and V_{oc}. P_{in} is simply the total incident optical power on the device. The amount of sunlight striking a solar cell at any given time can vary greatly, depending on the time of day, weather conditions, etc. For this reason, solar cell efficiency is evaluated under standard test conditions. The Standard Test Condition (STC) is an AM1.5G spectrum with total incident intensity of 1000 W/m^2 and a cell temperature of 25 °C.

Solar cells can be modeled by an equivalent circuit model. The equivalent circuit model consists of a current source representing the incident light intensity in parallel with a diode, a nonlinear resistive element. Parasitic resistance can be added to the model in terms of series resistance, R_s, and shunt resistance, R_{sh}. Series resistance represent series resistive losses mainly at the contacts but also at the base, emitter and metal grid. Shunt resistance represents leakage of current throughout the device. A schematic of the equivalent circuit model is shown in Figure 2.6 with R_s and R_{sh} resistances.

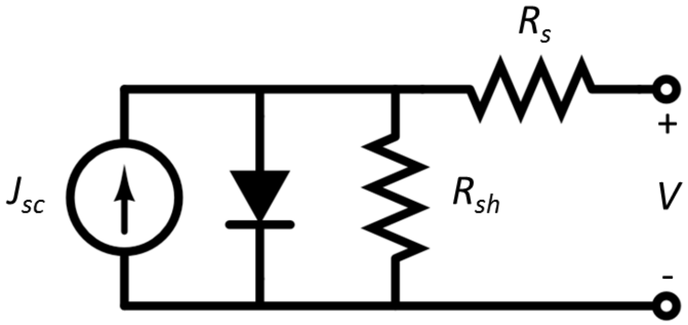

Figure 2.6. Equivalent circuit model for solar cell including series and shunt resistances.

The diode equation with parasitic resistances can be written as:

$$J = J_{sc} - J_0\left(e^{\frac{q(V+JAR_s)}{nk_BT}} - 1\right) - \frac{V + JAR_s}{R_{sh}} \qquad (2.37)$$

The effect of increasing the series resistance or decreasing the shunt resistance on solar cell *J-V* curve is shown in Figure 2.7. The *J-V* curves are obtained by simulating the equivalent circuit model shown in Figure 2.6 in LTSpice, a circuit simulator software, and changing the series resistance as in Figure 2.7 (a) or decreasing the shunt resistance as in Figure 2.7 (b). As can be seen from the curve, R_s should be as small as possible which means eliminating any possible resistive losses and ideally R_s is zero. While shunt resistance should be as large as possible with no leakage currents throughout the device, ideally R_{sh} is infinity.

2.7. Spectral Response and Quantum Efficiency

Quantum efficiency (QE) is an important measure of the spectral response of a solar cell. It is a measure of how good is the solar cell in converting an incident photon to electron-hole pair, and then collecting the carriers. The quantum efficiency for photons with energy below the band gap is therefore zero.

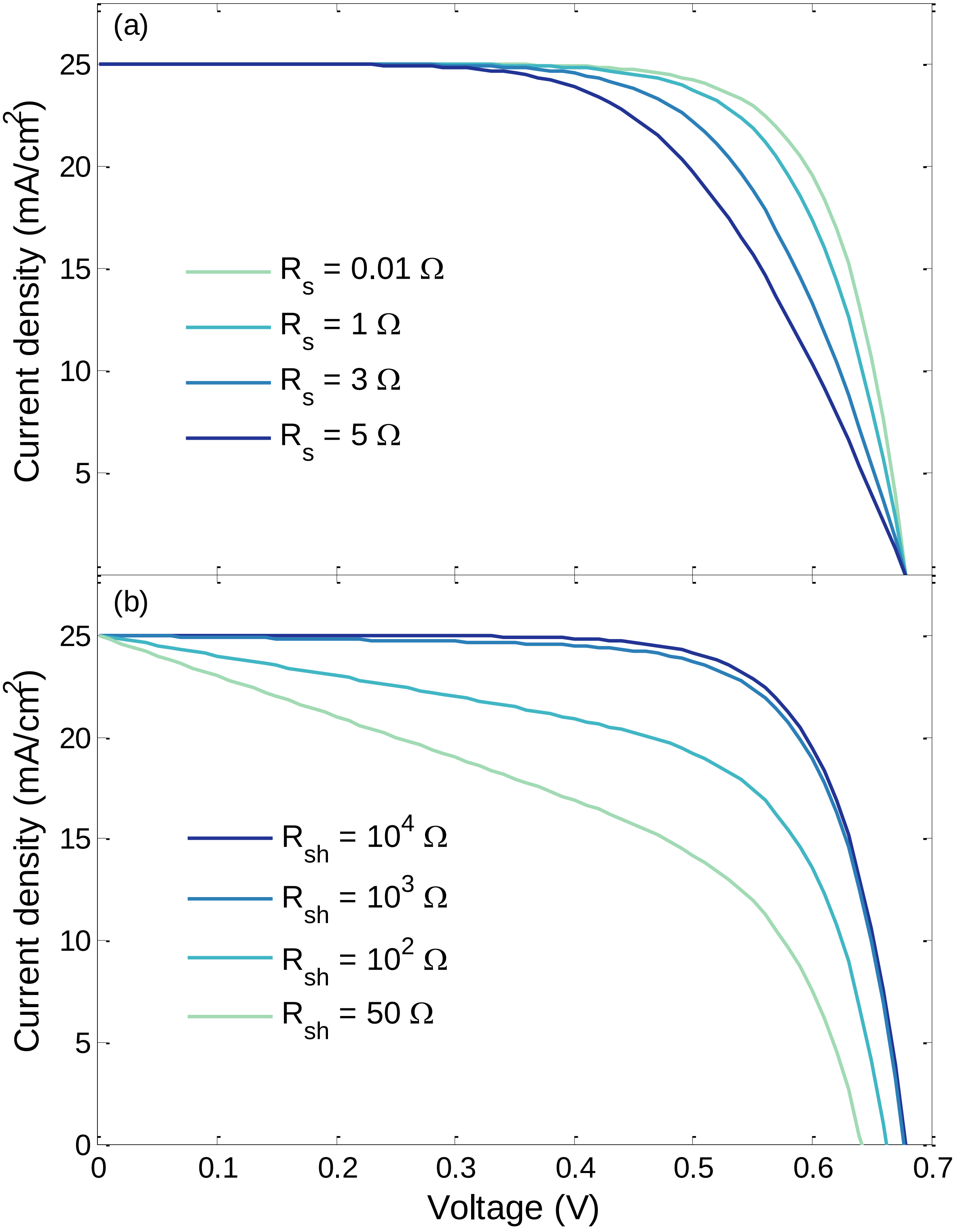

Figure 2.7. Effect of (a) increasing R_s and (b) decreasing R_{sh} on the *J*-*V* characteristics of a solar cell.

Two types of quantum efficiency of a solar cell are considered: External quantum efficiency (EQE) and internal quantum efficiency (IQE). EQE is defined as the ratio of the number of carriers contributing to the electrical current under short-circuit conditions to the number of incident photons with energy E_{ph}, therefore EQE is given by

$$EQE(\lambda) = \frac{J_{sc}(\lambda)}{q\phi(\lambda)} \tag{2.38}$$

where $\phi(\lambda)$ is the photon flux (photons/m^3) and is given by:

$$\phi(\lambda) = \frac{I_{in}(\lambda)}{hc/\lambda} = \frac{I_{in}(\lambda)}{E_{ph}(\lambda)} \tag{2.39}$$

where I_{in} is the incident spectral irradiance. IQE is defined as the ratio of the number of collected carriers contributing to the electrical current under short-circuit to the number of absorbed photons by the active layer of the solar cell, hence IQE is given by:

$$IQE(\lambda) = \frac{J_{sc}(\lambda)}{q\phi(\lambda)A_{\mathrm{PV}}(\lambda)} = \frac{EQE(\lambda)}{A_{\mathrm{PV}}(\lambda)} \tag{2.40}$$

where $A_{\mathrm{PV}}(\lambda)$ is the absorption in the active layer. IQE eliminates the effects of front surface reflectance, parasitic absorption, and transmittance at the back surface and therefore is higher than EQE but always less than 1. The solar cell's short-circuit current density is related to the EQE through

$$J_{sc} = q\int \phi(\lambda)\cdot EQE(\lambda)d\lambda \tag{2.41}$$

Another important parameter for solar cells and is related to the QE is the spectral response. The spectral response (SR) is defined as the ratio of the generated current by the solar cell to the incident power, where QE can be either IQE or EQE:

$$SR(\lambda) = q\frac{QE(\lambda)}{E_{ph}(\lambda)} \tag{2.42}$$

The quantum efficiency (both internal and external) and spectral response (both internal and external) of a typical silicon solar cell simulated in TCAD Senturus are shown in Figure 2.8. The reflectance is reduced by placing an optimized ARC composed of a silicon nitride (Si_3N_4) layer of thickness 80 nm. ARC is a thin non-absorbing thin film that is applied to the solar cell surface to reduce reflection. The thickness of the film is chosen specifically so that destructive interference occurs between waves reflected from the semiconductor and waves reflected from the top surface of the ARC layer so that no reflection. The thickness is calculated so that the wavelength in the dielectric material is one quarter the wavelength of the incoming wave and be calculated as follows:

$$d = \frac{\lambda}{4n} \tag{2.43}$$

where d and n are the ARC thickness and refractive index, respectively. Since Si_3N_4 has a refractive index of 2, therefore according to equation (2.43) an 80 nm thick layer would give zero reflection at 640 nm, as indicated in Figure 2.8.

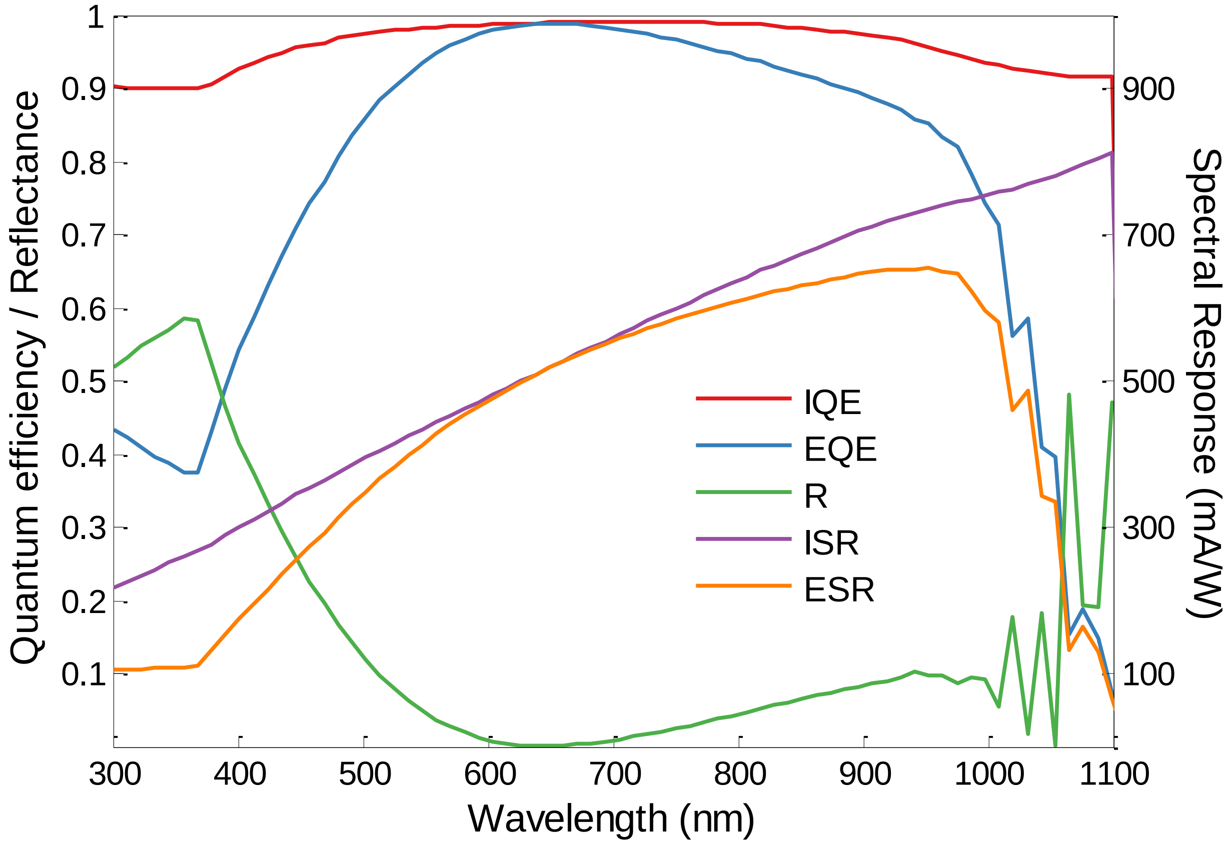

Figure 2.8. Quantum efficiency and spectral response of a simulated silicon solar cell in TCAD Sentaurus.

2.8. Efficiency Limits

Shockley-Queisser limit has long been recognized as the theoretical limit of the efficiency of an ideal single p-n junction solar cell [4]. The limiting efficiency is achieved based on the detailed-balance model which makes the following assumptions:

- A photon with energy greater than the bandgap of the cell is absorbed and generates an electron-hole pair with an IQE of 1.
- Only radiative recombination is allowed. That is, there are no recombination centers which reduce the lifetime and hence the collection efficiency of carriers that are a common feature of the materials that make real cells. Essentially, this and the previous point mean that the absorber is a perfect defect-free material with IQE = 1.
- Finally, the detailed-balance model makes the assumption that the number of photons absorbed by the cell must be equivalent to the number of photons reemitted through radiative recombination plus the number of electron-hole pairs extracted at the cell chemical potential by the contacts. The influence of photon recycling whereby the radiative recombination of electron-hole pairs are re-absorbed is accounted for in this theoretical limit.

The black body spectrum is frequently used in the literature as the incident spectrum since it eases the calculation and gives an analytical set of equations that can be used to quickly estimate the detailed-balance efficiency of a given cell. However, in this work we will be using an actual spectrum for comparison of the performance of various cell designs. The spectra used in the analysis are AM0, AM1.5G and AM1.5D, as shown in Figure 2.4.

The operating current density of a single-junction cell is calculated by a simple current balance defined as

$$J = q\left(\int G_{opt}dV - \int UdV\right) \tag{2.44}$$

where G_{opt} is the net optical generation rate of electron-hole pairs due to the incident solar spectrum, and U is the net recombination rate. The first term is the total generation of the electron-hole pairs throughout the volume per area is denoted as J_L, the light generated current density. The second term is the net recombination rate and in detailed balance calculations only radiative recombination is assumed. Substituting for the radiative recombination rate and integrating over the volume we can reach to the solar cell equation as [4]:

$$J(V) = J_{sc} - J_0\left(e^{\frac{qV}{k_BT}} - 1\right) \tag{2.45}$$

where the ideality factor is assumed 1 and J_{sc} is assumed equal to J_L. The short-circuit current is simply the integration of the incident photon flux for a given bandgap. The saturation current is dependent on the rate of radiative recombination at equilibrium and is given by:

$$J_0 = q\frac{2\pi k_BT}{h^3c^2}\int_{E_g}^{\infty}\frac{E^2}{e^{E/k_BT} - 1}dE \tag{2.46}$$

The integral is solved numerically. Now the open-circuit voltage is calculated by setting the current in equation (2.45) to zero:

$$V_{oc} = \frac{k_BT}{q}\ln\left(\frac{J_{sc}}{J_0} + 1\right) \tag{2.47}$$

Finally to find the efficiency we have to find the maximum power generated by the solar cell as a ratio of the incident power, as in equation (2.36). The maximum power point on J-V curve occurs at $V = V_m$ and $J = J_m$ where the product $P_m = J_m * V_m$ gives the largest possible power output of the device. The maximum power point is found by solving

$$\left.\frac{\partial \mathrm{P}}{\partial V}\right|_{V=V_m} = \left.\frac{\partial(JV)}{\partial V}\right|_{V=V_m} = \left.\left[J + V\frac{\partial J}{\partial V}\right]\right|_{V=V_m} = 0 \tag{2.48}$$

Eliminating J_{sc} from equation (2.45) using equation (2.47) we can rewrite the J-V relation in terms of V_{oc} as:

$$J(V) = J_0 \left(e^{\frac{qV_{oc}}{k_B T}} - e^{\frac{qV}{k_B T}} \right) \tag{2.49}$$

Multiplying equation (2.49) by V and differentiating with respect to V as in equation (2.48) we get,

$$J_0 \left[e^{\frac{qV_{oc}}{k_B T}} - \left(1 + \frac{q}{k_B T} V\right) e^{\frac{qV}{k_B T}} \right] = 0 \tag{2.50}$$

We solve the equation numerically to find V_m and then substitute $V = V_m$ in equation (2.49) to get J_m. The product will yield the maximum output power as a function of bandgap. The fill factor can then be calculated as:

$$FF = \frac{V_m J_m}{V_{oc} J_{sc}} \tag{2.51}$$

Figure 2.9 shows the calculated J_{sc}, V_{oc}, FF, and η as a function of bandgap energy for AM0, AM1.5G and AM1.5D spectra. The first observation is that the J_{sc} is higher for AM0 than AM1.5G since it has a higher power density (more photons) and therefore it is expected to have higher J_{sc}. The second observation, it is not surprising that J_{sc} increases as the bandgap decreases, since smaller bandgap materials can absorb more photons and hence suffer less from transmission losses where photons with energies below the bandgap are transmitted.

The open-circuit voltage increases almost linearly with increasing bandgap and shows very small dependence on the spectrum, as shown in Figure 2.9 (b) where the three curves for the three spectra lie on top of each other. This is expected since V_{oc} should be larger for larger bandgap materials. Analytically V_{oc} increases logarithmically with the ratio of J_{sc} to J_o, as in equation (2.47). Since J_o decreases significantly for larger bandgaps V_{oc} increases with increasing bandgap.

Fill factor shows an insignificant dependence on the spectrum, as shown in Figure 2.9 (c), and increases rapidly before reaching a plateau with increasing bandgap. As defined in equation (2.51) the fill factor depends on both J_{sc} and V_{oc} as well as the maximum power, P_{max}. Fill factor is generally reduced from recombination losses as well as series and shunt resistances.

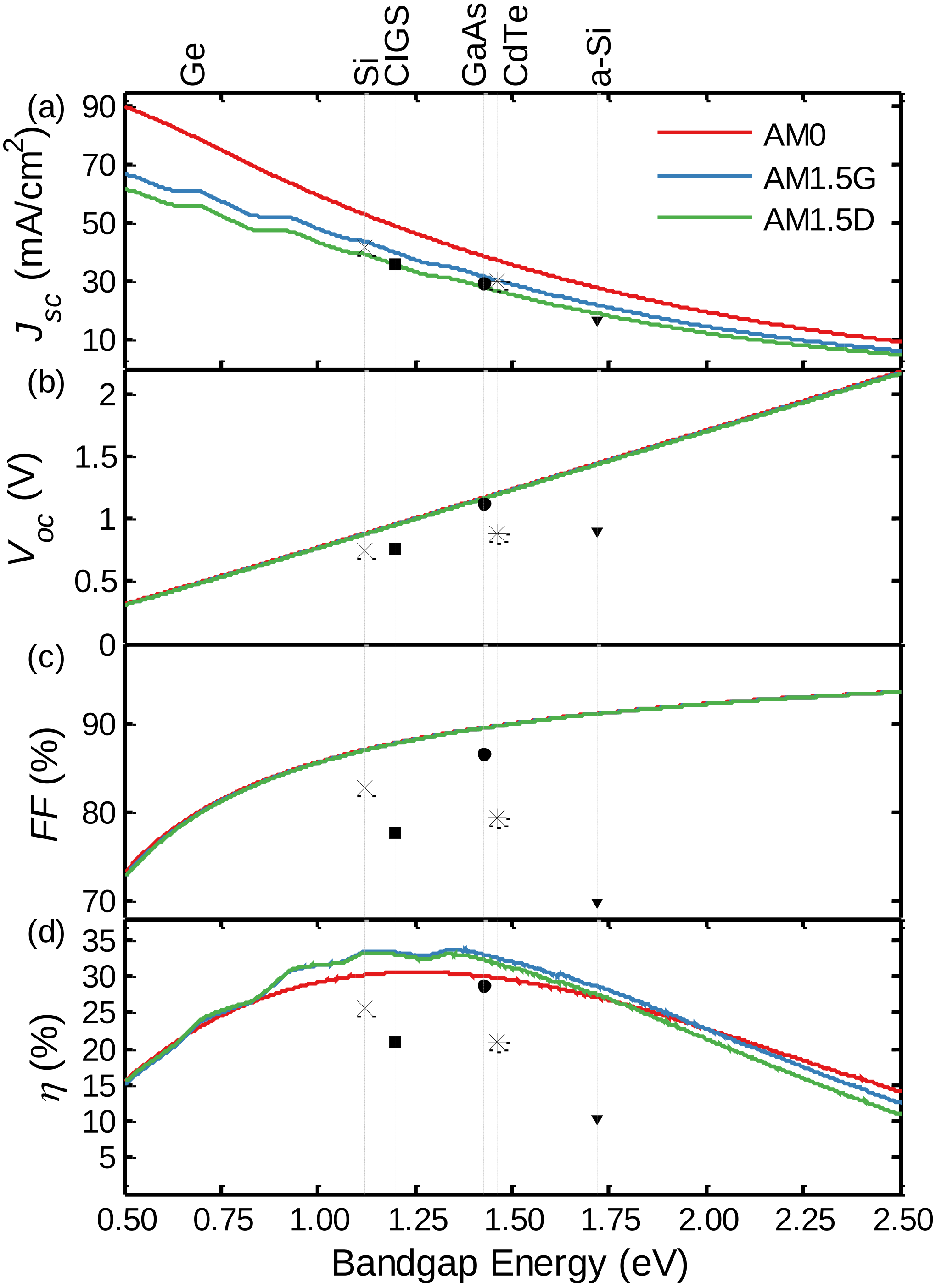

Figure 2.9. Dependence of the (a) short-circuit current density, J_{sc}, (b) open-circuit voltage, V_{oc}, (c) fill factor, *FF*, and (d) conversion efficiency as a function of bandgap energy in eV. Each incident photon with energy higher than bandgap is assumed to generate one electron and contribute to the total current under

three different spectra: AM0 (1349 W/m^2), AM1.5G (1000 W/m^2) and AM1.5D (900 W/m^2) and at T=300 K. Figures of merits of record cells (Si, GaAs, CIGS and CdTe) under AM1.5G spectrum are shown in black markers. The inset is shown the small variations in V_{oc} and *FF* due to different spectra.

Finally, the conversion efficiency is shown in Figure 2.9 (d) and it depends on J_{sc}, V_{oc}, FF as well as the incident power, as in equation (2.36). Since J_{sc} decreases and V_{OC} increases with increasing bandgap energy, we expect the efficiency (product of J_{sc} and V_{oc}) to have an optimum value as a function of bandgap. The incident power densities are 1349 W/m^2, 1000W/m^2 and 900W/m^2 for AM0, AM1.5G and AM1.5D, respectively. The optimum bandgap range is in 1.1 – 1.45 eV with the highest efficiency of 33% at 1.3 eV calculated for the AM1.5G spectrum. It is not surprising that GaAs solar cells have the highest record efficiencies for single-junction solar cells under AM1.5G spectrum with efficiency of 28.8% [5].

Also shown on Figure 2.9 as dotted vertical lines are some of the common materials for solar cells such as silicon, GaAs, CdTe, CIGS, Ge and amorphous silicon (a-Si) with bandgaps of 1.12 eV, 1.43 eV, 1.46 eV, 1.2 eV, 0.67 eV and 1.72 eV, respectively. The J_{sc}, V_{oc}, *FF* and efficiency for the record cells are also shown in Figure 2.9 for materials silicon (square), GaAs (circle), CdTe (astric), CIGS (cross), and a-Si (triangle) according to the latest efficiency tables [5].

It is worth noting that for crystalline silicon (c-Si) the upper bound limit of the J_{sc} is 43.8 mA/cm^2 while for a-Si it is 21.9 mA/cm^2. Comparing the c-Si limit with the short-circuit current density exhibited by the record efficiency cells, which is about 41.8 mA/cm^2 for silicon, and 16.36 mA/cm^2 for a-Si [5]. Therefore it seems that for silicon technology and other technologies such as GaAs, CIGS and CdTe, light-trapping strategies are very effective in ensuring an absorbance close to unity.

For silicon, the estimated V_{oc} can be as high as 750 mV while the V_{oc} for the record c-Si solar cell is 740 mV and for the mc-Si solar cell is 667.8 mV [5]. The c-Si silicon V_{oc} is very close to the upper limit while the mc-Si has lower V_{oc} due to bulk and surface recombination losses which are inherent to the multicrystalline nature of the material.

Chapter 3: Down-Conversion and Down-shifting Processes

3.1. Introduction

Down-conversion refers to a process in which a high-energy photon is absorbed and two or more lower-energy photons are emitted, with expected quantum yield higher than 100%, where quantum yield represents the ratio of re-emitted photons at longer wavelengths to absorbed photons. On the other hand, down-shifting (DS) process is similar to DC, but there is only one photon converted for every photon absorbed and therefore the quantum yield of the conversion process cannot exceed 100%. Both DC and DS layers are located on the top surface of a solar cell, and they convert photons in the UV/blue region of the incident spectrum to photons in the visible or near-IR for efficient absorption in the solar cell. As DC and DS processes require only one photon per conversion event, the intensity of converted photons scales linearly with the incident light intensity.

Down-conversion was first introduced in the 1950s by Dexter using rare earth ions [13]. The process involved simultaneous energy transfer from a donor ion to two acceptors ions, each accepting half the energy of the excited donor ion. Lanthanide ions are the most common materials for DC due to their unique and rich energy-level structure which allow for efficient spectral conversion [27].

Down-shifting was first introduced in the late 1970s by Hovel to improve the poor UV spectral response of silicon, GaAs, amorphous silicon and CdS-Cu_2S solar cells [14]. DS layers can be applied to improve solar cells with poor blue response and mitigate surface recombination losses; however, thermalization losses cannot be mitigated. Shifting the photons in the UV region to wavelengths where the quantum efficiency of the solar cell is higher than in the UV region enhances the carrier collection and therefore can effectively enhance the overall conversion efficiency.

The DC or DS layers consists of a material with a certain bandgap E_g in which an intermediate level is located between the highest energy level, E_2 and the lowest energy level, E_0. In case of a semiconducting material, the bandgap corresponds to the difference between the conduction band and the valence band. In case of an organic dye, the bandgap corresponds to the difference between highest occupied molecular orbital (HOMO) and the lowest unoccupied molecular orbital (LUMO). Figure 3.1 summarizes the general mechanisms in DC and DS layers where absorption of incident high-energy photons and re-emission at lower energies, can be achieved with a three-level system. The absorption of a high-energy photon leads to an electronic transition from the lowest level to the highest excited level. In case of DC, a two-step emission of two lower-energy photons accompanied by the radiative recombination of an electron from the highest level to the intermediate level then from the intermediate level to the lowest level. Therefore for each incident photon, two or more low-energy photons are emitted which leads to generation of electron-hole pairs in the solar cell and thus an increase in the short-circuit current. On the other hand, for the DS case, a fast non-radiative recombination generally takes place between the highest level and the intermediate level; followed by photon emission due to the radiative recombination of an electron in the intermediate level to the lowest level. Although there is one photon emitted for each incident photon absorbed, an increase in the electron-hole pair generation is expected since the probability of collecting the photons by the solar cell is higher in the visible region than in the UV/blue region.

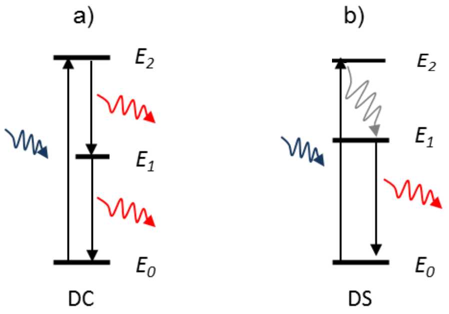

Figure 3.1. Schematic energy diagrams showing the different mechanisms in DC and DS. (a) A high energy photon (blue) is absorbed in the DC layer followed by emission of two lower-energy photons (red). (b) A high energy photon (blue) is absorbed in the DS layer and one lower-energy photon (red) is emitted with thermalization losses (grey).

Different materials can be used as DC or DS layers for all types of existing solar cells and can be categorized into three groups: rare-earth complexes, quantum dots, and organic dyes, as will be discussed in section 3.3 [28]. However there are some common properties that are desirable for these materials to have:

1. High quantum yield: Near unity PLQY for DS layers, and 200% or even 300% for DC layers.
2. Selective absorptivity: A relatively wide absorption spectrum is desirable to cover the region where the EQE of the cell is low due to interface recombination and window layer absorption. In addition the absorption coefficient has to be high in the short-wavelength region and near zero at longer wavelengths, thus transparent to long wavelength.
3. A narrow emission band where the emission peak coincides with the maximum EQE of the solar cell.
4. Absorption and emission overlap: The energy difference between the absorption and the emission spectra (Stokes' shift) has to be large enough to avoid losses due to re-absorption of the emitted photons.

Since DC and DS layers are located on the top surface of a solar cell, they disturb the reflectivity of the front surface of a solar cell. A low refractive index is usually desirable to minimize front reflections (more details will be discussed in chapter 4). On the other hand, re-emitted photons within the DC or DS layer can be directed to the solar cell by total internal reflection when the DC or DS layer has a high refractive index (ideally the same as the solar cell). Therefore it is very important to optimize the layer thickness of the DC or DS layer as well as decouple the DC or DS effect from the enhancement due to reflection losses from the front surface when studying the DC and DS processes. Decoupling the two effects is challenging, although it is easier from a modelling perspective as you can assume a DC or DS layer with zero PLQY. However, in experimental work it is very crucial in selecting the reference cell. Ideally the reference cell should have a non-absorbing layer but with a similar thickness and refractive index as the DC or DS layer. This is not feasible experimentally and therefore other techniques to decouple the two effects must be developed. Details of decoupling the effects by experimental data and optical modelling are discussed in Chapter 6.

Experimental work of DC and DS layers based on those three groups is summarized with most recent results in section 3.3. But first an overview of the efforts of modeling DC and DS from detailed balance to more practical studies is discussed in the next section.

3.2. Modelling

3.2.1. Upper Efficiency Limit

The Shockley-Queisser limit places the maximum solar conversion efficiency around 33% with a bandgap of 1.3 eV under the AM1.5G standard spectrum [4]. Trupke *et al* has studied the theoretical limit of DC for solar cells based on the hypothesis that no recombination losses occur when a DC layer is located on the front or rear surface of a single junction solar cell [11]. The schematic representation of the proposed model of a solar cell in combination with a DC layer is presented in Figure 3.2. In this case, the DC is a three-band system: (1) the absorption of a high-energy photon leading to a transition from the lowest level to the highest excited level representing a band-to-band transition, (2) a two-step recombination of the electron between the conduction band and an intermediate level and between the intermediate level and the valence band, accompanied by the emission of two lower-energy photons. These three types of transitions may be seen as three independent two-band systems with individual electrochemical potentials and can be represented by three solar cells C2, C3 and C4 that are connected in series. The two solar cells C3 and C4 with small bandgaps represent the intermediate transitions, whereas the band-to-band transitions are represented by C2. The DC is radiatively coupled to the solar cell which is represented by C1 in Figure 3.2.

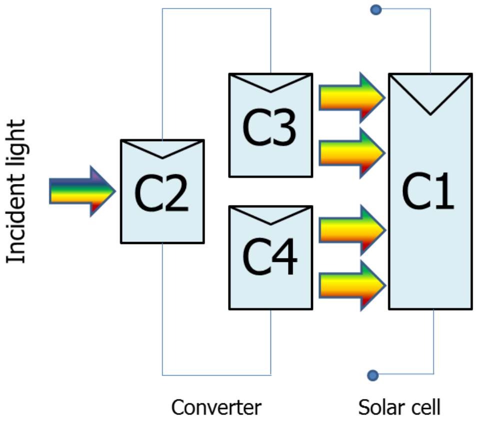

Figure 3.2. Equivalent circuit of the system. The luminescence layer is represented by three solar cells, C2, C3 and C4 connected in series representing the band-to-band transitions and the two intermediate transitions, respectively. C1 represents the solar cell.

Using the equivalent circuit model, the DC is described as follows: incident high-energy photons are absorbed by C2 which drives C3 and C4 into forward bias and causes them to emit photons, which are absorbed by the solar cell, C1.

A limiting efficiency of 39.63% is found for single-junction solar cell with bandgap of 1.05 eV for a rear-converter (RC). The refractive index of the solar cell and DC layer is assumed to be 3.6. For a front-converter (FC), the maximum efficiency is smaller, 36.8% for a bandgap of 1.1 eV, as shown in Figure 3.3. The efficiency decreases below the SQ limit for bandgaps higher than 2 eV since the down-converted photons are not absorbed by the solar cell and therefore are wasted. For smaller bandgap the maximum efficiency is lower than that for RC since only a portion of re-emitted photons (probably more than half) is directed towards the solar cell. If the absorption within the intermediate states is relaxed (only 1%) while allowing band-to-band absorption, a limiting efficiency of 38.6% is estimated for a bandgap of 1.1 eV. It was estimated that more than 90% of emission by the FC is in the direction of the solar cell for a solar cell and FC with refractive index of 3.6.

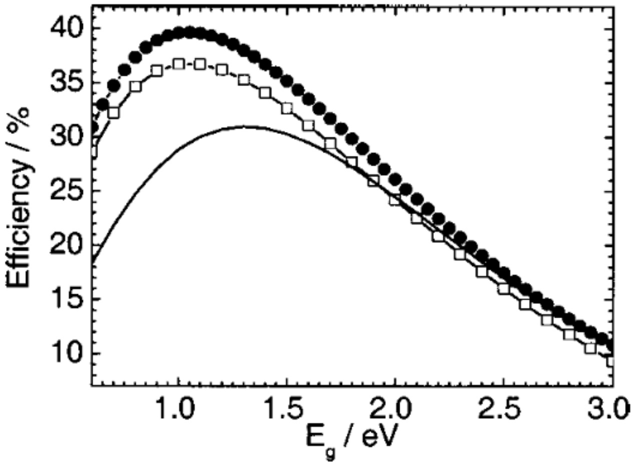

Figure 3.3. Efficiencies versus bandgap energy for Shockley–Queisser limit (solid line), downconverter at the front surface of a solar cell (empty squares), and downconverter at the rear surface of a bifacial solar cell. (solid circles). Reproduced with permission from [11].

Badescu *et al.* enhanced the model by considering the effects of non-unity radiative recombination and reflection losses from the surface [29]. First, the results of *Trupke et al.* are qualitatively confirmed. Then when front reflections are included in the model the limiting efficiency for a single-junction solar cell with bandgap 1.1 eV drops from 31% to 22%. Still both FC and RC configurations exhibit larger efficiency than that of a single cell with 26% and 27%, respectively. Varying the radiative recombination for both converter and cell only increases the efficiency for high (near-unity) radiative recombination efficiency values. Interestingly, they report in this case that the RC combination yields a higher efficiency than the FC combination for high-quality solar cells, while for low-quality solar cells, this is reversed. Extending the model to include more realistic materials and considering different refractive indices of the solar cell and DC layer, lead to the conclusion that FC may not always be beneficial [30].

Depending on the refractive index of the DC layer, up to half of the photons can be lost to the environment. Increasing the refractive index, n_{DC}, to match that of silicon increases the total internal reflection but unfortunately increases reflection at the air–DC interface. A proposed solution is introducing a second antireflection layer between the DC and the semiconductor; in this case, the efficiency of the device becomes independent of n_{DC} [30]. The inclusion of antireflection coating and light trapping texture show a limiting efficiency of 39.9% for a solar cell with bandgap of 1.1 eV [30].

Table 3.1. Maximum conversion efficiency for non-concentrated solar radiation for bandgap energy of 1.1 eV. In all cases, solar cell and converter refractive index are assumed 3.6. Both rear converter (RC) and front converter (FC) configurations were modeled.

Surface reflections	DC	Optimum efficiency	Reference
No	-	30.9%	[4]
No	RC	39.63%	[11]
No	FC	38.6%	[11]
Yes	-	22%	[29]
Yes	RC	27%	[29]
Yes	FC	26%	[29]

3.2.2. Spectrum Modification

There have been several research groups investigating the potential enhancement of DC and DS layers by modelling their effects on a solar cell performance. A system of a solar cell coupled to a DC or DS layer can be modelled by modifying the incident spectrum and using this modified spectrum as input data for solar cell simulation models in device simulation software. In this case, the incident photon flux $\phi_{inc}(\lambda)$, is reduced by the absorption of photons in the DC/DS layer. The number of absorbed photons in the DC/DS layer $\phi_a(\lambda)$ is calculated from the absorption coefficient of the DC/DS material through the Beer-Lambert law. Since the DC/DS will re-emit at longer-wavelength, the photon flux of the emitted photons $\phi_e(\lambda)$ is calculated from the emission spectrum. Since only a fraction of the absorbed photons will be re-emitted, a PLQY factor is used to account for this fraction. In addition, due to the isotropic emission of the DC/DS layer, only a part of the emitted photons are used by the solar cell. Thus T_{trap} is another factor used to determine the fraction of the re-emitted photons that are directed to the solar cell, which must be integrated over all emission angles. Therefore the modified photon flux that serves as input data for the solar cell simulation model is given by:

$$\phi_{mod}(\lambda) = \phi_{inc}(\lambda) - \phi_a(\lambda) + PLQY \cdot T_{trap}(\lambda) \cdot \phi_e(\lambda) \qquad (3.1)$$

Solar cell simulation models have been developed in different software packages with PC1D being the most popular due to its simplicity. PC1D is developed by the University of New South Wales in Australia [31]. Other sophisticated software packages include TCAD Sentaurus [32], Silvaco [33] and Crosslight [34].

Conversion efficiency of mc-Si solar cell modeled in PC1D with and without DS layers was evaluated by Jestin *et al* [35]. A reference mc-Si solar cell with a 106 nm SiO_2 ARC layer is compared with mc-Si with silicon nanocrystals (Si-nC) based DS layers of variable thicknesses. The simulated reference cell has an efficiency of 15.5% and when coupled to DS layer the efficiency decreases to 14.3% and 14.7% for DS layer thickness of 235 nm and 677 nm, respectively. Only 50% of the re-emitted photons are assumed to reach the solar cell. A system efficiency of 15.0% is achieved when the DS layer thickness is decreased to 80 nm. A positive enhancement to the system efficiency of 0.2% and 0.4% (absolute) is observed when the surface recombination velocity is increased to 10^5 cm/s and 10^6 cm/s, respectively, suggesting that DS layer are effective for solar cells with poor UV spectral response. While in [36], Silvaco software tool is used to model a Si-nC based DS layer on top of mc-Si. PLQY was assumed 10% at an emission peak centered at 799 nm. A relative increase of 6% in short-circuit current was simulated under standard spectrum AM1.5G.

The PC1D model was used to model quantum dots (QDs) dispersed in a PMMA layer on top of a mc-Si as a function of the concentration of quantum dots [37], [38]. When calculating the emitted photons, 75% of photons are assumed to be directed to the solar cell due to total internal reflection in the DS layer and a QD quantum yield of 80% was assumed. Simulated results using the modified spectra show a relative increase of 10% in short-circuit current for high concentration of QD. It is worth mentioning that re-absorption of photons in QDs was not considered in the model and therefore the relative increase in short-circuit current represents an upper limit.

The model for QD as DS with silicon solar cell was extended for non-AM1.5G spectra, including varying air mass between 1 and 10, for global, diffuse and direct spectra [38]. Spectra were modeled using SPCTRAL2 [39]. Relative increases in short-circuit current of 9.6%, 6.3% and 28.6% for AM1.5 global, direct and diffuse spectra, respectively, were simulated. The diffuse spectrum achieved the highest increase due to high UV and visible content compared to global and direct spectra. Similar results were achieved for higher AM values but with a lower increase in efficiency due to lower UV and visible content of spectra compared to AM1.5.

Further modeling taking into account more realistic irradiation patterns (as measured by a Dutch meteorological station on a yearly basis) shows that the improvement in the short-circuit current varies between 7% and 23% and is linearly related to the average photon energy (APE) [40], [41]. A 12.8% relative increase in the annual short-circuit current for the Dutch climate was determined using the annual distribution of average photon energy values and its linear relation with short-circuit current, which is to be compared with the 10% increase in case of the AM1.5G spectrum.

While solar cells are designed and tested according to standard test conditions (1000 W/m^2 irradiation, AM1.5G global spectrum, and cell temperature of 25°C); outdoor conditions exhibit daily and seasonal variations that affect the incident spectrum. Spectral conditions for solar cells vary from AM0 (extraterrestrial) via AM1 (equator, summer and winter solstice) to AM10 (sunrise, sunset). The weighted APE can be used to parameterize such spectral variations [42]. APE (using the range 300 to 1,400 nm) of AM1.5G is 1.674 eV, while the APEs of AM0 and AM10 are 1.697 and 1.307 eV, respectively. Furthermore, the APE of the AM1.5 diffuse spectrum, which is blue rich, is calculated to be 2.005 eV. As DC and DS effectively red-shift spectra, the more blue an incident spectrum contains (high APE), the higher the gain that can be expected. Therefore DC and DS mounted on top surface of solar modules can be more beneficial for regions with high diffuse irradiation fraction of the incident spectrum.

A Monte Carlo ray-tracing model was presented, in which photon transport phenomena in the converter and solar cell system are coupled to nonlinear rate equations that describe luminescence [43]–[45]. An in-house ray tracer software called *Raylene* was developed at the Australian National University [43], [44]. The software is used to investigate the effect of using violet, yellow, orange Lumogen-F organic dyes with mc-Si and CdTe modules. The PLQY of the mixture of organic dyes was assumed >95% and that 87% of emitted photons reach the PV module. A 0.3% absolute increase in efficiency is observed for mc-Si module when a mixture of violet and yellow dyes are used as DS layer [43]. Comparatively, simulation results show an increase in the efficiency of CdTe modules from 9.6% to 11.2% which corresponds to a relative increase of 17% when using mixture of violet, yellow and orange organic dyes as DS layer [44]. While in [45] the model was used to help select candidate materials for up-conversion (UC) and DC, but was set up for use with rare earth ions. Results show that for DC layers, the potential gain in J_{sc} may reach 7 mA/cm^2, with an optimistic set of parameters.

Table 3.2. Selected modeling work on DS layers coupled to single-junction solar cells.

Solar cell	***η***	**DS material**	**PLQY**	**Δ*η***	**Spectrum**	**Software**	**Ref**
mc-Si	15.5%	Si-nC	-	-0.5%	AM1.5G	PC1D	[35]
mc-Si	14.2%	Si-nC	10%	0.9%	AM1.5G	Silvaco	[36]
mc-Si	14.49%	QDs	80%	1.33%	AM1.5G	PC1D	[33]
mc-Si	14.5%	QDs	80%	0.9%	AM1.5D	PC1D	[38]
mc-Si	14.5%	QDs	80%	4.15%	AM1.5d	PC1D	[38]
mc-Si	14.8	Lumogen-F	> 95%	0.3%	AM1.5G	Raylene/PC 1D	[43]
a-Si	6.5%	QDs	80%	0	AM1.5G	PC1D	[37]
CdTe	9.6%	Lumogen-F	> 95%	1.6%	AM1.5G	Raylene	[44]

3.3. Experimental Down-Shifting Layers

3.3.1. Rare-Earth Ions

Lanthanide ions have been used for a long time as efficient luminescent materials in glass matrices for spectral conversion for a wide range of applications such as fluorescent tubes, lasers, LEDs, television and computer displays, optical fibres, optical amplifiers, and optical waveguides [46]–[48]. Lanthanides are a group of elements where the 4f inner shell is filled with electrons. They are mostly stable in the trivalent form and the ions have the electronic configuration $4f^n5s^25p^6$ where *n* varies from 0 to 14. The partly filled inner shell is responsible for the optical properties of the lanthanides. The energy level diagrams for the trivalent lanthanide ions have been constructed by Dieke and extended by Wegh *et al* [49], [50].

Examining the possible energy transfer mechanisms in single and couple lanthanide ions is sketched in Figure 3.4. In Figure 3.4 (a) only one ion is used and after the excitation with one high energy photon (purple line), two visible photons (red lines) can be emitted or alternatively IR photons with possible competing non-radiative recombination at different levels. The emission of two photons after absorption of a photon within one ion is usually referred to as quantum cutting. while if the emission of two photons is due to energy transfer between two different ions then it's called down-conversion, analogous to up-conversion [27]. Energy transfer between two ions can take one of the following three mechanisms, as shown in Figure 3.4 (b-d). Figure 3.4 (b) shows the emission of two photons from ion pairs via cross-relaxation between ions I to II (denoted by (1)) followed by energy transfer from ions I to II (denoted by (2)). Both energy transfer steps are followed by emission from ion II. Figure 3.4 (c-d) show mechanisms involving a single energy transfer between ions I and II and emission of photons by both ions. Several types of energy transfer processes between two rare earth ions can occur, especially in highly doped materials. The dominant mechanism behind this is usually the dipole–dipole resonant interaction between closely located ions. As the strength of the dipole–dipole interaction rapidly decreases with increasing distance between the ions, its overall importance depends strongly on the doping concentration, the host material, and the tendency of ions to form clusters.

The first experimental report of quantum yield above 100% was in 1974 and reported by two research groups where one ultraviolet photon (185 nm) is converted into two visible photons in YF_3:Pr^3 [51], [52], 20 years after the Dexter ‘s proposal of down-conversion in 1957 [53]. A UV photon is absorbed in the YF_3 host lattice, and the energy is transferred to the high energy $^1S_0$ level of Pr^{3+}. From there a visible photon (408 nm) is emitted after a transition to $^1I_6$ level followed by another transition to $^3H_6$ level where a second visible photon (620 nm) is emitted. This is an example of quantum cutting mechanism as shown in Figure 3.4 (a). The quantum yield was estimated to be 140 ± 15% [52]. Later, R. T. Wegh *et al.* showed the emission of two visible photons in $LiGdF_4$:Eu^{3+} when excited by a UV photon; however, in this case, two sequential energy transfer steps in the Gd^{3+}–Eu^{3+} couple were observed [27]. Here since the emission of the photons included energy transfer between Gd^{3+}–Eu^{3+} couple, it is referred to as down-conversion.

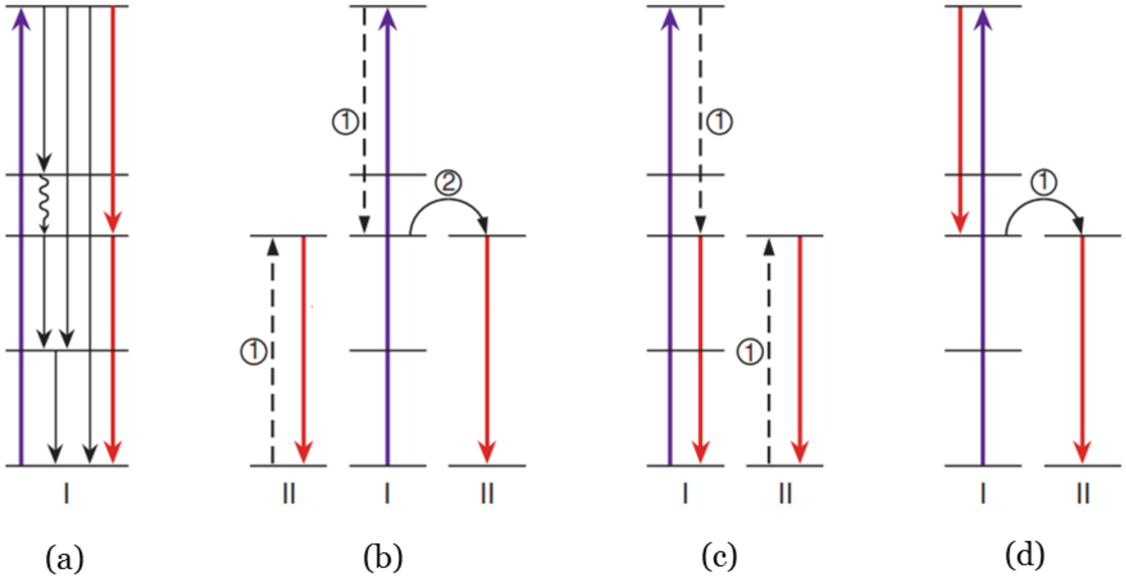

Figure 3.4. Quantum cutting mechanism for rare-earth ions: (a) two photon emission from single ion, and down-conversion mechanisms for rare-earth ions: (b) cross-relaxation from ion I to ion II and energy transfer from ion I to ion II, (c) cross-relaxation followed by emission from ions I and II and (d) emission from ion I followed by energy transfer to ion II then emission from ion II. Reproduced with permission from [27].

To that point the aim was to achieve quantum yield higher than unity with emission in the visible for light emitting devices. After the proposal of DC as a third generation technique for PV in 2002, lanthanides have gained attention as a potential candidate for DC layers. The first experimental demonstration of down-conversion for PV involved the Tb^{3+}–Yb^{3+} couple where quantum cutting was achieved through cooperative energy transfer from Tb^{3+} to two Yb^{3+} ions [54]. The experiment results in the emission of two photons at 980 nm from Yb^{3+} ions after cooperative energy transfer from an excitation at 485 nm, as shown in Figure 3.5. The energy transfer efficiency was estimated to be 88%. The DC quantum efficiency, η_{QE}, is related to the energy transfer efficiency, η_{ET}, by the following relation:

$$\eta_{QY} = \eta_I(1 - \eta_{ET}) + 2\eta_{II}\eta_{ET} \quad (3.2)$$

where η_I and η_{II} stand for the quantum efficiencies of the donor and acceptor ions (in this case Ce^{3+} and Yb^{3+}), respectively. Assuming that all the excited Yb^{3+} ions and the residual excited Ce^{3+} ions decay radiatively, i.e., $\eta_{Ce} = \eta_{Yb} =1$, the upper limit values of the DC quantum efficiency is calculated to be 188% [54].

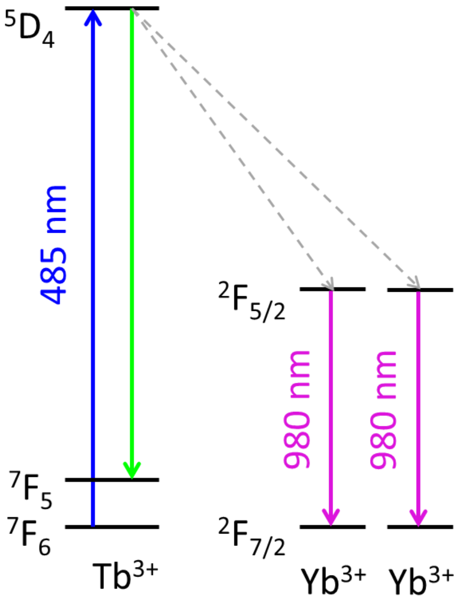

Figure 3.5. Schematic diagram of cooperative energy transfer from Tb to two Yb ions. Excitation of Tb^{3+} into the $^5D_4$ state is followed by energy transfer to two neighboring Yb^{3+} ions that are excited to $^2F_{5/2}$ state. Finally emission of 980 nm photons occurs after relaxation to the ground state of Yb^{3+}.

In two recent review papers, B.S. Richards and Strumpel *et al.* have presented the different single and couple lanthanide ions that could be considered for down-conversion for PV applications [55], [56]. The practical relevance of quantum cutting is, in fact, very limited for PV applications. Both in one-ion or two-ion systems, absorption is usually either in the vacuum UV, for example, the Pr^{3+} is excited at 185 nm or the Gd is excited at 202 nm, or in the UV-A and UV-B (280–360 nm), where there is no or very little irradiation in the terrestrial solar spectrum (~2% of total irradiation).

Considering the energy levels of all the lanthanide ions, it is evident that the energy-level structure of Ytterbium ion, Yb^{3+}, is ideally suited to be used in DC for PV applications. The Yb^{3+} ion has a single excited state denoted by $^2F_{5/2}$, which corresponds to emission range of 950 – 1150 nm peaking at 980 nm. The absence of other energy levels allows energy transfer from other lanthanides ions with higher excited states to Yb^{3+} emitting photons at 980 nm that can be efficiently absorbed by single-junction solar cells. Efficient DC by Yb^{3+} requires a donor ion with an energy level around 2.5 eV or higher and an intermediate energy level around 1.25 eV (equivalent to 980 nm). From Dieke's diagram one finds that there are several ions that can be coupled with Yb^{3+} such as Pr^{3+}, Er^{3+}, Nd^{3+}, Sm^{3+}, Dy^{3+}, and Ho^{3+} for a resonant two-step energy transfer process. Also cooperative sensitization is possible where energy transfer occurs from high excited state (250-500nm) of the donor to two neighboring acceptor ions without an intermediate level such as Tb^{3+}, as shown in Figure 3.5 [54], [57]. Selected systems for PV applications involving Yb^{3+} are reported in Table 3.3.

Most of the Yb^{3+} systems lack high absorptions and thus they present limited interest for solar energy conversion because the total amount of light which can be absorbed is small despite some impressive quantum yields. The luminescence intensity can be increased by using a broad-band absorbing ion such as Ce^{3+}. Unlike other trivalent lanthanides, Ce^{3+} has very high absorption cross section which originates from the allowed transition from the 4f ground state to the 5d excited one. Down-conversion for two near-infrared photons per absorbed blue photon was realized in the Ce^{3+}/Yb^{3+} ions co-doped borated glasses. Upon excitation of Ce^{3+} ion with an UV photon at 330 nm, two photons at 980 nm are emitted from the Yb^{3+} ions [58]–[60]. The cooperative energy transfer is initiated in the Ce^{3+} after excitation to the 5*d* followed by cooperative energy transfer to the $^2F_{5/2}$ state of Yb^{3+}, as depicted in Figure 3.6. The expected energy transfer efficiency and DC quantum yield are 74% and 174%, respectively [58], while in [59] the quantum yield was estimated to be much less due to non-radiative recombination.

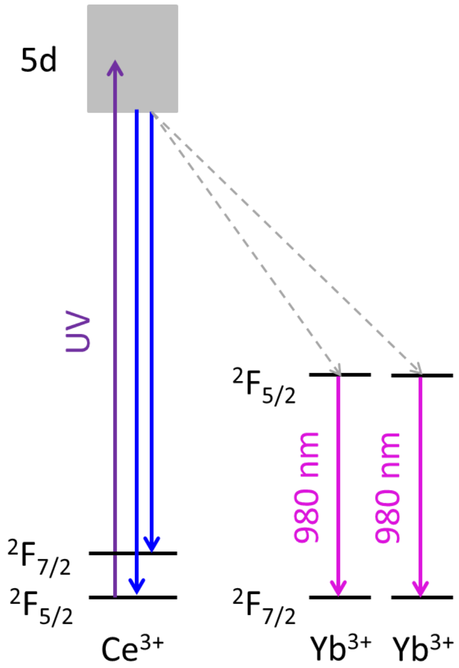

Figure 3.6. Schematic diagram of cooperative energy transfer from Ce^{3+} to two Yb^{3+} ions. Excitation of Ce^{3+} into the 5d level is followed by energy transfer to two neighboring Yb^{3+} ions that are excited to $^2F_{5/2}$ state. Finally emission of 980 nm photons occurs after relaxation to the ground state of Yb^{3+}.

The overall DC efficiency is enhanced by the introduction of an additional ion such as Tb^{3+} to the Ce^{3+}/Yb^{3+} couple in different host materials, despite the double energy-transfer Ce-to-Tb-to-Yb [61]–[63]. The energy transfer mechanism is shown in Figure 3.7. Haung *et al.* report an enhancement in Yb^{3+} emission intensity by a factor of 30 in the presence of Ce^{3+} [61]. However J. Sun *et al.* estimated the DC efficiency to be 132% [62]. In a more recent study it was reported that the near-infrared (NIR) emission intensity of Yb^{3+} in a tri-doped sample under excitation of 355 nm is 1.4 times that of Ce^{3+}–Yb^{3+} co-doped sample and is 23 times that of Tb^{3+}–Yb^{3+} co-doped phosphors with optimal composition [63].

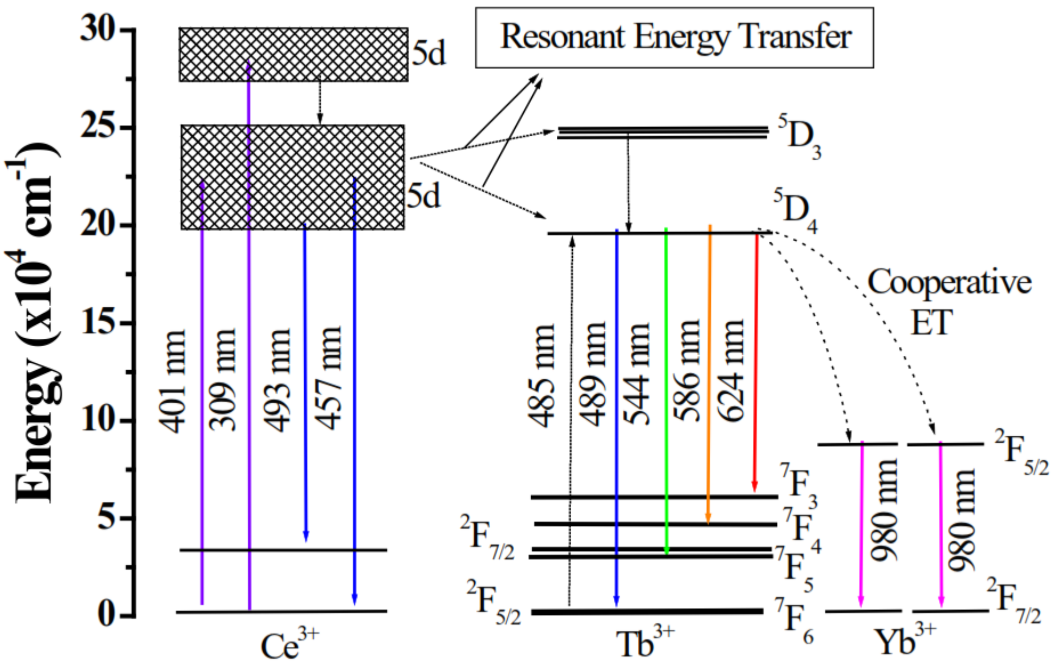

Figure 3.7. Schematic energy-level diagram of the ternary phosphor GdBO3:Ce,Tb,Yb. Dotted arrows denote either nonradiative or energy-transfer processes. Reproduced with permission from [61].

Until now, very few papers reported successful DC experiments with actual solar cells primarily due to the low quantum yields. In a recent paper, authors reported the coupling of a 3 mm sample of Pr^{3+}, Yb^{3+} codoped in Oxyfluoride glass to a 2 cm x 2 cm c-Si solar cell [64]. Despite a DC quantum yield of 158%, the EQE of the cell decreased after adding the DC layer. Two reasons may explain this deceptive result: reflection losses due to the added layer and, possibly, a lower quantum yield than initially calculated.

On the other hand, DS layers based on lanthanide ions are more popular. DS process is easier to put into practice than DC because there is no need to precisely match transition energies in the donor and acceptor ions. Eu is one of the most ions used in DS layers as it has many absorption lines in the UV spectral range and intense emission lines in the red spectral range. The absorption band extends from 200 – 440 nm and is centered at 310 nm. Whereas the emission band is in the range 580 – 650 nm with a main line at 612 nm related to the $^5D_0$ - $^7F_2$ transition and appears to be quite independent of the host material or the sensitizer [65].

Table 3.3. Selected DC systems containing Yb^{3+} ion and studied as potential candidates for enhancing the efficiency of silicon solar cells. The excitation, λ_{exc}. and emission, λ_{em}, wavelengths as well as the PLQY are indicated.

Sensitizer : Emitter	λ_{exc} (nm)	λ_{em} (nm)	PLQY	Ref
Pr^{3+} : Yb^{3+}	482	976	194%	[66]
Pr^{3+} : Yb^{3+}	441	980	140%	[67]
Pr^{3+} : Yb^{3+}	330	980	150%	[64]
Tm^{3+} : Yb^{3+}	474	970 - 1010	173%	[68]
Eu^{2+} : Yb^{3+}	260 - 400	980	164%	[69]
Nd^{3+} : Yb^{3+}	350	986	140%	[70]
Er^{3+} : Yb^{3+}	300 – 380 / 490	1000	195%	[71]
Er^{3+} : Yb^{3+}	350 – 415	1000/1540	~200%	[72]
Ho^{3+} : Yb^{3+}	287/535	985/1180	246%	[73]
Tb^{3+} : Yb^{3+}	488	1000	188%	[54]
Tb^{3+} : Yb^{3+}	485	1000	196%	[57]
Ce^{3+} : Yb^{3+}	330 (250 – 380)	980	174%	[58]
Ce^{3+} : Yb^{3+}	400 - 500	550/1030	96%	[59]
Ce^{3+} : Yb^{3+}	400 - 500	1000	60%	[60]
Tb^{3+}/Ce^{3+} : Yb^{3+}	320 - 390	980	132%	[62]
Tb^{3+}/Ce^{3+} : Yb^{3+}	320 - 390	980	110%	[63]

To our knowledge, the first demonstration of downshifting increasing the efficiency of both c-Si and a-Si solar cells dates back to 1997 [74]. Commercial c-Si PVC and a-Si PVC cells were coated with an organically modified silicate (ORMOSIL) composite phosphor films containing Eu^{3+} or Tb^{3+} ions. The rectangular sizes of the silicon cells were 2.5 x 5 and 5 x 8 cm for c-Si and a-Si, respectively. An absolute increase in the conversion efficiency of 1.2% was observed under AM1.5G illumination for the c-Si PVC cell coated with the ORMOSIL– Eu^{3+} complex, while the Tb^{3+} coating was detrimental. In order to lower the amount of light scattered by the ORMOSIL– Eu^{3+} complex coating, a silica gel layer was added resulting in an absolute increase in efficiency of 1.4%. The final absolute efficiency of the commercially available solar cell was 9.1%. Conversely, the efficiency of the a-Si PVC cell increased by 8% when an ORMOSIL– Tb^{3+} complex layer was added

[74]. It is worth mentioning here that despite the absolute enhancement in the cells, the conversion efficiencies of the cells are relatively low and therefore the impact when adding a DS layer is evident. In addition the reference cell was a bare cell with high reflection losses and these losses decrease by adding the DS layer. Therefore the increase in efficiency might be due solely to the decrease in reflection losses.

These results were confirmed 3 years later by the same authors [75]. The ORMOSIL–Eu^{3+} solution was dip-coated onto a quartz plate until a 300-nm thick film was obtained. A DS layer was then assembled from three such plates with Ag paste and coupled to commercially available c-Si PVC hybrid cells. The photovoltaic output of the composite device increased by 10–15% with respect to the uncoupled cell, that is adding about 1% to the absolute external quantum efficiency [75]. This is in fact a good performance because the absorption spectrum of the Eu^{3+} complex only marginally overlaps with the solar spectrum in the range of 300–390 nm, which represents merely 2% of the solar spectrum.

In another attempt, Eu^{3+} ions encapsulated into silicate glass by a sol-gel procedure resulted in a 1.03 mA/cm^2 increase in the short-circuit current density of a c-Si cell. [76]. In another report, a relative increase of 2.8% and 1.1% in the maximum power and short-circuit current density, respectively, of a silicon module were measured under AM1.5G conditions. [77]. A very recent report shows that Eu^{3+} incorporated in a PMMA matrix can enhance the UV response of a c-Si solar cell [78]. Only enhancement in the EQE was shown with estimation of 0.18% absolute increase in total efficiency. The authors argue that the introduction of Eu^{3+} ions not only enhances the cell by down-shifting effect, but also by protecting the PMMA from UV. They show good stability of the DS layer and PMMA at high temperatures. In addition, they perform a cost analysis claiming that adding a DS layer is cost effective.

Inorganic materials can be used as host materials for lanthanides ions such as Eu. In 2009, a study introducing Eu^{3+} ions into silica film by a sol-gel method as a DS layer for c-Si solar cell was reported. There was a ~10% relative increase in efficiency when the Eu was used as a DS layer [79]. To confirm the DS effect, the cell was compared with a solar cell with a silica film on the top surface so that there is almost no change in reflection losses when adding the Eu ions.

Other host materials such as $KCaGd(PO_4)_2:Eu^{3+}$ dispersed in PMMA were screen-printed on the top of the Si_3N_4 reflective layer of polycrystalline silicon solar cells to form a 3–4 mm thick film. Thus, the efficiency of the solar cells increased by 0.5% due to the conversion of 350–400 nm photons into red photons (580–710 nm) and to a lower reflectivity [80]. Screen-printed c-Si cells are drawing attention and downshifting has also been applied in an effort to improve their overall efficiency. Since lanthanide-doped inorganic phosphors are difficult to disperse in solvents, investigators have turned to yttrium hydroxide nanotubes doped with Eu^{3+}. This nanomaterial can be conveniently synthesized via the hydrothermal route at low temperature (180 °C) and is then spin cast on the front face of the cell. The authors claim that under AM1.5G illumination the yield of the cell increases from 15.2% to 17.2% upon adding the DS layer [81], an amazing 2% absolute. Moreover, the authors report that the open-circuit voltage of the cells was influenced. The measured EQE shows an increase in the 550 – 700 nm range, which does not correspond to the absorption spectrum of the Eu, which might suggest that the improvement was due to enhancement in the transmission of incident photons into the cell.

Other ions have also been used for DS, such as Dy and Sm [82]–[85]. Divalent and trivalent Sm ion in a $KMgF_3$ matrix have been shown to enhance the performance of CdTe solar cells by 5% [82]. The Sm ion PL has several peaks extending from 560 nm to 720 nm with the main peak centered at 694 nm, while it absorbs photons with wavelength below 500 nm with two main absorption peaks at 324 nm and 381 nm.

Crystalline titanium dioxide, TiO_2, with bandgap of 3.0 – 3.2 eV has been reported as a host material for rare earth materials [86]. TiO_2 is a good host material for its high refractive index, excellent transparency for visible/NIR light and low maximum phonon energy. The energy transfer to different rare earth ions (Sm^{3+}, Eu^{3+}, Yb^{3+}, Nd^{3+}, Er^{3+}, Tb^{3+} and Tm^{3+}) was tested and discussed by K. L. Frindell *et al.* [86]. Successful energy transfer from titania films to the lanthanides resulting in visible emission (Sm^{3+}, Eu^{3+}), NIR (Yb^{3+} and Nd^{3+}) and at 1540 nm (Er^{3+}) was reported. There was no fluorescence for

Tm^{3+} and Tb^{3+} ions which indicates no energy transfer from titania films to these rare earth ions. Energy transfer mechanism was suggested to take place between the defect levels, which have energy levels of around 19,000 – 21,000 cm^{-1}, and rare earth ions. It is evident from the excitation and emission spectra that down-shifting is occurring and not down-conversion. In addition there was no reporting of the conversion efficiency.

Table 3.4. Selected experimental results of different rare earth-based DS with different single-junction solar cells. The solar cell efficiency, η, is compared with the system efficiency, η_{sys}, composed of the solar cell and the DS layer. Both absolute, $\Delta\eta_A$, and relative, $\Delta\eta_R$, change in efficiency are reported.

SC	**η (%)**	**DS material**	**Host material**	**η_{sys} (%)**	**$\Delta\eta_A$ (%)**	**$\Delta\eta_R$ (%)**	**Spectrum**	**Ref**
c-Si	7.9	Eu^{3+}	ORMOSIL	9.3	1.4	18	AM1.5G	[74]
a-Si	3.2	Tb^{3+}	ORMOSIL	3.5	0.3	8	AM1.5G	[74]
c-Si	-	Eu^{3+}	PVA	-	-	2.8	AM1.5G	[77]
c-Si	11	Eu^{3+}	SiO_2	12.04	1.04	9.5	AM1.5	[79]
Si	16.52	Eu^{3+}	$KCaGd(PO_4)_2$	17.0	0.48	3	-	[80]
CdTe	-	Sm^{3+}	$KMgF_3$	-	-	5	AM1.5	[82]
DSSC	3.0	Dy^{3+}	LaVO4	3.7	0.7	23	Undefined	[83]
c-Si	15.3	Ce^{3+}	YAG	15.46	0.16	1	AM1.5	[85]
InGaP	9.28	Eu^{3+}	-	9.48	0.20	2	AM1.5G	[87]

3.3.2. Quantum Dots

Quantum dots (QD) are nanometer-sized features in semiconductors, which can be prepared by a number of methods such as colloidal synthesis, plasma synthesis or mechanical fabrication. The exact size and shape of the QD determine many of its electrical and optical properties. Quantum dots were first proposed for use in luminescent concentrators to replace organic dye molecules [88], [89]. QDs have advantages over organic dyes in that 1) their absorption edge can be tuned by changing the QD diameter 2) they have a broad absorption profile, 3) are inherently more stable than organic dyes, and 4) have relatively high quantum yield with more than 80%. On the other hand, the overlap of the absorption and the emission band can lead to significant reabsorption losses, although this can be minimized by spreading the size of QDs [88].

Common QDs used for DC and DS applications are CdSe [90], [91], CdS [91]–[95], Si-nC [96], ZnS [97] and PbS [98] with their absorption and emission bands summarized in Table 3.5. Multugin *et al.* claimed a two-fold increase in efficiency applying CdSe/ZnS core-shell QDs embedded in PMMA layer on top of mc-Si solar cell [90]. However the quality of their bare mc-Si solar cell was very poor, only 2.4% efficient.

Table 3.5. Common quantum dots used as down-shifting layers.

QD	**Absorption λ_{max} (nm)**	**Emission λ_{max} (nm)**	**Ref**
Si-nC	300 - 500	700 - 900	[35]
CdSe/ZnS	220 - 620	470 - 620	[91]
CdS	300 - 480	430 - 600	[95]

A series of reports on DS using QD were published from the National Chiao Tung University, Taiwan [93][94]. In [93] the authors demonstrated a 33% increase in efficiency when CdS QDs are used as a DS layer on top of c-Si nanopillar arrays. While there was only 2.8% relative increase in J_{sc}, there was about 15% relative increase in *FF* and the V_{oc} remained unchanged. They attributed the increase in *FF* due to the enhancement in series resistance but could not explain why. In addition there was an enhancement in reflectivity in the range of 400-1100 nm which mainly caused the increase in J_{sc}. They also tried the CdS QD on GaAs solar cell [94][95]. The conversion efficiency of a cell with QD increased by 3.35% and 0.55% when compared to GaAs solar cell with and without ARC, respectively [94]. The V_{oc} remained constant and *FF* degraded by less than 1%. However, most of the enhancement is believed to be due to lower reflection losses instead of DS effects, as the EQE of the cells show. Two years later a more conclusive report on using CdS and CdSe/ZnS on top of GaAs solar cell was presented [91]. The reflection losses and DS effects were decoupled analytically. Results show that out of the 25% relative enhancement, 24% was due to reflection losses while only 1% was due to DS effect.

Another common type of QD, or nanocrystals, for DS applications is Si-nC. Si-nC will be discussed in more detail in chapter 4, but some results are presented in this section for comparison. Si-nC are embedded into spin-on-glass (SOG) antireflection SiO_2 based solution and coupled to a standard silicon solar cell [96]. The Si-nC layer was estimated to be 130 nm thick with emission peak centered at 700 nm. A small improvement in short-circuit current density of 2.5 mA/cm^2 was observed. In [35], [99], a reference mc-Si solar cell with 105 nm SiO_2 ARC layer is compared with two mc-Si cells coupled with Si-nC (DS1 and DS2 layers) of layer thickness 235 nm and 677 nm, respectively. The measured efficiency of the reference cell under AM1.5G is 15% while for the mc-Si coupled with DS1 and DS2 the efficiency are 9.5% and 9.95% respectively. The degradation in efficiency is believed to be due to the high reflectance from the top surface of the DS layers. Decoupling of the down-shifting effect and the ARC effect was performed to show an enhancement in the IQE of 0.8% and 14% for DS1 and DS2, respectively, due to down-shifting effects when compared to the reference cell.

Table 3.6. Selected experimental results of different quantum dots-based DS with different single-junction solar cells.

SC	QD	Relative η (%)	Spectrum	Ref
c-Si	Si-nC	0.4	AM1.5	[96]
mc-Si	CdS/ZnS	211	Xe lamp	[90]
c-Si	CdS	> 4	AM1.5G	[92]
c-Si	Si-nC	No improvement	AM1.5G	[35]
c-Si nanopilar array	CdS	33	AM1.5G	[93]
GaAs	CdS	18.9	AM1.5G	[94]

3.3.3. **Organic Dyes**

Organic dyes were proposed in the 1970s as luminescent layers to enhance the UV response of single-junction solar cells [14], [100], [101]. The first experimental report by Hovel *et al.* examined the effect of adding fluorescent organic dyes to GaAs and a-Si solar cells. An absolute 2% increase in efficiency was observed for the GaAs solar cell while very small improvement in the case of a-Si. Hovel *et al.* indicated that careful design of ARC can further enhance the performance by minimizing reflection losses in

NIR regions. While these results were promising, the photostability of organic dyes over prolonged periods of UV exposure remains questionable.

Organic dyes nowadays exhibit relatively high absorption coefficients, close to unity quantum yield, and are easy to process in polymeric matrices [102]. Their drawbacks are their narrow absorption bands and their small overlap between absorption and emission profiles, which results in re-absorption losses. One way to overcome this drawback is by mixing several dyes within one layer in order to improve their absorption bandwidth and to expand their Stokes-shift [43], [44], [103]. Researchers choose dyes that are commercially available such as Lumogen® F, and Keyplast dyes for plastics from vendors such as BASF and Keystone [104], [105]. Table 3.7 shows the properties of some of the common commercial organic dyes used as down-shifting layers.

Table 3.7. Some of the commercial organic dyes that are used as down-shifting layers

Organic Dye	**Absorption λ_{max}**	**Emission λ_{max}**	**PLQY**	**Ref**
Lumogen® F V570	378 nm	413 nm	> 85%	[104]
Lumogen® F Y083	476 nm	490 nm	> 85%	[104]
Lumogen® F O240	524 nm	539 nm	> 90%	[104]
Lumogen® F R305	578 nm	613 nm	> 90%	[104]
MPI-505	450 nm	495 nm	> 85%	[106]
Sumipex 652	470 nm	520 nm	91%	[107]

Organic dyes are efficient DS layers when coupled to different solar cells such as c-Si [108], [109], mc-Si [107], [110], [111], a-Si [14], GaAs [14], CdTe [106], [112]–[116], CIGS [117], [118], and DSSC [14], [111]. Experimental work has advanced using organic dyes to implement the DS layers on encapsulated modules [117]. Some of the results are shown in Table 3.8 for different single-junction solar cells and modules. As can be seen, the absolute increase in efficiency is in the order of 1-2%, with relative efficiency enhancement as high as 29%. Some of the high relative efficiency improvements reported are due to the fact that the reference cell is a bare cell with no ARC, and thus suffers high reflectance losses to begin with. However a number of studies decouple the reflection losses from the downshifting effect after adding DS layers. A large increase in efficiency could be primarily due to enhancement in reflection losses while there is only a very small enhancement from down-shifting effect. In [117] the effects were decoupled and it was shown that when coupling an 80% dye to CIGS module, an increase of 1.5 mA/cm^2 to J_{sc} is observed. Out of this increase 0.5 mA/cm^2 was a result of reduced reflection losses while 1 mA/cm^2 due to the down-shifting effect. On the other hand, E. Klampaftis *et al.* demonstrated a maximum increase in J_{sc} of 2.3 mA/cm^2 based on an organic dye DS layer of 90% quantum efficiency [118]. However, 1.8 mA/cm^2 was due to better optical coupling into the cell, and only 0.5 mA/cm^2 due to the down-shifting effect.

Table 3.8. Selected experimental results of different organic dyes-based DS with different single-junction solar cells. The solar cell efficiency, η, is compared with the system efficiency, η_{sys}, composed of the solar cell and the DS layer. Both absolute, $\Delta\eta_A$, and relative, $\Delta\eta_R$, change in efficiency are reported.

SC	**η (%)**	**Organic dye**	**Host material**	**η_{sys} (%)**	**$\Delta\eta_A$ (%)**	**$\Delta\eta_R$ (%)**	**Spectrum**	**Ref**
GaAs	11.5	Coumarin (540), Rhodamine 6G	PMMA	13.5	2	17.4	AM0	[14]
mc-Si	5.14	MPI-503C (red)	Paint thinner	6.61	1.53	29	Undefined	[110]
mc-Si	6.03	MPI-507C (pink)	Paint thinner	7.65	1.62	27	Undefined	[110]
CdTe	9	Lumogen-F Y,O	PMMA	-	-	20	AM1.5G	[113]

A further interest that can be found in organic dyes, in addition to the efficiency enhancement of photovoltaics modules, is the coloration of the modules for their integration in urban environments [119]. Indeed, owing to the intrinsic properties of photoactive materials and antireflective coatings, solar cells appear to be dark. However, any coloration of the surface of the antireflective coating immediately lowers the energy conversion efficiency. A compromise is to change the refractive index and the thickness of the antireflection film.

While most work has been focused on system performance and PV enhancement, an interesting cost analysis was presented in [116]. Three factors that affect the effectiveness of a DS layer: PLQY, absorptivity and the actual cost per gram. The higher the PLQY means more enhancements to the solar cell and therefore higher annual energy yield is expected. Although an organic dye can be expensive, if it has high absorptivity, then only small amount is needed and therefore it might be cost effective to use it instead of a cheaper but less absorptive dye.

3.3.4. Summary

In summary, an overview of the DC and DS materials was presented in this section. Rare-earth materials have certainly some inimitable advantages such as high photostability and very little reabsorption losses. However, they have disadvantages such as very small absorption coefficients resulting in overall low DC enhancement. Yb ion has been the most suitable ion for PV applications as the emission line is at 980 nm. However the challenge remains in finding a sensitizer ion that both has high absorption coefficient and efficient energy transfer. Ce and Tb ions both remain good choices as they exhibit several absorption lines in the UV range of the spectrum.

Effectively it seems DC is only possible through rare earth ions, although there has been some reports claiming DC effects in QDs [120], [121]. While there is experimental evidence for DC effects in Si-nC, the efficiency still remains significantly below 200% [120]. In the case of the CdSe/ZnS QD [121], I believe the calculation of the internal quantum efficiency was not correct due to the exclusion of diffuse reflectance. More information on specular and diffuse reflectance will be presented in chapter 6

On the other hand, there have been several experimental reports on coupling different materials to single-junction solar cells for DS applications. While Eu ions and CdS QDs are good candidates, organic dyes show better results for their high PLQY and low cost. However, most DS layers are suitable for solar cells with poor UV response, otherwise the conversion efficiency of the cell might degrade when a DS layer is added on the top surface. In addition, while some of the research groups report high relative increase in efficiency, most of the enhancement is due to a decrease in reflection losses (ARC effects) with almost no, or very little, DS effects. In some cases, this is due to the fact that the reference cell is a bare cell or a very poor solar cell to start with.

In this thesis the focus is on Si-nC embedded in SiO_2 as a DS layer. Si-nC exhibit strong absorption below 500 nm with PL centered at 800 nm. Si-nC is the selected DS layer for our numerical simulation in chapter 5, and in our experimental results in chapter 6. However, it is important to understand the physical behaviour of Si-nC and therefore the next section is dedicated for the theory of Si-nC.

3.4. Silicon Nanocrystals

3.4.1. Luminescence from Silicon Nanocrystals

Silicon has been the dominant material in modern microelectronics technologies for over 50 years, owing to its natural abundance, low cost, stable and well-passivating native oxide, and universally adequate electrical properties. However, for all of its favourable properties, bulk silicon is a very poor luminescent material and thus has very limited applications in optoelectronics. While sufficient performance has been attained in other key components of silicon photonics including waveguides, modulators, and detectors [122], the continued lack of an efficient silicon-based light source remains a major obstacle, preventing silicon-based optoelectronic devices from becoming a viable technology.

The poor radiative efficiency of bulk silicon is a consequence of its indirect bandgap, a fundamental property of silicon band structure. In indirect bandgap materials such as silicon, the minimum of the conduction band is offset from the maximum of the valence band. As can be seen in Figure 3.8, the minimum of the conduction band is located at Γ point while the maximum of the valence band is close to X point [123]. As a result, there is a difference in the wave vectors of the initial and final states of electron transitions between the conduction band minimum and valence band maximum. Therefore, radiative recombination in silicon requires phonon mediation (*i.e.*, phonon absorption or emission) involving a phonon with a wave vector of equal magnitude and opposite direction to that of the initial state in order to conserve momentum [124]. Phonon assistance is a slow process due to the weak electron-phonon interaction. This leads to a substantial increase of the radiative lifetime to be on the order of milliseconds, which is very long compared to that in a direct bandgap semiconductor like GaAs, which has a radiative lifetime on the order of nanoseconds [125].

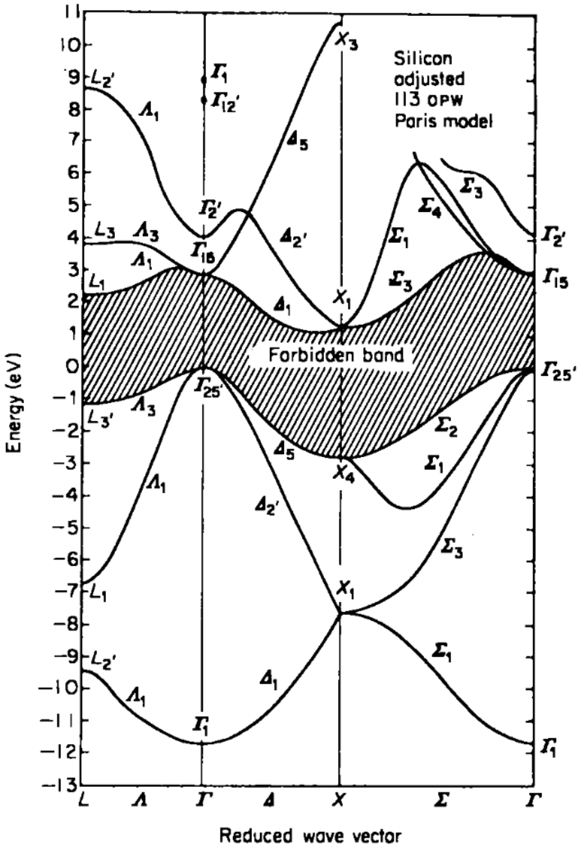

Figure 3.8. Energy band structure of silicon crystals. An offset in the k-space between the minimum of the conduction band and the maximum of the valence band exists for indirect semiconductors. Reproduced with permission from [123].

At room temperature, non-radiative processes such as Auger and SRH recombination dominate due to their relatively short lifetimes. Auger recombination rates are dependent on the doping level and becomes the dominant recombination process for high doping levels [126], [127]. By contrast, the SRH recombination rate is dependent on the concentration of deep trap states and typically has a lifetime on the order of nanoseconds [124]. The radiative and non-radiative lifetimes, denoted as τ_R and τ_{NR}, respectively, determine the radiative efficiency η of a semiconducting material as defined as:

$$\eta = \frac{\tau_{NR}}{\tau_R + \tau_{NR}} \tag{3.3}$$

In order to obtain efficient luminescence from a material, the radiative τ_R lifetime must be significantly shorter than the non-radiative τ_{NR} lifetime. At low temperatures where the non-radiative recombination rates are significantly reduced, the radiative recombination process becomes dominant and efficient luminescence has been observed under such conditions [128], [129]. Unfortunately, cooling to such extremes is impractical for most device applications and so it is necessary to devise methods of overcoming the limitations imposed by the indirect band structure. It was shown previously that the internal quantum efficiency of Si-nC samples annealed at 1250 °C can reach as close as 100% according to the ratio of the radiative to non-raditaive lifetimes [130].

3.4.1.1. **Origin of Luminescence**

After the discovery of visible luminescence from nanocrystals [131] and porous [132] silicon in 1990, challenges of silicon band structure were overcome by creating a strong confining potential for carriers inside the nanocrystals silicon embedded in large bandgap matrix such as SiO_x. The large bandgap matrix provides a high potential barrier for the carriers that define the energy spectrum of the nanocrystal. When the silicon dimensions are reduced sufficiently, the uncertainty in the charge carrier momentum exceeds the difference in the initial and final wave vectors. Having relaxed the requirement for conservation of momentum, so-called “quasi-direct” transitions can take place in which radiative recombination is allowed to occur without phonon mediation which significantly increases the light emission efficiency of the material. H. Takagi *et al* observed a shift in emission peak which is inversely proportional to the crystallite size for small nanocrystals with size ranging from 2.8 to 5 nm [131]. Three months later, L. T. Canham experimentally showed efficient visible red luminescence from porous silicon at room temperature when excited by blue or green laser [132]. The visible luminescence was attributed to the quantum confinement effects when the dimensions of silicon crystals are reduced beyond the exciton Bohr radius (~ 5 nm). According to the model devised by L. Brus, the energy of the first excited electronic state in a spherical semiconducting nanocluster ($\boldsymbol{E^*}$) can be approximated by Equation (3.4)

[133]. The equation includes terms for the bandgap energy of the bulk material (***E_g****), energy shifting due to quantum confinement effects on the electrons and holes, and Coulomb interactions between the charged particles.

$$E^* \cong E_g + \frac{\hbar^2\pi^2}{2R^2}\left(\frac{1}{m_e} + \frac{1}{m_h}\right) - \frac{1.8q^2}{\varepsilon R} \tag{3.4}$$

where R is the radius of the nanocrystal, m_e is the effective mass of electrons, m_h is the effective mass of the holes, and ε is the permittivity of the semiconductor.

Considerable research in the past two decades based on both theoretical and experimental studies investigated the origin of the luminescence from silicon nanocrystals in which two models have been proposed [131], [132], [134]–[140]. The first model describes the luminescence in Si-nC in terms of carrier quantum confinement effects [131], [132], [134]–[136]. The second model attributes the Si-nC luminesce to oxygen-related surface and/or interface defects in the SiO_2 films [137]–[140], while confirming the change in the silicon band structure due to quantum confinement. The absence of a generally accepted model is due to the variety of experimental results in the literature that is dependent on preparation conditions, method of fabrication, annealing temperature, annealing time, silicon composition and characterization accuracy, and in some cases results contradicted each other. In addition, the interpretation of the results of emission from a single nanocrystal is different than an ensemble of nanocrystals due to the various mechanisms of interaction amongst the nanocrystals in an ensemble such as Froster transfer, energy transfer between adjacent nanocrystals.

The first proposed model suggested that light emission was due to band-to-band radiative recombination of electron-hole pairs confined within the crystals. Experimental studies showed that the PL emission peak red-shifts with increasing the size of the Si-nC, which supports the quantum confinement theory. To further supress any luminesce from defects, hydrogen passivation of Si-nC was carried out [134]. It was observed that the PL peaks shape were the same while PL intensity increased by a factor of 2 suggesting that non-radiative recombination through the defect levels were reduced and that luminescence is indeed due to band-to-band radiative recombination. As a simple model, the bandgap of the Si-nC can be estimated by the following relation

$$E_g(d) = E_{g\_bulk} + \frac{C}{d^n} \tag{3.5}$$

where $E_g(d)$ is the estimated bandgap of the nanocrystal, E_{g_bulk} is the bandgap of the bulk silicon, C is a positive constant, d is the diameter of the nanocrystal, and n is a constant in the range 1 to 1.5. It is obvious that the bandgap of the nanocrystal is larger than the bulk and increases as the diameter of the nanocrystal decreases.

In the second model, it was found that as the crystallite size decreases to few nanometers, the PL emission peak did not shift to higher energy beyond 2.1 eV even for small crystallites below 3 nm [135], [138], [139], which contradicts the confinement theory that the bandgap of silicon increases beyond 3 eV when the size decreases below 2 nm and reaches 6 eV for size less than 1 nm [136]. In addition, the fact that surface passivation affect both the intensity the wavelength of emission peak suggests that PL from Si-nC is dominated by these defect centers. A three-level model was proposed to explain the luminescence of the Si-nC and is explained as follows [137], [140]. The absorption of photons is due to the band-to-band transition and is affected by the quantum confinement. A fast relaxation in the order of nanosecond to an interface state followed by a slow radiative recombination process in the order of (μs) emitting a photon with peak wavelength centered at 800 nm.

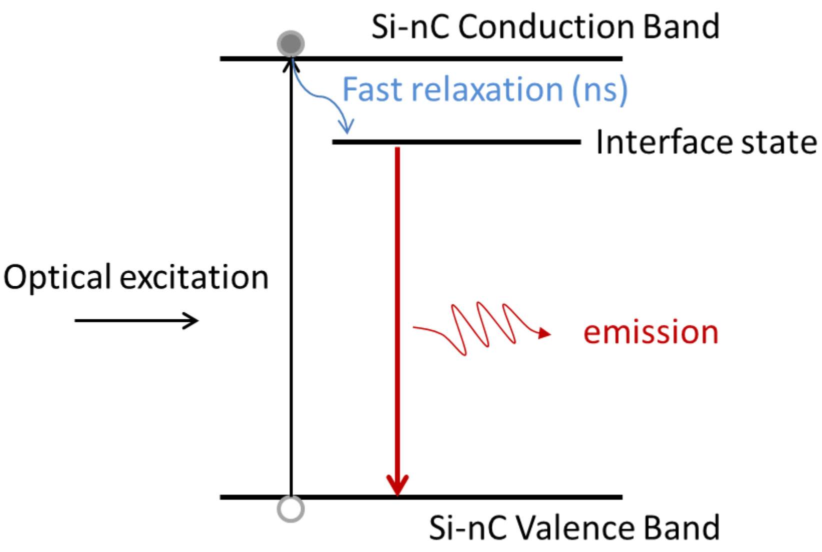

Figure 3.9. Schematic energy diagram of a three-level model to explain the luminescence of Si-nC from a defect level.

Wolkin *et al.* tried to explain the three level model by comparing the PL emission peaks of hydrogen- and oxide-passivated porous silicon samples [139]. In their work, it was found that hydrogen-passivated silicon nanocrystals emit light with an energy corresponding to free excitonic recombination for all sizes. However, there are three different recombination mechanisms in oxygen-passivated silicon nanocrystals. For crystallites of a size larger than 3 nm, recombination is via free excitons. For smaller diameters, electrons become localized on the Si atoms in Si=O bonds at the nanocrystal surface thereby reducing the emission energy below that of free excitonic recombination. At nanocrystal diameters below 2 nm, the holes also become localized on the Si atoms in Si=O bonds preventing the emission energy increasing with further reductions in size. The effects of the silicon nanocrystal size and passivation on the electronic states in silicon nanocrystals and the emission energy are illustrated in Figure 3.10 and Figure 3.11, respectively. Several other groups have suggested that absorption is due to band-to-band quantum confined silicon nanocrystals while emission is mainly due to transition between defect states in the passivation layer [137], [138].

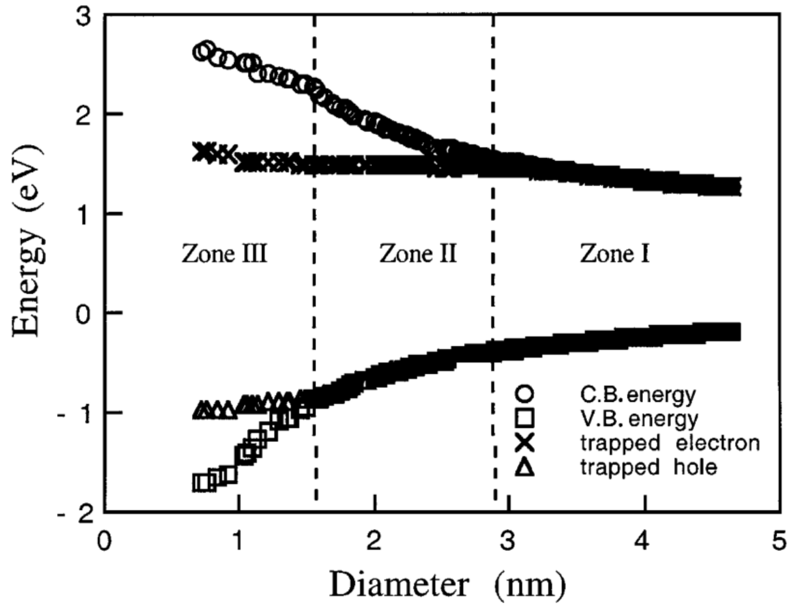

Figure 3.10. Electronic states in silicon nanocrystals as a function of crystallites diameter. As suggested by the quantum confinement model, bandgap increases with decreasing crystallites diameter. For oxygen – passivated samples, recombination is due to free excitons in zone I. In zone II, recombination is due to trapped electron and free hole. In zone III, recombination is due to trapped excitons. Reproduced with permission from [139].

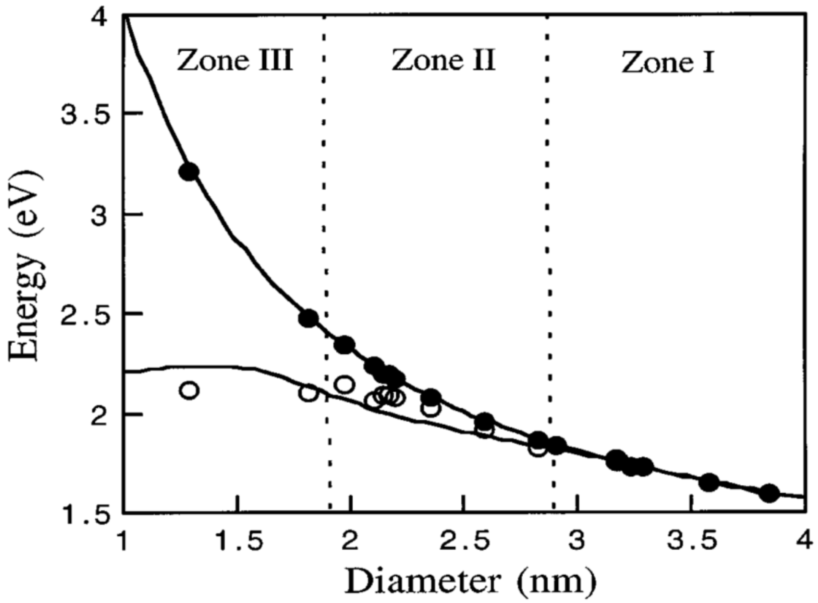

Figure 3.11. Comparison between experimental and theoretical PL energies in porous silicon as a function of crystallite diameter. The upper line is the free exciton band gap according to the quantum confinement model and the lower line is the lowest transition energy in the presence of a Si=O bond. The black and white circles represent the peak PL energies obtained from samples with different porosities kept under Ar atmosphere and exposed to air, respectively. In zone I the PL peak energies are identical, for both hydrogen- and oxygen –passivated samples. Reproduced with permission from [139].

Although it is certain that quantum confinement plays a fundamental role in determining the absorption and emission properties of Si-nC, an extension to the pure quantum confinement model is required in order to consider surface effects, especially when the nanocrystals have sizes smaller than 3 nm. Shallow surface trap states due to the formation of Si=O bonds have been shown to be able to fit the PL peak energy vs size data, as shown in Figure 3.11.

The PL of Si-nC has a Gaussian shape with a tunable emission peak ranging from 650 nm up to 950 nm. The position of the emission peak is dependent on the Si concentration and the annealing temperature while independent of the annealing time and excitation energies [134], [137]. It was shown that for a given Si concentration, the PL emission peak red-shifts with increasing annealing temperature [134]. Similarly, for a given annealing temperature, the PL emission peak red-shifts with increasing the Si concentration. In both cases, increasing the annealing temperature or Si concentration result in a larger diameter of the silicon nanocrystals. Figure 3.12 shows the dependence of the PL emission peak on the annealing temperature (1000 ˚C to 1300 ˚C) for different Si concentrations (35 to 44 *at.* %) for Si-nC embedded in SiO_x matrix and fabricated by PECVD [134]. The spread of the emission peak wavelength decreases with increasing annealing temperature: spectral range of 650 – 900 nm at 1100 ˚C to a narrow 830 – 950 nm at 1300 ˚C. Similarly, emission peak wavelength increases linearly from 1100 ˚C to 1300 ˚C for low Si concentration (35 *at.* %), while PL is not visible at annealing temperature of 1000 ˚C. However for the high Si concentration (44 *at.* %) the peak emission is contained within 50 nm spectral change when varying the annealing temperature. Although it is believed in [134] that the luminescence from Si-nC is due to carrier quantum confinement, it was not possible to further tune the emission peak for bandgaps beyond 2 eV (~ 650 nm) despite the small size of Si-nC reported.

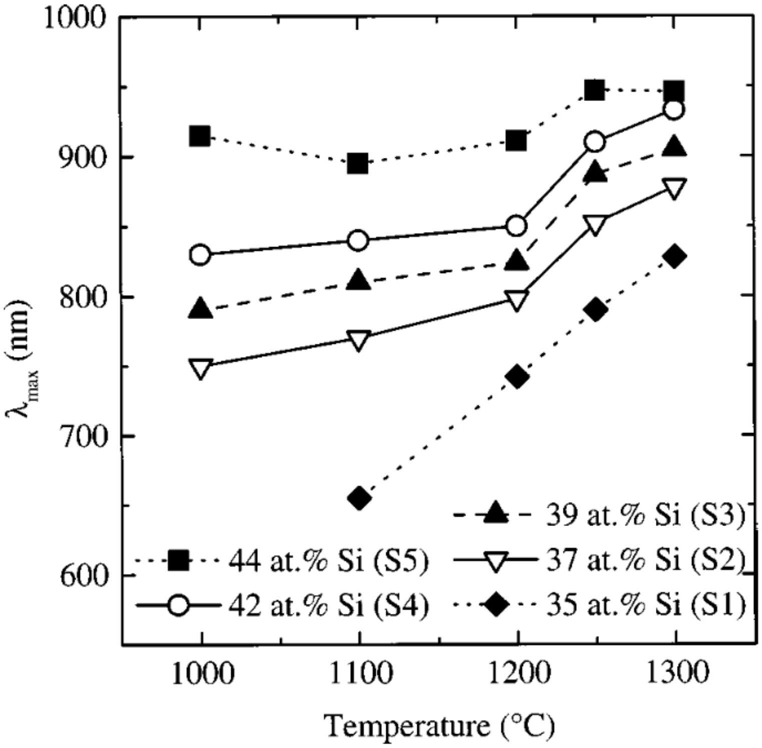

Figure 3.12. Change in PL emission peak as a function of annealing temperature for different si concentrations. Reproduced with permission from [134].

Timmerman et al. have demonstrated that quantum cutting, or down-conversion, is possible in closely spaced Si-nC embedded in SiO_2 matrix where two photons are emitted for each high-energy photon absorbed [120]. A high-energy (>3 eV) photon is absorbed in a Si-nC creating a hot electron-hole pair with excess energy. The excited electron deep in the conduction band then relaxes to the edge of the conduction band giving its energy to a neighbouring nanocrystal where an electron-hole pair is then excited. This energy transfer occurs through intraband Auger processes [26]. The excited electrons in both Si-nC then radiatively recombine, emitting two photons with energies half of the original exciting photon. A schematic of the down-conversion process in Si-nC is shown in Figure 3.13.

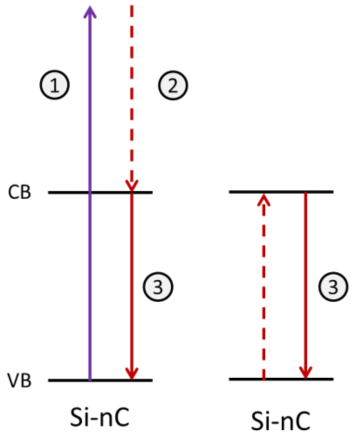

Figure 3.13. Down-conversion process via neighbouring Si-nC. (1) A high-energy photon excites an electron deep into the conduction band; (2) the excited electron relaxes to the edge of the conduction band transferring its energy to excite an electron in a neighbouring Si-nC through intraband Auger process; (3) the electrons in both Si-nC radiatively recombine, emitting two photons with lower energy than the original exciting photon.

The quantum cutting observation is supported by measuring the relative quantum yield of Si-nC samples. A linear increase in the relative quantum yield as a function of incident photon energy was observed for photons with energy greater than 3 eV, which coincides with double the estimated band gap of the Si-nC, 1.5 eV. Timmerman *et al.* extended their study to measure the quantum yield for different samples for photons with energies up to 5 eV to observe a step-like quantum yield curve as a function of the incident photons energy [141], as shown in Figure 3.14. The step-like quantum yield curve suggests the possibility of emission of 2 or more photons after the absorption of a single high-energy photon. Although the absolute quantum yield can vary from sample to another, the shape of the curve is very similar. In addition the position and the width of the steps are dependent on the size distribution of the nanocrystals. The quantum cutting process was explained as energy transfer to neighbouring nanocrystals within proximity. To confirm this observation, Timmerman *et al.* performed two more experiments [141]. First, quantum yield was measured for two samples with similar nanocrystals size but different concentrations with the lower concentration having lower quantum yield. The second experiment was done on a free-standing colloidal silicon nanocrystal and was showing a decrease in quantum yield as a function of photon energy. The decrease in the quantum yield is due to new trapping and recombination centers being activated.

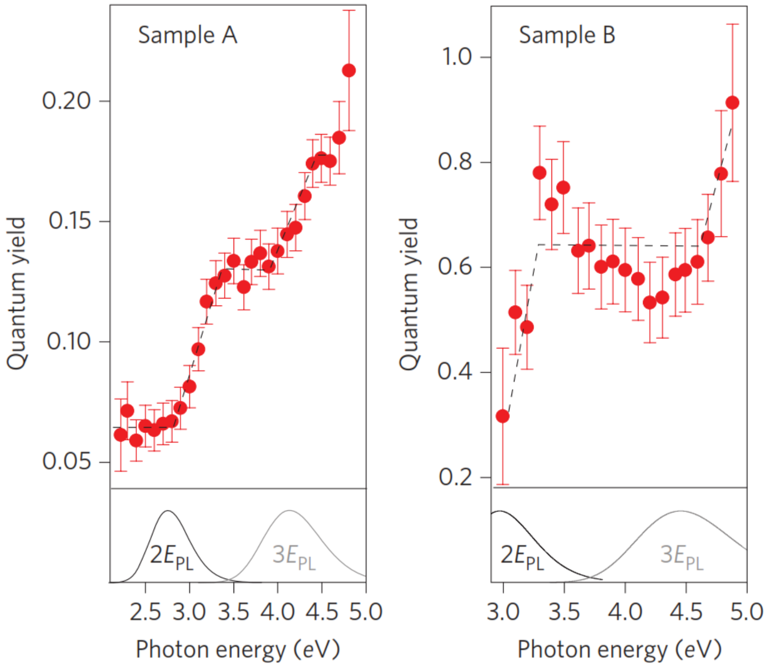

Figure 3.14. External quantum yield of photoluminescence as a function of photon energy for two Si-nC samples. Black dashed lines, indicating the ‘steps’, serve only as a guide to the eye. The lower panels show multiples of the photoluminescence spectra of each sample. Reproduced with permission from [141].

3.4.1.2. Silicon Nanocrystals as Down-Conversion Layers

Si-nC have a series of properties which makes them very attractive as a candidate material for down-conversion: (i) the photoluminescence quantum-efficiency can be very high achieving internal quantum efficiencies up to 100% [130], (ii) Si-nC show strong absorption in the UV (below 500 nm), (iii) the photoluminescence emission peak can be tuned in the range between 650 and 950 nm, (iv) a wide separation between the absorption and the emission profile. Therefore there have been several research groups using Si-nC embedded in SiO_x matrix as a down-conversion layer. Si-nC based down-conversion layer are used in this thesis for both modelling and experimental work.

3.4.1.3. **Quantum Yield of Silicon Nanocrystals**

One of the important characteristics of Si-nC is quantum yield (QY), or quantum efficiency. Quantum yield is defined as the ratio of the number of emitted photons to the number of absorbed photons. Experimentally quantum yield can be measured as per the previous definition using an integrating sphere with a photodetector and an excitation source such as laser or a monochromatic source [141]–[145]. The number of absorbed photons is represented by the decrease in the excitation source intensity when the sample is present. While the number of emitted photons is represented by the detected photoluminescence of the sample. Another way to measure the QY is by measuring the radiative and non-radiative decay rates and calculate the QY using the relation given in in equation (3.3) [130], [146]. Both measurements are equivalent and are generally accepted in the literature to report for the QY of Si-nC.

Quantum yield measurement of Si-nC has been an important subject of research for the past 2 decades. The reported QY ranges from few percent for oxidised Si-nC to high QY as 60% and 70% by passivating the si-nC with organic legends [142], [143]. Exposing these samples to air results in a significant decrease in QY and 5%-8% ensemble QY was reported [142]. Careful single Si-nC PL studies reported quantum yields as high as 59% [146], 88% [147] and 100% [130] for selected individual nanocrystals. However, the overall ensemble quantum yield in these studies was typically between 2% and 5%, since the ensemble quantum yield was limited by a majority of non-luminescent particles, or “dark nanocrystals”, while for a few single particles (bright nanocrystals) the quantum yield approached unity. Table 3.9 summarizes selected reports on QY of Si-nC over the past two decades for free standing and matrix embedded Si-nC. In summary, high QY of Si-nC can be achieved when fabricated in an oxygen-free environment and passivated with organic ligands, which might limit its commercialization process until proven stable over time.

Table 3.9. Selected reports on the quantum yield of free standing silicon nanocrystals.

	Passivation	**QY**	**λ_{exc} (nm)**	**λ_{em} (nm)**	**Ref**	**Year**
Free standing Si-nC	NA	88%	488	650	[147]	1999
	Oxidized	5 - 35%	325	660 – 785	[148]	2002
	No passivation	59%	488	750	[146]	2006
	Oxidized	100%	457	800	[130]	2006
	Oxidized	45%	390	720	[144]	2009
Ensemble Si-nC	Oxidized	~ 5%	355	660, 770, 970	[149]	1993
	Oxidized	5%	350	~700	[150]	1993
	Oxidized	3.9%	-	-	[151]	1999
	Organic ligands	62%	380	789	[142]	2006
	Organic ligands	60 - 70%	380 - 400	800	[143]	2006
	Oxidized	5 - 90%	250 – 460	-	[141]	2011
	Organic ligands	5 - 43%	365	750	[152]	2012
	Organic ligands	13 - 37%	400	600 – 750	[145]	2012

Chapter 4: Numerical Modelling of Solar Cells

4.1. Device Modelling

4.1.1. Introduction

Technology Computer-Aided Design (TCAD) Sentaurus by Synopsys is a commercial semiconductor device software package that solves the set of coupled partial differential equations including the diffusion and transport equations to model the structural properties and opto-electrical behaviour of complex epitaxial structures. The software package provides a selection of tools to perform the aforementioned calculations which provides structured application of the software with visualization aids to observe the physical properties inside the device structure under various forms of perturbation. The tools which have been used in this work include [32]:

Sentaurus Workbench (SWB), is a complete graphical environment for creating, managing, executing, and analyzing TCAD simulations. Its graphical user interface allows users to navigate and efficiently automate typical tasks associated with running TCAD simulations such as managing the information flow, including preprocessing of user input files, parameterizing projects, setting up and executing tool instances, parameter variations, and visualizing results with appropriate viewers. It automatically creates the output file of one tool and then, after its successful completion, passes the output files to the next tool in the queue, thereby removing the need for manual control by the user.

Epi, the user defines the basic structure of the device specifying the X and Y dimensions for 2D simulation or X, Y and Z dimensions for 3D simulations. For each epitaxial layer, the user defines the material, layer thickness, doping concentration, mesh refinement and mole fraction, including gradients in both doping and mole fraction. It also contains information about the source parameter files (<material>.tcl or <material>.par) to be used by MatPar tool (see next) to generate user-defined material parameter files. The

Epi tool generates a scheme command script automatically to create the multilayer structure as input to the *Sentaurus Structure Editor*.

MatPar, creates the material parameter files which will be used by the *Sentaurus Device* engine for simulating the electrical and optical characteristics of the device. The *.par* user defined files are imported to *Sentaurus Device*.

Sentaurus Structure Editor (SDE), is a device editor and process emulator based on CAD technology. It has three distinct operational modes: 2D structure editing, 3D structure editing, and 3D process emulation. It can utilize, as an input, a script file written by the user or input from *Epi* tool in order to create the device structure, or can be used as a stand-alone tool to create an epitaxial structure. It discretizes the structure into a mesh consisting of discrete points using a Delaunay mesh generator whereby the physical equations of interest will be solved. The output file created by this tool contains the geometrical, material, contact and doping information about the device. It is this file that is used by *Sentaurus Device* to perform device simulations.

Sentaurus Device (SDevice), numerically simulates the electrical behaviour of the modeled semiconductor device. It solves numerically the set of diffusion and transport equations depending on the physical parameters and boundary conditions defined by the user in the virtual device. The equations are solved at each discrete point in the mesh self-consistently until the user-defined convergence criteria are met. The numerical methods for solving this set of nonlinear equations are based on Newton's root finding algorithm.

***Sentaurus Visual* (*SVisual*)**, is a 1-D, 2-D, and 3-D visualization tool. The tool supports TCL scripting, enabling the extraction of simulated data for further analysis and post processing.

The simulation tool flow of TCAD Sentaurus is shown in Figure 4.1 and is summarized as follows. The layer structure of the device is defined in the *Epi* tool, where each layer‘s material information such as doping, thickness, and mole fraction are defined. The *Epi* tool then generates two files. A scheme commands file input to Sentaurus *Structure Editor* (SDE) with the structure and meshing information. The SDE completes the structure by adding more layers such as ARC layers and/or contacts, add doping profiles, and refining the mesh using a built-in tool (Sentaurus *Mesh Generator*). The output file is sent to Sentaurus *Device* (SDevice) for optical and electrical stimulations. The second output file from the *Epi* tool is used by the *Matpar* tool to generate the final parameter files which will be used by *SDevice*. The user-defined parameter files contain the properties of all materials in the structure such as bandgap, electron and hole effective masses, doping dependent mobilities, complex refractive indices, etc. However, the user can also generate material files without the use of MatPar. A literature review was done to find the relevant properties for the materials used in this work, as will be discussed in section 04.2. For simple structures such as a silicon solar cell, there is no specific need to use the *Ep*i and *MatPa*r tools. The structure of the device can solely be created in *SDE* and the corresponding material properties files are imported directly to *SDevice*. Optical and electrical simulations are then carried out in the *SDevice*. The optical simulation computes the reflection, transmission and absorption within each layer of the device structure accounting for the wavelength dependent complex refractive index of each material using the Transfer Matrix method (TMM). However, other methods such as ray tracing and finite-difference time domain are also available. The TMM method is adopted for its simplicity and efficiency, and will be discussed in section 4.1.2. The simulation can be done using the standard spectrum AM1.5G for producing *J-V* curves, or a tunable monochromatic source for quantum efficiency measurements. The partial differential equations are then solved in *SDevice* to find a numerical solution under specific illumination and bias conditions. The coupled partial differential equations are solved repeatedly as the bias is swept in order to produce the *J-V* curve. Whereas for the quantum efficiency simulation, the wavelength of the monochromatic source is swept and the equations are solved for short-circuit current condition, although can also be solved at a particular bias to produce quantum efficiency as a function of bias. Finally, the Sentaurus *Visual* tool is used to plot the output results of the simulation such as *J-V* curves, quantum efficiency, energy band diagrams, etc.

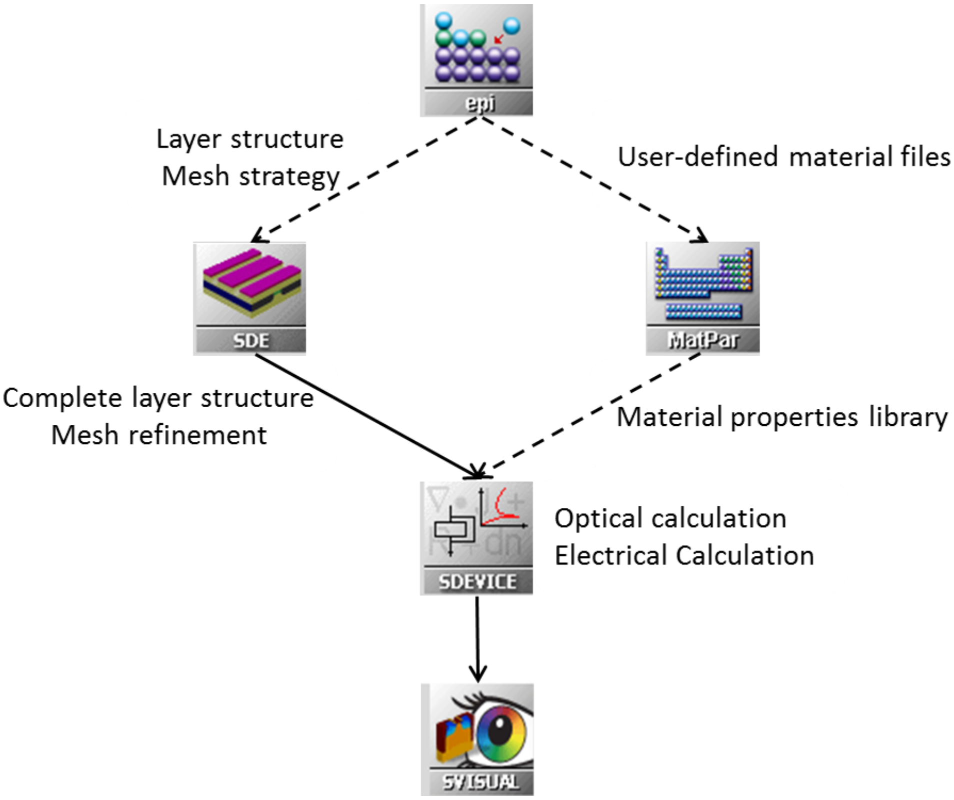

Figure 4.1. Simulation tool flow in TCAD Sentaurus showing the main tools for solar cell simulation. The tool flow with solid arrows is used for simple structures such as silicon solar cell where only one material is used.

4.1.2. Transfer Matrix Method

While there are multiple ways to simulate the reflection in thin films, such as the ray-tracing method [50] and the transfer matrix method (TMM) [153], the latter is more commonly used and will be used throughout this thesis. There are many references describing the TMM method with some variations [153]–[155], although the approach presented here is adopted from [153].

First we define the optical properties of a medium. Refractive index is defined as the ratio of the velocity of light in free space c to the velocity of light in the medium v. When the refractive index is real, it is denoted by n, but it is frequently complex and then is denoted by N.

$$N = \frac{c}{v} = n - ik \tag{4.1}$$

where k is the extinction coefficient and is related to the absorption coefficient α, as was defined in equation (2.2).

Light waves are electromagnetic in nature, and a homogeneous, linearly polarized harmonic wave may be represented by expressions of the form

$$E = E_0 exp\left[i\omega t - \left(\frac{2\pi N}{\lambda}\right)z + \Phi\right] \tag{4.2}$$

where E is the electric field, E_o is the electric amplitude, z is the distance along the direction of propagation, and Φ is an arbitrary phase. A similar expression holds for H, the magnetic field propagating perpendicular to the electric field, as:

$$H = H_0 exp\left[i\omega t - \left(\frac{2\pi N}{\lambda}\right)z + \Phi'\right] \tag{4.3}$$

The optical admittance is defined as the ratio of the magnetic and electric fields and is given by:

$$Y = \frac{H}{E} \tag{4.4}$$

where Y is usually complex. In free space, the optical admittance is real and is denoted by $\mathscr{Y}$. The optical admittance of a medium is associated with the refractive index by

$$Y = N\mathscr{Y} \tag{4.5}$$

For oblique incidence the wave is split into two linearly polarized components, one with the electric vector in the plane of incidence, known as p-polarized (or transverse magnetic field (TM)) and one with the electric vector normal to the plane of incidence, known as s-polarized (or transverse electric field (TE)). The propagation of each of these two waves can be treated quite independently of the other. Calculations are simplified only if energy flows normal to the boundaries and electric and magnetic fields parallel to the boundaries are considered, because then we have a formulation that is equivalent to a homogeneous wave.

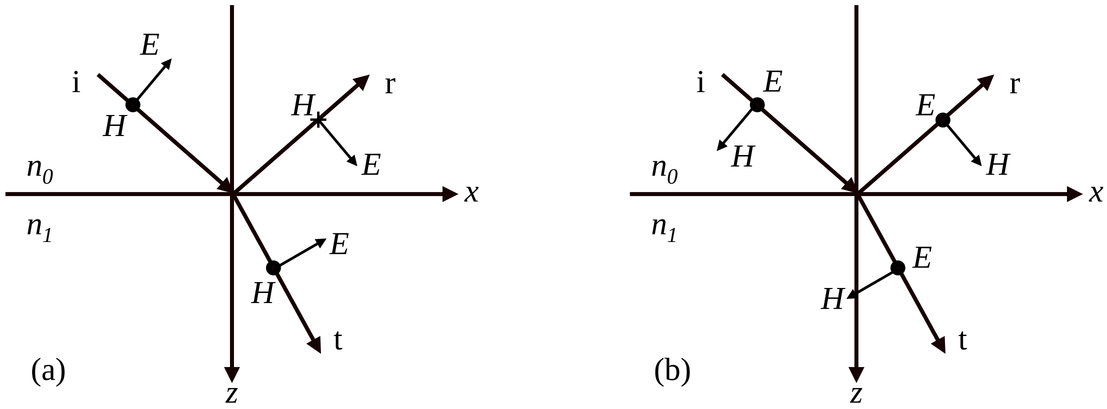

Figure 4.2. (a) Convention defining the positive directions of the electric and magnetic vectors for p-polarized light (TM waves). (b) Convention defining the positive directions of the electric and magnetic vectors for s-polarized light (TE waves).

At a boundary between two media, denoted by suffix 0 for the incident medium and by suffix 1 for the exit medium, the incident beam is split into a reflected beam and a transmitted beam. The expression for optical admittance is then modified to take into account the angle of incidence, θ_o, which is given by

$$\eta_{TM} = \frac{N}{cos\theta}\mathcal{Y} \qquad \text{and} \qquad \eta_{TE} = N\mathcal{Y}cos\theta \tag{4.6}$$

where θ_1 is calculated using Snell's law, in which complex angles may be included

$$N_0 sin\theta_0 = N_1 sin\theta_1 \tag{4.7}$$

The amplitude reflection and transmission coefficients are given by

$$r = \frac{E_r}{E_i} = \frac{\eta_0 - \eta_1}{\eta_0 + \eta_1} \tag{4.8}$$

and

$$t = \frac{E_t}{E_i} = \frac{2\eta_0}{\eta_0 + \eta_1} \tag{4.9}$$

The reflectance and transmittance can then be calculated from the amplitude reflection and transmission coefficients, assuming incident medium is absorption free, as follows

$$R = rr^* = \left(\frac{\eta_0 - \eta_1}{\eta_0 + \eta_1}\right)\left(\frac{\eta_0 - \eta_1}{\eta_0 + \eta_1}\right)^* \tag{4.10}$$

and

$$T = \frac{4\eta_0 \mathbb{R}\mathrm{e}(\eta_1)}{(\eta_0 + \eta_1)(\eta_0 + \eta_1)^*} \tag{4.11}$$

The above analysis can be extended in case of a thin film of material of thickness d covering the surface of a substrate, such as the case of a single layer ARC, as shown in Figure 4.3. The presence of two (or more) interfaces means that a number of beams will be produced by successive reflections and the properties of the film will be determined by the summation of these beams.

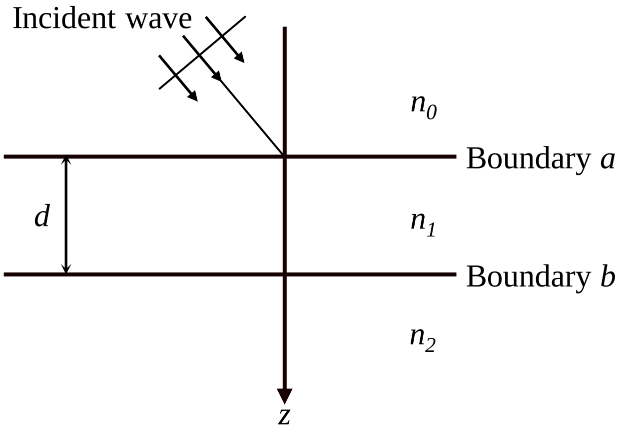

Figure 4.3. Plane wave incident on a thin film.

Calculating the forward and backward components of E and H at the interfaces, the final expression connects the tangential components of E and H at the incident interface with the tangential components of E and H transmitted through the final interface, which can be written in a matrix form as

$$\begin{bmatrix} E_a \\ H_a \end{bmatrix} = \begin{bmatrix} cos\delta & (isin\delta)/\eta_1 \\ i\eta_1 sin\delta & cos\delta \end{bmatrix} \begin{bmatrix} E_b \\ H_b \end{bmatrix} \tag{4.12}$$

where δ is the phase factor and is given by

$$\delta = 2\pi N_1 d cos\theta_1/\lambda \tag{4.13}$$

Normalizing equation (4.12) by dividing both sides by E_b, one can arrive to

$$\begin{bmatrix} E_a/E_b \\ H_a/E_b \end{bmatrix} = \begin{bmatrix} \mathrm{B} \\ \mathrm{C} \end{bmatrix} = \begin{bmatrix} cos\delta & (isin\delta)/\eta_1 \\ i\eta_1 sin\delta & cos\delta \end{bmatrix} \begin{bmatrix} 1 \\ \eta_2 \end{bmatrix} \tag{4.14}$$

where the input optical admittance is now defined as

$$Y = \frac{C}{B} \tag{4.15}$$

The matrix in equation (4.14) can be extended to include m-layers of thin films on the front surface of a substrate

$$\begin{bmatrix} \mathrm{B} \\ \mathrm{C} \end{bmatrix} = \left\{ \prod_{r=1}^{q} \begin{bmatrix} cos\delta_r & (isin\delta_r)/\eta_\mathrm{r} \\ i\eta_\mathrm{r} sin\delta_r & cos\delta_r \end{bmatrix} \right\} \begin{bmatrix} 1 \\ \eta_\mathrm{m} \end{bmatrix} \tag{4.16}$$

where the suffix m denotes the substrate. The reflectance, transmittance and absorbance are given by

$$R = \left(\frac{\eta_0 B - C}{\eta_0 B + C}\right)\left(\frac{\eta_0 B - C}{\eta_0 B + C}\right)^* \tag{4.17}$$

$$T = \frac{4\eta_0 \mathbb{R}\mathrm{e}(\eta_m)}{(\eta_0 B + C)(\eta_0 B + C)^*} \tag{4.18}$$

$$A = \frac{4\eta_0 \mathbb{R}\mathrm{e}(BC^* - \eta_m)}{(\eta_0 B + C)(\eta_0 B + C)^*} \tag{4.19}$$

4.2. Materials Properties

In this section an overview of the main semiconductors properties will be discussed. The focus will be on silicon and CIGS materials since solar cell designs using these two materials will be modeled later in this chapter.

4.2.1. Bandgap Structure

The intrinsic carrier density n_i is a fundamental quantity in semiconductor physics which plays a significant role in the simulation of solar cells. In fact, n_i has a strong impact on the recombination losses and carrier mobilities which limit the ultimate conversion efficiency of solar cells. Therefore, in order to model solar cells, n_i must be accurately determined. Prior to 1990, the most commonly adopted value for crystalline silicon at T = 300 K was n_i = 1.45 x 10^{10} cm^{-3} which was affected by significant deviations from experiments. In 1991, Sproul and Green measured the intrinsic concentration to be n_i = 1.0 x 10^{10} cm^{-3} at 300 K, which is still the most widely accepted value within the PV community [156]. However, recent theoretical investigations [157] reinterpreted the Sproul and Green experiment, demonstrating that their measurements were influenced by the bandgap narrowing (BGN), although at relatively low doping densities. BGN is the reduction of bandgap at particular high doping concentrations due to the broadening of impurity levels into am impurity band. Using a theoretical study based on the finite-temperature full random-phase approximation model of BGN proposed by Schenk [158], an accurate value for n_i = 9.65 x 10^9 cm^{-3} for undoped crystalline silicon was determined. The result is consistent with the experiments by Sproul and Green [156] and Misiakos and Tsamakis [159] which gave the effective n_i due to bandgap narrowing instead of n_i for undoped silicon. The effective intrinsic concentration, $n_{i,eff}$, is given by

$$n_{i,eff}^2 = n_i^2 e^{\Delta E_g/k_B T} \tag{4.20}$$

where ΔE_g is the bandgap narrowing due to doping. The temperature dependent bandgap relation was proposed by Varshni as [160]:

$$E_g(T) = E_g(0) - \frac{\alpha T^2}{T+\beta} \tag{4.21}$$

where $E_g(0)$ is the bandgap energy at 0 K , and α and β are material specific parameters. The temperature dependent bandgap energy for silicon is plotted in Figure 4.4 where $E_g(0)$ is 1.170 [161] and α and β are 3.2 eV/K and 4.3 K, respectively [32].

In Sentaurus, there are different models to model the bandgap narrowing such as Bennestt-Wilson, Del Alamo, Slotboom and Schenk [32]. The effective band gap is calculated as [32], p251:

$$E_{g,eff}(T) = E_g(T) - E_{bgn} \tag{4.22}$$

where E_{bgn} is determined by the bandgap narrowing model used.

The Schenk model is used for silicon and the bandgap narrowing as a function of donor and acceptor concentrations is shown in Figure 4.5.

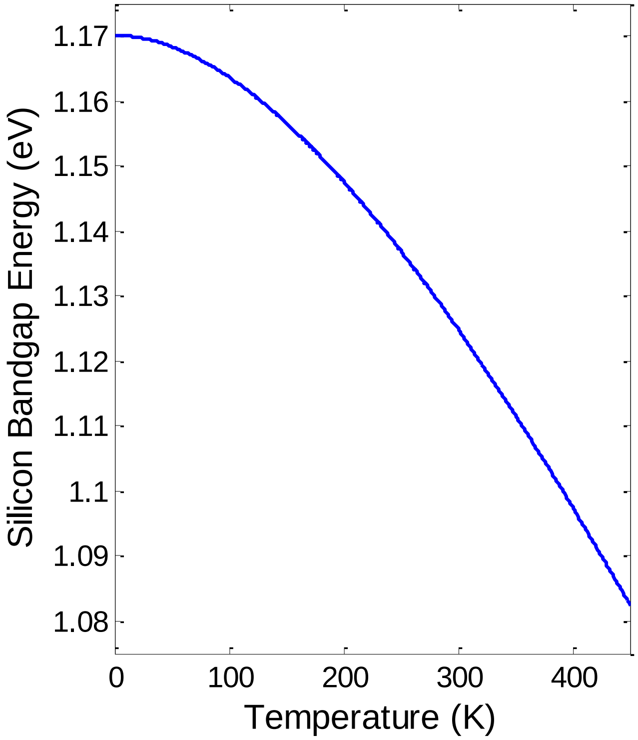

Figure 4.4. Temperature dependence of the intrinsic silicon bandgap energy after Varshni relation.

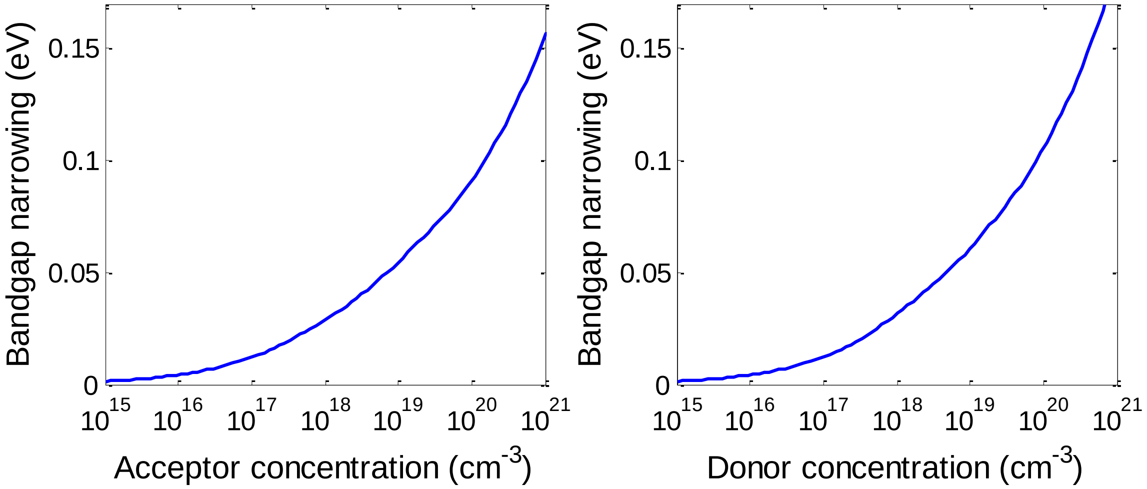

Figure 4.5. Bandgap narrowing due to acceptor (left) and donor (right) doping concentrations using the Schenk model.

In devices that contain different materials such as CIGS, the electron affinity χ is also important to determine the alignment of the conduction and valence bands at material interface. The electron affinity is defined as the difference between the lowest energy of the conduction band and the vacuum level. The affinity is temperature dependent and is affected by bandgap narrowing:

$$\chi(T) = \chi_0 + \frac{(\alpha + \alpha_2)T^2}{2(T + \beta + \beta_2)} + Bgn2Chi \cdot E_{bgn} \tag{4.23}$$

where χ_0 is material property representing the electron affinity at 0 K, and *Bgn2Chi* accounts for the split between conduction and valence bands due to bandgap narrowing, default value is 0.5. The bandgap of CIGS as a function of the molar fraction x can be written as [162]:

$$E_g = E_g(0) + \Delta E_g x - bx(1 - x) \tag{4.24}$$

where $E_g(0)$ is the bandgap energy of $CuInSe_2$, ΔE_g is the bandgap difference between $CuInSe_2$ and $CuGaSe_2$, b is the bowing coefficient, and the molar fraction x describes the concentration ratio of Ga and In as $In_{1-x}Ga_x$. $E_g(0)$ is in the range of 1 eV and ΔE_g is in the range of 0.6 eV while the bowing coefficients vary from 0.02 to 0.26. A good review on the bowing coefficient can be found in [163]. In our model the fitting parameters of 1.035, 0.653 and 0.264 for $E_g(0)$, ΔE_g, and b respectively are used after P. D. Paulson *et al.* [164]. The electron affinity as a function of molar fraction is given as:

$$\chi(x) = \chi(0) - \left(E_g(x) - E_g(0)\right) \tag{4.25}$$

where $\chi(0)$ is the electron affinity of CIS and is equal to 4.8 eV, $E_g(x)$ is the bandgap of CIGS, and $E_g(x)$ is the bandgap of CIS. The density of states for electrons and holes are calculated in Sentaurus using the following general formula [32], page 262:

$$N_{C,V}(T) = N_{C,V}(300\ K)\left(\frac{T}{300\ K}\right)^{\frac{3}{2}} \tag{4.26}$$

and the effective masses are calculated from the density of states as [32], page 262:

$$m_{e/p} = \left(\frac{N_{C/V}(300\ K)}{2.5094 \times 10^{19}}\right)^{\frac{2}{3}} \qquad (4.27)$$

The electron and holes effective masses of 0.09 and 0.71 [165], respectively, and therefore the electron and hole density of states are calculated from equation (4.27) to be 6.8 x 10^{17} cm^{-3} and 1.5 x 10^{19} cm^{-3} respectively.

4.2.2. **Optical Properties**

M. Green has reported the optical properties of silicon in 1995 and further updated them in 2008 [21], [166]. The data is given at 300 K over the 250 – 1450 nm range in 10 nm intervals. Calculated extinction coefficient is accurate up to 460 nm and beyond this wavelength the absorption coefficient is considered more accurate. Therefore in the range 460 – 1450 nm, the extinction coefficient from the absorption coefficient is calculated using the expression in equation (2.2). The absorption profile of crystalline silicon is plotted in Figure 4.6.

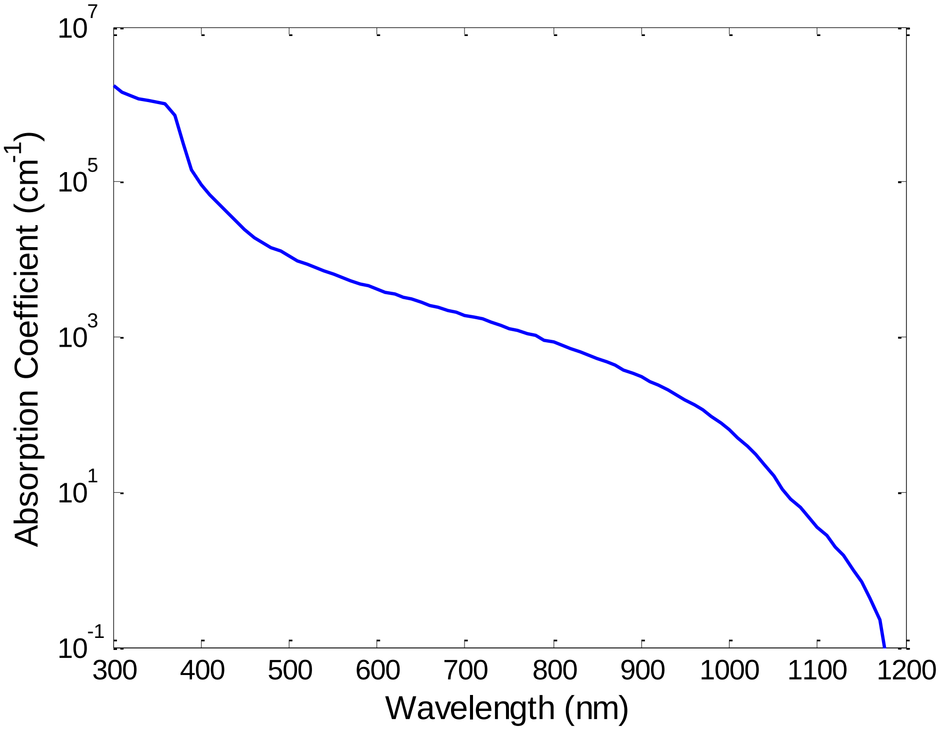

Figure 4.6. Absorption coefficient of silicon after M. Green [166].

CIGS is a direct bandgap material and therefore has a relatively sharp absorption edge near the bandgap with a high absorption coefficient compared to silicon. It requires a CIGS film of only 1 µm thickness to absorb more than 90% of the incident solar spectrum with photon energies higher than the bandgap. The complex refractive index for different molar fraction *x* is obtained from P. D. Paulson *et al* [164]. The calculated absorption profile for $CuIn_{1-x}Ga_xSe2$ with different (In,Ga) composition is plotted in Figure 4.7 for x = 0, 0.33, 0.45, 0.66 and 1.

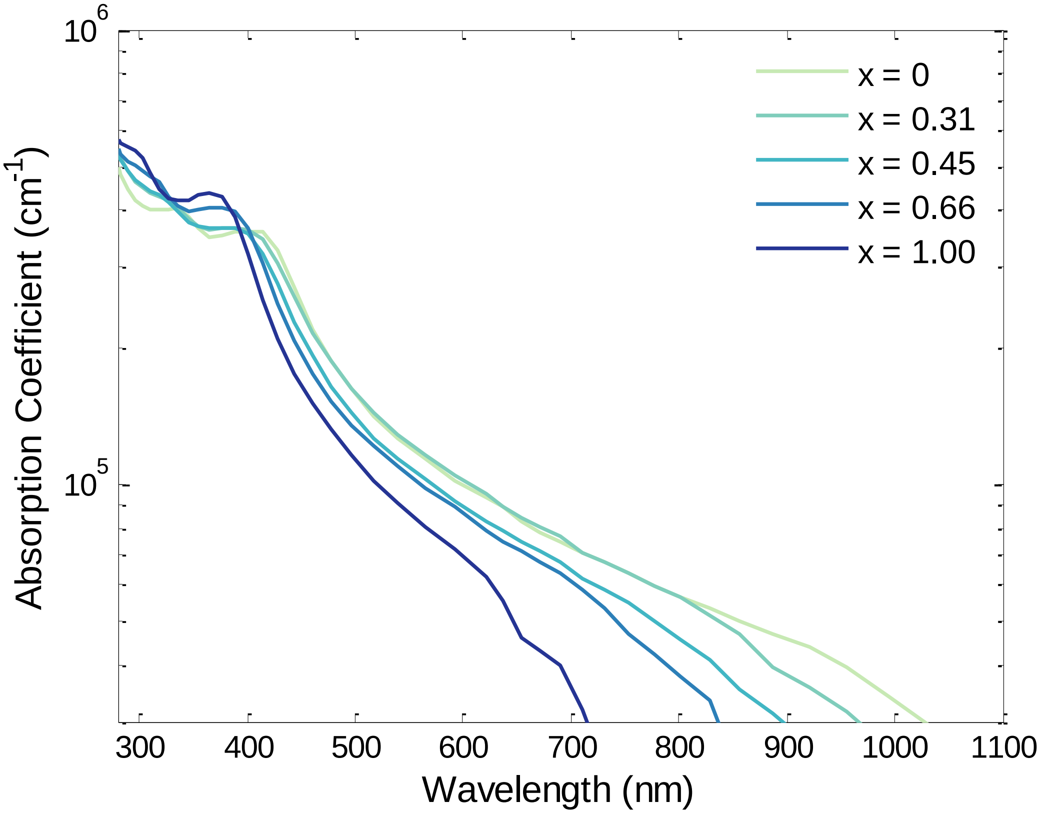

Figure 4.7. Absorption coefficient of $CuIn_{1-x}Ga_xSe2$ for molar fractions of 0, 0.31, 0.45, 0.66 and 1 [164].

4.2.3. **Carrier Mobility**

Electrons and holes are accelerated by electric fields, but their momentum is reduced because of various scattering processes such as from phonons, impurity ions, and surfaces. The carrier mobility is strongly linked to local electric field, lattice temperature and doping concentration. In presence of low electric fields, carriers are almost in equilibrium with the lattice and the mobility depends on phonon and impurity scattering which leads to mobility degradation. In case of high electric field intensity the carrier mobility is reduced because the carriers -that gain energy- have more probability to take part of more scattering processes. The simplest form is a temperature dependent mobility expression and it accounts for phonon scattering. It is called constant mobility model and it is doping independent. It is given by [32] (p302),

$$\mu = \mu_L \left(\frac{T}{300\ K}\right)^{-\zeta} \tag{4.28}$$

where $\mu_L$is the mobility due to lattice scattering and it is a property of the material, T is the lattice temperature, and ζ is an empirical fitting parameter.

It was recommended by Altermatt's review paper to use the Klaassen's mobility model for silicon since it accounts for majority and minority carrier mobilities. The model is implemented in Sentaurus using the Phillips unified mobility model. More information on the Klaassen model is found in [167].

On the other hand there is a large spread in mobility values reported for CIGS [20]. In addition, it has been reported that mobilities do not change significantly over hole concentrations ranging from 10^{16} to 10^{19} cm^{-3} [168]. Therefore, in our model, the electron and hole mobilities are are fixed at 200 and 25 cm^2/Vs, respectively [168].

4.2.4. Recombination Processes and Minority Carrier Lifetimes

Radiative, Auger and SRH recombination losses and carrier lifetimes were discussed sections 2.3 and 2.4, respectively. Under most conditions, the recombination rate for each mechanism, in each region, is dependent on the population of excess minority carriers in that region. As the bias on a cell increases from the short circuit toward the open-circuit condition, the excess minority carrier populations increase exponentially as a function of bias voltage. Usually one of these mechanisms, in one particular region of the device, is dominant and limits the open-circuit voltage.

The radiative recombination is modeled in Sentaurus using the equation

$$R_{rad,net} = B_{rad} \cdot (np - n_i^2) \tag{4.29}$$

where B_{rad} is the radiative recombination coefficient. Radiative recombination is very low in silicon and therefore it is usually ignored. Auger recombination dominates over SRH recombination at high doping concentrations, and it is modeled in Sentaurus as,

$$R_{Aug} = \left(C_n n + C_p p\right)\left(np - n_{i,eff}^2\right) \tag{4.30}$$

where C_n and C_p are material specific coefficients. The coefficients can be extended to be temperature dependent such that:

$$C_n(T) = \left(A_{A,n} + B_{A,n}\left(\frac{T}{T_0}\right) + C_{A,n}\left(\frac{T}{T_0}\right)^2\right) \cdot \left[1 + H_n \cdot e^{-\frac{n}{N_{0,n}}}\right] \tag{4.31}$$

and

$$C_p(T) = \left(A_{A,p} + B_{A,p}\left(\frac{T}{T_0}\right) + C_{A,p}\left(\frac{T}{T_0}\right)^2\right) \cdot \left[1 + H_p \cdot e^{-\frac{p}{N_{0,p}}}\right] \tag{4.32}$$

where T_o = 300 *K*. A_A, B_A, C_A, and H are fitting parameters for electrons and holes and are material specific parameters.

SRH recombination is implemented in Sentaurus using the formula in equation (2.24), rewritten again here:

$$R_{net}^{SRH} = \frac{np - n_i^2}{\tau_{SRH,p}(n + n_t) + \tau_{SRH,n}(p + p_t)} \tag{4.33}$$

where $\tau_{SRH,n}$ and $\tau_{SRH,p}$ are the SRH carrier lifetimes for electrons and holes, respectively, and n_t and p_t are the trap concentrations at the trap level. The doping dependence of the SRH lifetimes is modeled in Sentaurus with the Scharfetter relation given in equation (2.28), rewritten again:

$$\tau_{dop}\left(N_{A,0} + N_{D,0}\right) = \tau_{min} + \frac{\tau_{max} - \tau_{min}}{1 + \left(\frac{N_{A,0} + N_{D,0}}{N_{ref}}\right)^{\gamma}} \tag{4.34}$$

where τ_{min}, τ_{max}, N_{ref} and γ are material constants. For silicon $\tau_{min} = 0$ and $\gamma = 1$. The surface SRH recombination is activated in Sentaurus at interfaces. The formula implemented is similar to the bulk SRH given in equation (4.9) and is given in (2.26), rewritten here again:

$$R^{SRH}_{surf,net} = \frac{np - n_i^2}{\frac{(n+n_t)}{S_p} + \frac{(p+p_t)}{S_n}} \tag{4.35}$$

where n_s and p_s are the electron and hole concentrations at the surface, n_t and p_t are the electron and hole concentrations at the defect energy level, E_t and the S_p and S_n are the minority carrier surface recombination velocities (SRV) for holes and electrons, respectively, and is expressed in units of cm/s. The doping dependence of surface recombination velocities are modeled in Sentaurus according to [169]:

$$\mathrm{s} = s_0 \left[1 + \mathrm{s_{ref}} \left(\frac{N_{A,0} + N_{D,0}}{N_{ref}}\right)^{\gamma}\right] \tag{4.36}$$

where s_0, s_{ref}, N_{ref} and γ are material constants. In our simulations, we assume minority carrier surface recombination is doping independent by setting s_{ref} to zero.

The dominant recombination process in silicon is SRH recombination process and it increases considerably for multicrystalline wafers due to grain boundaries. At high doping concentrations (>1 x 10^{17} /cm^3), the Auger recombination becomes the dominant process, as shown in Figure 4.8. The coefficients used in the simulation are shown in Table 4.1 and they are based on Altermatt review paper [170].

Table 4.1. Coefficients of three main recombination processes in silicon solar cells [170].

Process	**Parameter**	**Electrons**	**Holes**
Auger	A_A (cm^6/s)	2.8 x 10^{-31}	7.91 x 10^{-32}
	B_A (cm^6/s)	0	-1.239 x 10^{-32}
	C_A (cm^6/s)	0	3.231 x 10^{-32}
	H	8	8
	N_O (cm^{-3})	2.5 x 10^{17}	2.5 x 10^{17}
Radiative	B_{rad} (cm^3/s)	4.73 x 10^{-15}	4.73 x 10^{-15}
SRH	τ_{max} (s)	1.5 x 10^{-3}	1.5 x 10^{-3}
	N_{ref} (cm^{-3})	1 x 10^{18}	1 x 10^{18}

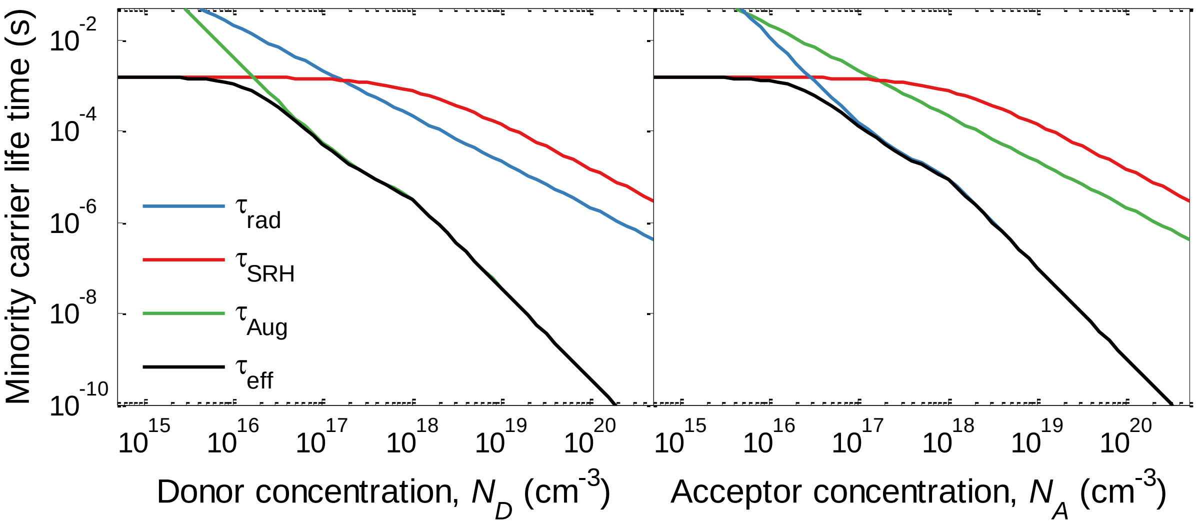

Figure 4.8. Minority carrier life times of radiative, SRH, Auger and the effective life time for holes in *n*-type silicon (left) and electrons in *p*-type silicon (right). Parameters used to calculate life times are based on Altermatt review paper [170].

A polycrystalline CIGS solar cell is composed of grains arranged at random orientations. The grains are relatively large, on the order of 1 µm, and therefore the material is crystalline over the width of a grain. However at the grain boundaries, intrinsic defects such as dislocations, vacancies, interstitials (misplaced atoms) and antisite defects, introduce electronic states within the bandgap that affect the transport and recombination properties. These electronic states will behave depending on their position within the bandgap of the material and their capture cross-section. Shallow defects close to the conduction band act as acceptor defect levels and attract electrons. Similarly, shallow defects close to the valence band act as donor defect levels and attract holes. Deeper defect levels close to the center of the bandgap are called recombination centers and attract both carriers.

It has been reported in the literature that the PL decay time in a CIGS solar cell is much longer than that in the as-grown films [171], [172]. This was explained as due to the deposition of CdS or other buffer layers that passivates the CIGS film surface. W. Metzger *et al.* have shown that the life time decreases by two orders of magnitude when high quality CIGS films are exposed to air. Therefore deposition of CdS protects the CIGS film and hence results in longer life times.

The recombination coefficients for the three processes are summarized in Table 4.2 [173]. Auger process is negligible in CIGS materials and therefore disabled in the simulations. SRH is usually the dominant recombination process up to a doping concentration of 10^{17} cm^{-3}, where radiative recombination becomes the dominant process for higher doping concentration, as shown in Figure 4.9.

Table 4.2. Recombination coefficients for the recombination processes in CIGS.

Process	**Parameter**	**Electrons**	**Holes**
Auger	A_A (cm^6/s)	0	0
	B_A (cm^6/s)	0	0
	C_A (cm^6/s)	0	0
	H	0	0
	N_0 (cm^{-3})	0	0
Radiative	B_{rad} (cm^3/s)	2.67×10^{-9}	2.67×10^{-9}
SRH	τ_{max}	3×10^{-9}	3×10^{-9}
	N_{ref} (cm^{-3})	1×10^{18}	1×10^{16}

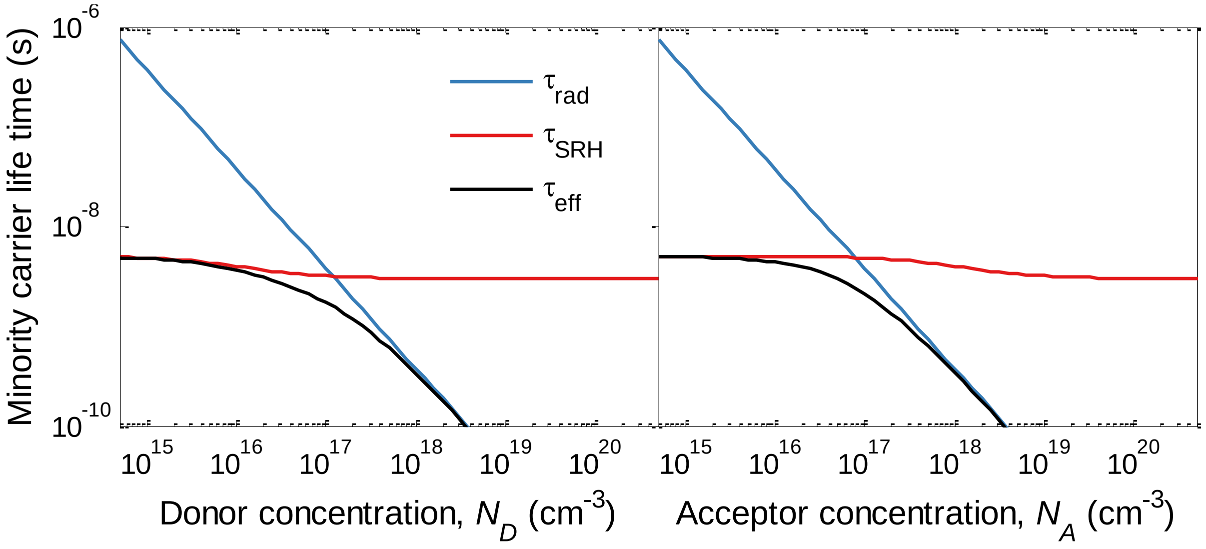

Figure 4.9. Minority carrier life times of radiative, SRH and the effective life time for holes (left) and electrons (right) for CIGS. Parameters used to calculate life times are based on [173].

4.3. Solar Cell Models and Results

In this section, the models for different solar cells are discussed. The developed models will be used in examining the effect of adding DC and DS layers, as will be seen in chapter 6. Therefore the objective of the models developed in this section is not to find the best solar cell design, or to fit experimental design. The objective is to develop a solar cell model that represents commercial grade solar cells based on well-known material parameters.

4.3.1. Silicon Solar Cells

Silicon photovoltaics have dominated the PV market from the beginning and they share more than 80% of the PV market today despite the emerging thin-film and concentrated photovoltaic technologies. One of the reasons for silicon to be dominant in PV comes from the fact that microelectronics has developed silicon technology to a great extent.

Numerical modelling of silicon solar cells had evolved over the years to optimize the cell design. The simulation of solar cells depends on the material parameters, as mentioned in section 4.1. Although silicon is the most researched material due to its wide use in both photovoltaic and microelectronics industries, more accurate material properties such as intrinsic carrier concentration, minority carrier mobility and recombination coefficients, are being published that further improves the developed models.

Typical *p-n* homojunction cells require a number of features such as: (1) a substrate thickness exceeds the absorption depth for efficient light absorption unless there is a light trapping mechanism, (2) junction should be shallow compared to diffusion length to avoid having a dead layer especially when one carrier type has very poor mobility, such as holes in silicon, (3) emitter should be doped heavily to improve conductivity, (4) reflection of light should be minimized by means of light trapping techniques.

4.3.1.1. Structure

Most commercial silicon modules are constructed by connecting a number of solar cells (50, 60 or 72) in series. Each cell has a surface area of almost 15 x 15 cm^2. With the enhancement in light trapping, cells are now thinner with a thickness of 180 µm. To model the solar cell it is not required to simulate the whole structure as the solar cell is highly symmetric. Therefore a small part of the cell is simulated. The smallest symmetry element spreads out horizontally from the middle of the front metal finger to the midpoint between two front metal fingers, whereas vertically, the whole structure must be simulated. Thus, the symmetry element for a planar solar cell is only in 2-D. Figure 4.10 shows the smallest symmetry element for the simulated silicon solar cell with a width of 600 µm and thickness of 180 µm.

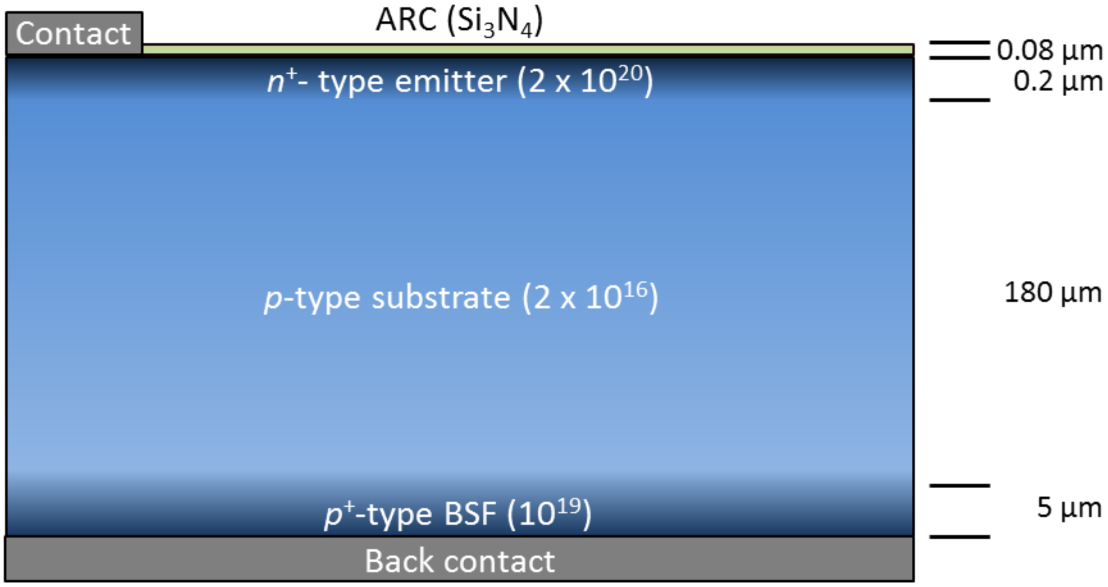

Figure 4.10. A two dimensional schematic of crystalline silicon solar cell implemented in TCAD Sentaurus. The structure is 600 µm wide and 180 µm deep with a contact width of 5 µm. Schematic is not to scale.

A silicon solar cell is a p-n junction in its simplest form. The silicon substrate is boron doped p-type with a background doping of 2×10^{16} cm^{-3}. The emitter is n-type and can be achieved by adding pentavalent phosphorus atoms, which introduces an extra electron to the silicon atom, hence it is called donor atom. Phosphorus impurity atoms can be added to the substrate either by ion implantation or diffusion. Ion implantation allows greater control of the doping but is more costly and therefore diffusion is the preferred method commercially. The diffused doping profile can be modeled as a Gaussian or error function. Here the emitter is phosphorus doped using a Gaussian function with a peak doping concentration of 2×10^{20} cm^{-3}. The layer between the bottom contact and the substrate is usually heavily doped *p*-type to form an Ohmic contact, and referred to as back surface field (BSF). BSF is also designed to form a potential barrier to the minority carriers near the *p*-contact. While the introduction of impurity atoms degrades the material quality, it is required to reduce the series resistance in the emitter and increases the built-in potential which enhances the open-circuit voltage. The BSF has a boron doping profile which is modeled using a Gaussian function with a peak doping concentration of 1×10^{19} cm^{-3}. Both emitter and BSF doping profiles are shown in Figure 4.11.

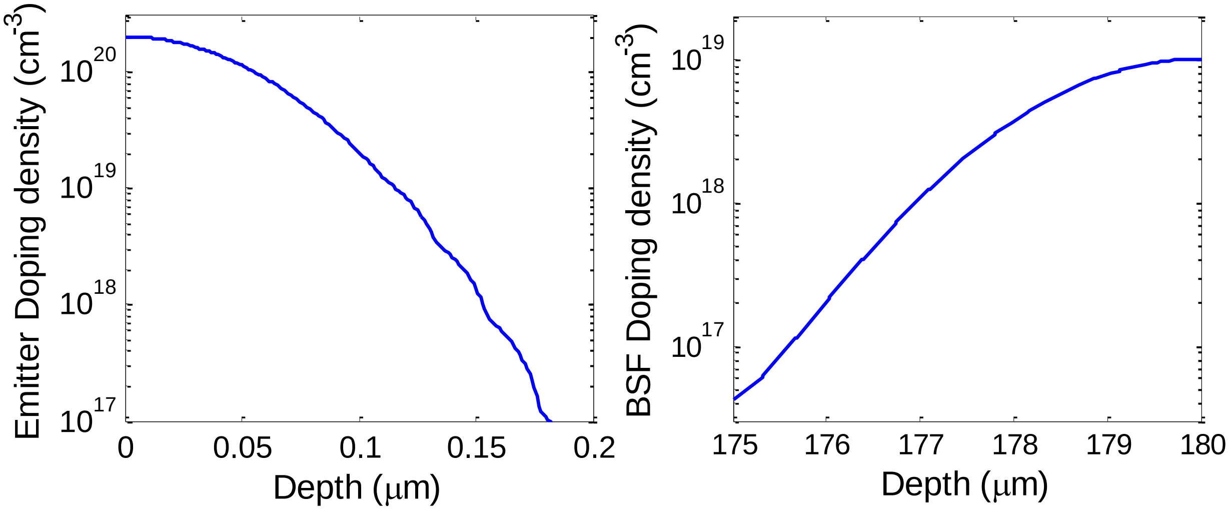

Figure 4.11. Simulated doping concentrations for (a) n^+ emitter and (b) p^+ BSF. Both doping profiles are modeled in TCAD Sentaurus as Gaussian shapes with peak values of 2×10^{20} cm^{-3} for emitter and 1×10^{19} cm^{-3} for BSF.

The substrate should be as thick as possible to allow for maximum absorption and in addition they are not affected by surface recombination at the rear surface. However they suffer from series resistance. A typical thickness in the range of 200 – 300 μm is common in industry for easier fabrication and handling of moderate thickness despite the cost of using extra silicon. With advanced light trapping techniques and procedures to handle thinner wafers, it is possible to achieve wafers in the range of 150 – 200 μm with the same absorption as a 200 – 300 μm thick wafer.

Contacts are added to the top and bottom of the structure. The front contact finger is 12 μm thick silver with a width of 5 μm, which is equal to half of the width of the front contact finger. Front contacts should be wide to minimize series resistance, whereas reducing this will decrease shadowing; implying design trade-offs. The back contact covers the whole width of the device (600 μm).

The ARC is a thin optical layer with refractive index between that of the semiconductor (silicon in our case) and air. For silicon the refractive index of ARC should be around 2. Suitable materials for silicon solar cell are silicon nitride (SiN_x), silicon dioxide (SiO_2), tantalum oxide (Ta_2O_5) and titania (TiO_2). The layer thickness is optimized to achieve zero reflection at a specific wavelength, usually 650 nm, where the incident photon flux is at maximum. An ARC can reduce reflections in the visible range to below 5% as compared with about 40% for a bare cell. In addition, an ARC layer can act as a passivating layer, thus reducing surface recombination.

A graded mesh strategy along X and Y directions are adopted for the numerical modelling. The mesh strategy is fine at vertices near interfaces where the solution to the coupled differential equations varies strongly with distance, such as near the space charge region or at interfaces, otherwise the convergence errors become significant. On the other hand, the bulk region can have a course mesh vertices spacing. The advantage of the graded mesh strategy compared to the uniform mesh strategy is minimizing computational time while maintaining numerical accuracy near at interfaces. A schematic of a solar cell with graded mesh strategy simulated in Sentaurus is shown in Figure 4.12. It takes about 43 minutes to perform *J-V* simulation for the structure below.

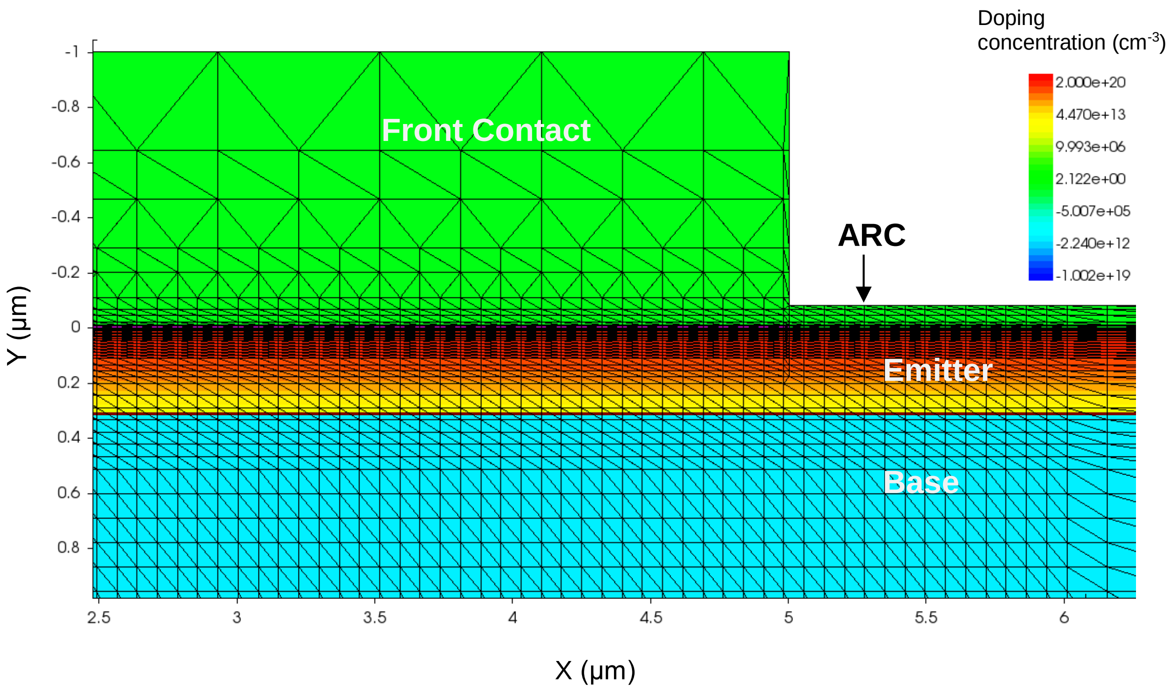

Figure 4.12. Generated structure in Sentaurus showing the graded mesh strategy for the silicon solar cell.

Table 4.3. Main Parameters of the simulated silicon solar cell.

	Parameter	**Value**
Front contact	Contact resistivity (Ω cm^2)	2 x 10^{-3}
Front ARC	Material	Si_3N_4
	Thickness (nm)	80
Emitter (n^+)	Depth (µm)	0.2
	Doping Concentration (/cm^3)	2 x 10^{20}
	Surface recombination velocity (cm/s)	10^3
Substrate layer	Thickness (µm)	180
	Doping Concentration (/cm^3)	2 x 10^{16}
	SRH life time (seconds) $\tau_n = \tau_p$	7.5 x 10^{-5}
	Radiative recombination Coefficient (cm^3/s)	4.73 x 10^{-15}
Back Surface Field (BSF)	Depth (µm)	5
	Doping Concentration (/cm^3)	1 x 10^{19}
	Surface recombination velocity (cm/s)	10^3
Back contact	Contact resistivity (Ω cm^2)	5 x 10^{-3}

The main design parameters used to simulate the silicon solar cell are summarized in Table 4.3. These parameters are based on review papers [170], [174] and some conventional silicon modules [175]–[177] that usually have efficiency in the range of 16% with the exception of the SunPower x-series monrcrystalline silicon modules that have efficiency of 21% [175].

4.3.1.2. **Energy Bandgap Diagram**

Examining the bandgap of the silicon solar cell under different conditions helps us understand the changes in the majority and minority carriers. Figure 4.13 shows the band energy diagram of the silicon solar cell under at equilibrium, short-circuit and open-circuit. At equilibrium, the electric field due to ionized donors and acceptors opposes diffusion of majority carriers across the depletion layer. However some majority carriers cross the junction and thus become minority carriers. Minority carriers will travel a distance on average equal to the carrier diffusion length before they recombine. Minority carriers can be also drifted to the other side by the electric field at the junction thus creating a drift current. The drift current is balanced by the diffusion current so that the net current flow is zero. At equilibrium, the Fermi levels (dashed lines) of *p*- and *n*-type layers are equal and constant throughout the device, as shown in Figure 4.13 (a). This implies no net current is flowing. The difference between the work function (not shown in this figure) of both layers is represented as built-in bias and is dependent on the doping concentrations of donor and acceptors as well as the intrinsic concentration of silicon.

At short-circuit condition and under illumination the quasi Fermi levels split, as shown in Figure 4.13 (b). Light is absorbed within the active region, creating a population of minority carriers in the emitter and the base. In the emitter and the base, there is a gradient in the minority carrier quasi-Fermi levels (and hence in the minority carrier concentrations). This gradient will cause minority carriers to diffuse towards the junction, where the electric field within the depletion region accelerates them across the junction and into the base (in the case of minority electrons) or into the emitter (in the case of minority holes). The front and back surface fields effectively prevent any diffusion away from the junction. With carriers steadily flowing in this way, a current can be collected at the device terminals.

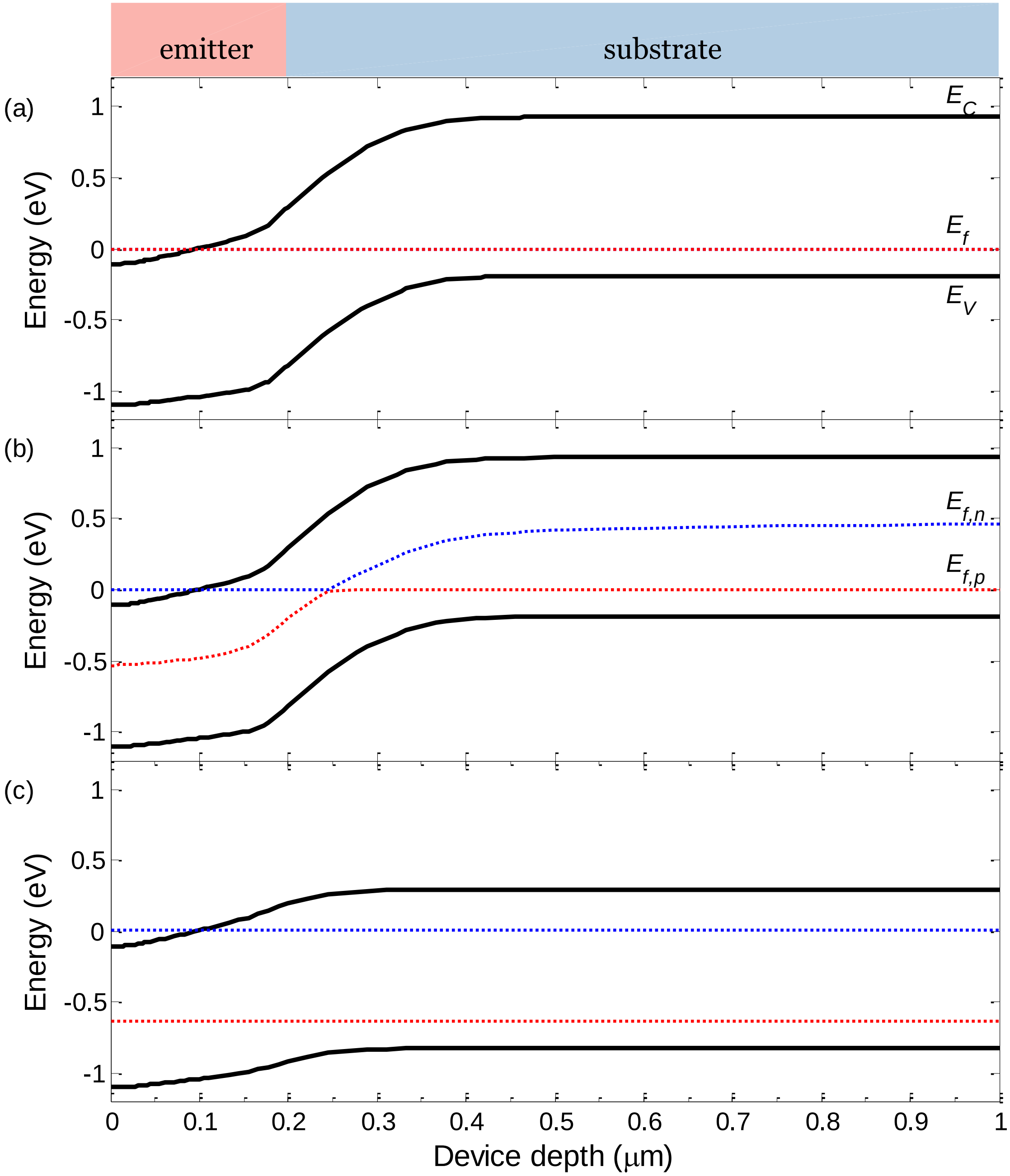

Figure 4.13. Band diagram of silicon solar cell under (a) equilibrium, (b) short-circuit current and (c) open-circuit voltage conditions. The top and bottom black lines are the conduction and valence bands, respectively. The dotted blue line is the electron quasi fermi level while the dotted red line is the hole quasi fermi level.

At a particular bias, the width of the depletion region is reduced to the point that carriers are no longer accelerated across the depletion region, and the current is reduced to zero. This condition is open circuit (Figure 4.13 (c)). With zero net current, the quasi-Fermi levels are again flat, and carrier concentrations are increased since they are not being removed through the external circuit.

4.3.1.3. Simulated Results

The performance of the silicon solar cell in terms of J_{sc}, V_{oc}, *FF* and efficiency are simulated by sweeping the voltage of the device under illumination using the AM1.5G standard spectrum. Simulated results for silicon solar cells show a 17.7% efficiency with J_{sc} of 36 mA/cm^2 and V_{oc} of 0.64 V. These results are comparable to the average commercial cells which vary from 15% up to 21% by SunPower for monocrystalline silicon modules.

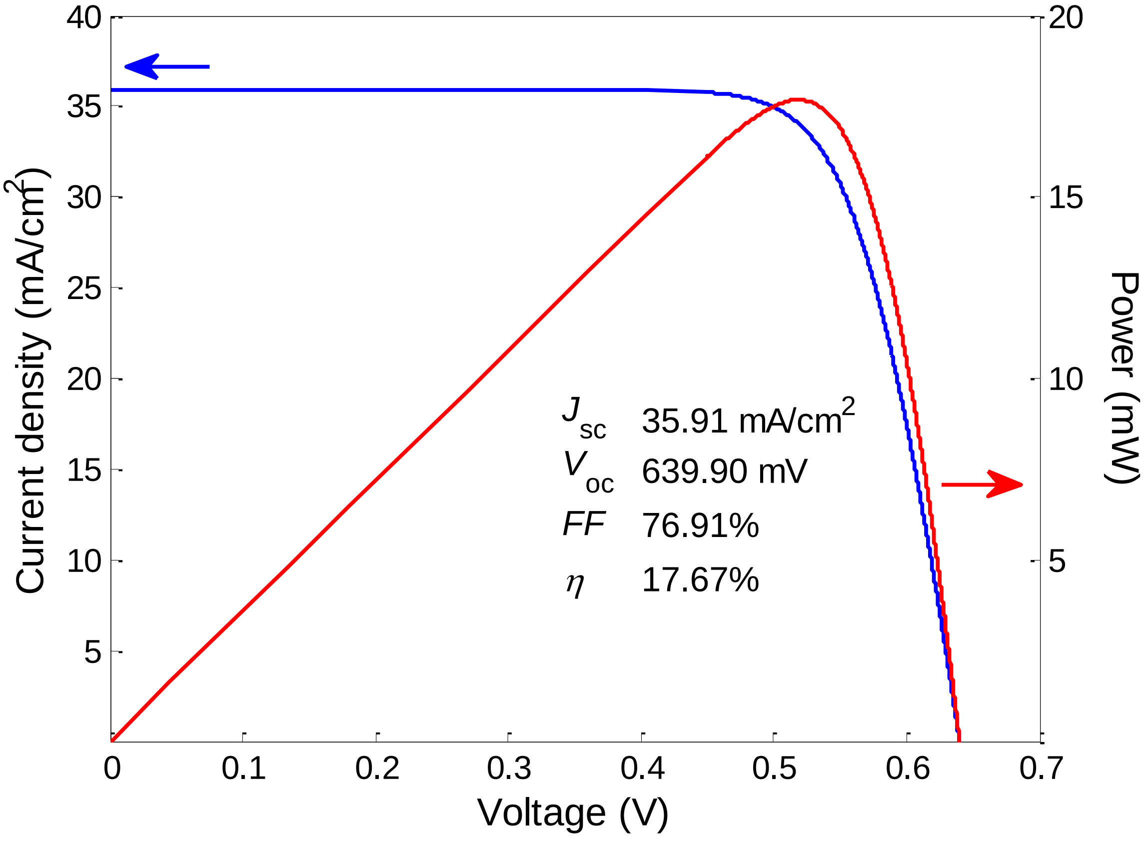

Figure 4.14. Simulated *J–V* curve for silicon solar cell with design parameters in Table 4.3.

Another important characterization of a solar cell is the quantum efficiency. To simulate the quantum efficiency of the silicon solar cell, a full wavelength sweep is required within the range of the illumination spectrum. The EQE of the silicon solar cell along with the reflectance are shown in Figure 4.15 . The ARC layer is optimized to minimize reflection losses in the 500 – 700 nm where the flux of photons is a maximum in the solar spectrum.

The shape of the EQE located in the long-wavelength region is dictated by the absorption coefficient of silicon. As mentioned before silicon is an indirect bandgap material and therefore the absorption profile reduces gradually as it approaches the bandgap. In addition the oscillations seen at the long-wavelength of the EQE are due to the internal reflectivity of the structure. These fast oscillations in the reflectance originate from the constructive and destructive interference at the back surface of the solar cell.

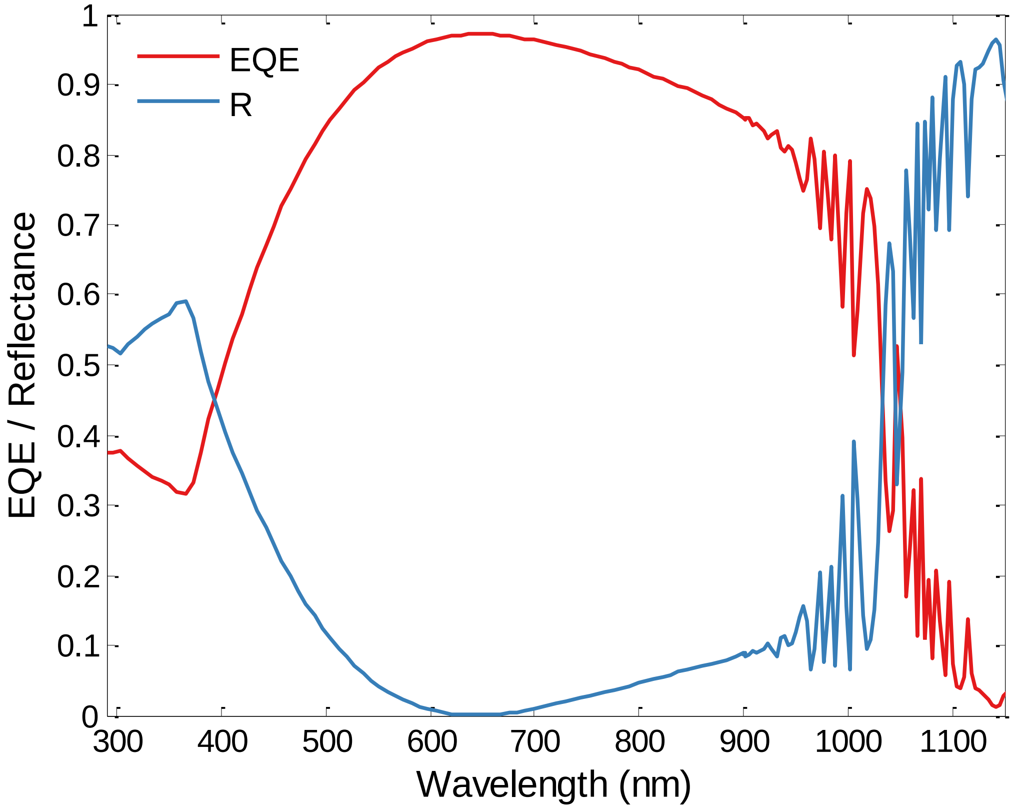

Figure 4.15. Simulated external quantum efficiency and reflectance of silicon solar cell model.

4.3.1.4. Design Considerations

In this section certain parameters such as doping concentration, layer thicknesses and recombination will be varied to study their effects on the solar cell performance.

Substrate: The substrate is only lightly doped to increase the minority electron diffusion length and to limit Auger recombination. On the other hand, higher doping is favored when SRH recombination is present, since recombination is proportional to the excess density which decreases, for a given voltage, as doping increases. This is balanced with a reduction of lifetime itself. High doping also helps to minimize the series-resistance losses associated with the transport of carriers to the back face in thick cells with the majority-carrier contact at the back.

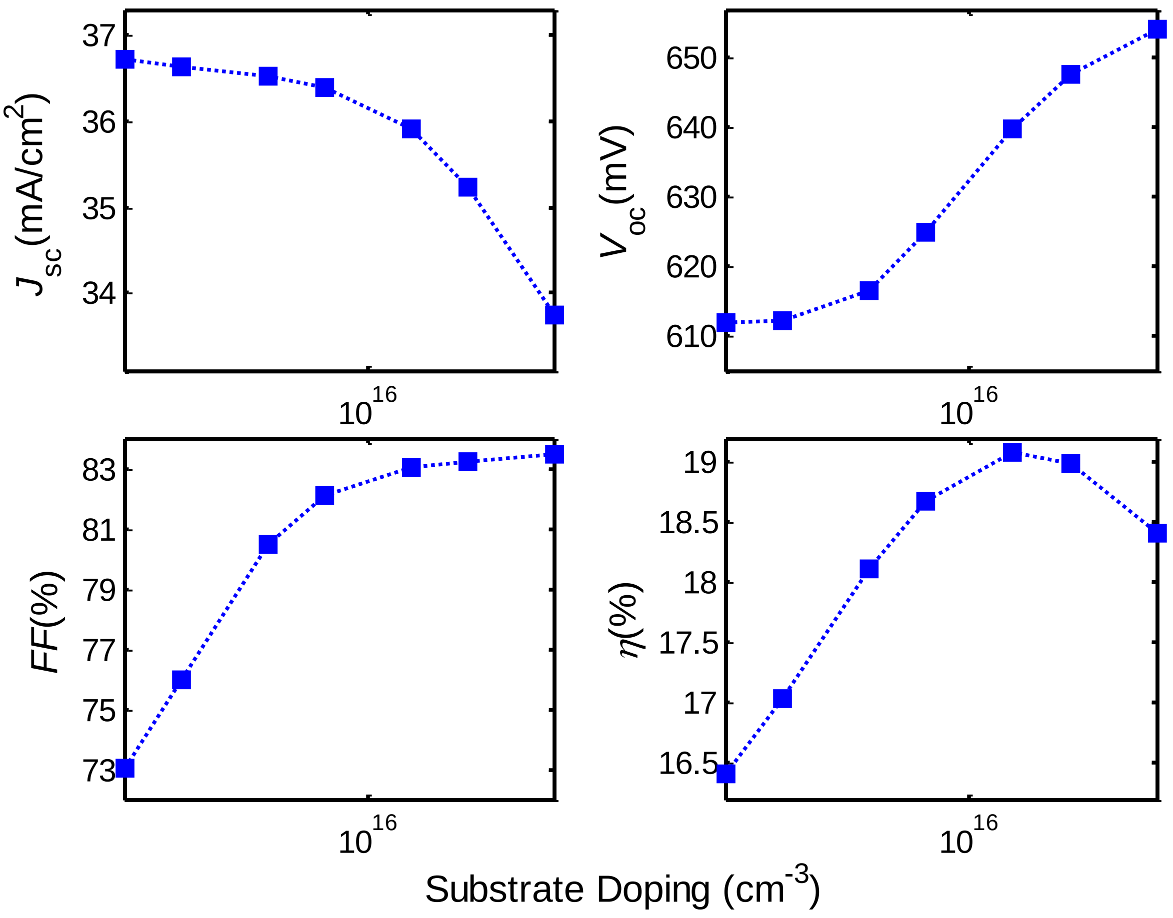

Figure 4.16. The effect of varying the substrate doping concentration. The dotted line is guide to the eye.

As can be seen in Figure 4.16 the J_{sc} is reduced as the substrate doping concentration increases, this is mainly due to the decrease in diffusion length which causes generated minority carriers to recombine faster. On the other hand, the *FF* and V_{oc} are enhanced as doping concentration increases as a result of reducing recombination by reducing the equilibrium minority carrier excess. The maximum efficiency is therefore found for a substrate doping concentration of 10^{16} cm^{-3}.

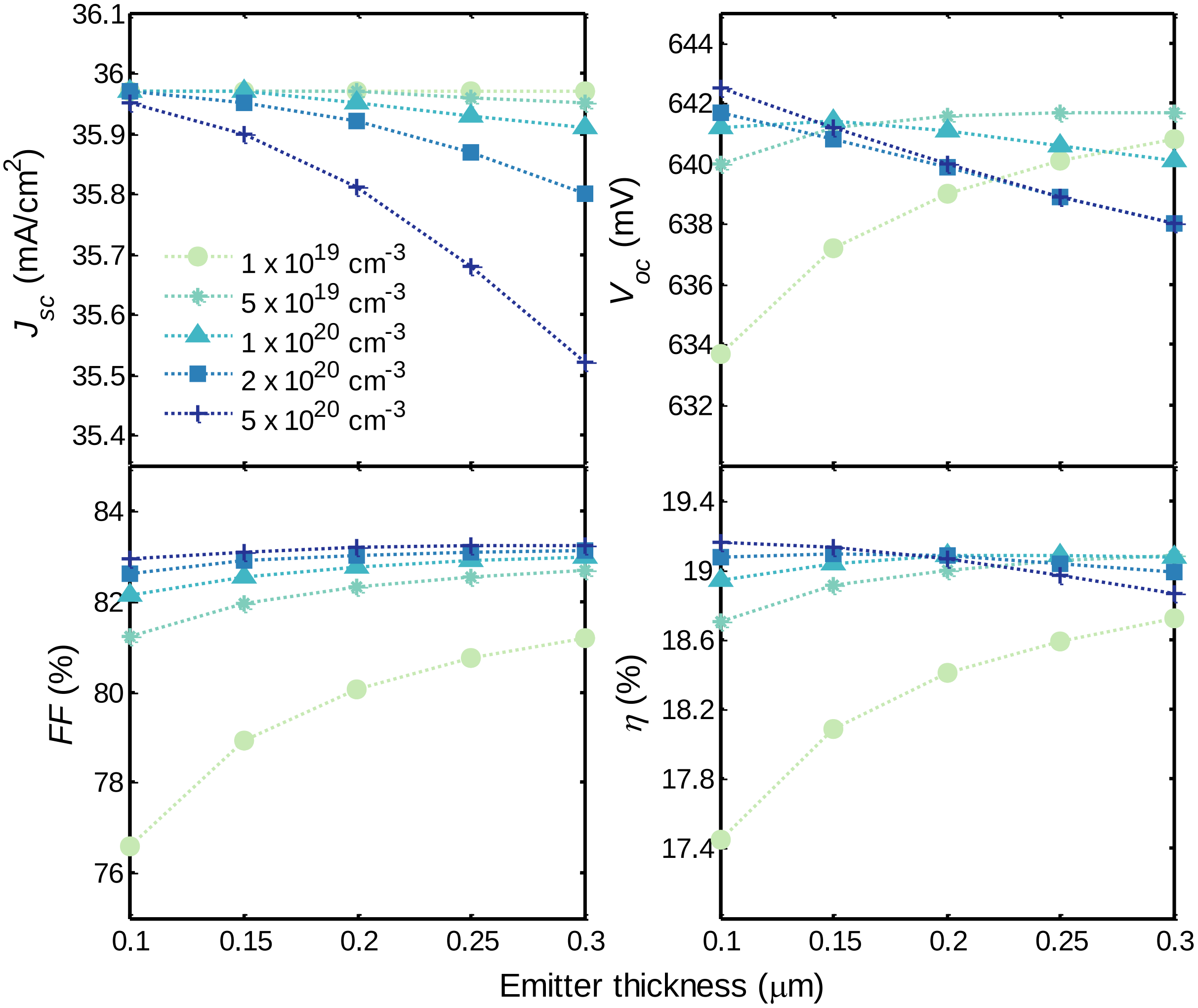

Figure 4.17. The effect of varying the emitter doping concentration and junction thickness.

Emitter: The emitter is usually heavily doped to reduce series resistance. Sheet resistance can also be reduced by increasing the emitter thickness for a fixed doping. However, a large fraction of light is absorbed close to the surface and therefore the emitter should be thin so that generated carriers are within a diffusion length of the p-n junction. Thus there is an optimum emitter doping concentration and thickness in order to optimize the cell efficiency. Figure 4.17 illustrates the effect of varying the emitter doping concentration and junction thickness.

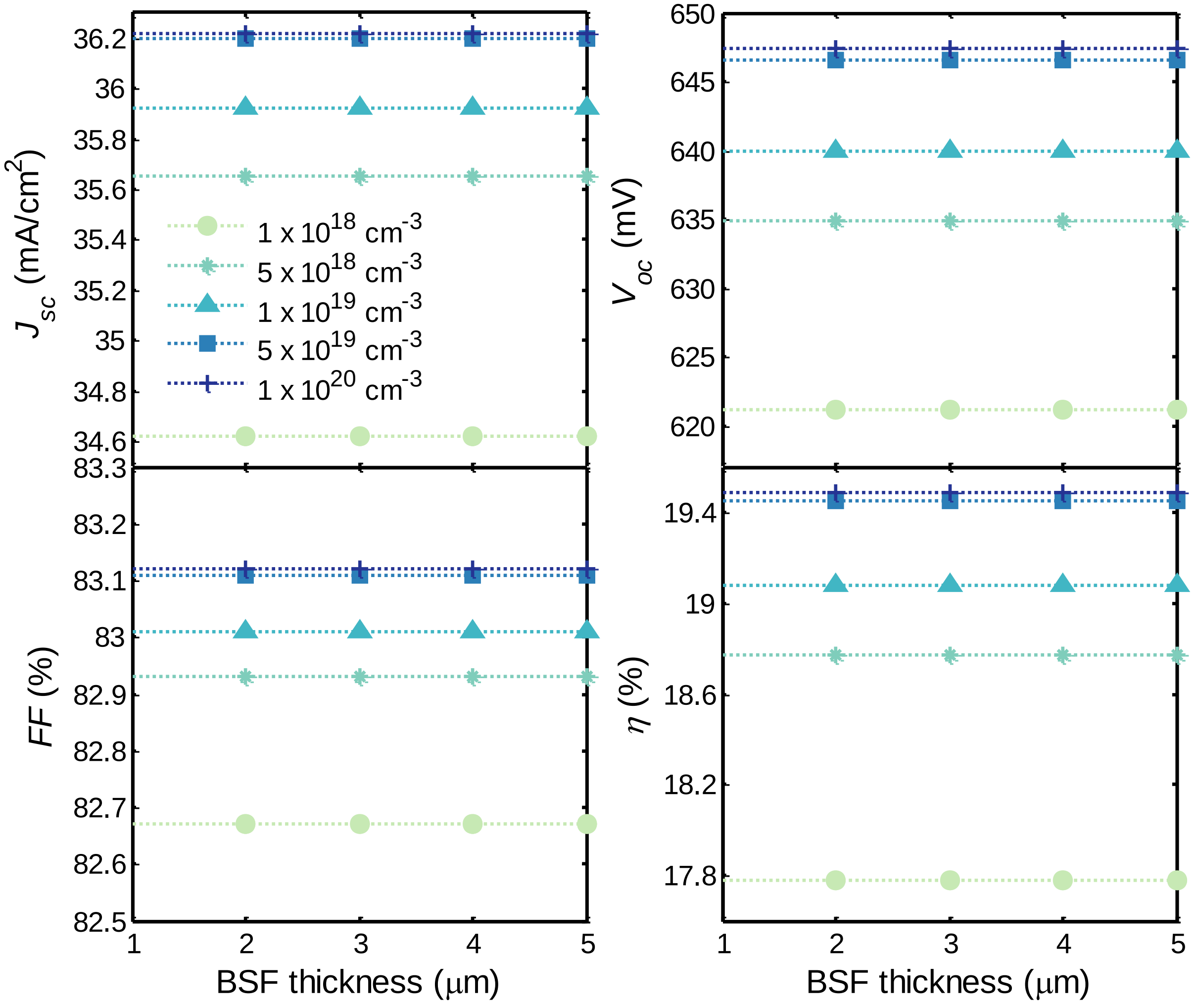

Figure 4.18. The effect of varying the BSF thickness and doping concentration

Back surface field: Rear surface recombination can be reduced by forming a heavily doped layer at the back surface of the *p*-type base. The p^+-p junction forms a potential barrier to the minority electrons, and therefore reduces the effect of rear surface recombination. In addition the p^+-p junction adds to the built-in bias and therefore enhances V_{oc}. Figure 4.18 illustrates the effect of varying the BSF thickness and doping concentration.

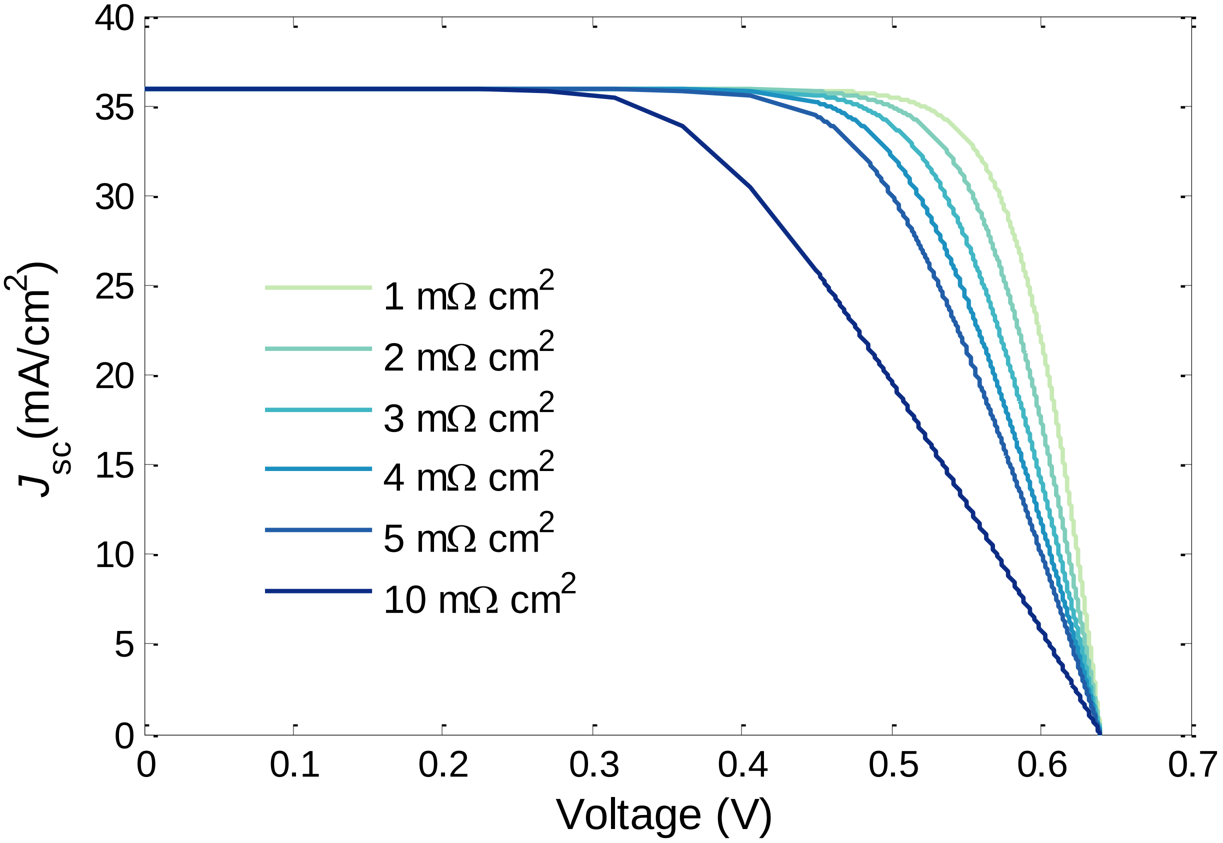

Figure 4.19. Effect of increasing the front contact series resistance on the *J-V* curve.

Series resistance: The main impact of series resistance is to reduce the fill factor, although excessively high values may also reduce the short-circuit current, as was shown in Figure 2.7 in chapter 2. Figure 4.19 presents the effect of increasing the series resistance on the *J-V* curve. As can be seen the *FF* is highly affected.

Surface recombination: The surface recombination velocity has a significant impact on the variations of quantum efficiency of the solar cell. Higher surface recombination velocity implies that the rate of recombination of charge carriers in the solar cell increases and hence less carriers are collected. Figure 4.20 illustrates how the EQE of the silicon solar cell decreases in the short-wavelength range when increasing the front surface recombination velocity. Similarly if the back surface recombination velocity is increased, the long-wavelength part of the EQE would be decreased.

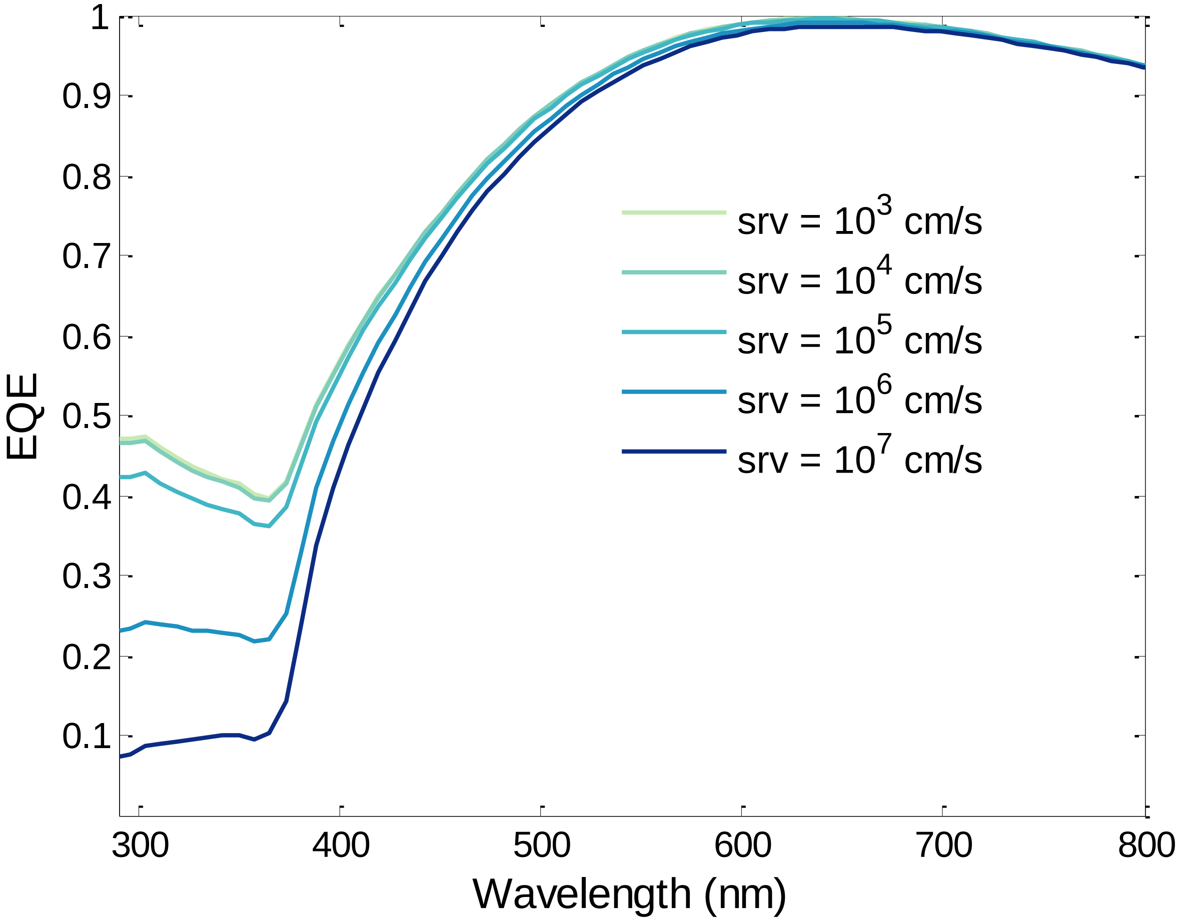

Figure 4.20. Effect of increasing the surface recombination velocity on the short-wavelength part of the external quantum efficiency of the silicon solar cell.

4.3.2. **CIGS Solar Cells**

Thin film Cu(In,Ga)Se_2 (CIGS) solar cells have attracted considerable attention due to their low cost and high efficiency. CIGS solar cell efficiencies have been shown to systematically exceed 20% by NREL [178], ZSW [179], and Solibro [180]. Large area commercial CIGS modules have achieved efficiencies up to 17% by Solar Frontier [181].

CIGS solar cells are composed of a hetrostructure junction with a wider bandgap *n*-type material, which is typically CdS. The wide bandgap shifts the generation profile directly into the absorber layer, which is referred to the CIGS layer, since the larger bandgap energy minimizes absorption in the *n*-type layer. Such configuration can form a very efficient solar cell. In this case, the *n*-type emitter layers are often referred to as "window" layers, due to their intended photon transparency.

$CuInSe_2$ and $CuGaSe_2$ are both chalcopyrite semiconductors with direct bandgaps of 1.0 eV and 1.7eV, respectively. By exchanging In and Ga in the crystal, the bandgap can be varied between these values. Experimentally, the best efficiencies for CIGS have been obtained with bandgap of 1.2 eV, which corresponds to a molar fraction (Ga/(In+Ga)) of 0.3 [178], [179]. Characterization of CIGS thin films with different molar fractions have shown that while adding gallium enhances the mobility of the material and therefore V_{oc} up to molar fractions of about 0.5. Beyond that V_{oc} does not improve monotically due to recombination centers deep in the bandgap as the bandgap gets wider.

While the fabrication of CIGS solar cells has evolved recently with four new record efficiencies in the past 3 years, numerical modelling is still catching up. Unlike silicon, numerical modelling of CIGS solar cells is requires extensive literature review for a number of reasons: 1) the relatively complicated structure of the solar cell with more than three different materials, 2) the lack of consistent material properties for all layers especially CIGS thin-film, 3) the lack of solid understanding of some recombination losses.

Numerical modelling of CIGS solar cells had been developed by a number of research groups [182]–[186]. The model used in this thesis is based on a baseline model developed in SUNLAB by Frederic Bouchard and Alex Walker in 2013 [183]. The material properties such as bandgap, optical constants, electron affinity, carrier mobilities, and lifetimes have been updated with more common data found in the literature.

4.3.2.1. **Structure**

CIGS solar cells are almost always designed in a substrate configuration starting from soda-lime glass. The back contact is typically sputtered molybdenum (Mo) and a thin layer of $MoSe_2$ forms at the CIGS/Mo interface due to diffusion of selenium from CIGS into Mo.

The CIGS absorber material is deposited by a great variety of processes that can be roughly categorized into vacuum co-evaporation and two-step selenization processes [187]. Co-evaporation deposits all elements simultaneously on a heated substrate. Intentionally or un-intentionally, gradients in the composition can be created. Selenization processes deposit all metals onto a film and react them in Se atmosphere to form the intended compound. Since CIGS is a direct bandgap material with a high absorption coefficient, a layer of thickness 2 - 3 µm is sufficient to absorb > 95% of the photons with energy higher than the material bandgap. The CIGS layer is doped *p*-type with typical doping concentration in the range 10^{16} - 10^{17} cm^{-3}.

CdS buffer layers are typically deposited on top of the CIGS absorber by chemical bath deposition. A buffer layer, such as CdS has proven beneficial to device performance. The CdS act as the *n*-type material with doping concentration in the range 10^{17}-10^{18}. CdS is the most popular buffer layer for CIGS solar cells. The typical thickness of CdS is 50 nm but it can range from 40 nm to 60 nm. Increasing the CdS thickness decreases the current collection and therefore it should be as thin as possible. The quantum efficiency at wavelength below 520 nm is proportional to the CdS thickness as it is commonly assumed that most electron-hole pairs generated in the CdS layer are not collected. Despite the low content of cadmium in CIGS solar cells that can be handled safely with respect to environment concerns and hazards, researchers are looking into replacing the CdS layer. The two approaches to achieve Cd-free solar cells are either omitting the CdS layer and deposit ZnO layer directly on the CIGS absorber layer, or find another material to replace CdS. A number of buffer layers have been proposed such as ZnS and ZnSe [20]. Solar Frontier produces the highest Cd-free CIGS modules with efficiency of 17.5% [181]. A good review of alternative buffer layers can be found here [187].

Highly doped ZnO window layers are typically deposited by RF-sputtering and act as transparent conductive oxide. Sometimes a thin layer of high-resistance (HR) ZnO is deposited on top of the CdS buffer layer. Studies suggested that the role of the HR ZnO layer is to reduce the impact of randomly occurring shunt paths in the device [187],

[188]. The HR ZnO layer does not degrade the performance of the solar cell as long as it is less than 100 nm thick. A thin metal grid is usually deposited on the top of the ZnO:Al layer for laboratory solar cells to increase current collection and reduce contact resistance. Commercial solar cells are usually monolithically connected in series to form modules with no metal grids, which is one advantage of thin film technology [187].

CIGS solar cells do not suffer high reflection losses (< 10%) like silicon solar cells (~30%), since the ZnO top layer has a low refractive index of 2, unlike silicon which has a refractive index of 3.6, thus suffers high reflection losses. However for laboratory cells it is beneficial to add an ARC layer to further reduce reflection losses. The common material for such cells is MgF_2 which has a refractive index of 1.4. A typical device structure is shown in Figure 4.21.

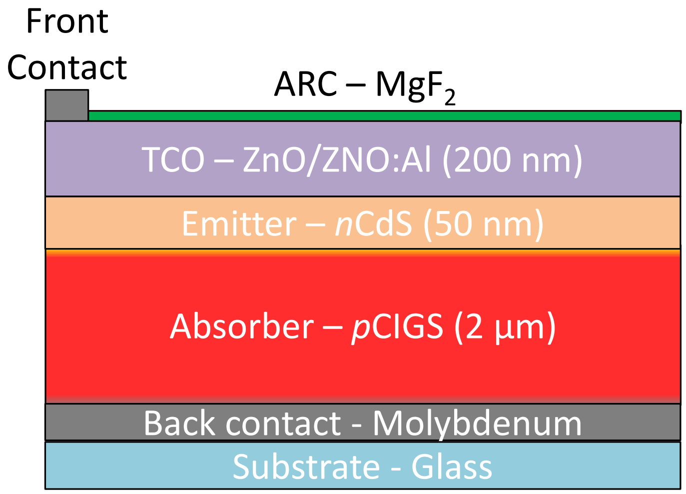

Figure 4.21. Schematic of typical structure of CIGS solar cell.

The CIGS solar cell model adopts typical material parameters reported in the literature and are summarized in Table 4.4 [165], [183], [189], [190].

4.3.2.1. **Energy Bandgap Diagram**

The band alignment at the interface of CdS/CIGS is Type I with conduction band offset (CBO) of 0.3 eV, which was guided by experimental and theoretical studies [191]. The ZnO/CdS interface is Type II. The band diagram at short-circuit condition is shown in Figure 4.22.

Table 4.4. Parameter set for CIGS, CdS and ZnO for the simulation of CIGS solar cells.

Parameter	**Symbol**	**CIGS**	**CdS**	**ZnO**
Bandgap	E_g (eV)	1.2	2.5	3.4
Electron affinity	χ (eV)	4.8	4.5	4.8
Density of states	N_C (/cm^3)	6.8×10^{17}	1.3×10^{18}	3.0×10^{18}
Density of states	N_V (/cm^3)	1.5×10^{19}	9.1×10^{18}	1.7×10^{19}
Effective electron mass	m_e/m_o	0.09		
Effective hole mass	m_h/m_o	0.72		
Dielectric constant	$\varepsilon/\varepsilon_o$	13.6	10	6.8
Layer thickness	d (nm)	2000	50	200
Donor concentration	N_D (/cm^3)	-	10^{17}	10^{20}
Acceptor concentration	N_A (/cm^3)	2.5×10^{16}	-	-
SRH lifetime	τ_{SRH} (sec)	3×10^{-9}	3×10^{-9}	3×10^{-9}

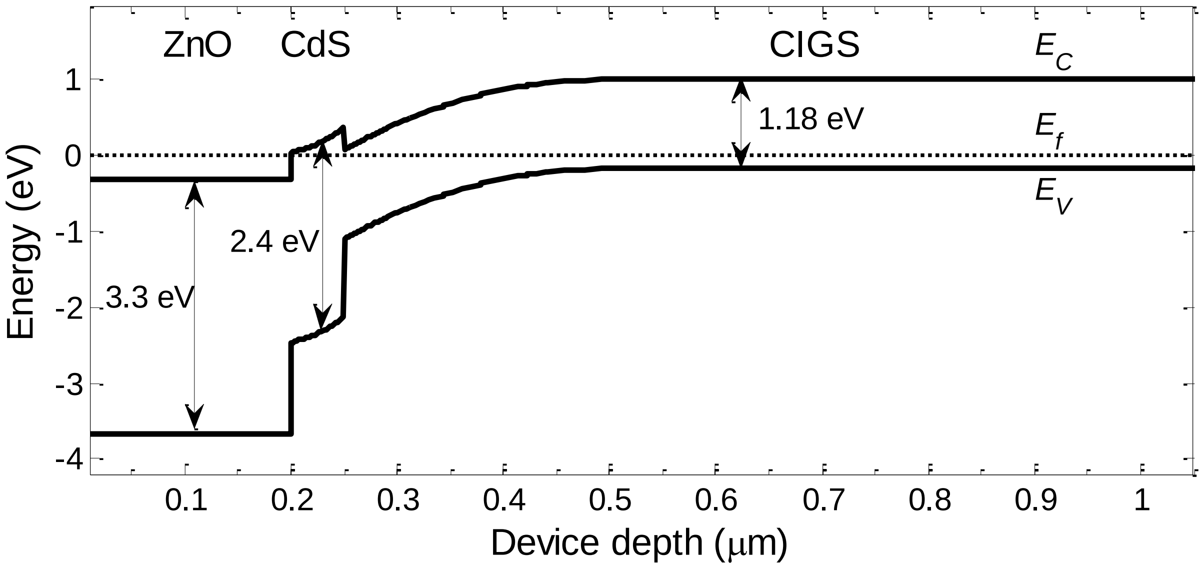

Figure 4.22. Band diagram of CIGS solar cell under short-circuit conditions.

4.3.2.2. **Simulated Results**

Simulated *J-V* curve of CIGS solar cell under illumination of AM1.5G spectrum is shown in Figure 4.23. A J_{sc} of 31.9 mA/cm^2 is achieved which is lower than the world record J_{sc} of 35.7 mA/cm^2. The J_{sc} can probably be further enhanced by adding an ARC layer. The V_{oc} of 0.67 V is highly lower than the record V_{oc} of 0.76 V, this can be attributed to a graded absorber layer in case of the world record solar cell. The overall efficiency of the simulated solar cell is 16.34% with a relatively good fill factor of 76.8%.

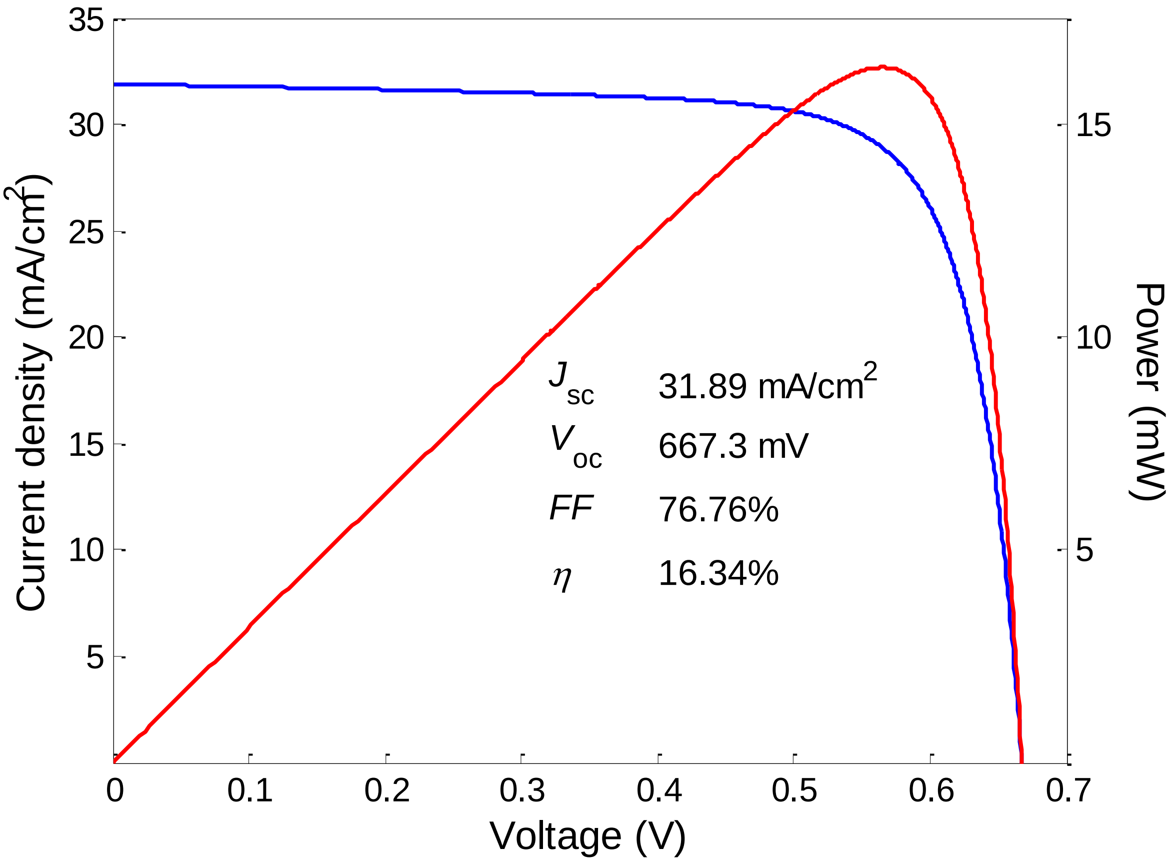

Figure 4.23. Simulated *J-V* curve for CIGS solar cell.

Simulated quantum efficiency of CIGS solar cells is shown in Figure 4.24. Front surface reflection lowers the EQE of the solar cell and can be usually minimized with an ARC layer. The irregularity of the reflectance is due to the different materials in the structure with different refractive indices.

The ZnO layer absorbs photons of wavelength < 400 nm and CdS absorbs photons of wavelength < 520 nm. While only a small percentage of the absorbed photons in the CdS layer contribute to carrier generation, photons absorbed in ZnO layer are completely lost. Therefore, the IQE of a typical CIGS solar cell shows poor response in the short-wavelength region (280 – 500 nm) with a much better response in the visible-near-infrared region (600 –1000 nm). Finally the low response in long-wavelength range is due to recombination losses and incomplete absorption of photons near the CIGS bandgap edge. The longer the wavelength, the deeper the generation of carriers, and the higher the likelihood of recombination.

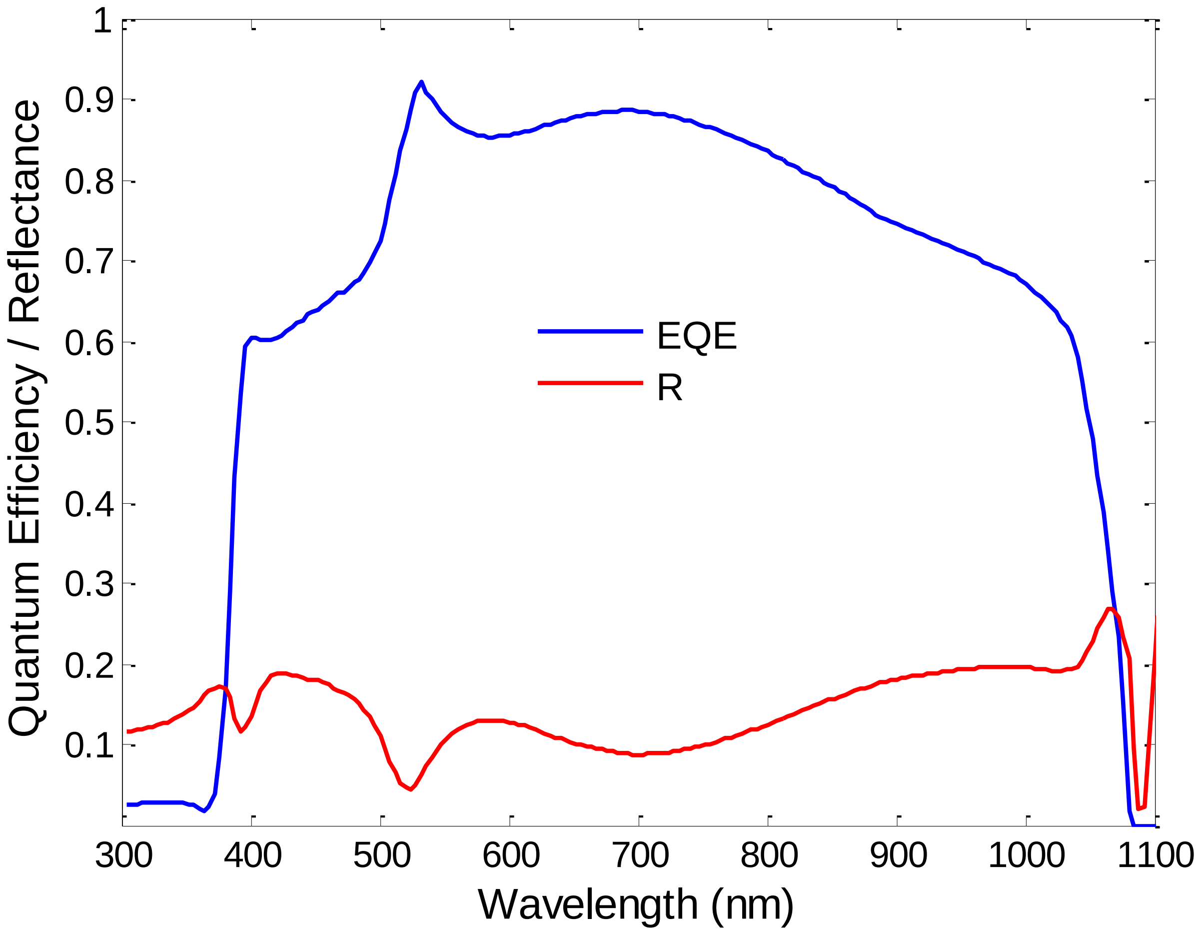

Figure 4.24. Simulated quantum efficiency curve of CIGS solar cell showing the EQE (blue) and reflectance (red).

4.3.2.3. Design Considerations

ARC layer: Simulated reflectance and EQE of solar cell with 120 nm MgF_2 layer on top surface is shown in Figure 4.25. As can be seen, the reflection losses are almost negligible in the range 600 – 800 nm which is reflected in an increased EQE. The solar cell efficiency increases to 18% mainly due to an increase in J_{sc} by ~4 mA/cm^2. The effect of the ARC layer on the solar cell performance is summarized in Table 4.5.

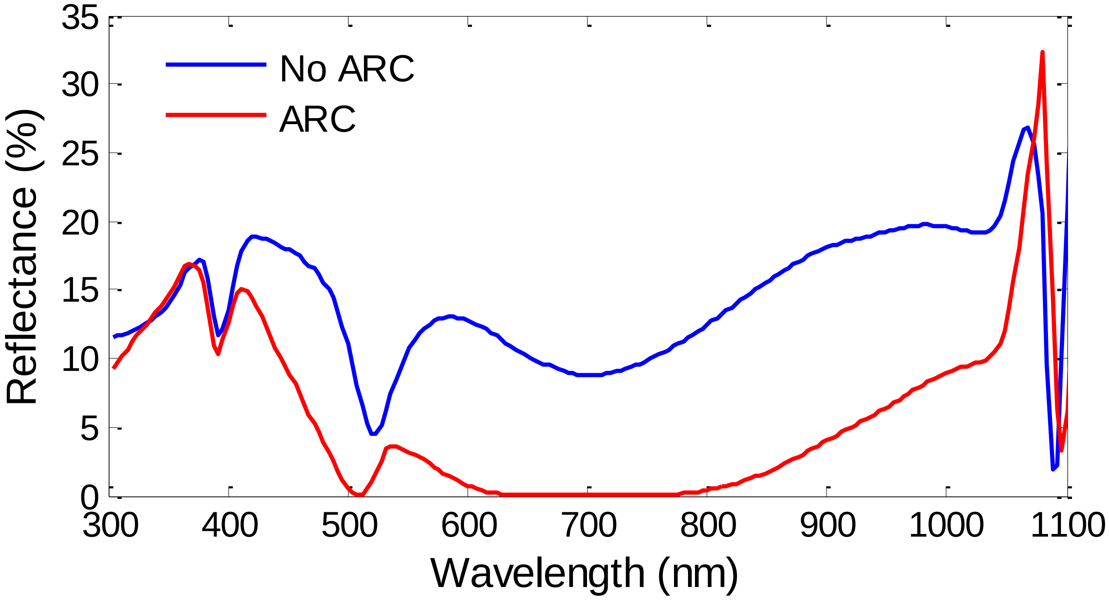

Figure 4.25. ARC layer effect on the reflectance of CIGS solar cell.

Table 4.5. *J*-*V* metrics for CIGS solar cell with and without ARC layer.

	J_{sc} (mA/cm^2)	V_{oc} (mV)	*FF* (%)	η (%)
No ARC	31.89	667	76.8	16.3
ARC	35.68	671	76.9	18.4

Surface recombination: The surface recombination near the CdS/CIGS interface is varied in the model in order to change the short-wavelength spectral response of the solar cell. High surface recombination at an interface is representative of poor deposition techniques which can lead to high levels of defects. This contributes to degradation processes that significantly impact the performance of the solar cell, especially in the UV region. In this model, the SRV at the CdS/CIGS is varied from 10^4 to

10^8 cm/s to model the effects of various levels of interface quality. Figure 4.26 shows the simulated EQE of the CIGS solar cells with different SRV values. Table 4.6 summarizes the *J*-*V* characteristics of the simulated CIGS solar cell.

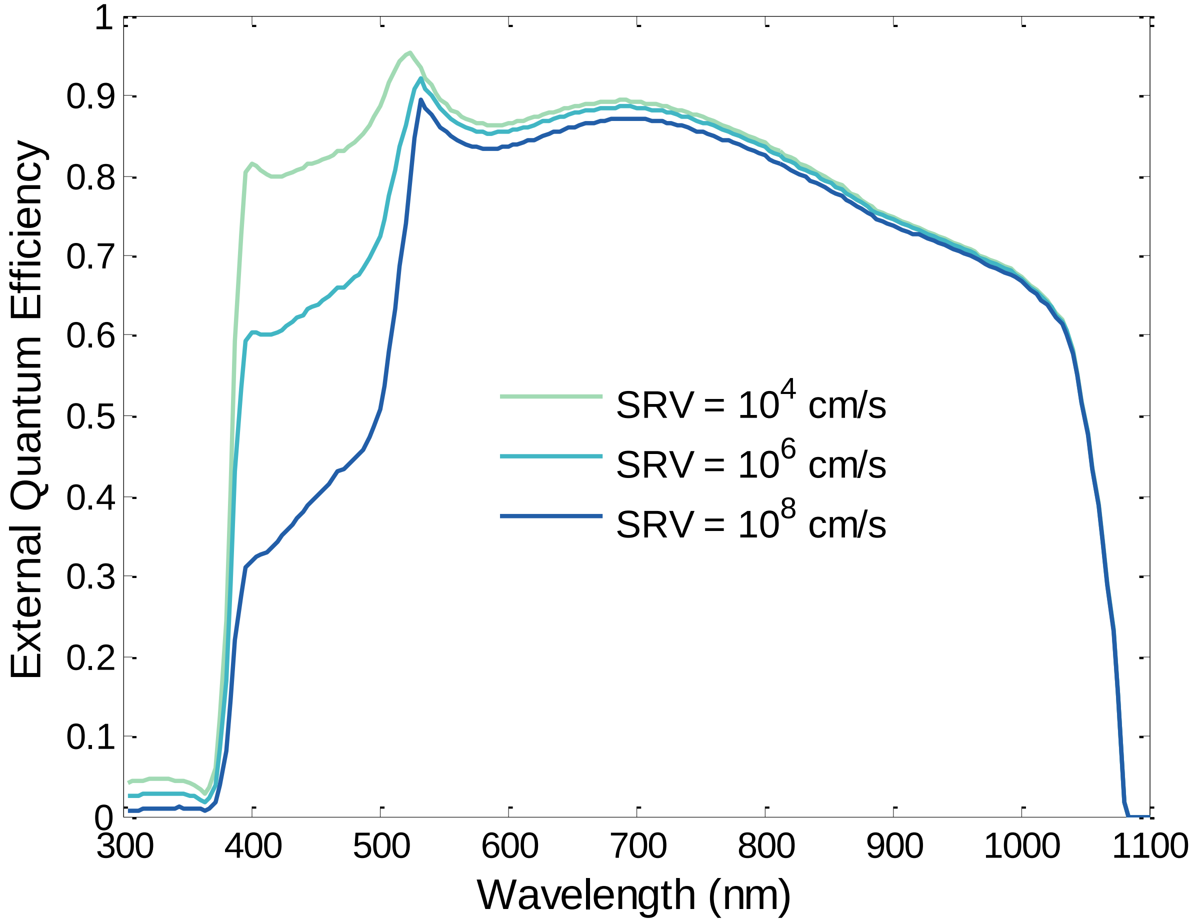

Figure 4.26. External quantum efficiency (EQE) of CIGS solar cells with different surface recombination velocities (SRV).

Table 4.6. Simulated results for the CIGS solar cell with different surface recombination velocities.

SRV (cm/s)	**J_{sc} (mA/cm²)**	**V_{oc} (mv)**	***FF* (%)**	**η(%)**
$1\text{x}10^4$	33.15	677	77.2	17.3
$1\text{x}10^5$	32.98	675	77.2	17.2
$1\text{x}10^6$	31.89	667	76.8	16.3
$1\text{x}10^7$	30.24	660	76.8	15.3
$1\text{x}10^8$	29.96	658	76.8	15.1

Chapter 5: Modelling of DC and DS layers

In this chapter the model for down-conversion and down-shifting layers is presented along with a study of coupling DC/DS layers to different solar cells. First, the basic numerical model is explained with emphasis on the input parameters to the model. Key parameters such as the calculation of the fraction of re-emitted photons directed to the solar cells are discussed in detail, including a comparison using different methods. The basic model is further improved by adding a layer thickness optimization technique. The model is then implemented and the effect of DC and DS layers is examined starting from ideal layers and ideal cells to more realistic parameters. Then the effect of coupling a practical material for DS layer such as Si-nC is examined where measured parameters are input to the model. Two solar cells are included in our study here, a silicon and a CIGS solar cell. Finally the two different effects arising from adding a DS or DC layer are explored with a focus on decoupling the two effects. Therefore, the enhancement due to each effect is reported independently.

5.1. Model

DC and DS layers located on the front surface of a solar cell essentially tailor the incident spectrum to be more efficiently absorbed by the solar cell. In light of this, their effects are modelled by modifying the incident spectrum according to their absorption and emission spectra. Thus the incident spectrum is converted to photon flux $\phi_{inc}(\lambda)$ by dividing by the photon energy, E_{ph}, and it is then reduced by the number of absorbed photons, ϕ_a, in the DC layer to give the transmitted photon flux, ϕ_t, so that:

$$\phi_t(\lambda) = \phi_{inc}(\lambda) - \phi_a(\lambda) \tag{5.1}$$

The absorbed photon flux primarily depends on DC layer properties such as the absorption coefficient and thickness. The integrated photon flux of the emitted photons $\phi_e(\lambda)$ is calculated from the integrated photon flux of the absorbed photons. Since the DC re-emits at a longer-wavelength, the integrated photon flux of the emitted photons will be centred according to the emission peak of the DC layer. Due to the isotropic emission of photons within the DC layer, only a fraction of the emitted photons are directed to the solar cell. This fraction of the re-emitted photons that are directed to the solar cell is denoted as T_{trap}. Another important factor that is used in calculating the number of emitted photons is the PLQY of the DC layer. The emitted photons are then added to the transmitted photon flux to give the modified photon flux:

$$\varphi_{mod}(\lambda) = \varphi_t(\lambda) + PLQY \cdot T_{\text{trap}}(\lambda) \cdot \varphi_e(\lambda) \qquad (5.2)$$

Accordingly, the final equation for the modified photon flux is

$$\varphi_{mod}(\lambda) = \phi_{inc}(\lambda) - \phi_a(\lambda) + PLQY \cdot T_{\text{trap}}(\lambda) \cdot \varphi_e(\lambda) \qquad (5.3)$$

The modified photon flux is then converted to the modified spectrum which serves as input data for the solar cell simulation model. This was an overview of the basic DC model, more details on each input parameter is explained in the following sections.

5.1.1. Incident Spectrum

The incident spectrum is the standard AM1.5G spectrum that is used for standard test conditions. However, other spectra can also be used such as AM0 and AM1.5D. As a DC layer effectively red-shifts the incident spectrum, the more blue an incident spectrum contains, the more gain that can be expected in terms of solar cell efficiency. Therefore, DC applications will be more beneficial for regions with high diffuse irradiation fraction, or with very low air mass such as AM0, due to the Rayleigh scattering being stronger in the blue. In contrast, it is expected that solar cells with DC layers will perform poorly in regions with high direct irradiation fractions, such as around the equator, or in early morning and evening due to the high air mass value.

5.1.2. Absorption Profile

The absorption of a DC layer can be calculated from the absorption coefficient and the thickness of the DC layer through the Beer-Lambert law, as defined in equation (2.1). However, in this work the transfer matrix method is used to calculate absorption in the DC layer in order to consider interference effects resulting from other layers/interfaces.

It is favorable to have a high absorption coefficient in the UV/blue region (<500 nm) where the spectral response of commercials solar cells is usually poor.

5.1.3. Emission Profile

Depending on the DC layer the emission profile can be modeled using different profiles. For the purpose of this work where Si-nC are considered as the DS layer, the emission profile follows a Gaussian distribution and is given as

$$g(\lambda) = ae^{-\frac{(\lambda-\lambda_{\mathrm{peak}})^2}{2\sigma^2}} \tag{5.4}$$

where a is the amplitude, λ_{peak} is the center wavelength of the Gaussian distribution and σ is the standard deviation of the Gaussian function, which is related to the full width half maximum (FWHM) by, FWHM = $2\sqrt{2ln2}\,\sigma$. The integrated PL must be normalized, so for a Gaussian distribution this gives:

$$PL(\lambda) = \frac{g(\lambda)}{\int g(\lambda')d\lambda'} = \frac{e^{-\frac{(\lambda-\lambda_{peak})^2}{2\sigma^2}}}{\sigma\sqrt{2\pi}} \tag{5.5}$$

Since the DC re-emits at longer-wavelength, the integrated photon flux of the emitted photons has a Gaussian distribution profile centred according to the emission peak of the DC layer. It is desirable for DC layers to have an emission peak where the EQE of the solar cell is the highest, which is usually in the range 700 – 900 nm for silicon. In addition, a narrow emission profile is desirable over a wide emission profile.

5.1.4. PLQY

PLQY represents the ratio of re-emitted photons at longer wavelengths to absorbed photons, as defined previously. The higher the PLQY, the higher the expected enhancement to the solar cell. It is not only desirable to have high PLQY, but if PLQY is below a certain threshold then it is likely that degradation in the solar cell is observed. The threshold is dependent on a number of parameters such as, the incident spectrum, IQE of the solar cell, DC absorption and emission profiles, and T_{trap}.

5.1.5. T_{trap}

T_{trap} represents the fraction of the re-emitted photons that are directed to the solar cell. The geometric factor T_{trap} can be as low as 50% depending on the refractive indices of the DC layer, the solar cell and the medium above the DC layer (usually air). The number of photons that is directed to the solar cell can be maximized by making use of total internal reflection as light travels from a medium with high refractive index to a medium with lower refractive index. Total internal reflection occurs when the incident angle is larger than the critical angle, otherwise photons emitted with incident angle smaller than the critical angle will probably be refracted and thus escape the structure from the upper surface of the DC layer. The critical angle is given by:

$$\theta_c = \sin^{-1}\left(\frac{n_{sup}}{n_{DC}}\right) \tag{5.6}$$

where n_{DC} and n_{sup} are the refractive indices of the DC layer and the superstrate (assumed air), respectively. The critical angle increases as n_{DC} increases, as shown in Figure 5.1 for a DC layer with refractive index in the range 1 to 3.6. Integrating over the critical angle cone, the escape cone loss is given by [14]:

$$T_{esc} = \frac{4n_{sup}n_{DC}}{\left(n_{sup} + n_{DC}\right)^2} \cdot \frac{1 - cos\theta_c}{2} \tag{5.7}$$

where the first term accounts for the transmission of photons from the DC layer to air and the second term accounts for the fraction of emitted photons that lies within the solid angle subtended by this escape cone. T_{rap} is the complement of T_{esc}, and is plotted in Figure 5.1 as a function of the DC refractive index. T_{trap} is as low as 50% when $n_{DC} = 1 = n_{sup}$ and increases as n_{DC} increases. For a DC layer with refractive index of 3.6 (same as silicon), only 1.34% of the emitted photons are lost.

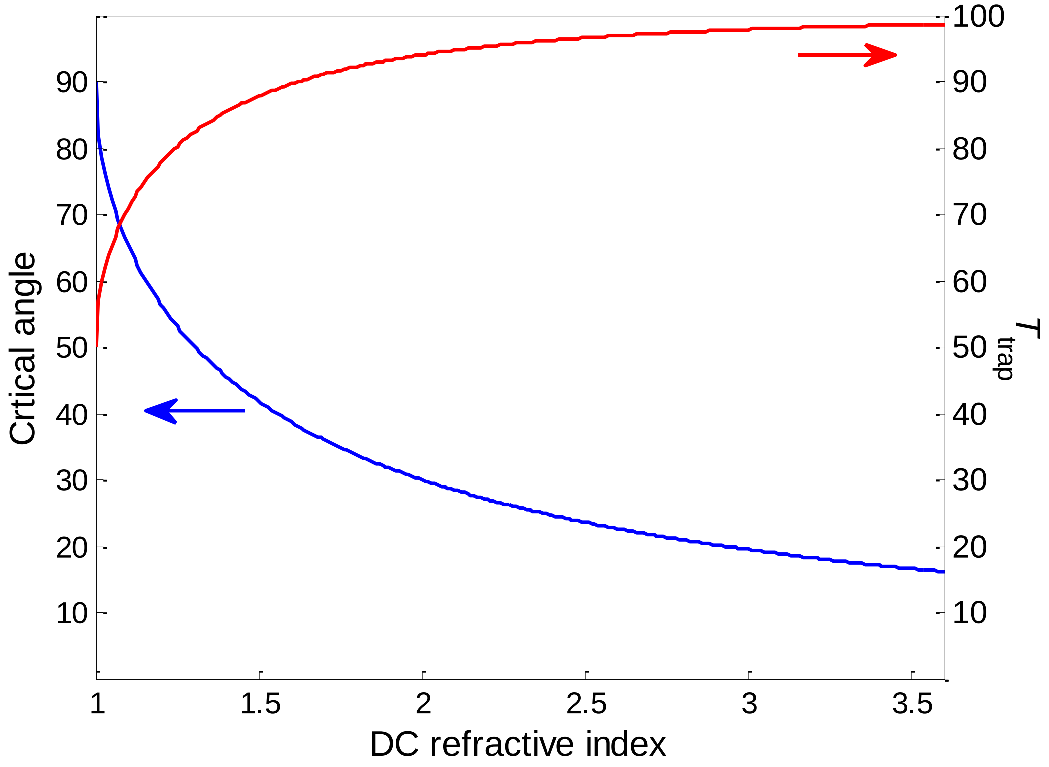

Figure 5.1. Critical angle (blue) and T_{trap} (red) as a function of the DC refractive index and assuming emerging medium is air with n_a = 1.

Figure 5.1 suggests that a DC layer with high refractive index is favorable in order to maximize T_{trap} factor. However a DC layer with high refractive index will increase the front-side reflection of incident photons. In fact, an optimum refractive index of DC layer for minimum front-side reflections is calculated as

$$n_{DC} = \sqrt{n_{sup} \cdot n_{sub}} \tag{5.8}$$

where n_{sup} and n_{sub} are the refractive indices of the superstrate and substrate, respectively. In this case where n_{sup} = 1 (for air) and n_{sub} = 3.6 (silicon), the optimum value for n_{DC} ~1.9. In order to get a feel of the favourable value for n_{DC} that both reduce front reflections and T_{esc}, the front surface reflection is calculated according to equation (4.10) and is plotted in Figure 5.2. Fortunately the optimum n_{DC} lies in the range 1.5 – 2, where most materials used for ARC layer such as Si_3N_4 and SiO_2 or encapsulation materials such as glass and PMMA have refractive index in this range. T_{esc} is in the range of 5 – 12% for n_{DC} range of 1.5 – 2.

Escape cone losses are very good in calculating a first estimate of the T_{trap} factor. However the DC layer thickness is not considered which can be either *thin* or *thick*. If the layer is thin, which is usually the case, then interference effects must be considered to accurately calculate T_{trap}.

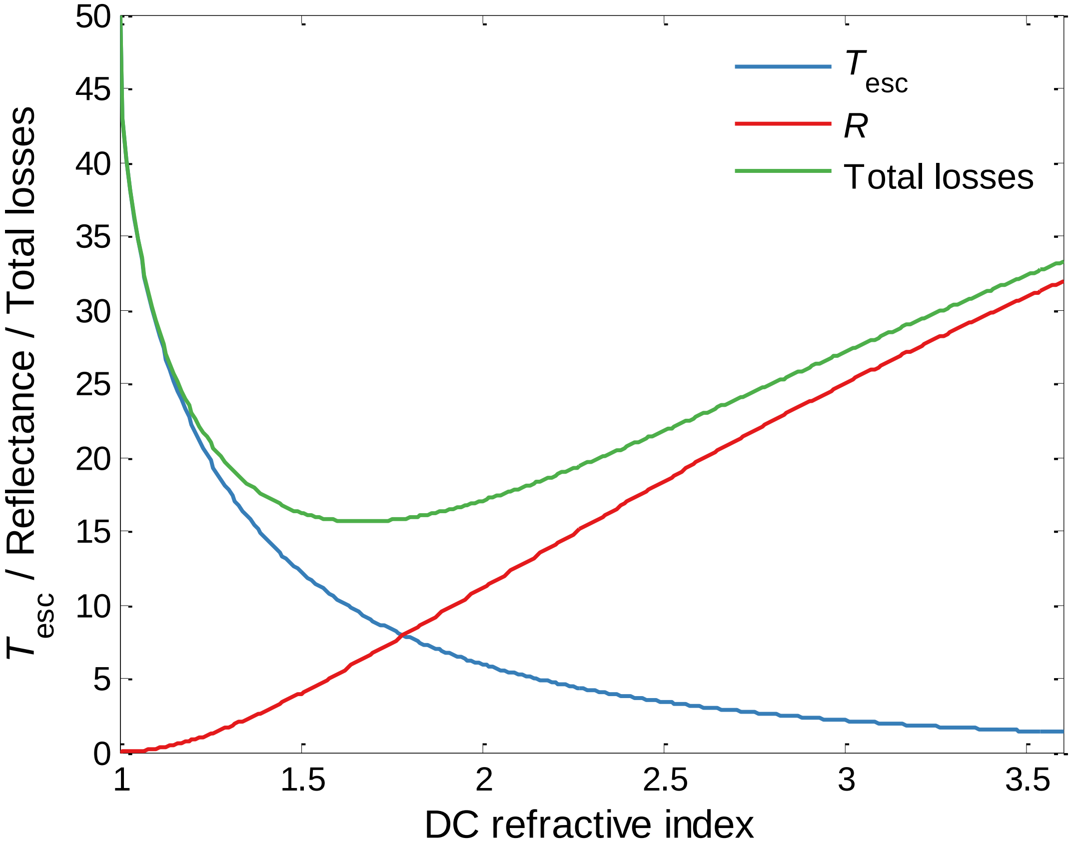

Figure 5.2. T_{esc} (blue) calculated from equation (5.7), front surface reflectance, R, (red) calculated from equation (4.10) and the sum of both gives the total losses (green). The minimum of total losses suggests an optimum n_{DC} in the range 1.5 – 2.

In order to overcome the escape losses limitations, a more sophisticated model has been adopted to calculate T_{trap} for a stack of thin layers acting as DC layer. The interference effects have been calculated using the equivalence of power radiated by a dipole antenna [192]. The theory provides a formula for the calculation of the radiated power of a dipole antenna, depending on the location and the orientation of the antenna, and includes the effect of absorbing media. The radiated power of a dipole antenna is then related to the probability for the emission of a photon by a dipole transition.

The stack of thin-film structure, shown in Figure 5.3, consists of an emitting medium with a thickness d_e and refractive index n_e located between two stacks of thin-film layers. The surrounding layers have thicknesses d_i and refractive indices n_i. The layers' thicknesses are on the order of one wavelength and lateral dimension that are much larger, thus a one dimensional structure is assumed. In addition the emitting layer is assumed a non-absorbing layer with real refractive index, while other layers can be either non-absorbing layers with real refractive index, or absorbing layers with complex refractive index. The stack ends in half-infinite media with indices of refraction n_+ and n_- in the z+ and z- direction, respectively.

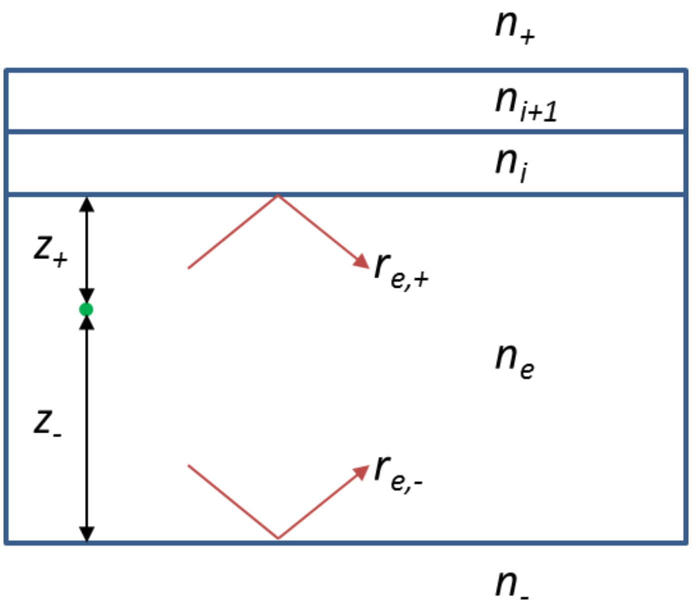

Figure 5.3. The emitting layer with refractive index ne is located within intermediate layers with refractive indices of n_+, n_i, n_{i+1} and n_-. The amplitude reflection coefficients for plane waves emitted from a point source located Z+ from the top of the emitting layer are r_{e+} and r_{e-} for the z+ and z- directions.

The amplitude of the wave vector for a material with refractive index n_i is given by:

$$k_i = \frac{2\pi n_i}{\lambda} \qquad (5.9)$$

Considering the z-axis to be perpendicular to the plane of the structure, the z-component of the wave vector is given by:

$$k_{z,i} = \sqrt{k_i^2 - k_{x,i}^2 - k_{y,i}^2} \qquad (5.10)$$

The wav vector, k_i, is related to the z-component of the wave vector, $k_{z,i}$, by the incident angle , θ_i, as:

$$k_{z,i} = k_i cos\theta_i \tag{5.11}$$

The amplitude reflection and transmission coefficients of a wave in medium n_i on an adjacent medium with index n_{i+1} are

$$r_{i,i\pm1}^{\mathrm{TM}} = \frac{\frac{k_{z,1}}{n_i^2} - \frac{k_{z,i\pm1}}{n_{i\pm1}^2}}{\frac{k_{z,1}}{n_i^2} + \frac{k_{z,i\pm1}}{n_{i\pm1}^2}} \quad and \quad r_{i,i\pm1}^{\mathrm{TE}} = \frac{k_{z,1} - k_{z,i\pm1}}{k_{z,1} + k_{z,i\pm1}} \tag{5.12}$$

$$t_{i,i\pm1} = 1 + r_{i,i\pm1} \tag{5.13}$$

The total Fresnel reflection and transmission coefficients are calculated for all layers in the structure starting from the outer-most layer and iterated using:

$$r_{i,j} = \frac{r_{i,i\pm1} + r_{i\pm1,j}\exp\left(2jk_{z,i+1}d_{i+1}\right)}{1 + r_{i,i\pm1}r_{i\pm1,j}\exp\left(2jk_{z,i+1}d_{i+1}\right)} \tag{5.14}$$

$$t_{i,j} = \frac{t_{i,i\pm1}t_{i\pm1,j}\exp(2jk_{z,i+1}d_{i+1})}{1 + r_{i,i\pm1}r_{i\pm1,j}\exp(2jk_{z,i+1}d_{i+1})} \tag{5.15}$$

which yields the total reflection and transmission coefficients for TE and TM modes in both directions $r_{e,\pm}^{TM,TE}$ and $t_{e,\pm}^{TM,TE}$. The reflection coefficients referenced to the location of the emitting source within the structure is given as:

$$a_{\pm}^{\mathrm{TM,TE}} = r_{e,\pm}^{\mathrm{TM,TE}}\exp\left(2jk_{z,e}z_{\pm}\right) \tag{5.16}$$

The power density per unit dk^2 is calculated depending on the location and orientation of the dipole antenna. The power densities K for a dipole that is oriented perpendicular to the x-y plane are given by:

$$K_{\perp}^{\mathrm{TM}} = \frac{3}{4}Re\left[\frac{\kappa^2(1 - a_{+}^{\mathrm{TM}})(1 + a_{-}^{\mathrm{TM}})}{k_e^3 k_{z,e}(1 - a^{\mathrm{TM}})}\right] \quad \text{and} \quad K_{\perp}^{TE} = 0 \tag{5.17}$$

Similarly, the power densities K for a dipole that is oriented parallel to the x-y plane are given by:

$$K_{\parallel}^{\mathrm{TM}} = \frac{3}{8} Re\left[\frac{k_{z,e}(1-a_{+}^{\mathrm{TM}})(1-a_{-}^{\mathrm{TM}})}{k_e^3 k_{z,e}(1-a^{\mathrm{TM}})}\right] \quad \text{and} \quad K_{\parallel}^{TE} = \frac{3}{8} Re\left[\frac{(1+a_{+}^{\mathrm{TE}})(1+a_{-}^{\mathrm{TE}})}{k_e k_{z,e}(1-a^{\mathrm{TE}})}\right] \quad (5.18)$$

For a randomly oriented dipole antenna, with equal probability for all directions in space, we get:

$$K_{\mathrm{RND}}^{\mathrm{TM}} = \frac{1}{3} K_{\perp}^{TM} + \frac{2}{3} K_{\parallel}^{TM} \quad \text{and} \quad K_{\mathrm{RND}}^{\mathrm{TE}} = \frac{1}{3} K_{\perp}^{\mathrm{TE}} + \frac{2}{3} K_{\parallel}^{\mathrm{TE}} \quad (5.19)$$

Finally the ratio of the emitted power density in the downward direction to the total power density will give the transmittance in the downward direction, T_{trap}. T_{trap} is integrated over all emission angles to remove the angular dependence and the final form retains its wavelength dependence.

5.1.6. Optimization of DC Layer Thickness

DC layers mounted on the top surface of a solar cell affect the photon flux transmitted into the solar cell and therefore mostly influence the J_{sc}. As in the design of ARC layers, the objective is to minimize surface reflections and thus achieve the maximum J_{sc} possible. For a DC or DS layer with a stack of thin films, this can be treated the same as a multi-layer ARC layers. Therefore the optimum refractive of index of m^{th} layer, n_m, of a multilayer ARC consisting of M layers is given by [193]:

$$n_m = n_{sup}^{\left(\frac{M+1-m}{M+1}\right)} \cdot n_{sub}^{\left(\frac{m}{M+1}\right)} \quad (5.20)$$

where for a single layer $M = 1$ and the equation reduces to equation (5.8). This expression suggests what the required refractive index should be to give zero reflections at a specific wavelength, for example, at 650 nm where the spectrum irradiance is the highest. Then, materials with the closest refractive index to the design value are chosen and the layer thicknesses are optimized to maximize J_{sc} using the following equation:

$$J_{sc} = q \int \phi(\lambda) \cdot EQE(\lambda) d\lambda \quad (5.21)$$

where $\phi(\lambda)$ is the incident photon flux, and EQE is the external quantum efficiency of the solar cell. In presence of DC layer, the photon flux reaching the solar cell is modified by the DC layer and as a result the EQE expression has to be modified to take into consideration the DC absorption and emission, where EQE_{tot} is the EQE of a solar cell with a DC layer applied on front surface.

$$EQE_{tot}(\lambda) = EQE_{\text{ARC}} + \Delta EQE_{\text{DC}} \tag{5.22}$$

The first term describes the EQE of the solar cell with a DC layer (or an ARC layer) considering only the change to the front-side reflections. In other words no re-emission from the DC layer. Therefore EQE_{ARC} accounts for the fraction of transmitted photons to the solar cell and is expressed as:

$$EQE_{\text{ARC}}(\lambda) = \Big(1 - R_{\text{tot}}(\lambda) - A_{\text{p}}(\lambda)\Big) \cdot IQE_{\text{ref}}(\lambda) \tag{5.23}$$

where $R_{\text{tot}}(\lambda)$ is the total reflectance of the device with the DC layer on the top surface, $A_{\text{p}}(\lambda)$ is the parasitic absorption which includes the absorption in the DC layer and is calculated by TMM, and IQE_{ref} is the IQE of the reference cell and is calculated according to equation (2.40). This equation applies to any ARC layer since the DC effects are not considered. The second term in equation (5.23) describes the portion of re-emitted photons by the DC layer that is directed to the solar cell and is given by:

$$\Delta EQE_{DC}(\lambda) = \text{PLQY} \cdot A_{\text{DC}}(\lambda) \cdot \int PL(\lambda') \cdot T_{trap}(\lambda') \cdot IQE_{\text{ref}}(\lambda') d\lambda' \tag{5.24}$$

where A_{DC} is the absorption in the DC layer, PL is the emission profile of the DC layer, T_{trap} is the fraction of re-emitted photons that are directed to the solar cell, as was discussed in section 5.1.5, and IQE_{ref} is the IQE of the reference cell.

Thus the DC layer thickness can be optimized by substituting equations (5.22)-(5.24) into equation (5.21) in order to find the optimum thickness that will maximize J_{sc}. Figure 5.4 summarizes the steps in modelling a DC layer with layer thickness optimization.

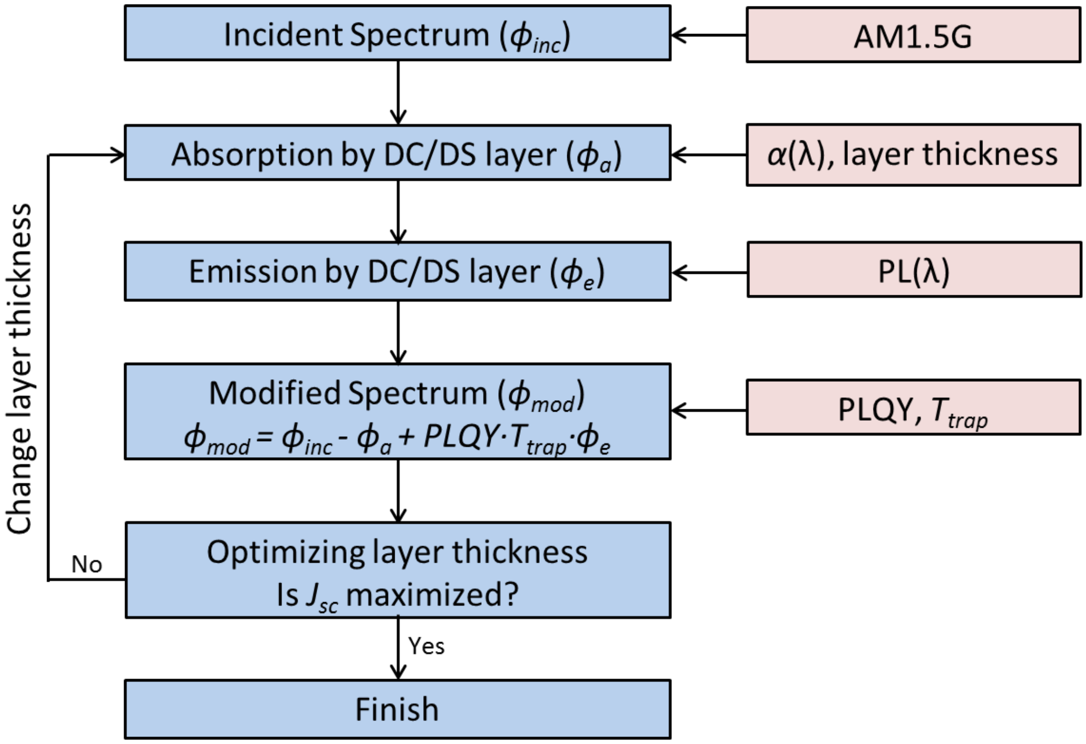

Figure 5.4. A flowchart of the simulation procedure with layer optimization.

5.2. Simulation Results

After developing the model for either DC or DS layers, now it is time to present the implementation using the numerical model. In this section, four cases are being explored, namely, ideal DC and solar cells, ideal DC layers, Si-nC as DS layer with both silicon and CIGS solar cells. The input parameters to the model will be explained in each case with simulation results presented and discussed.

5.2.1. Ideal Case

Here the upper limit for the DC layer will be explored. DC layers are assumed to be ideal optical layers in that they absorb all incident photons with energy greater than the DC layer bandgap (E_g). The energy of re-emitted photons is centred at an intermediate level assumed to be exactly at half the DC bandgap ($E_g/2$). The emission profile will be assumed as a single wavelength (equivalent to half the DC bandgap) or a Gaussian profile with FWHM of 100 nm, which represents a more particle profile, as shown in Figure 5.5. The PLQY is assumed 200%.

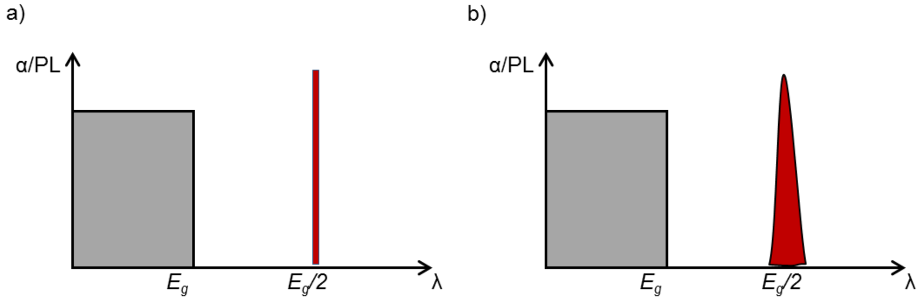

Figure 5.5. Absorption (grey area) and emission (red area) spectra for ideal DC layer. The bandgap of the DC is E_g and the emission is at $E_g/2$. Emission is assumed a) line or b) Gaussian distribution.

To explore the upper limit for the DC layer, the minimum total losses are assumed According to Figure 5.2 the minimum total losses of 15.6% occur for a DC layer with refractive index of 1.6. In this case the T_{trap} is 90% as obtained from equation (5.5). It is important to know that the reflectance calculated here is relative to the superstrate and does not take into consideration the DC layer thickness, the substrate refractive index or the incident wavelength.

The modified spectrum is calculated from equation (5.3) and is shown in Figure 5.6 for a DC with bandgap 3 eV.

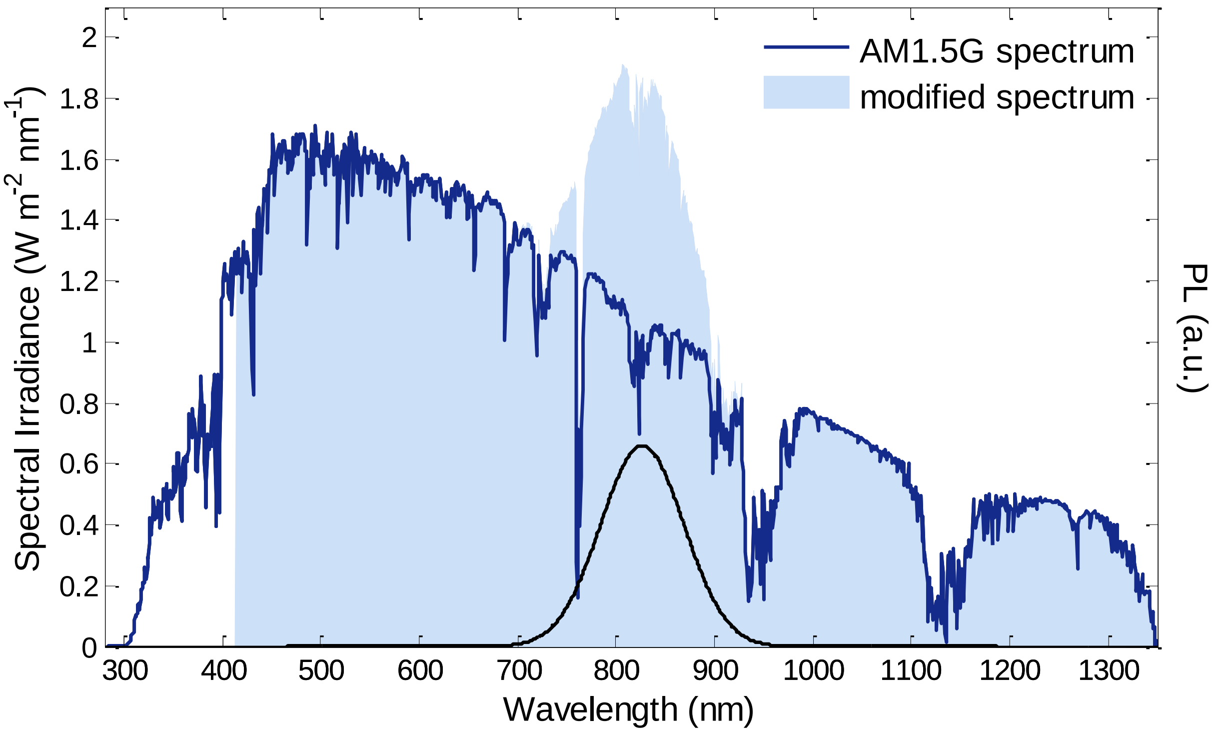

Figure 5.6. Modified spectrum (light blue fill) effected by a DC layer with a bandgap of 3.0 eV (413 nm) and PLQY = 200%. The AM1.5G spectrum is also presented (dark blue line) to highlight the changes to the modified spectrum. The emission profile (black line) of the DC layer is modeled as a Gaussian function centered at 1.5 eV (826 nm) with FWHM = 100 nm.

An ideal solar cell is assumed with EQE of 1, i.e. no reflectivity, and a bandgap of 1.1 eV (λ=1127 nm). The calculated short-circuit current density of the solar cell is 45.9 mA/cm^2 for incident spectrum AM1.5G using equation (5.21). This represents the upper limit for silicon solar cells without a DC. The J_{sc} for the solar cell and DC layer is also calculated but with the modified spectrum instead of the standard AM1.5G spectrum. The results are plotted in Figure 5.7 for the reference solar cell and when DC layer is coupled assuming either a Gaussian or line emission. When adding the DC layer, a maximum J_{sc} of 57 mA/cm^2 is achieved and as expected it is for a DC layer with bandgap 2.2 eV where the emission is at 1.1 eV, same as the bandgap edge of the ideal silicon solar cell. As the bandgap of the DC layer increases, the enhancement J_{sc} decreases due to the fact that there are less photons to be down-converted. However J_{sc} never goes below the J_{sc} of the reference ideal solar cell. On the other hand, when the DC bandgap is below 2 eV, all the photons absorbed are wasted since they are emitted at

1 eV, which is below the bandgap of the solar cell. Therefore a degradation in the solar cell performance is observed and the J_{sc} decreases to ~30 mA/cm^2 in this case. In the case that a Gaussian distribution is assumed for DC emission, it is noted that the maximum J_{sc} for a DC bandgap of 2.2 eV is lower than the case of line emission, since in case of a Gaussian emission not all of remitted photons will be absorbed by the solar cell due to the fact the Gaussian function is centered at 1.1 eV. This is an important observation since in real systems a Gaussian-like emission is expected and therefore the bandgap of the DC has to be higher than twice the bandgap of the solar cell. Finally, a maximum relative enhancement of 24% is calculated for a DC bandgap of 2.2 eV, which is very close to the detailed-balance calculations that show a 25% relative increase in system efficiency [11].

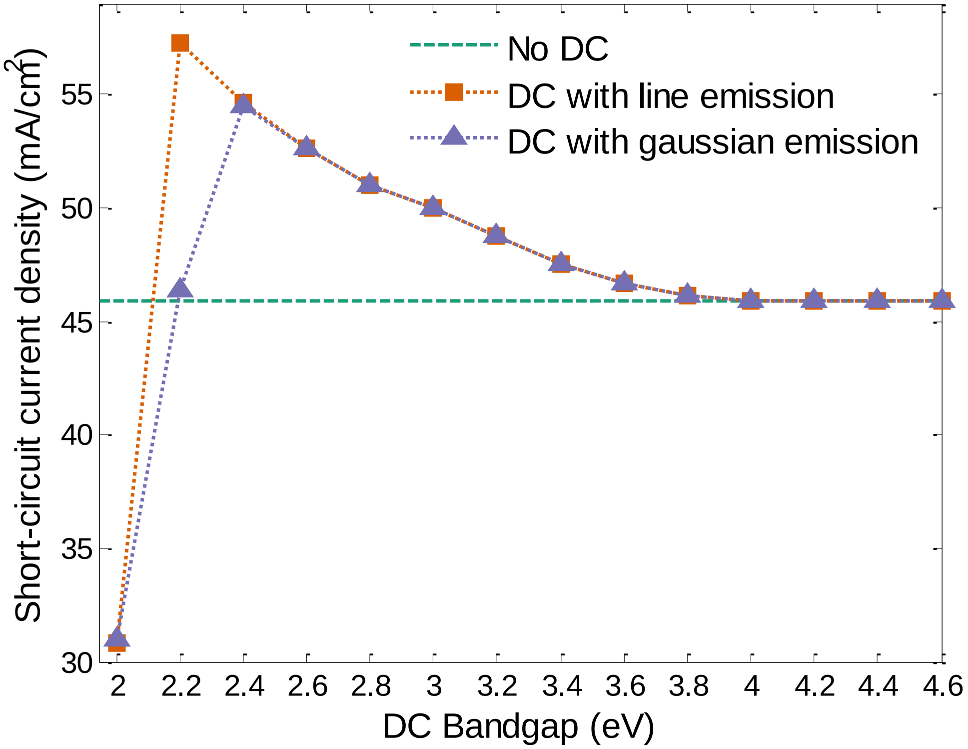

Figure 5.7. Short-circuit current density for ideal DC as a function of DC bandgap with emission profiles as a line (blue) and Gaussian (red). The J_{sc} for ideal silicon solar cell with AM1.5G incident spectrum is shown as well (green). The dotted lines are guide to the eye.

5.2.2. **Ideal DC and DS Layers**

In this section, an ideal DC layer is still assumed. However, the solar cell model considers realistic loss mechanisms such as radiative and non-radiative recombination. This approach is particularly useful when studying how changes in a cell's spectral response affect the overall improvement gained by adding DC due to effects such as surface recombination. In addition the study is expanded to model ideal DS layers as well.

DC and DS layers are assumed to be ideal optical layers in that they absorb all incident photons with energy greater than the DC or DS layer bandgap (E_g). For the DC, the energy of re-emitted photons is centred at an intermediate level assumed to be exactly at half the DC bandgap ($E_g/2$), as in the previous section. On the other hand, for the DS layer we assume photons are re-emitted at the DS bandgap (E_g). Although it has been shown that DS materials can have emission profiles that are red-shifted from the absorption edge, or bandgap energy, we assume emission is at the bandgap since we are modeling an ideal absorption profile.

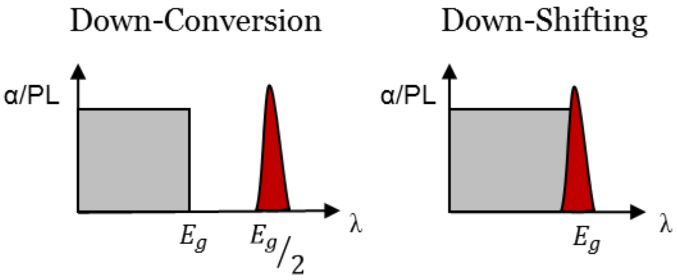

Figure 5.8. Absorption (α) and emission (PL) spectra for ideal DC and DS layers. The bandgap of the DC and DS are E_g and the emission is at $E_g/2$ and E_g for DC and Ds layers, respectively.

In both the DC and DS cases, the photons are re-emitted according to a Gaussian energy distribution, as shown in Figure 5.8 (red). The PLQY is varied from 0 to 200% for DC layers and from 0 to 100% for DS layers. The modified spectrum is calculated from equation (5.3) and is shown in Figure 5.9 for a DC layer with a bandgap of 3.1 eV and 150% efficiency, along with the standard AM1.5G spectrum and the EQE of the reference solar cell.

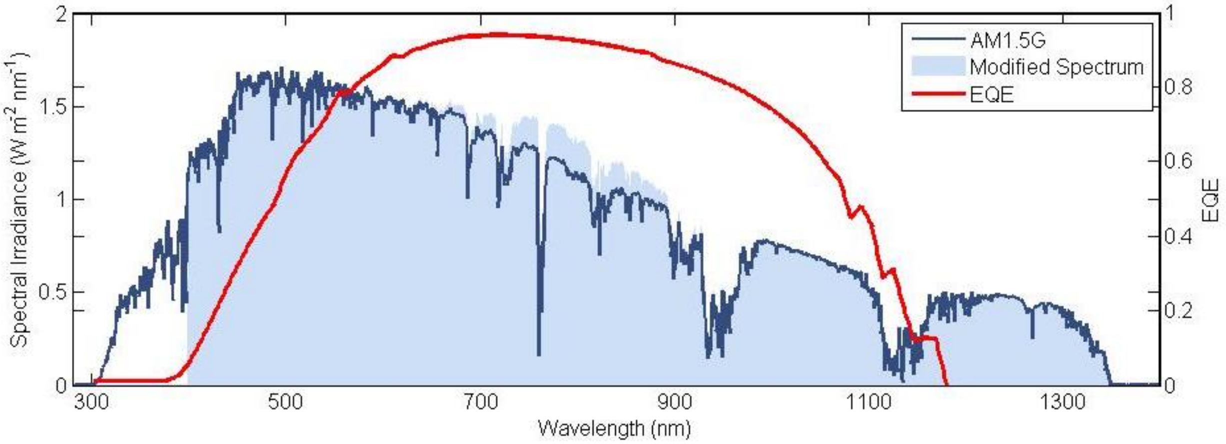

Figure 5.9. Modified spectrum (light blue fill) effected by a DC layer with a bandgap of 3.1 eV and PLQY = 150%. The AM1.5G spectrum is also presented (dark blue line) to highlight the changes to the modified spectrum. The external quantum efficiency of the silicon solar cell simulated in TCAD Sentaurus is shown in red line.

The effect of varying the DC or DS PLQY on the overall performance of the silicon solar cell as a function of the DC or DS layer bandgap is studied. For each case, simulated device efficiencies are compared to simulations of a control structure in order to identify the minimum PLQY required to observe an improvement in the overall photovoltaic efficiency. The control simulations consist of the same silicon solar cell model illuminated by the AM1.5G spectrum normalized to 1000 W/m^2.

For the DC model, it can be seen in Figure 5.10 (a) that a minimal DC efficiency threshold of 1% occurs for a DC bandgap of ≥ 3.4 eV (≤ 365 nm). Such a low threshold is explained by the negligible EQE of the solar cell (shown in blue in Figure 5.10 (a)) at ≤ 365 nm. As a result, any absorbed photons in this region will contribute to the current density of the solar cell and thus enhance the efficiency. As the DC bandgap decreases < 3.4 eV, the DC absorption profile encroaches further into increasingly efficient regions of the solar cell's spectral response. Thus, the DC efficiency must increase in order to compensate for this and provide an overall net benefit to the photovoltaic efficiency. It is important to note that the reported thresholds are highly dependent on the spectral response of the solar cell.

The simulations also reveal that for a perfectly efficient DC layer (PLQY = 200%), in conjunction with the solar cell spectral response studied herein, the most effective DC bandgap is 2.6 eV, as shown in Figure 5.10 (c). In contrast, the detailed balance limit predicts the most effective DC bandgap is 2.2 eV for an ideal Si solar cell [11]. The difference is that in this study a Gaussian profile is assumed for emission. The solar cell efficiency increases as the bandgap decreases since there are more photons being absorbed up to the optimum bandgap. Decreasing the bandgap beyond the optimum point shifts photons to lower regions of the EQE and thus the performance deteriorates. As shown in Figure 5.10 (c), the photovoltaic efficiency increases from 14.2% to 16.6%; this corresponds to a relative increase in efficiency of 17%.

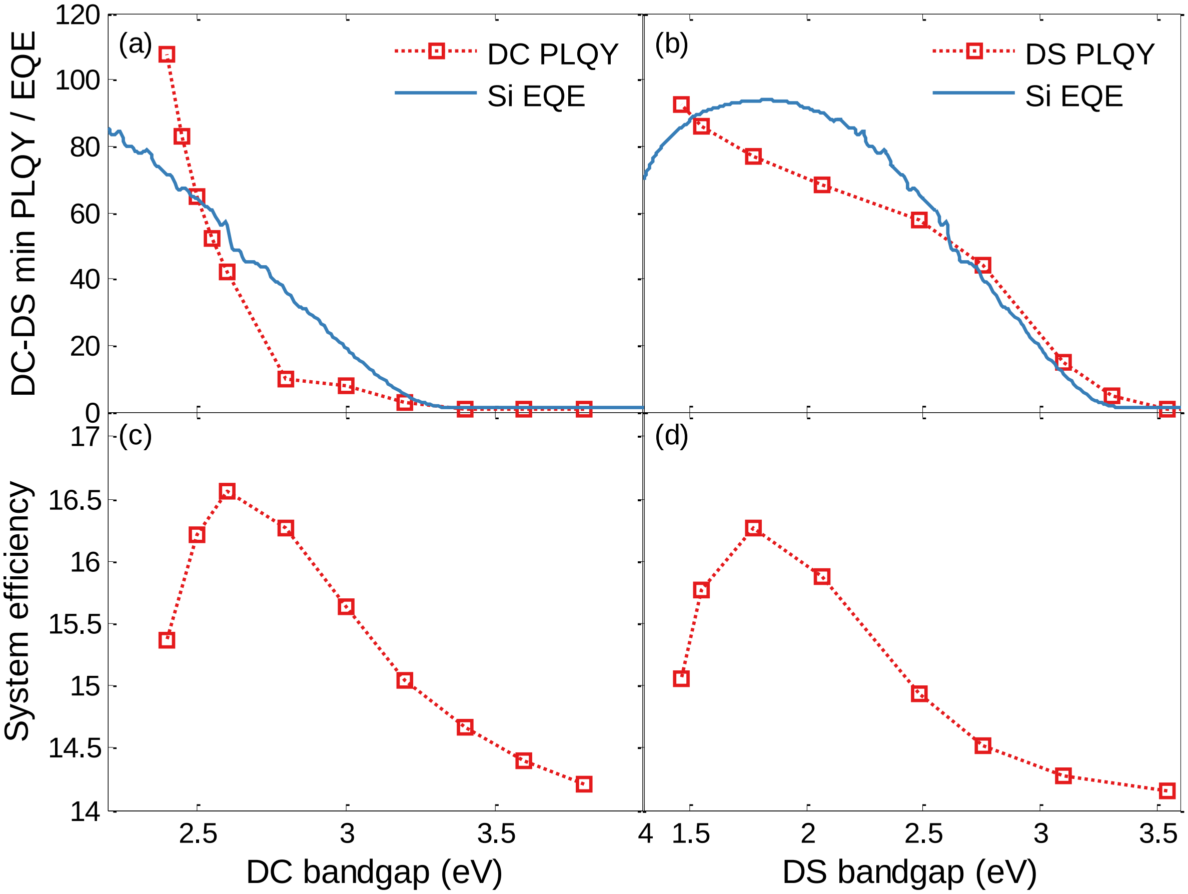

Figure 5.10. Simulation results for ideal DC and DS layers when coupled to a silicon solar cell. Minimum PLQY required for a top-mounted, DC layer (a) and DS layer (b) as a function of the DC and DS bandgap, respectively. Solar cell efficiency when coupled with (c) a 200% efficient DC layer, as a function of DC bandgap, and d) a 100% efficient DS layer, as a function of the DS bandgap.

For the DS model, the minimum DS efficiency required to effect an enhancement in the photovoltaic efficiency is the same as for the DC case (1%) since the EQE of the solar cell below 365 nm is negligible. However, as the bandgap of the DS decreases, the absorption of the DS layer begins to overlap the region of increasing EQE which therefore increases the minimum required DS layer efficiency, similarly to the DC case. Comparing the DC case to the DS case (Figure 5.10 (a) vs. Figure 5.10 (b)), the minimum DS efficiency follows the EQE of the solar cell since photons are emitted at those energies, whereas the minimum DC efficiency increases sharply as the bandgap decreases since the emitted photons are emitted at half the bandgap energy, which falls in a region of low EQE.

For a perfectly efficient DS layer (PLQY = 100%), the maximum achievable photovoltaic efficiency is 16.3% at a DS bandgap of 1.8 eV, showing a 15% relative increase in efficiency above the base value of 14.2%. This maximum efficiency is very close to the optimal DC case, as there are many more photons being absorbed by a DS with bandgap of 1.8 eV than by a DC with bandgap of 2.6 eV. In addition, the optimum bandgap for an ideal DS layer coincides with the maximum point of the EQE, since the re-emitted photons are centred at the DS layer bandgap, as can be seen in Figure 5.10 (d).

5.2.3. **Si-nC as DS Layer**

In this section the performance effects of Si-nC embedded in a silicon dioxide matrix to act as a DS layer mounted on the top surface of crystalline silicon and polycrystalline CIGS solar cells are explored numerically. The choice of solar cells was based on that silicon is the dominant technology in the market and thus it is a natural choice. On the other hand, CIGS solar cells suffer from losses in the ZnO and CdS layers (<550 nm) as mentioned in chapter 4. In addition DC and DS layers are beneficial for small bandgaps solar cells and both solar cells have relatively small bandgap (1.1 eV) as compared with GaAs, CdTe and a-Si solar cells.

Si-nC embedded in SiO_2 matrix is an attractive candidate for a DS layer, as explained in chapter 3. Si-nC exhibit a wide absorption profile below 500 nm and strong emission profile with a peak centered at 800 nm ± 100 nm. For this study, experimental samples of Si-nC were fabricated by plasma-enhanced chemical vapour deposition (PECVD) at McMaster University [194]. Their optical properties were measured using variable-angle ellipsometric spectroscopy from 300 nm to 1700 nm. The measured absorption and PL spectra are shown in Figure 5.11, which were used as the optical properties of the Si-nC DS layer within the numerical model. More information on the growth and characterization of the Si-nC can be found in Appendix A.

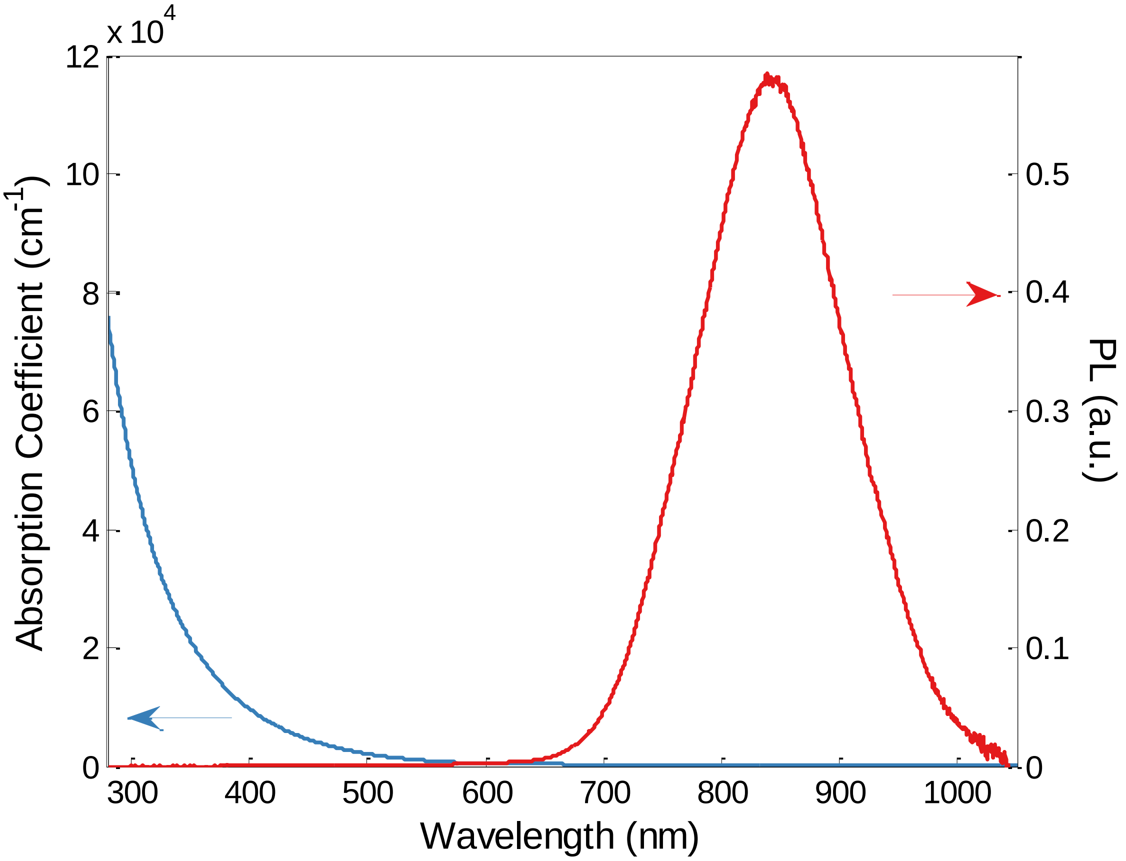

Figure 5.11. Measured absorption profile (blue line) and photoluminescence emission spectrum (red line) from a sample fabricated at McMaster University. The PL is centered at 840 nm with full wave half maximum (FWHM) of 150 nm.

5.2.3.1. **Si-nC Coupled to Silicon Solar Cells**

Si-nC as a DS layer can reduce the surface recombination losses by shifting high-energy photons to lower-energy photons where they are absorbed more efficiently by the solar cell, ie. higher IQE. The model developed in chapter 4 is used in this simulation with varying SRV. The simulated IQE of the solar cells under study in this section are shown in Figure 5.12 with varying the SRV from 10^3 to 10^7 cm/s to model the quality of the front surface. The efficiency parameters are summarized in Table 5.1 for four different solar cells (A-C).

Table 5.1. Simulated results for the silicon solar cell with different surface recombination velocities.

Cell	SRV (cm/s)	J_{sc} (mA/cm^2)	V_{oc} (mv)	*FF* (%)	η (%)
A	1×10^3	33.26	633.3	77.5	16.3
B	1×10^5	32.97	630.9	77.4	16.1
C	1×10^7	31.96	623.5	77.4	15.4

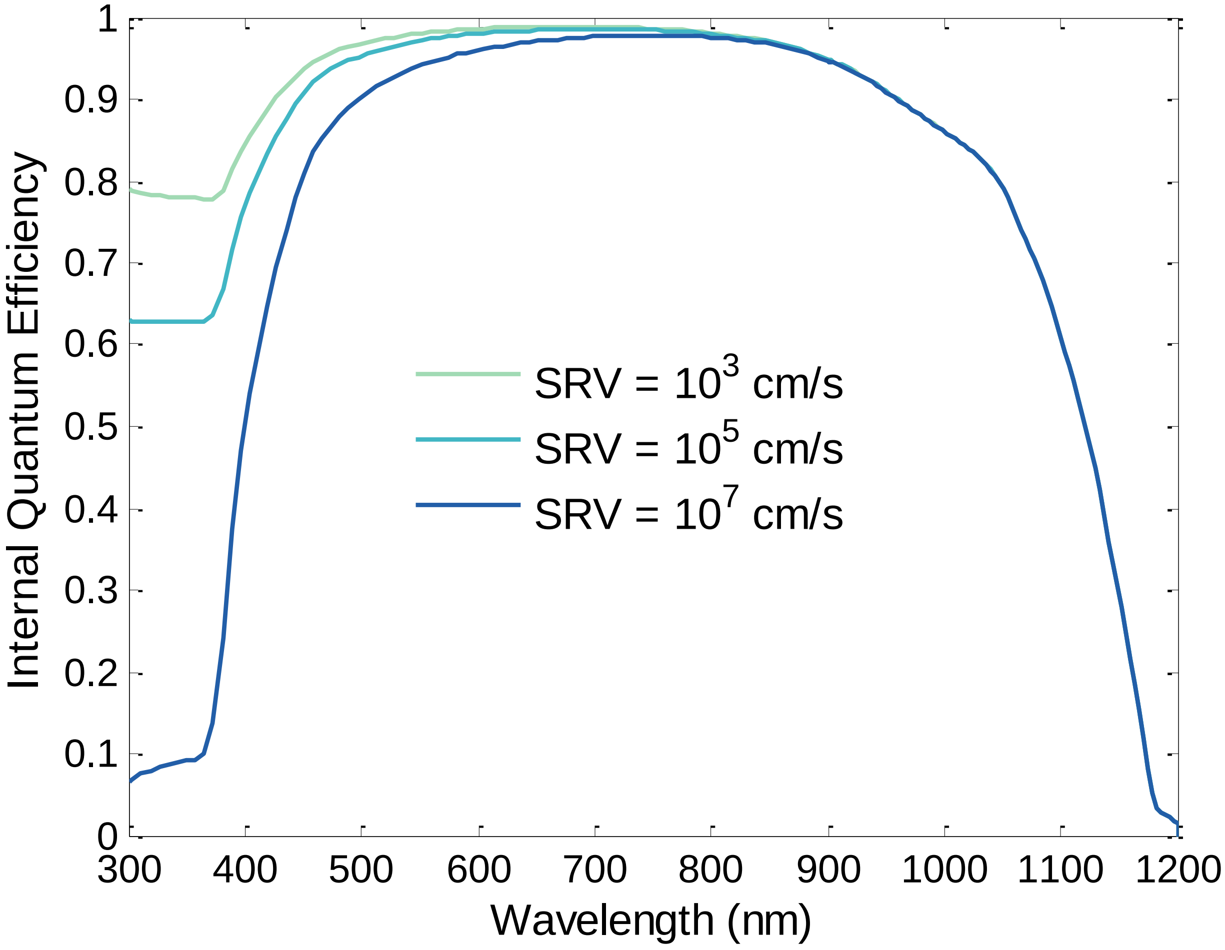

Figure 5.12. Internal quantum efficiency of silicon solar cells with different surface recombination velocities (SRV).

The optimization of the Si-nC and SiO_2 layers was carried out by finding the layer thicknesses that maximize the short-circuit current density of the solar cell using equations (5.23) to (5.25). The thickness range investigated was 0 – 300 nm and 0 – 1000 nm for SiO_2 and Si-nC layers, respectively. Figure 5.13 shows the short circuit current density of cell A as a function of the Si-nC thickness calculated using a PLQY = 20%. The color lines refer to different thickness values of the SiO_2 layer.

The dependence of J_{sc} on the DS double layer thickness is dependent on the double layer transmittance, the emission of the Si-nC, and the IQE of the solar cell. For a given SiO_2 thickness, a different Si-nC thickness maximizes the J_{sc}. In fact, the oscillatory behaviour of J_{sc} is a result of interference effects, which depends both on the refractive index and thickness of each layer. Different thickness combinations produce different phases between the wave reflected from the double layer stack top surface and the wave reflected from the Si-nC/Si interface. This thickness dependent effect explains the different thicknesses at which the short-circuit current has a maximum in Figure 5.13.

In addition, Figure 5.13 shows that the J_{sc} increases as the Si-nC layer thickness increases until a maximum is reached. Moreover a cell coated with a SiO_2/Si-nC double layer stack shows a better performance than a cell coated with a single Si-nC layer, since the maximum J_{sc} obtained with a single Si-nC layer (yellow line) is lower than the one obtained with the double layer stack (SiO_2 thicknesses of 30, 50 and 70 nm).

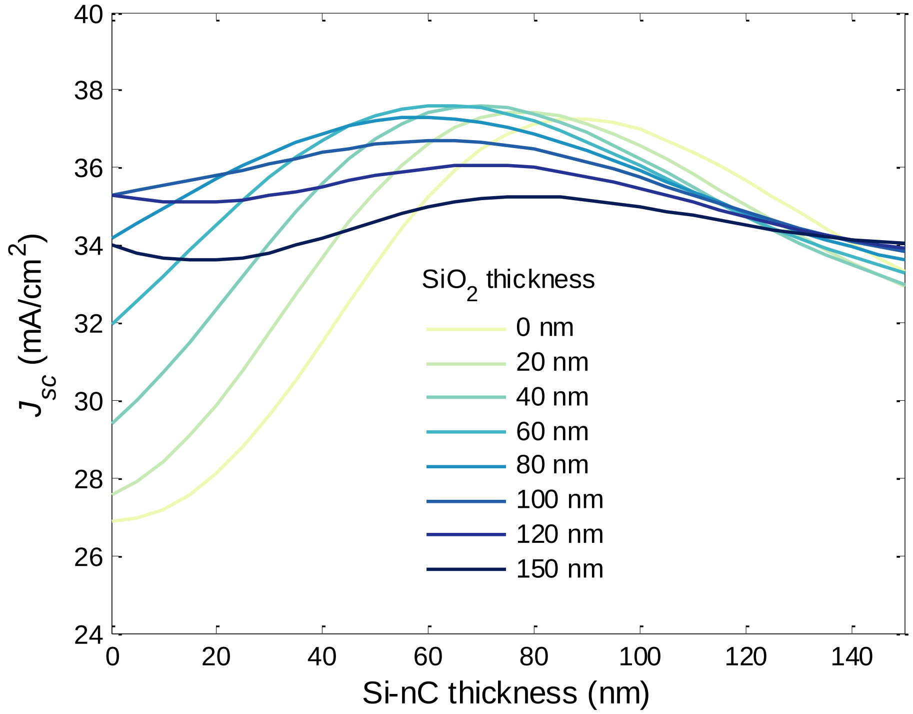

Figure 5.13. Short-circuit current density, J_{sc}, as a function of Si-nC and SiO_2 layer thicknesses for silicon cell with SRV = 10^3 cm/s based on PLQY of 20%.

The optimum stack parameters for cells A and C are shown in Figure 5.14 as a function of PLQY. Note that the Si-nC layer thickness increases and SiO_2 layer thickness decreases. The increase in Si-nC is mainly due to the fact that as PLQY is higher there is chance that the absorbed photons within the DS layer will be better utilized by the solar cell. The decrease in SiO_2 layer thickness is to achieve an optimum ARC performance as the Si-nC layer increases. This applies for all three cells but it is also noted that Si-nC layer must be thicker for lower quality cells. It is interesting to find that the layer thickness differ only by few nanometers. This means that the double layer stack is not very sensitive to PLQY and SRV for this specific solar cell design. It is therefore expected that the double layer stack acts mainly as ARC layer with very small DS effects.

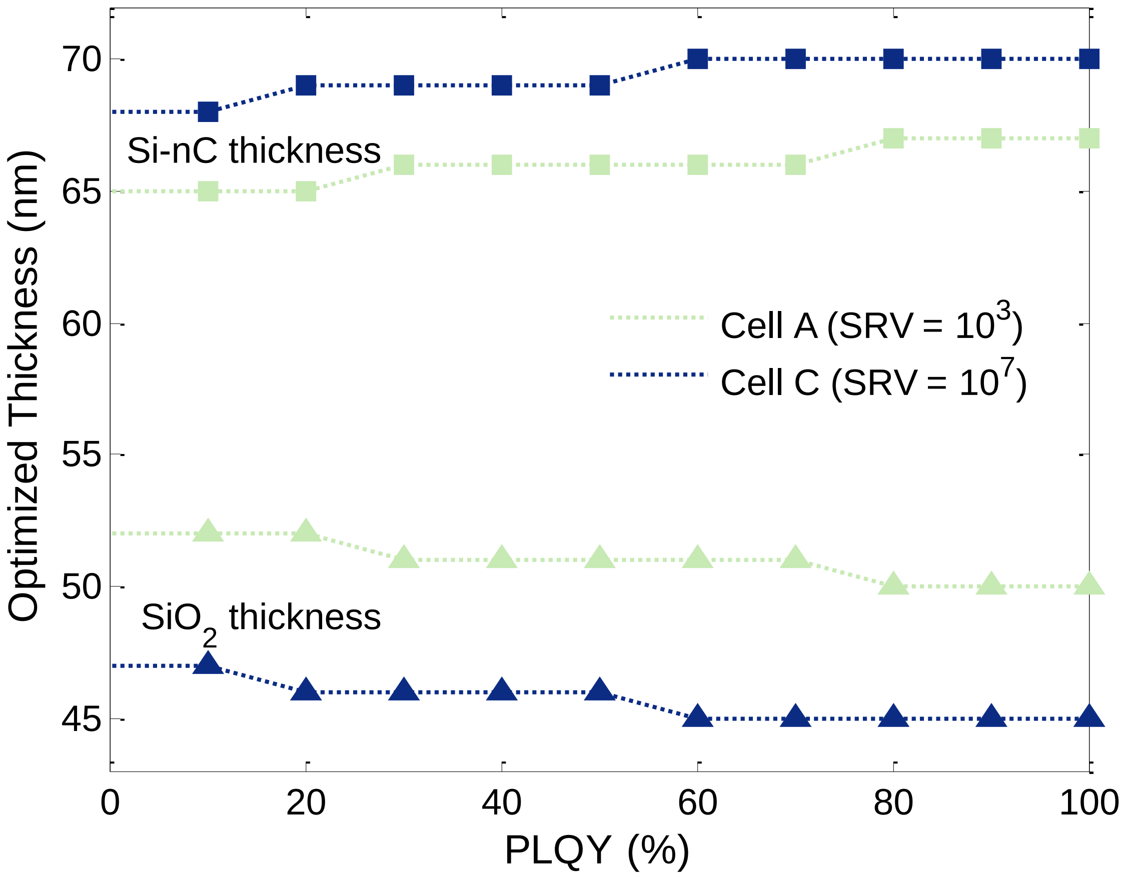

Figure 5.14. Optimized layer thicknesses for Si-nC (squares) and SiO₂ (triangles) layers that maximize J_{sc} of cell A (blue) and C (green) as a function of PLQY. Dotted lines are guide to the eye.

To investigate the efficiency enhancement to the solar cells due to the DS layer, the cells are compared with a reference cell coated with a 110 nm thick of SiO₂ acting as ARC layer. In addition, the cells with the DS layer where PLQY = 0 can be used to single out the DS effect from the Si-nC emission from the combined ARC action of the double stack structure.

Figure 5.15 shows the EQE of the reference cell with only a SiO₂ layer and the solar cell with a double layer Si-nC/SiO₂ with PLQY =0 and 20%. Overall, there is an enhancement in the EQE when compared to the reference cell due to both ARC and DS effects. The ARC effect is evident when comparing the reference cell with the solar cell with DS where PLQY = 0 (red and green curves). There is almost an increase in EQE in all wavelengths. Integrating both EQEs and taking the difference will give us the enhancement in J_{sc} due to ARC effect. Now to examine the DS effect, we compare the two cells with DS where PLQY = 0 and 20% (green and blue). The EQE match very well except in the short-wavelength region, as expected, due to the DS enhancement. Integrating both EQE and taking the difference will give us the enhancement in J_{sc} due to DS effect.

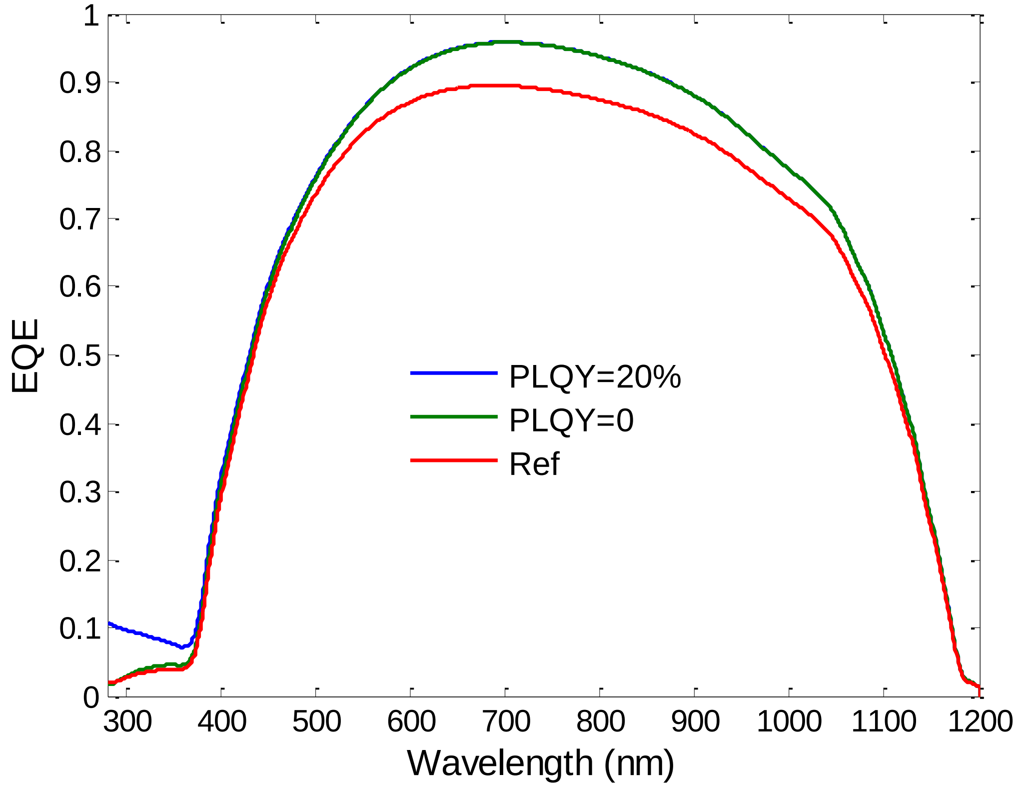

Figure 5.15. EQE of the reference cell (red line), solar cells with DS, PLQY = 0% (green line) and PLQY = 20% (blue line). All cells have SRV = 10^7 cm/s.

The J_{sc} as a function of SRV is shown in Figure 5.16 for the reference cell, PLQY = 0, 50% and 100%. The total J_{sc} enhancement for SRV = 10^5 cm/s is 2.88 mA/cm^2, 2.68 mA/cm^2, and 2.48 mA/cm^2, for DS layers with PLQY = 100%, 50% and 0%, respectively. ARC effect is the dominant effect with an increase in J_{sc} of 2.4 mA/cm^2. While only 0.4 mA/cm^2 and 0.2 mA/cm^2 due to DS effect for DS layer with PLQY = 100% and 50%, respectively. This corresponds to 6.8% and 1.14% relative increase in J_{sc} due to ARC and DS effects, respectively, for DS with PLQY = 100%. It is feasible to decouple the two effects in simulation as the PLQY can be set to zero.

However experimentally this it is not possible to set the PLQY to zero and therefore another method of decoupling must be derived, as will be discussed in the next chapter. It is worth mentioning that failing to decouple the two effects might lead to wrong conclusions on the DS efficiency to enhance a solar cell, especially when the reference cell chosen has high surface reflections, for example a bare cell. In this case the main enhancement will be due to ARC effect with little or even negative DS effect.

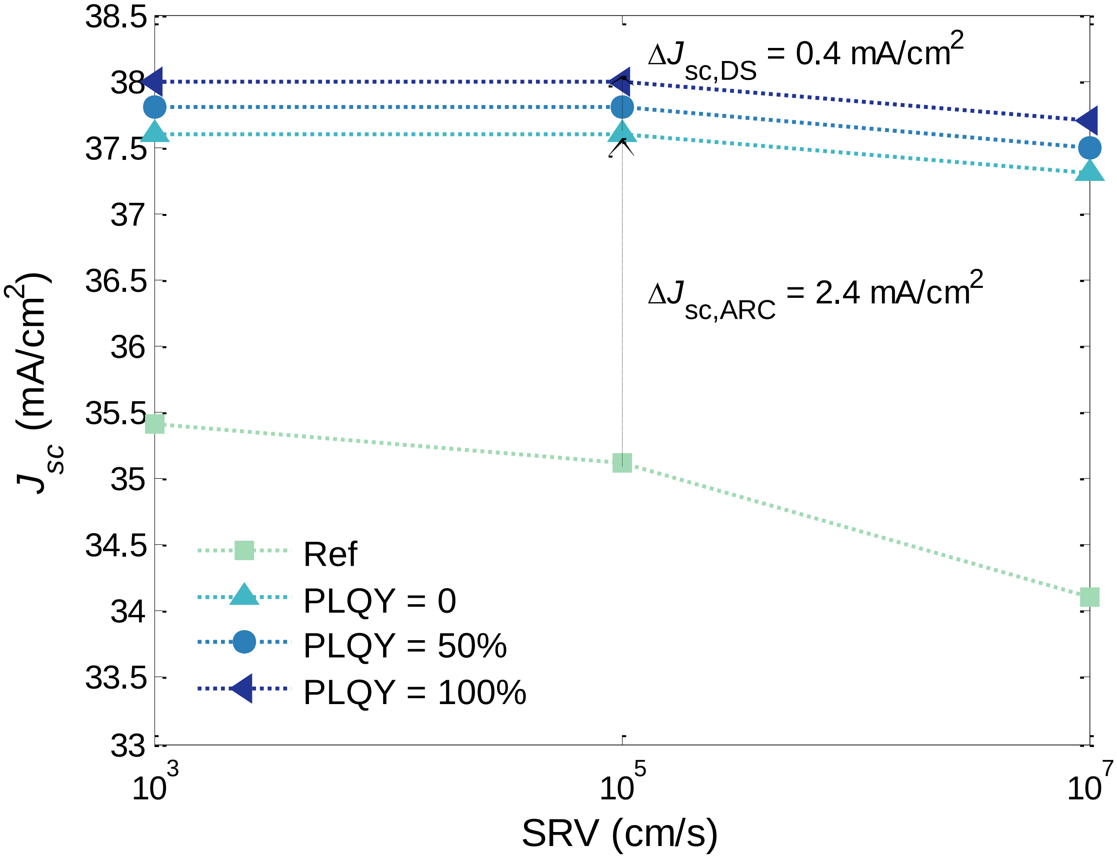

Figure 5.16. Short-circuit current density as a function of surface recombination velocity for reference, DS with PLQY=0, 50% and 100%.

Finally J_{sc} contributions due to ARC effect and DS effect as a function of PLQY for solar cell D is shown in Figure 5.17. $J_{sc,ref}$ is the short-circuit density when integrating the EQE of the reference cell. $\Delta J_{sc,ARC}$ is the short circuit density due to the ARC effects and is almost constant as a function of PLQY. There are very small changes but this is due to the change in layer thickness, as was shown in Figure 5.13. $\Delta J_{sc,DS}$ is the short-circuit density due to the DS effects and it increases as the PLQY increases to reach a maximum value of 0.42 mA/cm².

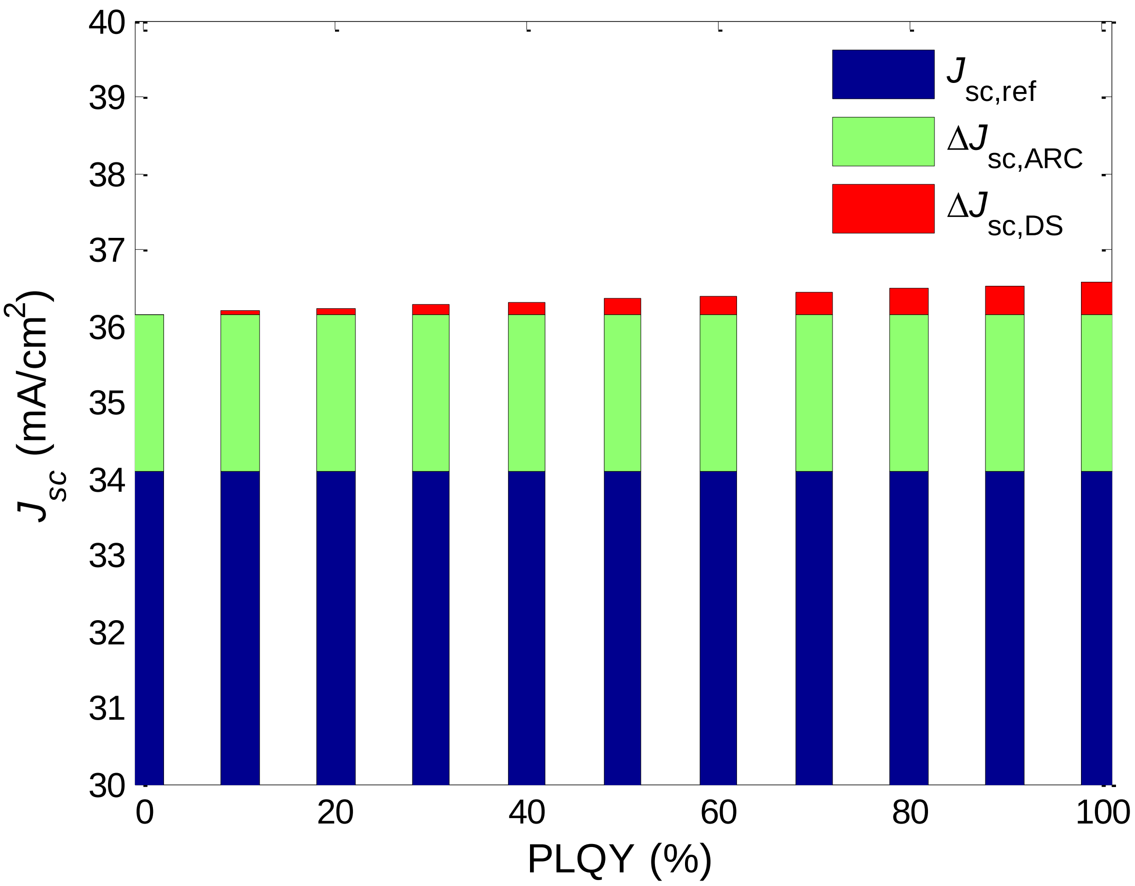

Figure 5.17. Contributions to J_{sc} enhancement due to ARC effect, $\Delta J_{sc,ARC}$, and DS effects, $\Delta J_{sc,DS}$, as a function of PLQY for solar cell D (SRV = 10^7 cm/s).

5.2.3.2. **Si-nC Coupled to CIGS Solar Cells**

The CIGS solar cell model developed in chapter 4 is used in this section to explore the effects of Si-nC as DS layer. Si-nC absorb in the UV-blue region up to 500 nm, in the same spectral region as CdS. As a result, photons that would be absorbed in the CdS layer are instead absorbed in the DS layer. In this study, five test CIGS solar cells of increasingly poor CdS/CIGS interface quality are considered, where the surface recombination is used to model said quality. The EQE of the CIGS solar cell are shown in Figure 4.26. For each cell, the thicknesses of the double stack SiO_2 and the Si-nC layers are optimized by maximizing J_{sc} for different values of the Si-nC PLQY using equations (5.23) - (5.25). Figure 5.18 shows J_{sc} as a function of the Si-nC layer thickness calculated for a PLQY of 20% for a CIGS solar cell with SRV = 10^7 cm/s. Figure 5.18 indicates that a maximum J_{sc} occurs for Si-nC layer thickness of 50 nm and SiO_2 layer thickness of 90 nm. For a DS layer in the absence of SiO_2 (yellow line), there are more reflections from the top surface and therefore results in lowest J_{sc}. This is expected since the refractive index of ZnO and SiO_2 are 2 and 1.5, respectively, and therefore SiO_2 is a perfect intermediate layer between air and ZnO. Si-nC has higher refractive index of 1.9 and as a result does not act as a good ARC compared to SiO_2.

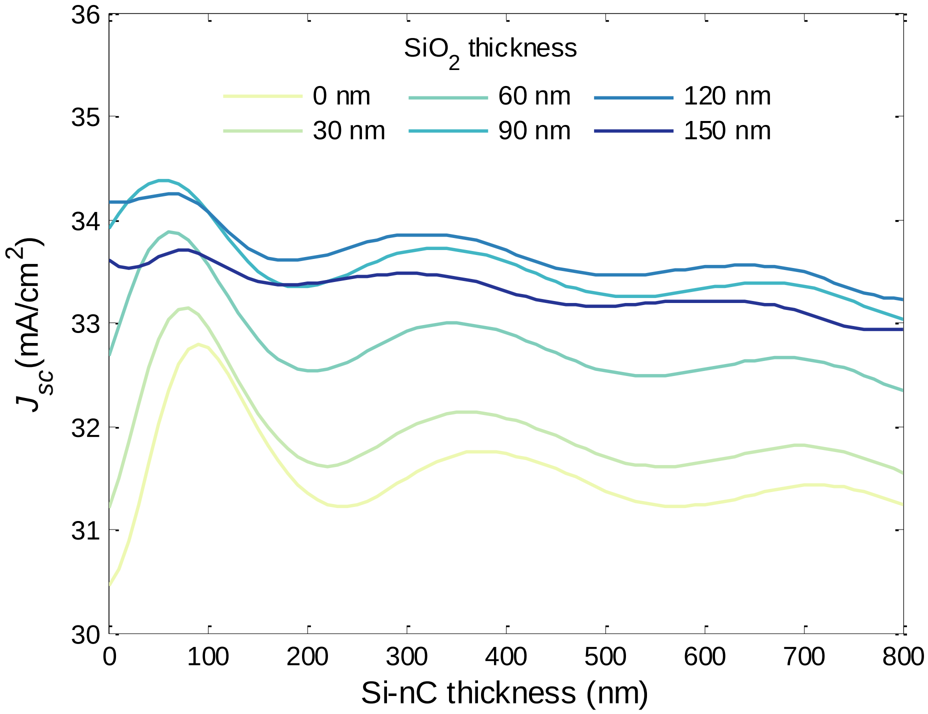

Figure 5.18. Short-circuit current density, J_{sc}, as a function of Si-nC and SiO_2 layer thicknesses for CIGS cell with SRV = 10^7 cm/s based on PLQY of 20%.

Moreover, for Si-nC layers with low PLQY, J_{sc} decreases as the layer thickness increases, since only a small fraction of the absorbed photons by Si-nC is re-emitted to the solar cell. Therefore, there is a negative effect on the cell performance for increasing Si-nC layer thickness. However, for higher PLQY, the J_{sc} increases as the thickness increases until an optimum thickness of Si-nC layer is reached. Figure 5.19 shows the same cell as in the Figure 5.18 but with a DS layer where PLQY is 80%. The J_{sc} increases as the Si-nC layer thickness increases until a plateau is reached at around 3000 nm. Although this is a very thick layer of Si-nC to grow experimentally, for the purpose of simulation, this represents the optimum layer thickness.

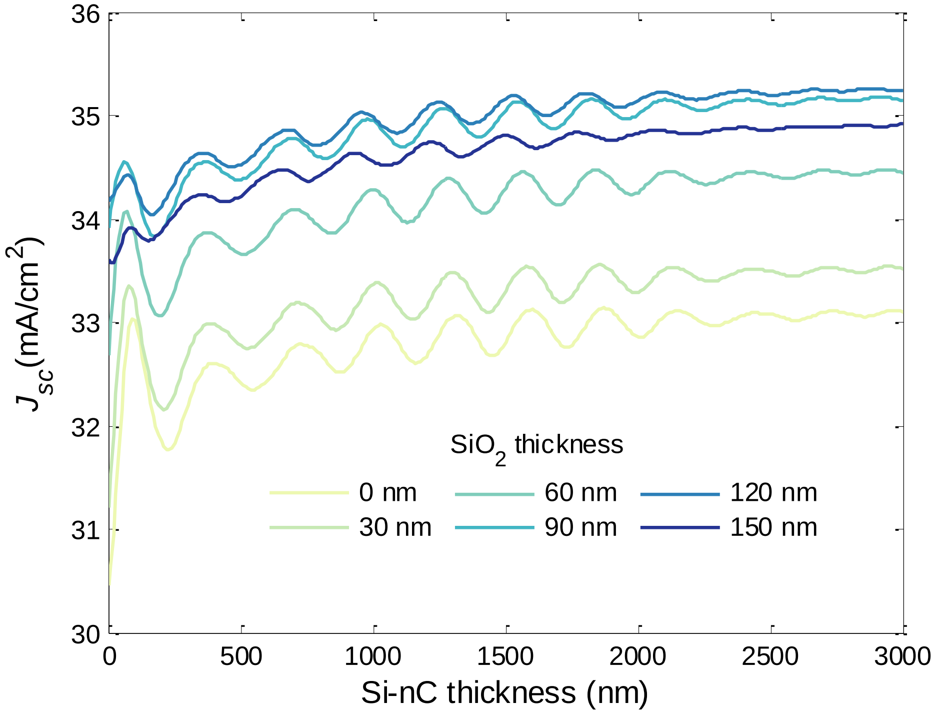

Figure 5.19. Short-circuit current density, J_{sc}, as a function of Si-nC and SiO_2 layer thicknesses for CIGS cell with SRV = 10^7 cm/s based on PLQY of 80%.

After investigating other cells, the same trend was observed for the highest efficiency: thin Si-nC layer for low PLQY and a thick layer for high PLQY (> 60%). Thin Si-nC layer along with the SiO_2 act as a good ARC layer, especially for low PLQY DS layers. This is noticed as the first peak in all curves in Figure 5.19. As the Si-nC increases the DS effect increases and therefore can surpass the first peak as in the case of high PLQY, as shown in Figure 5.19. This observation is confirmed for other calls for different PLQYs as shown in Figure 5.20 and hence the step response of the Si-nC layer thickness. Figure 5.20 shows the optimized Si-nC layer thickness as a function of PLQY for different CIGS cells. For a PLQY < 50% the layer thickness is in the range 50 – 60 nm, which acts mainly as a double layer ARC stack with the SiO_2 layer. Cells with poor UV spectral response (i.e. a high SRV at the front surface) benefit more strongly from the DS layer, and once the PLQY > 50%, the DS effect has higher impact. Cells with better

UV spectral response (SRV = 10^4 cm/s) take advantage of the DS effect only when PLQY > 70%. The SiO_2 layer thickness is almost constant independent of the PLQY and is in the range 100 – 110 nm.

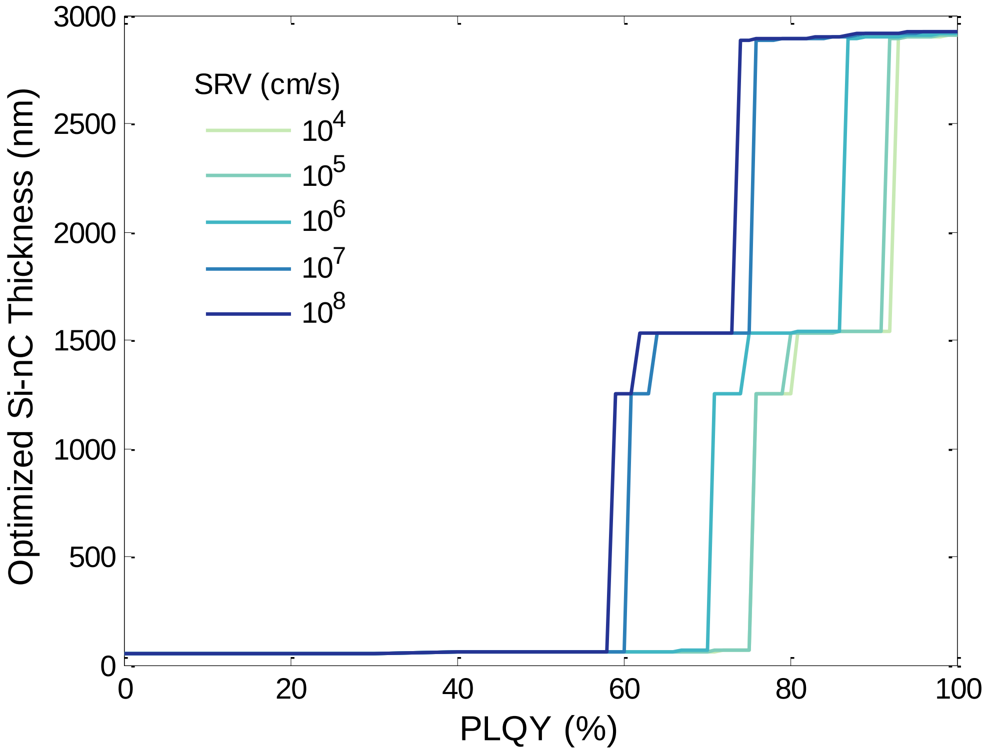

Figure 5.20. Optimized Si-nC layer thicknesses that maximize J_{sc} of cells with different SRVs as a function of PLQY.

To investigate the efficiency enhancement to the solar cells due to the DS layer, the cells are compared with a reference cell that has no ARC layer. In addition, the cells are also compared to a passive cell, which is a CIGS cell with a DS layer on the top surface but with zero re-emission of absorbed photons, i.e. an PLQY = 0. The passive cell is used to single out the DS effect from the ARC effect.

The simulation results are compared based on the EQE where the EQE of the reference cell, and cells with PLQY 0 and 80% are shown in Figure 5.21. It is evident that there is a major improvement in the EQE of the cell due to improved optical coupling into the cell arising from introducing the DS layer, as observed by the higher magnitude EQE for the green and blue data (passive and active cells respectively). This represents the biggest enhancement to the reference cell, thus the ARC influence is the largest.

The enhancement of the EQE for the active cell in the long-wavelength region is similar to the passive cell. The important benefit of the active cell over the passive cell is the additional increase in the EQE in the short-wavelength region (300-500 nm). The EQE of the passive cell is below that of the reference in the range < 370 nm due to the strong absorption of Si-nC in this region. It is evident from the EQE of the cell with DS layer where PLQY =20% that there is enhancement in the region < 380 nm. This increase in EQE is due to the DS effects.

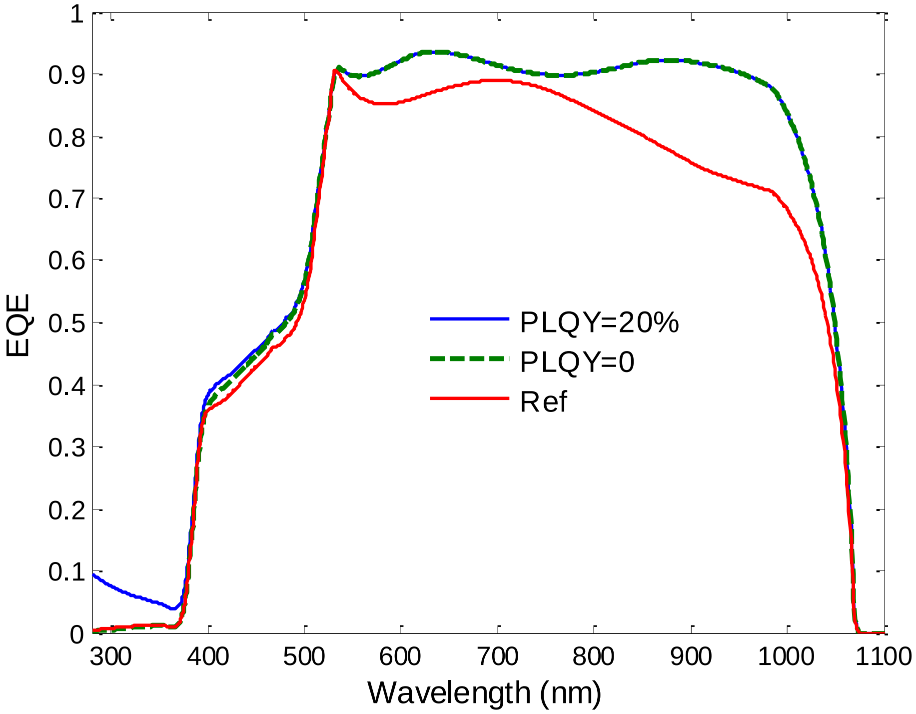

Figure 5.21. EQE of a reference cell with no DS (red line), two cells with PLQY = 0% (green dotted line) and PLQY = 20% (blue line). All cells have SRV = 10^7 cm/s

Figure 5.22 shows the short-circuit current density, J_{sc}, of the simulated reference, and active (PLQY = 20%, 50%, 70% and 100%) CIGS solar cells as a function of the surface recombination velocity at the CdS/CIGS interface. The reduced reflectivity caused by the enhanced ARC properties of the DS layers is the dominant effect when compared the active cells with the reference cell. For the cells with PLQY < 60% the DS effect is very small even for the highest SRV value, as shown in Figure 5.20. Therefore the J_{sc} shown in Figure 5.22 as a function of SRV for cells with PLQY = 20% and 50% are very similar with very small portion of $\Delta J_{sc,DS}$ (0.15% and 0.43%, respectively). As the PLQY increases the DS effect becomes more visible and therefore the $\Delta J_{sc,DS}$ increases for DS layers with PLQY of 70% and 100%. While DS effect increases only for cells with SRV =10^7 cm/s and 10^8 cm/s for a DS layer with PLQY = 70%, for perfect DS layer (PLQY = 100%) the DS effect is dominant for all cells.

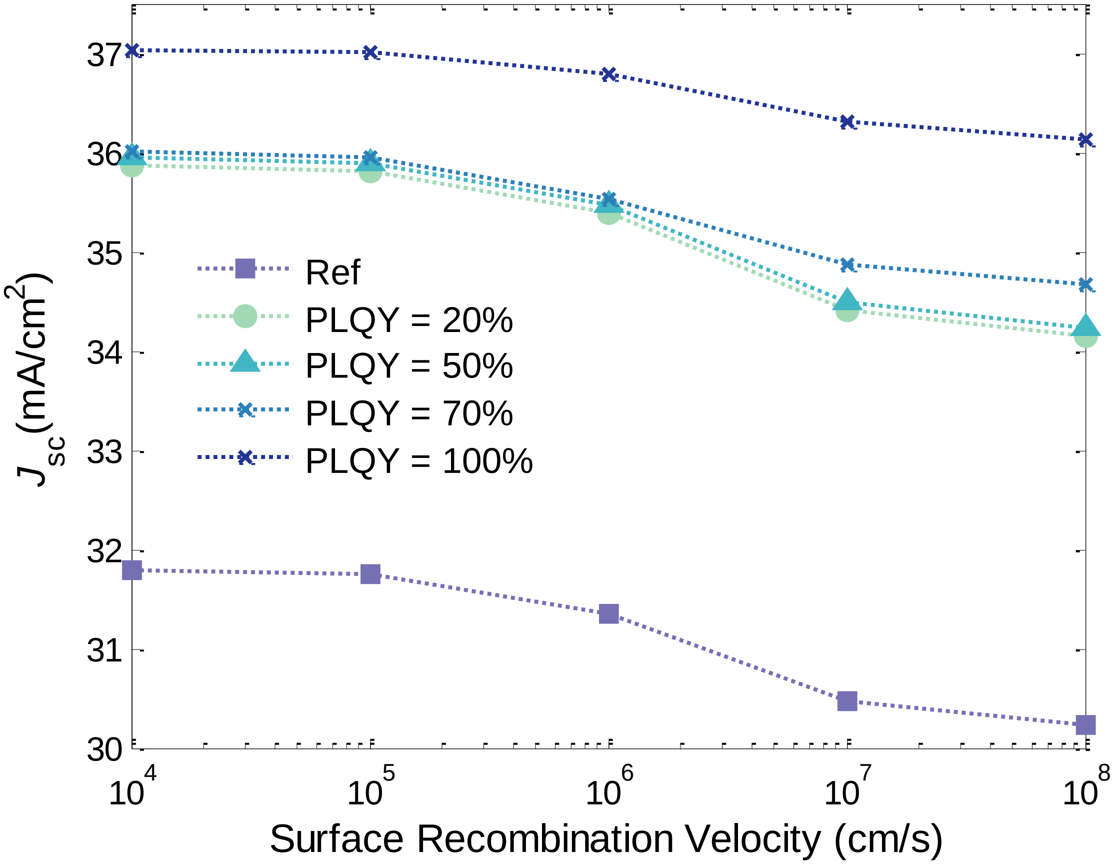

Figure 5.22. Short-circuit current density as a function of surface recombination velocity at the CdS/CIGS interface for reference, passive and active cells. Active cells have DS layers with PLQY 20%, 50%, 70% and 100%.

In order to decouple the ARC and DS effects for the CIGS solar cell, the J_{sc} is compared with that of a passive cell. However the passive solar cell must have a DS layer with the same layer thickness as the active solar cell since the active cell has a very thick Si-nC layer (2990 nm). This was not an issue in the case of silicon solar cell discussed in the last section since the layer thickness varied by less than 10 nm for all DS layers independent of the PLQY, as shown in Figure 5.14.

Figure 5.23 shows the active cell and the passive cell with the same DS layer thickness as the active cell for comparison. It is evident that the DS effect is dominant in this case. At low SRV values, the passive cell performance has degraded when compared with the reference cell. In this case a negative ARC effect is observed. The absorption in the thick DS layer explains this negative effect. When SRV increases (>10^7 cm/s) the passive cell is performing better than the reference cell and as a result a positive ARC effect is observed. The DS effect is almost constant over the SRV change with relative enhancement in J_{sc} of 18%. The ARC effect is -1.4% for good cells (SRV = 10^4 cm/s) and increases to 1.5% for poor cells (SRV = 10^8 cm/s).

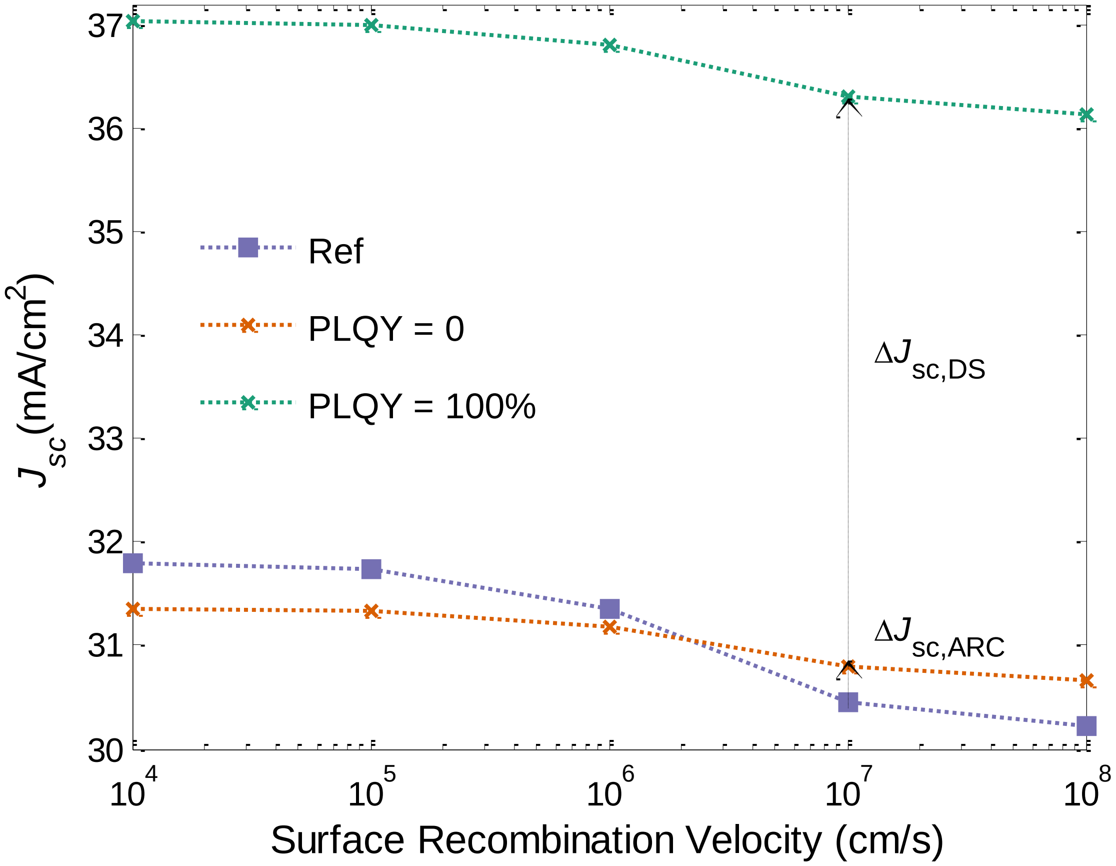

Figure 5.23. Short-circuit current density as a function of surface recombination velocity at the CdS/CIGS interface for reference, passive and active cells for PLQY =100%. The passive cell has DS layer thickness similar to the active cell.

5.3. Summary

A numerical model for DC and DS layers has been presented which considers the absorption and emission profiles, PLQY, and reflection losses of the layers. The input parameters to the model have been discussed in details with emphasis on $T_{\text{trap}}(\lambda)$, the fraction of re-emitted photons by the DC layer in the direction of the solar cell. In other models reported in the literature this parameter is constant (independent of λ) and based on escape cone calculations. In addition, the model is improved to include the optimization of DC and DS layer thicknesses to maximize the short-circuit current density.

The effect of coupling idealized optical DC layers to an ideal silicon solar cell has been presented to report the upper limit of the efficiency enhancement expected as compared to detailed balance. A maximum of 57 mA/cm^2 is achieved when applying an ideal DC layer compared with 45.9 mA/cm^2 for an ideal cell with no DC layer; this is a 24% relative increase in J_{sc}. Moreover, ideal DC and DS layers were coupled to a model representative of a commercial-grade silicon solar cell using the device simulator and the efficiency enhancement was explored for such a cell. The simulation results show that the optimum DC bandgaps have increased from 2.2 eV for the ideal cell case to 2.6 eV when coupled to this more realistic silicon solar cell. This is due to the Gaussian distribution of the DC emission in the second case as opposed to line emission profile. In addition the EQE of the modeled solar cell is low near the bandgap of the solar cell, as opposed to 1 in case of ideal cell.

Furthermore, the effects of coupling Si-nC based DS layers to silicon and polycrystalline CIGS solar cells have been studied using a device simulator. The Si-nC embedded in SiO_2 have been fabricated and characterized at McMaster University as part of a collaborative project. The measured ellipsometry parameters as well as the photoluminescence profile were used to calibrate the DS model. For the silicon solar cell, a maximum increase in J_{sc} of 8.4% was achieved for a perfect DS layer (PLQY = 100%) as compared to a reference cell, where 7.2% was due to ARC effect and only 1.2% was due to DS effect. The layer thickness did not vary significantly during the optimization process which indicates that the ARC effect was dominant. On the other hand, there an increase in J_{sc} of 19.5% was achieved for the CIGS solar cell when coupled to a perfect DS layer. The DS effect was dominant with 18%, while the ARC effect contributes only 1.5% to the total J_{sc} enhancement. Therefore for these specific silicon and CIGS solar cell designs, the Si-nC embedded in a SiO_2 matrix based DS layer is more effective with the CIGS solar cell given PLQY is > 60%, otherwise an enhancement of 13% in J_{sc} is observed due to ARC effect.

Chapter 6: Characterization of Silicon Solar Cells and Silicon Nanocrystals

6.1. Experimental Setups

6.1.1. Quantum Efficiency Measurements

A Newport IQE-200 quantum efficiency measurement system is used to measure the quantum efficiency of different silicon solar cells. In the EQE measurement, the number of carriers collected is compared to the number of incident photons at a specific wavelength. Therefore a tunable monochromatic source is used to shine light on the solar cell, while two electrical probes are used to measure the current generated by the solar cell. The system uses a Xenon lamp as its monochromator light source. The monochromatic modulated beam is obtained using the system consisting of an Oriel 1/8 m monochromator, a chopper with a digital lock-in amplifier set at 87 Hz, order-sorting filters, and collimating lenses. The beamsplitter delivers the light simultaneously to the device under test (DUT) and to the reference detector (CH1). Light reflected

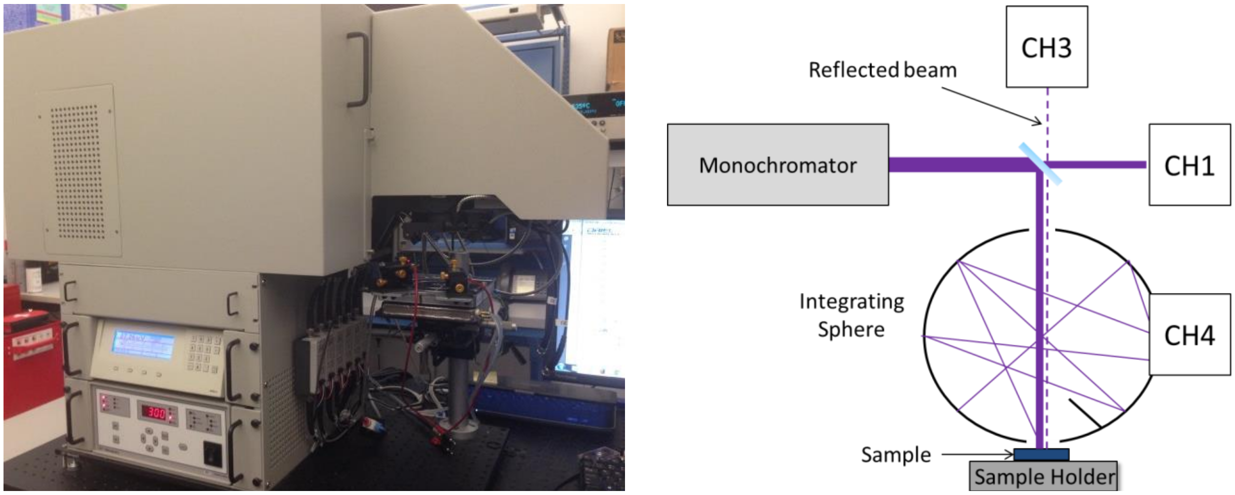

Figure 6.1. A picture of IQE-200 system with integrating sphere not installed, and a simplified schematic of IQE-200 setup.

directly from the sample can be detected using the specular reflectance detector (CH3). When the integrating sphere is installed, diffuse reflectance can be measured using the diffuse reflectance detector (CH4). The three detectors are calibrated using NIST traceable reference samples.

6.1.2. Oriel Solar Simulator

The Oriel 92191 solar simulator (SS) is powered by a 1600 W xenon lamp and is capable of uniformly illuminating an area of 2″ by 2″ at up to 150 suns. A number of air mass filter sets are used to correct the output spectrum to roughly match the required solar spectrum such as: AM0, AM1D, AM1.5G, AM1.5D, and AM2D. In addition a number of nickel plated mesh filters are used to achieve the required intensity. A reference silicon solar cell is used to calibrate the intensity of the SS.

6.2. Experimental Results

6.2.1. Monocrystalline Silicon Solar Cells

Monocrystalline silicon solar cells were fabricated at the Carleton University MicroFabrication Facility coordinated by Professor Garry Tarr as part of fourth year course, ELEC4703. Two types of silicon wafers were used: Float Zone (FZ) and Czochralski (Cz) according to the growth method of silicon crystals. *p*-type <100> silicon wafers were used as a substrate. The emitter was doped by phosphorus diffusion using an eight-stack Bruce Model BDF-8 furnace bank. The front metal (Ti/AG) is composed of metal fingers with different spacing for current collection. The back contact is made of a 0.5 µm thick aluminum layer that covers completely the back surface. A titanium silica layer was deposited on wafer PV14-1A to act as ARC layer, while wafer PV14-LC did not have any ARC layer. The size of the cells on both wafers is 10 mm by 10 mm each. Table 6.1 summarizes the parameters for the fabrication process.

Table 6.1. Fabrication process parameters of silicon solar cells

	PV14-1A	**PV14-LC**
	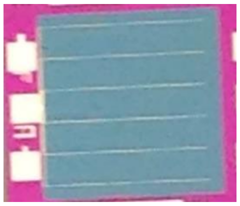	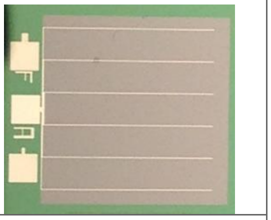
Wafer diameter	300 mm	300 mm
Wafer type	Cz p<100>	FZ p<100>
Wafer resistivity	1 – 4 Ω-cm	0.17 – 0.23 Ω-cm
Phosphorus Diffusion	10 Ω-cm²	80 Ω-cm²
Antireflection coating	Titanium silica	None

Figure 6.2 shows cross-sectional scanning electron microscopy (SEM) image of fabricated silicon solar cell (PV14-1A).

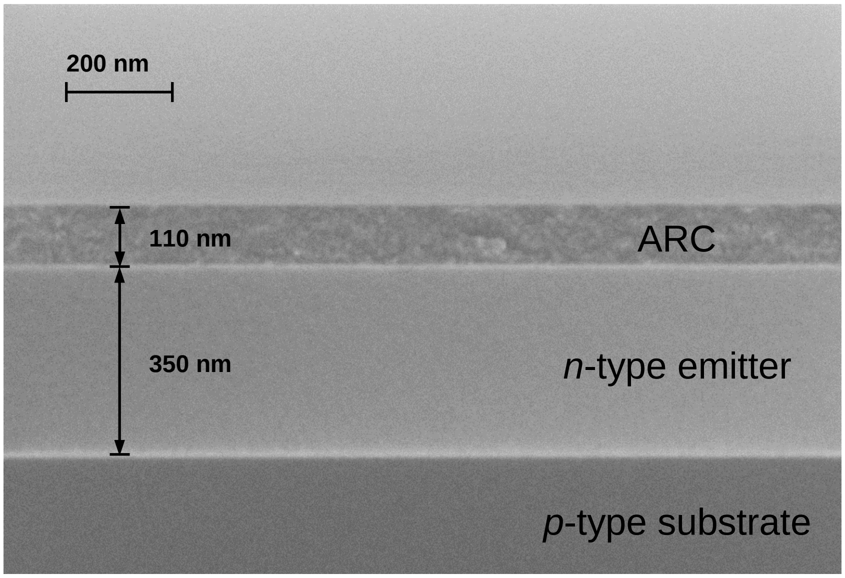

Figure 6.2. Cross-sectional SEM image of PV14-1A silicon solar cell.

PV14-1A wafer was sent to McMaster University for measurement of the optical properties of the ARC layer. Ellipsometry measurements were performed using a JA Woollam M2000UI variable-angle spectroscopic ellipsometer. Figure 6.3 shows the optical constants for the titanium silica ARC layer. The refractive index is close to 2 for wavelengths longer than 500 nm, which is close to the ideal refractive index of an ARC layer for silicon solar cells. A non-zero extinction coefficient, k, is observed in the short-wavelength region and hence there is absorption by the ARC at wavelengths below 650 nm.

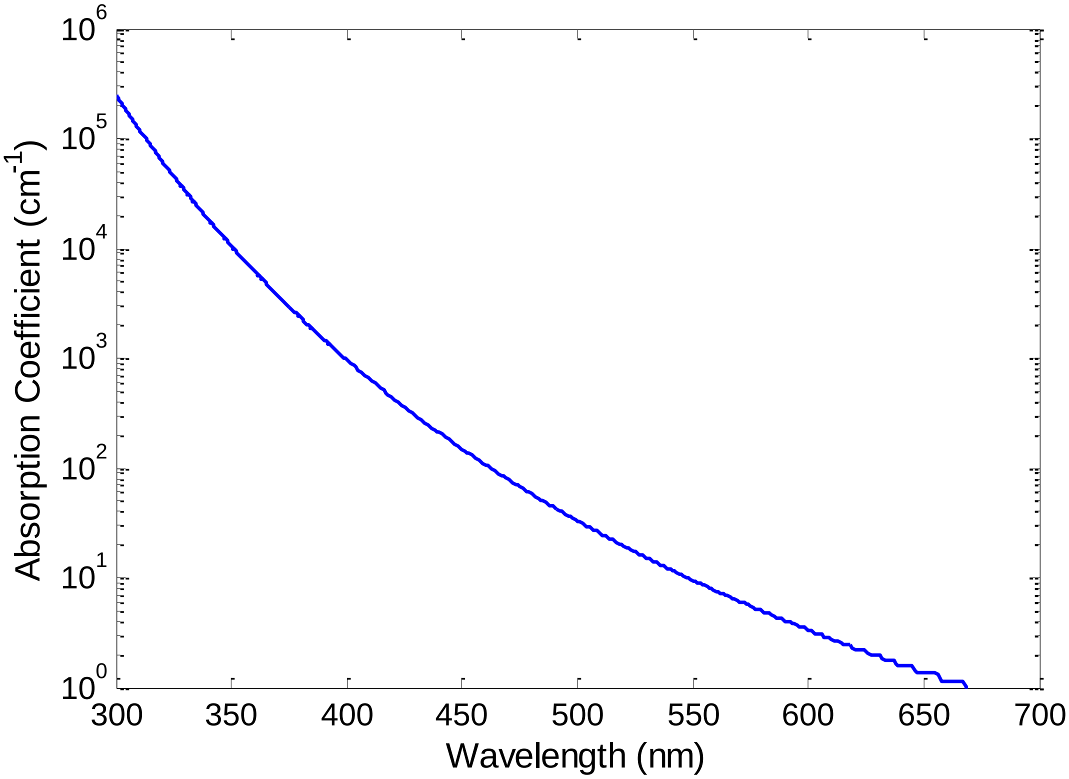

Figure 6.3. Absorption coefficient of titanium silica ARC layer calculated from the measured extinction coefficient.

Current-Voltage (*I-V*) measurements are taken for the two cells with the Oriel SS approximating the AM1.5D spectrum. A Keithley 2420 source meter unit with a 4-probe connection to the solar cell is used to sweep the voltage and measure the generated current. *I-V* curves for the solar cells are shown in Figure 6.4. As expected PV14-1A-1 (1 is the cell number on the wafer) has higher I_{sc} as the ARC layer reduces reflection losses. On the other hand, PV14-LC-7 (7 is the cell number on the wafer) has higher *FF* and V_{oc} because of better wafer quality which reduces SRH recombination losses. In addition the PV14-LC-7 has higher substrate doping than PV14-1A-1, as deduced from the sheet resistivity shown in Table 6.1. A high substrate doping concentration reduces SRH recombination losses and therefore V_{oc} is increased. This is at the expense of a lower J_{sc}

due to longer diffusion lengths which causes minority carriers to recombine faster, as was discussed in Figure 4.16. The results are summarized in Table 6.2.

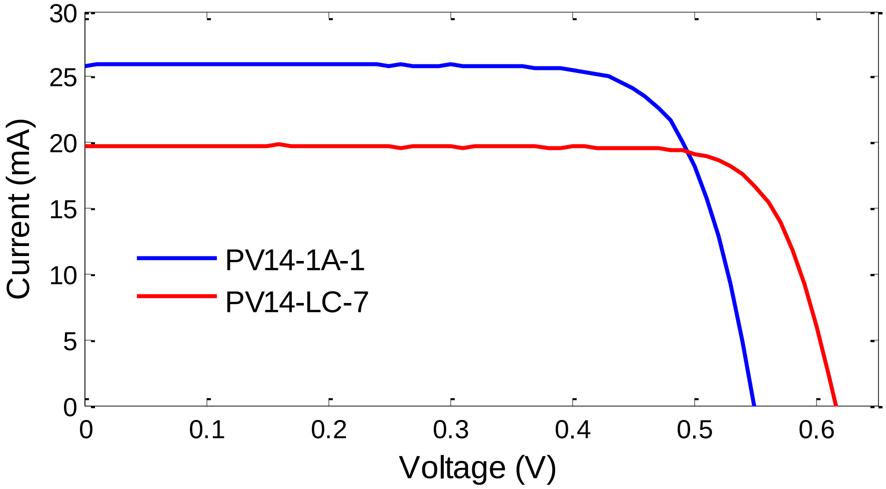

Figure 6.4. Measured *I-V* curve of solar cells PV14-1A-1 (blue) and PV14-LC-7 (red) under one sun.

Table 6.2. Solar cells measured parameters.

	Cell area (cm²)	***I_{sc}* (mA)**	***V_{oc}* (V)**	***FF* (%)**	***η* (%)**
PV14-1A-1	1	25.9	0.550	76.36	10.9
PV14-LC-7	1	19.7	0.615	80.14	9.7

To investigate the spectral response of the solar cells, the EQE and total reflectance are measured using the IQE-200 setup. The total reflectance is measured using an integrating sphere to capture all of the light that is not absorbed, including scattered light. As shown in Figure 6.5, the total reflectance has a minimum at 900 nm, which is not typical for ARC layers designed for solar cells. ARC layers for solar cells are designed to have minimum reflectance around 600 nm where the incident intensity is the highest. On the other hand the diffuse reflectance is relatively low and accounts for scattered light that escapes the device in all directions. The high diffuse reflectance at long wavelengths is due to scattered photons with energy close to the bandgap of the silicon material and therefore has small possibility of being reabsorbed by the active material. With no integrating sphere the scattered light would be lost and would mistakenly be attributed to absorption by the device. This is especially important for the short wavelengths since an error in absorption at these wavelengths can significantly affect the shape of the IQE curve.

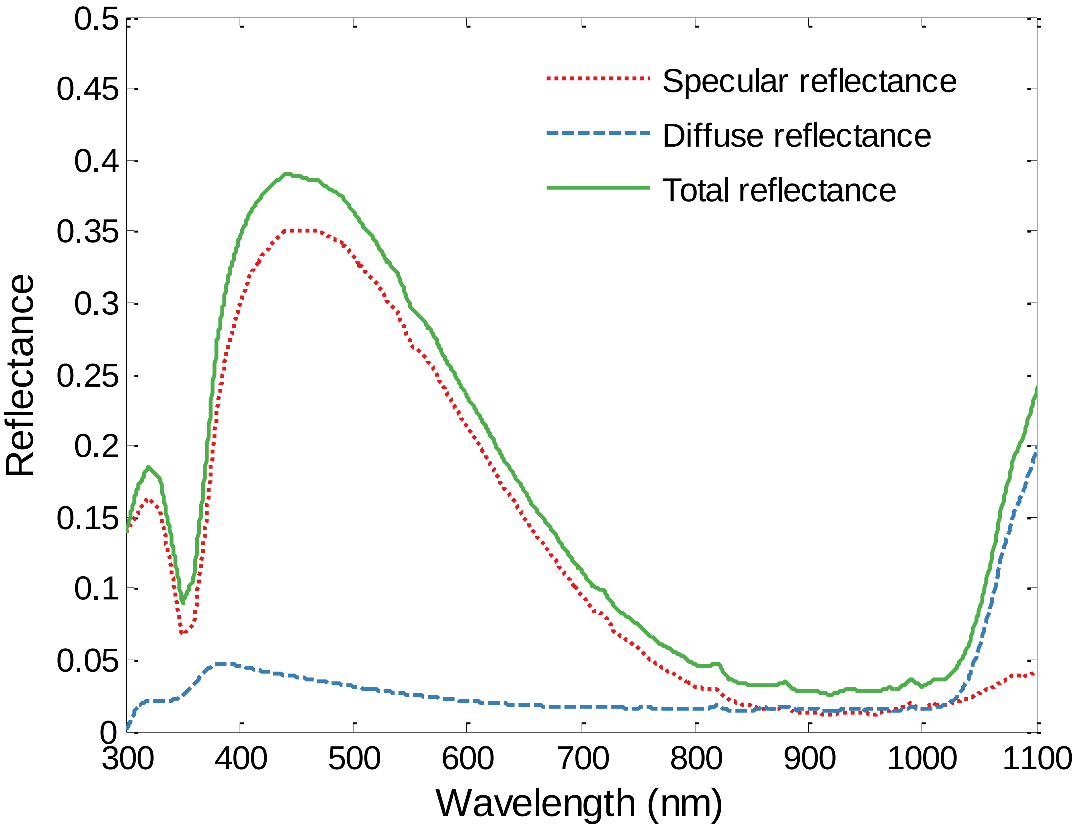

Figure 6.5. Measured specular and diffuse reflectance using an integrating sphere for a silicon solar cell with titanium silica as an ARC layer.

The IQE is calculated using equation (2.40) and therefore absorption in the active layer must be measured. Determining the absorption in the active layer can be challenging in cases where there are parasitically absorbing layers in the device, and usually requires optical modelling to relate experimental measured total absorption to the absorption in each layer. The absorption in each layer cannot be independently measured due to interference effects. Therefore the transfer matrix method is used to calculate interference of coherent and reflected waves at each interface in the device [195].

Using the measured values for the real and imaginary parts of the complex refractive index (*n* and *k*, respectively, as a function of wavelength), the absorption in each layer of the device is calculated with an optical model using a transfer matrix formalism, as discussed in section 4.1.2. From this, the parasitic absorption (absorption in the parts of the device that are not part of the active layer) is separated from the total absorption. Rather than using the optical model to predict the absorption in the active layer, which is the main contribution of the total absorption, the modeled parasitic absorption is subtracted from the experimentally measured total absorption. Therefore by subtracting the parasitic absorption from the experimentally measured data the error due to disagreement between the model and the measurements is minimized. The results are plotted in Figure 6.6.

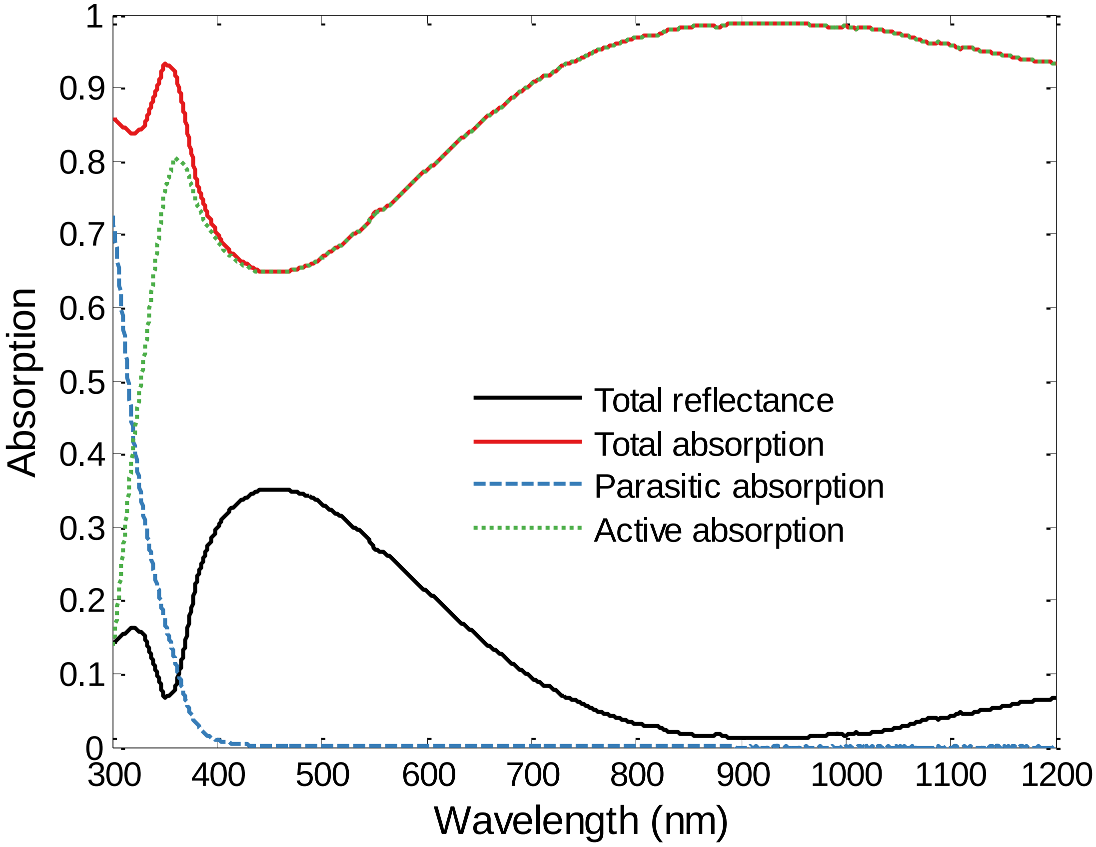

Figure 6.6. Measured total absorption, simulated parasitic absorption and calculated absorption in the active layer as a function of wavelength for a silicon solar cell.

Therefore equation (2.40) becomes:

$$IQE(\lambda) = \frac{EQE(\lambda)}{1 - R(\lambda) - A_{\mathrm{p}}(\lambda)} \tag{6.1}$$

where R is the total reflectance and in this case includes diffuse reflectance, and A_{p} is the modeled parasitic absorption.

Figure 6.7 shows the measured EQE and total reflectance as well as the calculated IQE of the solar cell. The poor UV response of the solar cell is due to the parasitic absorption in the ARC layer but also due to high surface recombination. The EQE increases gradually as the reflectance decreases with maximum EQE in the 700 nm - 800 nm range. Typically ARC layers are designed such that a minimum reflectivity is around 600 nm where most of the power of the solar spectrum exists; here the zero reflectance is shifted to longer wavelengths and hence the ARC layer is thicker than what it should be. The gradual decrease of the EQE at longer-wavelengths could have been improved if a back surface field existed to enhance the collection of carriers at the bottom contact.

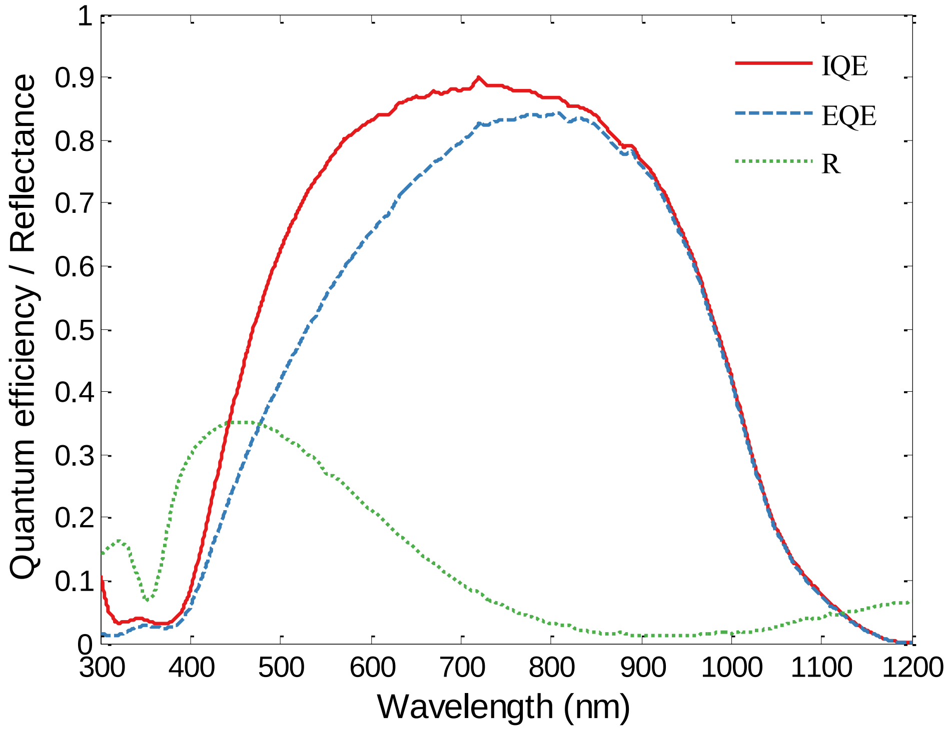

Figure 6.7. Measured EQE and total reflectance of the silicon solar cell. The IQE is calculated according to equation (6.1).

The IQE, EQE and reflectance of PV14-LC-7 is shown in Figure 6.8. Since there is no parasitic absorption then equation (6.1) reduces to only the reflectance term in the denominator and hence no optical modelling is required. The reflectance is relatively high due to the absence of ARC layer. Nevertheless the UV spectral response is almost 30%, which is much higher when compared with PV14-1A-1. This is due to the absorption in the ARC layer in addition to poor surface passivation in case of PV14-1A-1. The IQE is relatively high up to almost 700 nm then it gradually decreases until it reaches the band edge of silicon. This could have been improved by applying a BSF at the back of the cell to enhance the collection of carriers at the bottom contact. Comparing the IQE of the two cell, it is evident that PV14-LC-7 in Figure 6.8 has higher IQE and this is mainly due to the better quality of the wafer with less impurities and defects and hence less SRH recombination.

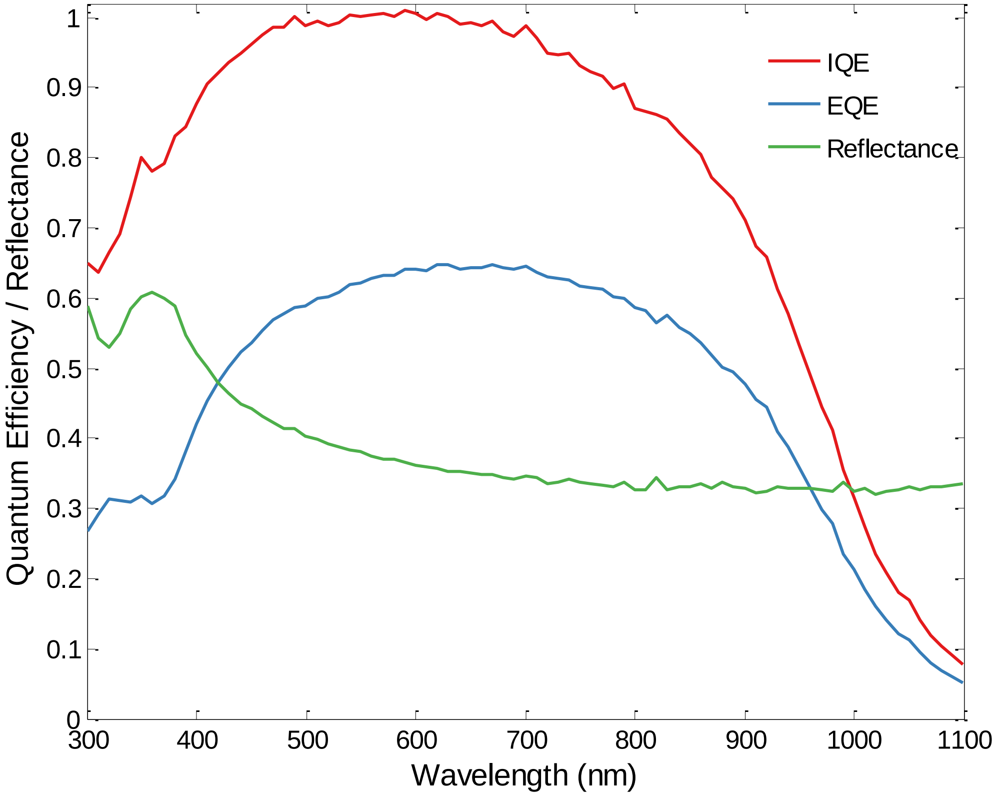

Figure 6.8. Measured external quantum efficiency and reflectance of PV14-LC-7 silicon solar cell. The IQE is calculated according to equation (6.1).

In the next section, the effect of DS layer on the cell performance is investigated. Analysis from this section is used to decouple the ARC and DS effects.

6.2.2. DS Layer Mounted on Silicon Solar Cell

After measuring the quantum efficiency of the silicon solar cell, the next logical step is to characterize the Si-nC and silicon solar cell as a system. Silicon nanocrystals embedded in silicon oxide matrix were fabricated at McMaster University using a Plasma-Enhanced Chemical Vapour Deposition (PECVD) system. The Si-nC were grown on fused silica substrates followed by annealing using a quartz tube furnace. The fused silica Spectrosil 2000 UV coverslips (CFS-2525) are 0.5 mm thick from UQD Optics [196]. The sample used here has been annealed at a temperature of 1135 °C with estimated thickness of 484 nm. The measured PL and absorption coefficient are shown in Figure 5.11. More information on the growth process can be found in Appendix A.

The double layer Si-nC/SiO_2, is placed on the top surface of the silicon solar cell with the Si-nC layer facing the solar cell, as shown in Figure 6.9. A refractive index matching liquid from Cargille is used between the Si-nC and the silicon solar cell to eliminate the reflection losses associated with the Si-nC/air interface [197]. The IQE-200 setup is used to characterize the solar cell with the DS layer.

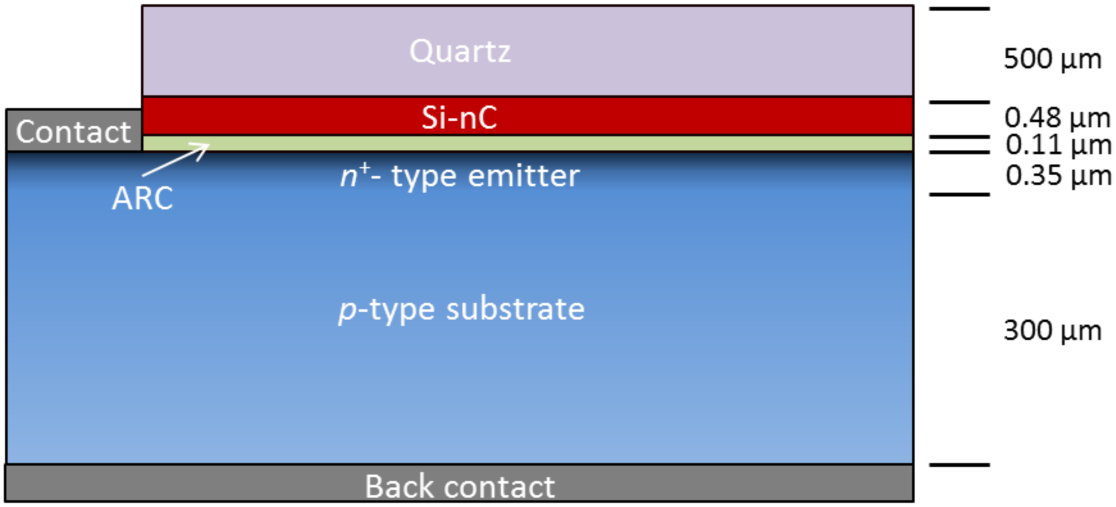

Figure 6.9. A two dimensional schematic of silicon solar cell with a titanium silica ARC layer. A double DS layer consisting of quartz and Si-nC is placed on the top surface. Schematic is not to scale.

The measured EQE and specular reflectance for the silicon solar cell with and without the DS layer are shown in Figure 6.10. It is clear that there is enhancement in the EQE from 500 – 680 nm and below 400 nm. However, there is clear degradation in the EQE at longer wavelengths (> 680 nm). The enhancement and degradation in the wavelength range 500 – 1200 nm are due to ARC effects, which include absorption in the DS layer. The very small enhancement below 400 nm is mainly due to DS effects. In order to confirm these observations the ARC and DS effects must be decoupled, as will be discussed in the next section.

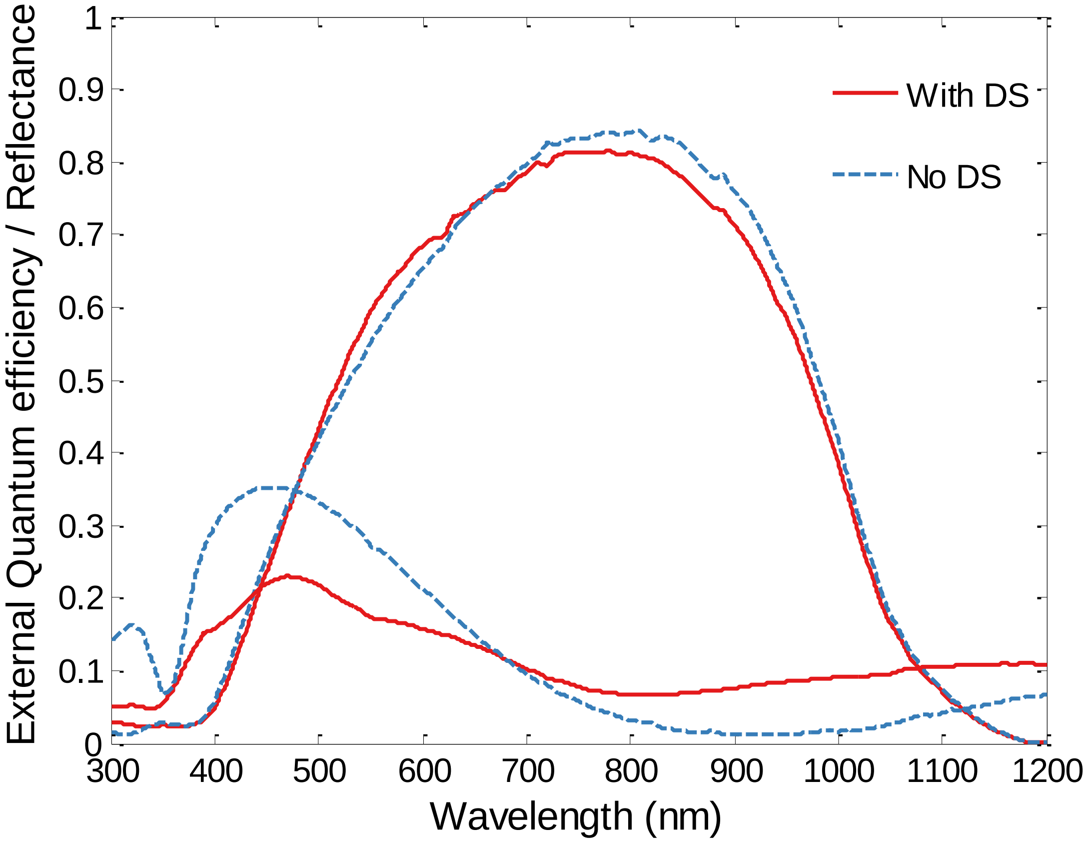

Figure 6.10. Measured EQE and specular reflectance for silicon solar cell (PV14-1A-1) with (solid red) and without (dotted blue) DS layer.

In order to calculate IQE of the solar cell with the DS layer, the parasitic absorption must be modeled. The parasitic absorption includes absorption in the ARC layer as well as the DS layer, as shown in Figure 6.11. The Si-nC absorb strongly up to 500 nm. Since the DS layer is relatively thick, the parasitic absorption is dominated by absorption in the DS layer with negligible absorption in the underlying ARC layer. The total reflectance is represented by the specular reflectance only and is shown in Figure 6.11. Finally, the active absorption can be determined from the total absorption less the modeled parasitic absorption.

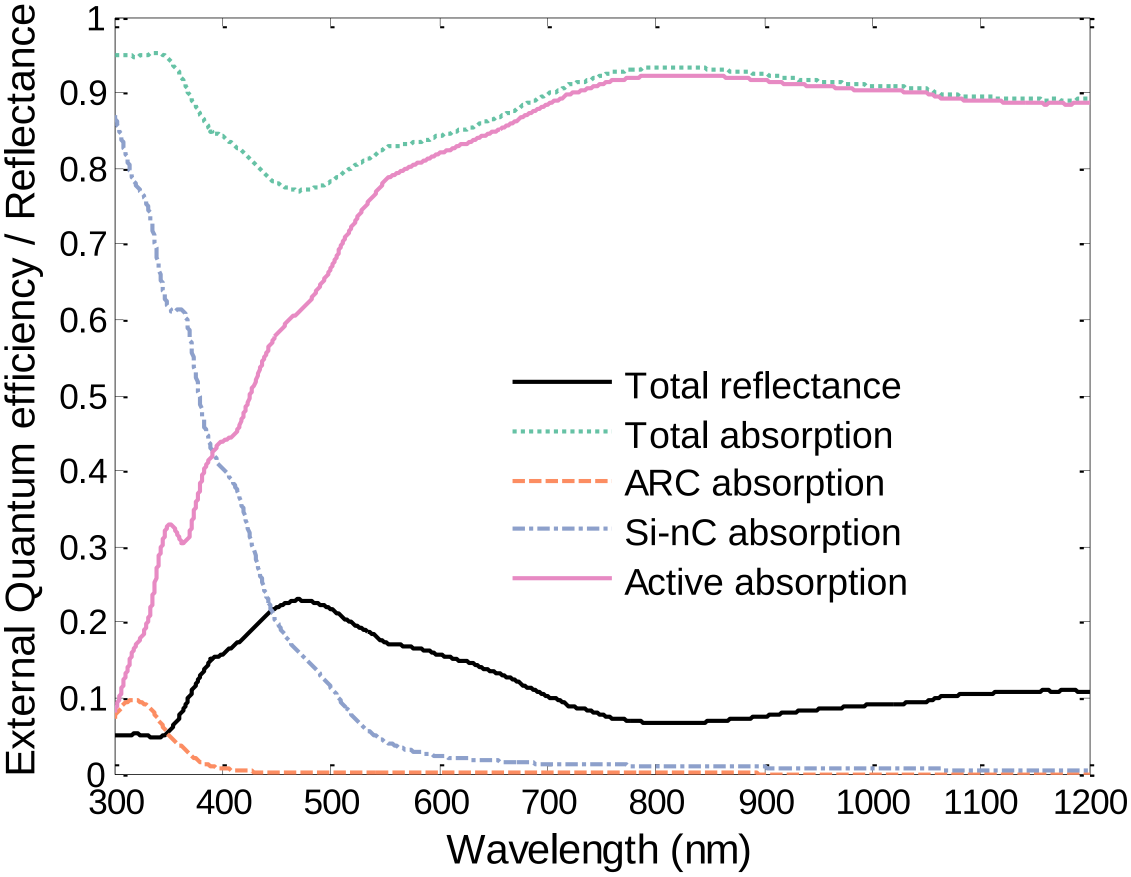

Figure 6.11. Measured reflectance, total absorption, simulated parasitic absorption and calculated absorption in the active layer as a function of wavelength for a silicon solar cell coupled to Si-nC based DS layer.

After computing the active absorption, now the IQE for the solar cell with the DS layer can be determined from equation (6.1), as shown in Figure 6.12. As observed from the figure, IQE_{tot} is higher than IQE_{ref} in the range below 400 nm due to the DS effect. The DS layer absorbs significant number of photons in the UV range but due to low quantum yield of the layer, only a few photons are re-emitted and hence a small contribution to the electrical current is obtained. The agreement between the two curves show the accuracy of the measurement and the optical modelling of the layers. The difference between the two curves in the range > 500 nm is less than 2%.

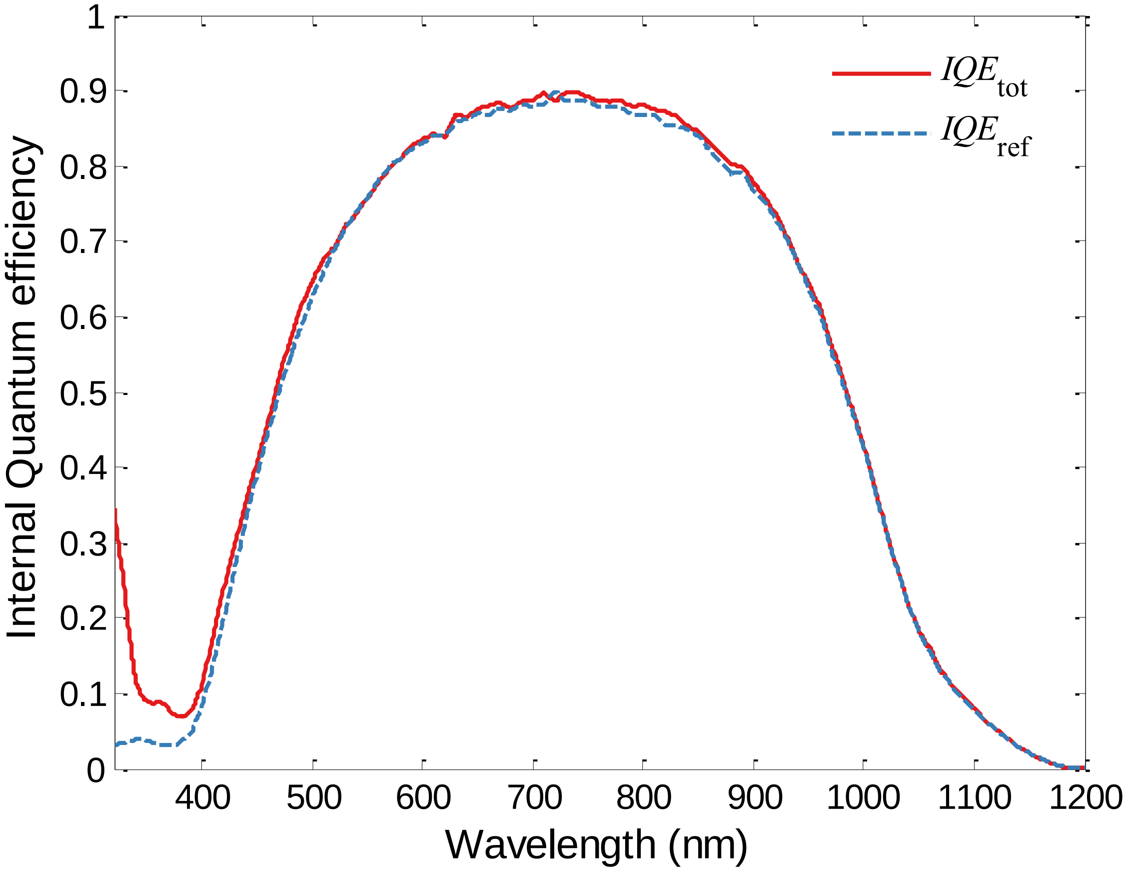

Figure 6.12. Calculated IQE of the solar cell with and without the DS layer.

The J_{sc} for the reference cell and after adding the DS layer can be calculated by integrating the EQE as in equation (2.41). The reference cell has $J_{sc,ref}$ of 25.14 mA/cm^2 assuming AM1.5G standard spectrum, which is very close to the measured J_{sc} in the last section of 25.9 mA/cm^2. The $J_{sc,tot}$ for the solar cell with DS layer is 24.70 mA/cm^2, which means a total degradation of 0.44 mA/cm^2 is observed. This is due to the low efficiency of the DS layer sample used in this work. Only few of the photons absorbed in the layer are contributing to the current that otherwise all those photons would have been contributing to the current if the DS layer is not mounted. In addition the layers thicknesses are not optimized and therefore there is also degradation due to ARC effects. Whether there is enhancement or degradation, it is very useful to decouple the ARC effects from the DS effects. In the next section expressions are derived to decouple the two effects.

6.2.3. Decoupling ARC and DS effects

In the last section, the short-circuit current density for a silicon solar cell with and without a DS layer was calculated. An overall degradation in J_{sc} was observed due to the DS layer. However both ARC and DS effects are observed as a result of adding a DS layer to the solar cell and the two effects are mingled together in the short-wavelength range. However, in the longer wavelength where there is no absorption in the DS layer, or very little, the ARC effect is dominant. In most studies the two effects are not decoupled and only the total enhancement or degradation is reported. Therefore, it is crucial to decouple the two effects as the total enhancement can be due to mainly ARC effects, especially if the reference cell has no or a poor ARC layer.

The first step is to calculate the EQE of the solar cell due to ARC effect only from the DS layer (assuming no re-emission) from equation (5.23). Figure 6.13 shows the measured EQE_{tot} and the calculated EQE_{ARC}. When comparing EQE_{tot} and EQE_{ARC} they agree very well down to 400 nm beyond which the EQE_{tot} is slightly higher. The small difference between the two curves below 400 nm is due to the DS effects, as deduced from equation (5.22).

The short-circuit current density components due to each effect are calculated as follows:

$$\Delta J_{\mathrm{sc,ARC}} = q\int \phi(\lambda)\cdot\left(EQE_{\mathrm{ARC}}(\lambda) - EQE_{\mathrm{ref}}(\lambda)\right)d\lambda \tag{6.2}$$

and

$$\Delta J_{\mathrm{sc,DS}} = J_{\mathrm{sc,tot}} - J_{\mathrm{sc,ref}} - \Delta J_{\mathrm{sc,ARC}} \tag{6.3}$$

where q is the electronic charge, ϕ is the photon flux density, and $J_{\mathrm{sc,tot}}$, and $J_{\mathrm{sc,ref}}$, are the short-circuit current densities of the reference solar cell and the solar cell with DS layer mounted on top surface, respectively, which were calculated in the previous section. The calculated total degradation due to ARC effects ($\Delta J_{sc,ARC}$) is -0.61 mA/cm², while a small enhancement due to DS effect ($\Delta J_{sc,DS}$) is observed to be to 0.17 mA/cm².

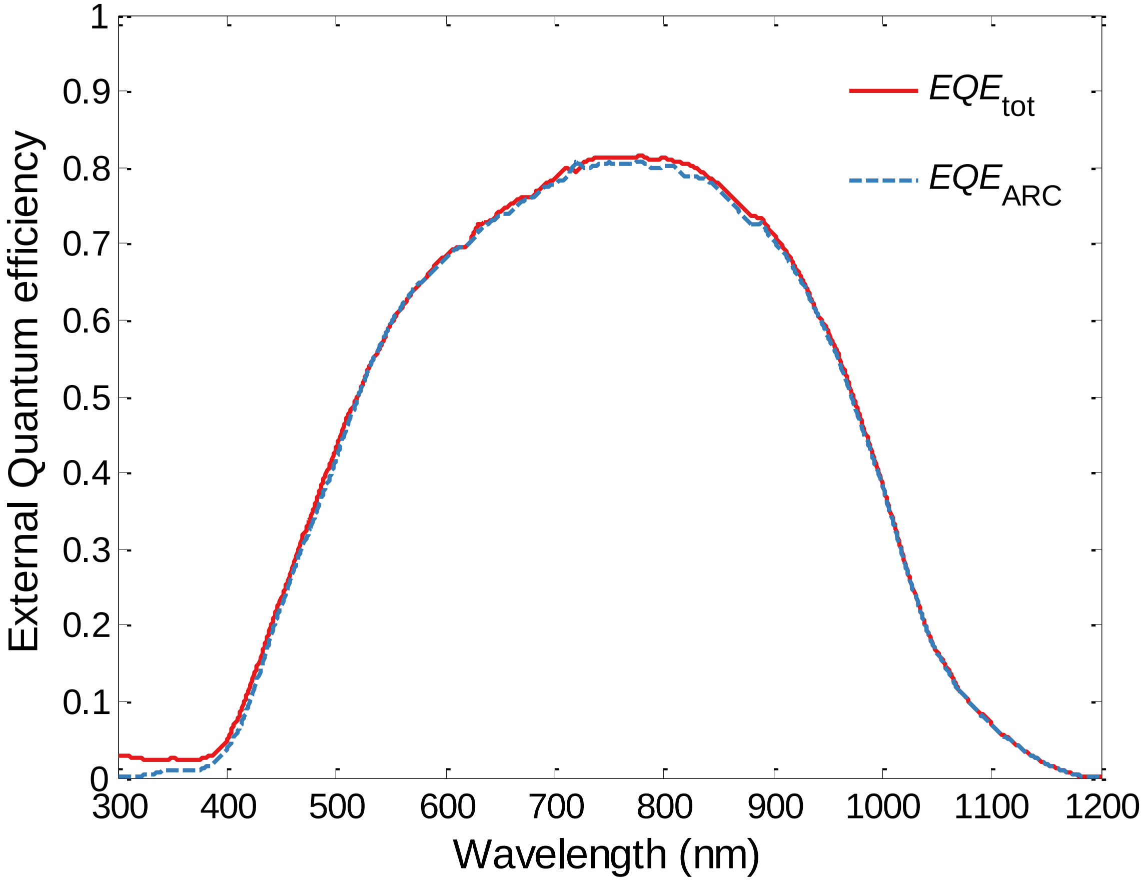

Figure 6.13. Measured EQE of the solar cell with DS layer and calculated EQE including ARC effects from equation (5.23).

The total enhancement as well as the enhancement due to each effect can be computed as a percentage as follows:

$$\eta_{tot} = \frac{J_{sc,tot} - J_{sc,ref}}{J_{sc,ref}} \tag{6.4}$$

$$\eta_{ARC} = \frac{\Delta J_{sc,ARC}}{J_{sc,ref}} \tag{6.5}$$

$$\eta_{DS} = \frac{\Delta J_{sc,DS}}{J_{sc,ref}} \tag{6.6}$$

and the results are summarized in Table 6.3.

Table 6.3. Decoupling the ARC and DS effects with illustrating the short-circuit current density contributions from each effect.

$J_{sc,ref}$	25.14 ± 0.50 mA/cm²
$J_{sc,tot}$	24.70 ± 0.49 mA/cm²
$\Delta J_{sc,ARC}$	-0.61 ± 0.12 mA/cm²
$\Delta J_{sc,DS}$	0.17 mA/cm²
η_{tot}	-1.75%
η_{ARC}	-2.43%
η_{DS}	0.68%

The equations above are used to decouple the ARC and DS effects using combined measured data and optical modelling. The parameters that need to be measured are the EQE and reflectance of both the reference cell and the cell with the DS layer. In addition the parasitic absorption must be calculated using TMM. This method is *only* valid if the reference cell has the same cell design as the cell under test, specifically the electrical properties. It does not matter if the reference cell has an ARC layer or not as this is considered in the IQE of the reference cell. A flowchart of the required steps to decouple the ARC and DS effects are summarized in Figure 6.14.

The conversion efficiency of the DS layer can be estimated from the measured EQE of the solar cell with DS layer. The Si-nC re-emits a fraction of the absorbed photons at longer wavelengths according to the photoluminescence quantum yield of the Si-nC. Most of the re-emitted photons reach the underlying solar cell while a small fraction are lost through the front surface, side or reflected from the DS/solar cell interface. All these losses contribute to the DS efficiency. Thus the DS efficiency, η_{DS}, describes the fraction of re-emitted photons that are transmitted to the underlying solar cell. Investigating equation (5.24), the EQE describing the DS effect can be expressed as:

$$\Delta EQE_{\mathrm{DS}} = A(\lambda)\ \cdot \eta_{\mathrm{DS}}(\lambda) \int PL(\lambda') \cdot IQE_{\mathrm{ref}}(\lambda') d\lambda' \qquad (6.7)$$

where $A(\lambda)$ is the absorption in the DS layer, η_{DS} is the DS efficiency, $PL(\lambda')$ is the experimental photoluminescence of DS layer, and IQE_{ref} is the IQE of the reference cell.

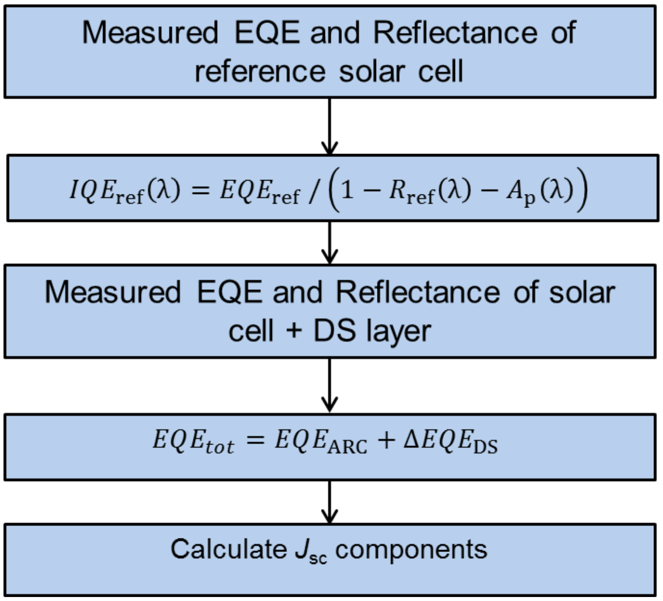

Figure 6.14. A flowchart of the decoupling effects procedure.

Substituting equation (6.6) in equation (5.22) and solving for the DS efficiency we arrive at:

$$\eta_{DS}(\lambda) = \frac{EQE_{\mathrm{tot}} - EQE_{\mathrm{ARC}}}{A(\lambda) \int PL(\lambda') \cdot IQE_{\mathrm{ref}}(\lambda') d\lambda'} \qquad (6.8)$$

The Si-nC PL is approximated by a Gaussian distribution with center wavelength of 842 nm and is shown in Figure 6.15 along with the measured PL. The measured PL was excited using a laser beam with centered at 325 nm. Therefore using equation (6.8) the DS efficiency at 325 nm is estimated to be 3%.

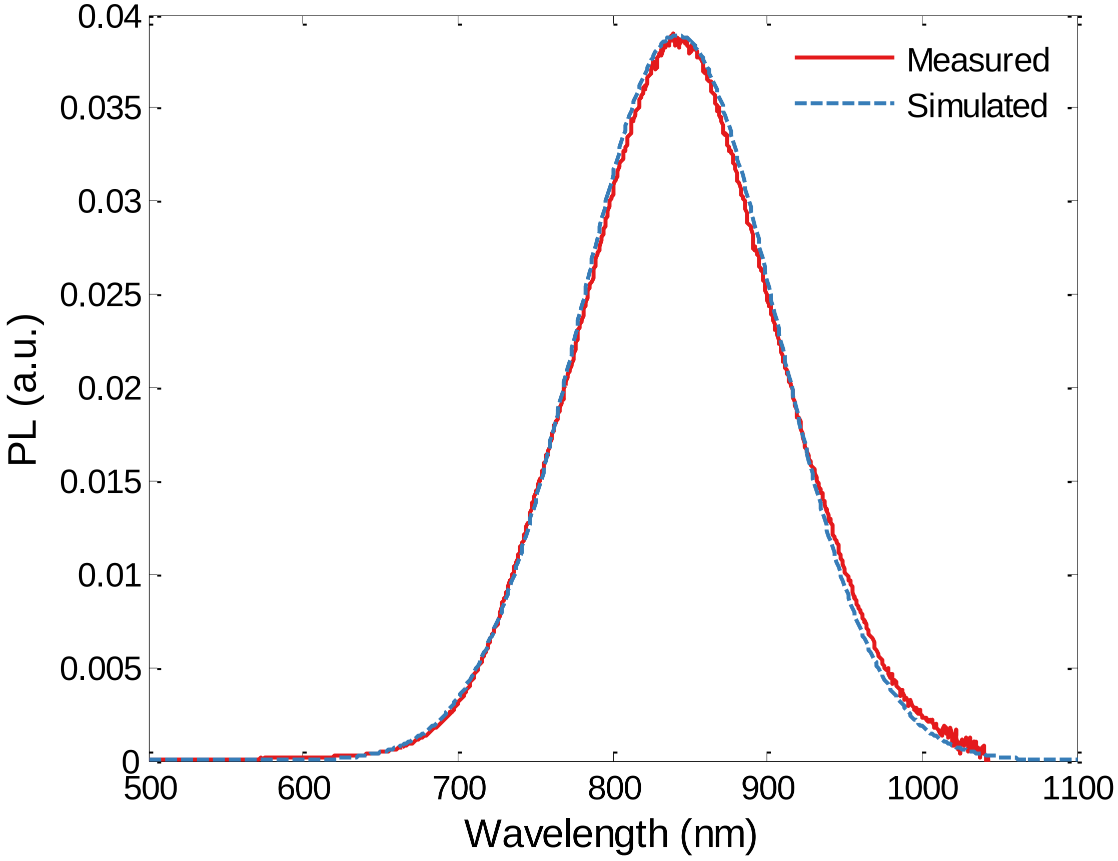

Figure 6.15. Measured (solid red) photoluminescence of the Si-nC. A Gaussian distribution (dotted line) is plotted with center wavelength of 842 nm.

6.2.4. Improvements to Decoupling ARC and DS effects

In the previous two sections the decoupling of the ARC and DS effects was discussed and results were presented. The experiment can be further improved by making use of the integrating sphere and measure the diffuse reflectance of the solar cell coupled to DS layer. Diffuse reflectance is important in DC/DS applications for the following reasons: 1) the emission from Si-nC is isotropic and therefore can be only collected using an integrating sphere, 2) the front surface is not uniform and as a result there are some scattered photons, 3) in experiments where the refractive index matching liquid is used, it adds a non-uniform thin layer at the Si-nC/silicon interface, and thus it causes some scattering.

Using an integrating sphere adds to the accuracy of the experiment. However the detected diffuse reflectance is due to scattered photons from the Si-nC/silicon interface, or from the isotropic emission of the Si-nC, or a combination of both. Since the re-emitted photons have wavelengths different than the incident photon wavelength, the measured diffuse reflectance must be carefully analyzed. Failure to carefully analyze the data can lead to significant errors.

In order to distinguish between diffusely reflected photons with the same wavelength as the incident photons (~350 – 500 nm), and the re-emitted photons which are centered at 840 nm, a long wavelength pass (LWP) filter can be installed before Ch4 detector to block all photons with wavelengths longer than 500 nm. Therefore the measured photon flux represent only the diffuse reflectance. To detect the re-emitted photons from the DS layer, a short wavelength pass (SWP) filter should be installed before the Ch4 detector to block all photons with wavelength below 500 nm. The detected photon flux can then be multiplied by the calibration file assuming emission at 840 nm. Finally the IQE can be determined as follows:

$$IQE(\lambda) = \frac{EQE(\lambda)}{1 - R_s(\lambda) - R_d(\lambda) - A_{\mathrm{p}}(\lambda) - E_d(\lambda)} \tag{6.9}$$

where R_{s} is the measured specular reflectance, R_{d} is the measured diffuse reflectance (with LWP filter installed), A_{p} is the modelled parasitic absorption, and E_{d} is the measured diffuse reflectance of the re-emitted photons from the DS layer (with SWP filter installed).

Chapter 7: Conclusions

Down-conversion (DC) process is an optical process where two or more photons are converted to longer-wavelengths. Down-shifting (DS) is a similar process but only one photon is shifted to longer wavelengths where the solar cell absorbs efficiently. Candidate materials for DC and DS layers were categorized to three groups: Rare-earth (RE) ions, quantum dots (QD) and organic dye. Yb^{3+} ion is one of the potential candidates for DC layers for photovoltaic applications since it exhibits an emission line around 980 nm, which is below the bandgap for silicon and CIGS solar cells. However, to date there are still no ground breaking results due to the weak absorption of the RE ions. QDs have the advantage of tuning the emission profile by changing the size of the QD, but they suffer from re-absorption due to the overlap between the emission and absorption profiles. Organic dyes are becoming more popular in the literature as DS layers for photovoltaic applications due to their almost unity photoluminescence quantum yield (PLQY), low cost, and flexibility in changing the absorption and emission profiles by mixing dyes. However, just like organic solar cells, the photostability of such dyes is still a challenge. Unless a breakthrough occurs in RE and QDs as DC and DS layers, organic dyes seem to be the only successful candidate.

Models of monocrystalline silicon and polycrystalline $CuIn_xGa_{1-x}Se$ (CIGS) solar cells were developed in a semiconductor device simulator. The models were based on extensive literature review to find the most accurate material properties such as carrier mobilities, recombination life times, optical properties and bandgap structure. Simulated results for monocrystalline silicon solar cells show efficiency of 17.7% with short-circuit current density (J_{sc}) of 36 mA/cm^2 and open-circuit voltage (V_{oc}) of 0.64 V. These results are comparable to the average commercial cells which vary from 15% up to 21%. On the other hand the simulated CIGS solar cell shows efficiency of 16% with J_{sc} of 31.9 mA/cm^2 and V_{oc} of 0.67 V. The J_{sc} can be improved by adding an anti-reflection coating (ARC) layer while the V_{oc} is usually enhanced by grading the absorber layer. In other words the molar fraction of the CIGS material is varied gradually to better collect the photons while achieving higher V_{oc}. Nevertheless, the objective in this thesis was not to optimize the design but rather to develop a model that is comparable to commercial grade solar cells. Both models are used to explore the effect of DS layers when mounted on top surface of these cells.

DC and DS layers can be modeled by tailoring the incident solar spectrum to emulate their effects. A model is developed to compute the spectral modifications in the incident spectrum caused by the DC or DS layers using a custom built code. The modified spectrum is then used as an input to a device simulator to evaluate the solar cell performance. First, the effect of ideal DC layers mounted on ideal silicon solar cells (ie. IQE = 1) is investigated. An upper limit of J_{sc} of 57 mA/cm^2 is achieved for a DC layer of bandgap 2.2 eV. This is a 24% relative increase when compared to J_{sc} of 46 mA/cm^2 of an ideal cell with no DC layer. Secondly, ideal DC and DS layers are used to evaluate the performance of a silicon solar cell modeled in a device simulator. The PLQY as a function of DC and DS bandgaps is presented. For a perfect DS layer (PLQY = 100%), a 15% relative increase is achieved with an optimum bandgap of 1.8 eV. The same relative increase is achieved with a perfect DC layer (PLQY = 200%) with optimum bandgap of 2.6 eV. The model is then calibrated using measured optical properties and photoluminescence profile of fabricated silicon nanocrystals (Si-nC) embedded in a SiO_2 matrix. The effect of Si-nC based DS layer is investigated with silicon and CIGS solar cells modeled in a device simulator. The DS model is further enhanced to include layer thicknesses optimization to maximize J_{sc}. In addition, the DS effect due to shifting of photons is decoupled from the ARC effect which is due to the change in surface reflections. The decoupling is realized by assuming a DS layer with the same layer thickness but with no re-emission (PLQY = 0) i.e. a passive layer. Therefore the ARC effect can be obtained by comparing the passive cell with the reference cell, while the DS effect is computed by comparing the active cell with the passive one. It is very important to decouple the two effects as in some cases a relatively large enhancement can be achieved only because the reference cell has no ARC layer. Therefore the enhancement can be mainly due to ARC effects with very little or no DS effects. For the simulated silicon solar cell, a maximum increase in J_{sc} of 8.4% was achieved for a perfect DS layer

(PLQY = 100%) as compared to a reference cell, where 7.2% was due to ARC effect and only 1.2% was due to DS effect. The layer thickness did not vary significantly during the optimization process which indicates that the ARC effect was dominant. On the other hand, there an increase in J_{sc} of 19.5% was achieved for the CIGS solar cell when coupled to a perfect DS layer. The DS effect was dominant with 18%, while the ARC effect contributes only 1.5% to the total J_{sc} enhancement. Therefore for these specific silicon and CIGS solar cell designs, the Si-nC embedded in a SiO_2 matrix based DS layer is more effective with the CIGS solar cell given PLQY is > 60%, otherwise an enhancement of 13% in J_{sc} is observed due to ARC effect.

To fully explore the effect of Si-nC based DS layers, the Si-nC layer is mounted on top of a monocrystalline silicon solar cell fabricated at Carleton University. The solar cell is characterized at SUNLAB and showed an efficiency of 11% with J_{sc} and V_{oc} equal to 26 mA/cm^2 and 0.55 V, respectively. The ARC layer has non-zero extinction coefficient up to 400 nm and this caused a poor UV spectral response. The Si-nC on top of the silicon solar cell is characterized as a system using the IQE-200 setup at SUNLAB, University of Ottawa. The poor performance of the Si-nC layer caused an overall degradation to the solar cell performance. However, the external quantum efficiency (EQE) of the system and the solar cell are analyzed and expressions are derived to decouple the ARC effects from the DS effects. To the author knowledge this has not been done experimentally so far.

References

[1] P. Kasibhatla and W. Chameides, “G8 Leadership is Critical to Curbing Energy-Related CO2 Emissions,” 2007. [Online]. Available: https://nicholasinstitute.duke.edu/sites/default/files/publications/g8-leadership-is-critical-to-curbing-energy-related-co2-emissions-paper.pdf. [Accessed: 18-Nov-2015].

[2] J. G. J. Olivier, Greet Jansseens- Maenhout, M. Muntean, and Jeroen A.H.W Peters, “Trends In Global CO_2 Emissions,” 2013.

[3] “©Fraunhofer ISE: Photovoltaics report,” 2016.

[4] W. Shockley and H. J. Queisser, “Detailed Balance Limit of Efficiency of p-n Junction Solar Cells,” *J. Appl. Phys.*, vol. 32, no. 3, pp. 510 – 519, 1961.

[5] M. A. Green, K. Emery, Y. Hishikawa, W. Warta, and E. D. Dunlop, “Solar cell efficiency tables (version 48),” *Prog. Photovoltaics Res. Appl.*, vol. 24, no. 7, pp. 905–913, Jul. 2016.

[6] A. De Vos, “Detailed balance limit of the efficiency of tandem solar cells,” *Journal of Physics D: Applied Physics*, vol. 13, no. 5. pp. 839–846, 2000.

[7] A. Luque and A. Marti, “Increasing the efficiency of ideal solar cells by photon induced transitions at intermediate levels,” *Phys. Rev. Lett.*, vol. 78, no. 26, pp. 5014–5017, 1997.

[8] S. Kolodinski, J. H. Werner, T. Wittchen, and H. J. Queisser, “Quantum efficiencies exceeding unity due to impact ionization in silicon solar cells,” *Appl. Phys. Lett.*, vol. 63, no. 1993, pp. 2405–2407, 1993.

[9] P. Würfel, “Solar energy conversion with hot electrons from impact ionisation,” *Sol. Energy Mater. Sol. Cells*, vol. 46, no. 1, pp. 43–52, 1997.

[10] T. Trupke, M. Green, and P. Würfel, “Improving solar cell efficiencies by up-conversion of sub-band-gap light,” *J. Appl. Phys.*, vol. 92, no. 7, p. 4117, 2002.

[11] T. Trupke, M. Green, and P. Würfel, “Improving solar cell efficiencies by down-conversion of high-energy photons,” *J. Appl. Phys.*, vol. 92, no. 3, p. 1668, 2002.

[12] A. Shalav, B. Richards, and M. Green, “Luminescent layers for enhanced silicon solar cell performance: Up-conversion,” *Sol. Energy Mater. Sol. Cells*, vol. 91, no. 9, pp. 829–842, May 2007.

[13] D. Dexter, “A theory of sensitized luminescence in solids,” *J. Chem. Phys.*, vol. 21, no. 5, 1953.

[14] H. Hovel, R. Hodgson, and J. Woodall, “The effect of fluorescent wavelength shifting on solar cell spectral response,” *Sol. Energy Mater.*, vol. 2, pp. 19–29, 1979.

[15] S. Fischer, A. Ivaturi, B. Frohlich, M. Rudiger, A. Richter, K. W. Kramer, B. S. Richards, and J. C. Goldschmidt, “Upconverter silicon solar cell devices for efficient utilization of sub-band-gap photons under concentrated solar radiation,” *IEEE J. Photovoltaics*, vol. 4, no. 1, pp. 183–189, 2014.

[16] C. M. Johnson, P. J. Reece, and G. J. Conibeer, “Up-conversion luminescence enhancement in erbium-doped porous silicon photonic crystals for photovoltaics,” in *Proceedings of SPIE*, 2011, vol. 7933, p. 79330I.

[17] J. de Wild, J. K. Rath, A. Meijerink, W. G. J. H. M. van Sark, and R. E. I. Schropp, “Enhanced near-infrared response of a-Si:H solar cells with β-NaYF4:Yb^{3+} (18%), Er^{3+} (2%) upconversion phosphors,” *Sol. Energy Mater. Sol. Cells*, vol. 94, no. 12, pp. 2395–2398, Dec. 2010.

[18] S. M. Sze and K. K. Ng, *Physics of Semiconductor Devices, 3rd Edition*. 2007.

[19] J. Nelson, *The Physics of solar cells*. 2003.

[20] A. Luque and S. Hegedus, *Handbook of Photovoltaic Science and Engineering*. Chichester, UK: John Wiley & Sons, Ltd, 2010.

[21] M. A. Green and M. J. Keevers, “Optical properties of intrinsic silicon at 300 K,” *Prog. Photovoltaics Res. Appl.*, vol. 3, no. 3, pp. 189–192, 1995.

[22] S. S. Ou, O. M. Stafsudd, and B. M. Basol, “Optical properties of electrochemically deposited CdTe films,” *J. Appl. Phys.*, vol. 55, no. 10, p. 3769, 1984.

[23] R. E. Treharne, A Seymour-Pierce, K. Durose, K. Hutchings, S. Roncallo, and D. Lane, “Optical Design and Fabrication of Fully Sputtered CdTe/CdS Solar Cells,” *J. Phys. Conf. Ser.*, vol. 286, p. 012038, 2011.

[24] M. I. Alonso, M. Garriga, C. A. Durante Rincón, E. Hernández, and M. León, “Optical functions of chalcopyrite CuGaxIn1-xSe2 alloys,” *Appl. Phys. A Mater. Sci. Process.*, vol. 74, no. 5, pp. 659–664, 2002.

[25] M. Planck, “On the Theory of the Energy Distribution Law of the Normal Spectrum,” *Verhandl. Dtsch. Phys. Ges.*, vol. 2, no. 1900, p. 237, 1900.

[26] “Reference Solar Spectral Irradiance: Air Mass 1.5.” [Online]. Available: http://rredc.nrel.gov/solar/spectra/am1.5/. [Accessed: 08-Dec-2015].

[27] R. Wegh, H. Donker, K. Oskam, and A. Meijerink, “Visible quantum cutting in $LiGdF_4$: Eu^{3+} through downconversion,” *Science (80-.).*, vol. 283, no. 5402, pp. 663–666, Jan. 1999.

[28] E. Klampaftis, D. Ross, K. R. McIntosh, and B. S. Richards, “Enhancing the performance of solar cells via luminescent down-shifting of the incident spectrum: A review,” *Sol. Energy Mater. Sol. Cells*, vol. 93, no. 8, pp. 1182–1194, Aug. 2009.

[29] V. Badescu, A. De Vos, A. M. Badescu, and A. Szymanska, “Improved model for solar cells with down-conversion and down-shifting of high-energy photons,” *J. Phys. D. Appl. Phys.*, vol. 40, no. 2, pp. 341–352, Jan. 2007.

[30] V. Badescu and A. De Vos, “Influence of some design parameters on the efficiency of solar cells with down-conversion and down shifting of high-energy photons,” *J. Appl. Phys.*, vol. 102, no. 7, pp. 0–7, 2007.

[31] P. A. Basore and D. A. Clugston, “PC1D version 4 for Windows: from analysis to design,” in *Proceedings of 25th IEEE Photovoltaic Specialists Conference - 1996*, 1996, pp. 377–381.

[32] Synopsys Inc., “Sentaurus Device User Guide, Version G-2012.06,” 2012.

[33] “Silvaco.” [Online]. Available: http://www.silvaco.com/products/tcad/device_simulation/device_simulation.html. [Accessed: 05-Jan-2016].

[34] “Crosslight.” [Online]. Available: http://crosslight.com/products/apsys/. [Accessed: 05-Jan-2016].

[35] Y. Jestin, G. Pucker, M. Ghulinyan, L. Ferrario, P. Bellutti, A. Picciotto, A. Collini, A. Marconi, A. Anopchenko, Z. Yuan, and L. Pavesi, “Silicon solar cells with nano-

crystalline silicon down shifter: experiment and modeling," *Proc. SPIE 7772, Next Gener. Photonic Cell Technol. Sol. Energy Convers.*, vol. 77720B, 2010.

[36] F. Sgrignuoli, G. Paternoster, A. Marconi, P. Ingenhoven, A. Anopchenko, G. Pucker, and L. Pavesi, "Modeling of silicon nanocrystals based down-shifter for enhanced silicon solar cell performance," *J. Appl. Phys.*, vol. 111, no. 3, p. 034303, 2012.

[37] W. G. J. H. M. van Sark, A. Meijerink, R. E. I. Schropp, J. A. M. van Roosmalen, and E. H. Lysen, "Enhancing solar cell efficiency by using spectral converters," *Sol. Energy Mater. Sol. Cells*, vol. 87, no. 1–4, pp. 395–409, May 2005.

[38] W. G. J. H. M. van Sark, "Enhancement of solar cell performance by employing planar spectral converters," *Appl. Phys. Lett.*, vol. 87, no. 15, p. 151117, 2005.

[39] R. E. Bird and C. Riordan, "Simple Solar Spectral Model for Direct and Diffuse Irradiance on Horizontal and Tilted Planes at the Earth's Surface for Cloudless Atmospheres," *J. Clim. Appl. Meteorol.*, vol. 25, no. 1, pp. 87–97, 1986.

[40] B. Houshyani Hassanzadeh, A. C. de Keizer, N. H. Reich, and W. G. J. H. M. van Sark, "The Effect of a Varying Solar Spectrum on the Energy Performance of Solar Cells," *22nd Eur. Photovolt. Sol. Energy Conf.*, no. September, pp. 2652 – 2658, 2007.

[41] W. G. J. H. M. van Sark, "Calculation of the Performance of Solar Cells With Spectral Down Shifters Using Realistic Outdoor Solar Spectra," *22nd Eur. Photovolt. Sol. Energy Conf.*, no. September, pp. 566 – 570, 2007.

[42] T. Ishii, K. Otani, A. Itagaki, and K. Utsunomiya, "A simplified methodology for estimating solar spectral influence on photovoltaic energy yield using average photon energy," *Energy Sci. Eng.*, vol. 1, no. 1, pp. 18–26, 2013.

[43] K. R. Mcintosh and B. S. Richards, "Increased mc-Si module efficiency using fluorescent organic dyes: A ray-tracing study," *Conf. Rec. 2006 IEEE 4th World Conf. Photovolt. Energy Conversion, WCPEC-4*, vol. 2, pp. 2108–2111, 2007.

[44] B. S. Richards and K. R. McIntosh, "Overcoming the poor short wavelength spectral response of CdS/CdTe photovoltaic modules via luminescence down-shifting: Ray-tracing simulations," *Prog. Photovoltaics Res. Appl.*, vol. 15, no. 1, pp. 27–34, 2007.

[45] C. Del Cañizo, I. Tobías, and J. Pérez-Bedmar, "Implementation of a Monte Carlo method to model photon conversion for solar cells," *Thin Solid Films*, 2008.

[46] J.-C. G. Bünzli and C. Piguet, "Taking advantage of luminescent lanthanide ions," *Chem. Soc. Rev.*, vol. 34, no. 12, p. 1048, 2005.

[47] P. Urquhart, "Review of rare earth doped fibre lasers and amplifiers," *IEE Proc. J Optoelectron.*, vol. 135, p. 385, 1988.

[48] A. J. Kenyon, "Recent developments in rare-earth doped materials for optoelectronics," *Prog. Quantum Electron.*, vol. 26, no. 4–5, pp. 225–284, 2002.

[49] G. Dieke, *Spectra and Energy Levels of Rare Earth Ions in Crystals*. New York: Wiley Interscience, 1968.

[50] H. T. Wegh, A. Meijerink, and R. Lamminma, "Extending Dieke ' s diagram," vol. 89, pp. 1002–1004, 2000.

[51] J. L. Sommerdijk, A. Bril, and A. W. de Jager, "Two photon luminescence with ultraviolet excitation of trivalent praseodymium," *J. Lumin.*, vol. 8, no. 4, pp. 341–343, 1974.

[52] W. W. Piper, J. A. DeLuca, and F. S. Ham, "Cascade fluorescent decay in Pr3+-doped fluorides: Achievement of a quantum yield greater than unity for emission of visible light," *J. Lumin.*, vol. 8, no. 4, pp. 344–348, Feb. 1974.

[53] D. L. Dexter, "Possibility of Luminescent Quantum Yields Greater than Unity," *Phys. Rev.*, vol. 108, no. 1953, pp. 630–633, 1957.

[54] P. Vergeer, T. Vlugt, M. Kox, M. den Hertog, J. van der Eerden, and A. Meijerink, "Quantum cutting by cooperative energy transfer in $Yb_xY_{1-x}PO_4$:Tb^{3+}," *Phys. Rev. B*, vol. 71, no. 1, p. 014119, Jan. 2005.

[55] B. S. Richards, "Luminescent layers for enhanced silicon solar cell performance: Down-conversion," *Sol. Energy Mater. Sol. Cells*, vol. 90, no. 9, pp. 1189–1207, May 2006.

[56] C. Strümpel, M. McCann, G. Beaucarne, V. Arkhipov, A. Slaoui, V. Švrček, C. del Cañizo, and I. Tobias, "Modifying the solar spectrum to enhance silicon solar cell efficiency—An overview of available materials," *Sol. Energy Mater. Sol. Cells*, vol. 91, no. 4, pp. 238–249, Feb. 2007.

[57] Q. Y. Zhang, C. H. Yang, and Y. X. Pan, "Cooperative quantum cutting in one-dimensional $(Yb_xGd_{1-x})Al_3(BO_3)_4$: Tb^{3+} nanorods," *Appl. Phys. Lett.*, vol. 90, no. 2, pp. 4–7, 2007.

[58] D. Chen, Y. Wang, Y. Yu, P. Huang, and F. Weng, "Quantum cutting downconversion by cooperative energy transfer from Ce^{3+} to Yb^{3+} in borate glasses," *J. Appl. Phys.*, vol. 104, no. 11, p. 116105, 2008.

[59] J. Ueda and S. Tanabe, "Visible to near infrared conversion in Ce^{3+}–Yb^{3+} Co-doped YAG ceramics," *J. Appl. Phys.*, vol. 106, no. 4, p. 043101, 2009.

[60] S. Ye, J. J. Zhou, S. T. Wang, R. X. Hu, D. P. Wang, and J. R. Qiu, "Broadband downshifting luminescence in Cr^{3+}-Yb^{3+} codoped garnet for efficient photovoltaic generation," *Opt. Express*, vol. 21, no. 4, pp. 4167–4173, 2013.

[61] X. Y. Huang, D. C. Yu, and Q. Y. Zhang, "Enhanced near-infrared quantum cutting in $GdBO_3$: Tb^{3+}, Yb^{3+} phosphors by Ce^{3+} codoping," *J. Appl. Phys.*, vol. 106, no. 11, pp. 2–8, 2009.

[62] J. Sun, G. Sun, Y. Sun, and L. Han, "Luminescence properties and energy transfer investigations of tri-doped Sr_3AlO_4F:Ce^{3+},Tb^{3+},Yb^{3+} phosphors," *Opt. Mater. (Amst).*, vol. 36, no. 7, pp. 1097–1100, May 2014.

[63] J. Zhao, C. Guo, and T. Li, "Enhanced near-infrared emission by co-doping Ce^{3+} in Ba_2 $Y(BO_3)_2$ Cl:Tb^{3+} , Yb^{3+} phosphor," *RSC Adv.*, vol. 5, no. 36, pp. 28299–28304, 2015.

[64] J. Zhou, Y. Teng, S. Ye, G. Lin, and J. Qiu, "A discussion on spectral modification from visible to near-infrared based on energy transfer for silicon solar cells," *Opt. Mater. (Amst).*, vol. 34, no. 5, pp. 901–905, Mar. 2012.

[65] A. Le Donne, M. Dilda, M. Crippa, M. Acciarri, and S. Binetti, "Rare earth organic complexes as down-shifters to improve Si-based solar cell efficiency," *Opt. Mater. (Amst).*, vol. 33, no. 7, pp. 1012–1014, May 2011.

[66] D. Chen, Y. Wang, Y. Yu, P. Huang, and F. Weng, "Near-infrared quantum cutting in transparent nanostructured glass ceramics," *Opt. Lett.*, vol. 33, no. 16, p. 1884, Aug. 2008.

[67] B. M. van der Ende, L. Aarts, and A. Meijerink, "Near-Infrared Quantum Cutting for Photovoltaics," *Adv. Mater.*, vol. 21, no. 30, pp. 3073–3077, Aug. 2009.

[68] L. Xie, Y. Wang, and H. Zhang, "Near-infrared quantum cutting in YPO_4: Yb^{3+}, Tm^{3+} via cooperative energy transfer," *Appl. Phys. Lett.*, vol. 94, no. 6, pp. 10–13, 2009.

[69] J. Zhou, Y. Zhuang, S. Ye, Y. Teng, G. Lin, B. Zhu, J. Xie, and J. Qiu, "Broadband downconversion based infrared quantum cutting by cooperative energy transfer from Eu^{2+} to Yb^{3+} in glasses," *Appl. Phys. Lett.*, vol. 95, no. 14, pp. 3–6, 2009.

[70] J. M. Meijer, L. Aarts, B. M. van der Ende, T. J. H. Vlugt, and A. Meijerink, "Downconversion for solar cells in YF_3: Nd^{3+}, Yb^{3+}," *Phys. Rev. B*, vol. 81, no. 3, p. 035107, Jan. 2010.

[71] J. J. Eilers, D. Biner, J. T. van Wijngaarden, K. Krämer, H.-U. Güdel, and A. Meijerink, "Efficient visible to infrared quantum cutting through downconversion with the Er^{3+}–Yb^{3+} couple in $Cs_3Y_2Br_9$," *Appl. Phys. Lett.*, vol. 96, no. 15, p. 151106, 2010.

[72] V. D. Rodríguez, V. K. Tikhomirov, J. Méndez-Ramos, A. C. Yanes, and V. V. Moshchalkov, "Towards broad range and highly efficient down-conversion of solar spectrum by Er^{3+}–Yb^{3+} co-doped nano-structured glass-ceramics," *Sol. Energy Mater. Sol. Cells*, vol. 94, no. 10, pp. 1612–1617, Oct. 2010.

[73] D. C. Yu, S. Ye, X. Y. Huang, and Q. Y. Zhang, "Enhanced three-photon near-infrared quantum splitting in β-$NaYF_4$:Ho^{3+} by codoping Yb^{3+}," *AIP Adv.*, vol. 2, no. 2, p. 022124, 2012.

[74] T. Jin, "Photovoltaic Cell Characteristics of Hybrid Silicon Devices with Lanthanide Complex Phosphor-Coating Film," *J. Electrochem. Soc.*, vol. 144, no. 11, p. 4054, 1997.

[75] K. MacHida, H. Li, D. Ueda, S. Inoue, and G. Adachi, "Preparation and application of lanthanide complex incorporated ormosil composite phosphor films," *J. Lumin.*, vol. 87, pp. 1257–1259, 2000.

[76] T. Fukuda, S. Kato, E. Kin, K. Okaniwa, H. Morikawa, Z. Honda, and N. Kamata, "Wavelength conversion film with glass coated Eu chelate for enhanced silicon-photovoltaic cell performance," *Opt. Mater. (Amst).*, vol. 32, no. 1, pp. 22–25, 2009.

[77] A. Le Donne, M. Acciarri, D. Narducci, S. Marchionna, and S. Binetti, "Encapsulating Eu^{3+} complex doped layers to improve Si-based solar cell efficiency," *Prog. Photovoltaics Res. Appl.*, vol. 17, no. 8, pp. 519–525, Dec. 2009.

[78] T. Monzón-Hierro, J. Sanchiz, S. González-Pérez, B. González-Díaz, S. Holinski, D. Borchert, C. Hernández-Rodríguez, and R. Guerrero-Lemus, "A new cost-effective polymeric film containing an Eu(III) complex acting as UV protector and down-converter for Si-based solar cells and modules," *Sol. Energy Mater. Sol. Cells*, vol. 136, pp. 187–192, May 2015.

[79] Z. J. Cheng, L. K. Pan, F. F. Su, M. L. Cao, and Z. Sun, "Eu^{3+} doped silica film as luminescent down-shifting layer for crystalline Si solar cells," *Surf. Rev. Lett.*, vol. 16, no. 5, pp. 669–673, 2009.

[80] C. Yen-Chi, H. Woan-Yu, and C. Teng-Ming, "Enhancing the performance of photovoltaic cells by using down-converting $KCaGd(PO_4)_2$:Eu^{3+} phosphors," *J. Rare Earths*, vol. 29, no. 9, pp. 907–910, 2011.

[81] C. Cheng and J. Yang, "Hydrothermal Synthesis of Eu^{3+} -Doped $Y(OH)_3$ Nanotubes as Downconversion Materials for Efficiency Enhancement of Screen-Printed Monocrystalline Silicon Solar Cells," *IEEE Electron. Device Lett.*, vol. 33, no. 5, pp. 697–699, 2012.

[82] B.-C. Hong and K. Kawano, "PL and PLE studies of $KMgF_3$:Sm crystal and the effect of its wavelength conversion on CdS/CdTe solar cell," *Sol. Energy Mater. Sol. Cells*, vol. 80, no. 4, pp. 417–432, Dec. 2003.

[83] J. Liu, Q. Yao, and Y. Li, "Effects of downconversion luminescent film in dye-sensitized solar cells," *Appl. Phys. Lett.*, vol. 88, no. 17, pp. 17–20, 2006.

[84] H. Dong-Bing, Y. Chun-Lei, C. Ji-Meng, L. Shun-Guang, and H. Li-Li, "A novel Ce^{3+}/Tb^{3+} Codoped Phosphate Glass as Down-Shifting Materials for Enhancing Efficiency of Solar Cells," *Chinese Physics Letters*, vol. 27, no. 11. p. 114208, 2010.

[85] G. Shao, C. Lou, and D. Xiao, "Enhancing the efficiency of solar cells by down shifting YAG: Ce^{3+} phosphors," *J. Lumin.*, vol. 157, pp. 344–348, 2015.

[86] K. L. Frindell, M. H. Bartl, M. R. Robinson, G. C. Bazan, A. Popitsch, and G. D. Stucky, "Visible and near-IR luminescence via energy transfer in rare earth doped mesoporous titania thin films with nanocrystalline walls," *J. Solid State Chem.*, vol. 172, no. 1, pp. 81–88, Apr. 2003.

[87] X. Sheng, C. J. Corcoran, J. He, L. Shen, S. Kim, J. Park, R. G. Nuzzo, and J. A. Rogers, "Enhanced ultraviolet responses in thin-film InGaP solar cells by down-shifting," *Phys. Chem. Chem. Phys.*, vol. 15, no. 47, pp. 20434–20437, 2013.

[88] K. Barnham, J. L. Marques, J. Hassard, and P. O'Brien, "Quantum-dot concentrator and thermodynamic model for the global redshift," *Appl. Phys. Lett.*, vol. 76, no. May 2015, p. 1197, 2000.

[89] A. J. Chatten, K. W. J. Barnham, U. Blieske, N. J. Ekins-Daukes, M. A. Malik, J. L. Marques, and M. L. Williams, "Characterising quantum dot concentrators," *Photovolt. Spec. Conf. 2000. Conf. Rec. Twenty-Eighth IEEE*, pp. 865–868, 2000.

[90] E. Mutlugun, I. M. Soganci, and H. V. Demir, "Photovoltaic nanocrystal scintillators hybridized on Si solar cells for enhanced conversion efficiency in UV.," *Opt. Express*, vol. 16, no. 6, pp. 3537–3545, 2008.

[91] H.-V. Han, C.-C. Lin, Y.-L. Tsai, H.-C. Chen, K.-J. Chen, Y.-L. Yeh, W.-Y. Lin, H.-C. Kuo, and P. Yu, "A Highly Efficient Hybrid GaAs Solar Cell Based on Colloidal-Quantum-Dot-Sensitization," *Sci. Rep.*, vol. 4, pp. 1–9, 2014.

[92] Z. Cheng, F. Su, L. Pan, M. Cao, and Z. Sun, "CdS quantum dot-embedded silica film as luminescent down-shifting layer for crystalline Si solar cells," *J. Alloys Compd.*, vol. 494, no. 1–2, pp. L7–L10, 2010.

[93] H.-C. Chen, C.-C. Lin, H.-W. Han, Y.-L. Tsai, C.-H. Chang, H.-W. Wang, M.-A. Tsai, H.-C. Kuo, and P. Yu, "Enhanced efficiency for c-Si solar cell with nanopillar array via quantum dots layers," *Opt. Express*, vol. 19, no. September, p. A1141, 2011.

[94] C.-C. Lin, H.-C. Chen, Y. L. Tsai, H.-V. Han, H.-S. Shih, Y.-A. Chang, H.-C. Kuo, and P. Yu, "Highly efficient CdS-quantum-dot-sensitized GaAs solar cells," *Opt. Express*, vol. 20, no. March, p. A319, Mar. 2012.

[95] H.-C. Chen, C.-C. Lin, H.-V. Han, K.-J. Chen, Y.-L. Tsai, Y.-A. Chang, M.-H. Shih, H.-C. Kuo, and P. Yu, "Enhancement of power conversion efficiency in GaAs solar cells with dual-layer quantum dots using flexible PDMS film," *Sol. Energy Mater. Sol. Cells*, vol. 104, pp. 92–96, 2012.

[96] V. Svrček, A. Slaoui, and J. C. Muller, "Silicon nanocrystals as light converter for solar cells," *Thin Solid Films*, vol. 451–452, pp. 384–388, Mar. 2004.

[97] C. Y. Huang, D. Y. Wang, C. H. Wang, Y. F. Y. T. Chen, Y. T. Wang, Y. T. Jiang, Y. J. Yang, C. C. Chen, and Y. F. Y. T. Chen, "Efficient light harvesting by photon downconversion and light trapping in hybrid ZnS nanoparticles/Si nanotips solar cells," *ACS Nano*, vol. 4, no. 10, pp. 5849–5854, 2010.

[98] S. M. Geyer, J. M. Scherer, N. Moloto, F. B. Jaworski, and M. G. Bawendi, “Efficient luminescent down-shifting detectors based on colloidal quantum dots for dual-band detection applications,” *ACS Nano*, vol. 5, no. 7, pp. 5566–5571, 2011.

[99] Z. Yuan, G. Pucker, A. Marconi, F. Sgrignuoli, A. Anopchenko, Y. Jestin, L. Ferrario, P. Bellutti, and L. Pavesi, “Silicon nanocrystals as a photoluminescence down shifter for solar cells,” *Sol. Energy Mater. Sol. Cells*, vol. 95, no. 4, pp. 1224–1227, Apr. 2011.

[100] W. H. Weber and J. Lambe, “Luminescent greenhouse collector for solar radiation.,” *Appl. Opt.*, vol. 15, no. 10, pp. 2299–2300, 1976.

[101] A. Goetzberger and W. Greube, “Solar energy conversion with fluorescent collectors,” *Appl. Phys. A Mater. Sci. Process.*, vol. 14, no. 2, pp. 123–139, 1977.

[102] A. A. Earp, G. B. Smith, J. Franklin, and P. Swift, “Optimisation of a three-colour luminescent solar concentrator daylighting system,” *Sol. Energy Mater. Sol. Cells*, vol. 84, no. 1–4, pp. 411–426, 2004.

[103] L. R. Wilson and B. S. Richards, “Measurement method for photoluminescent quantum yields of fluorescent organic dyes in polymethyl methacrylate for luminescent solar concentrators.,” *Appl. Opt.*, vol. 48, no. 2, pp. 212–20, 2009.

[104] “BASF.” [Online]. Available: https://www.basf.com/ca/en.html. [Accessed: 21-Dec-2015].

[105] “Keystone.” [Online]. Available: http://www.dyes.com/Default.aspx. [Accessed: 18-Dec-2015].

[106] T. Maruyama and R. Kitamura, “Transformations of the wavelength of the light incident upon CdS/CdTe solar cells,” *Sol. Energy Mater. Sol. Cells*, vol. 69, no. 1, pp. 61–68, Aug. 2001.

[107] T. Maruyama, A. Enomoto, and K. Shirasawa, “Solar cell module colored with fluorescent plate,” *Sol. Energy Mater. Sol. Cells*, vol. 64, no. 3, pp. 269–278, 2000.

[108] K. R. McIntosh, G. Lau, J. N. Cotsell, K. Hanton, D. L. Bätzner, F. Bettiol, and B. S. Richards, “Increase in external quantum efficiency of encapsulated silicon solar cells from a luminescent down-shifting layer,” *Prog. Photovoltaics Res. Appl.*, vol. 17, no. 3, pp. 191–197, May 2009.

[109] A. . Mansour, “On enhancing the efficiency of solar cells and extending their performance life,” *Polym. Test.*, vol. 22, no. 5, pp. 491–495, 2003.

[110] T. Maruyama, “Solar Cell Module Coated with Fluorescent Coloring Agent,” *J. Electrochem. Soc.*, vol. 146, no. 12, p. 4406, 1999.

[111] L. H. Slooff, R. Kinderman, A. R. Burgers, N. J. Bakker, J. A. M. van Roosmalen, A. Büchtemann, R. Danz, and M. Schleusener, “Efficiency Enhancement of Solar Cells by Application of a Polymer Coating Containing a Luminescent Dye,” *J. Sol. Energy Eng.*, vol. 129, no. 3, p. 272, 2007.

[112] B. C. Hong and K. Kawano, “Organic dye-doped thin films for wavelength conversion and their effects on the photovoltaic characteristics of CdS/CdTe solar cell,” *Japanese J. Appl. Physics, Part 1 Regul. Pap. Short Notes Rev. Pap.*, vol. 43, pp. 1421–1426, 2004.

[113] T. S. Parel, L. Danos, and T. Markvart, “Application of concentrating luminescent down-shifting structures to CdS/CdTe solar cells with poor short wavelength response,” *Sol. Energy Mater. Sol. Cells*, vol. 140, pp. 306–311, 2015.

[114] D. Ross, E. Klampaftis, J. Fritsche, M. Bauer, and B. S. Richards, “Increased short-circuit current density of production line CdTe mini-module through luminescent down-shifting,” *Sol. Energy Mater. Sol. Cells*, vol. 103, pp. 11–16, 2012.

[115] L. Danos, T. Parel, T. Markvart, V. Barrioz, W. S. M. Brooks, and S. J. C. Irvine, “Increased efficiencies on CdTe solar cells via luminescence down-shifting with excitation energy transfer between dyes,” *Sol. Energy Mater. Sol. Cells*, vol. 98, pp. 486–490, Mar. 2012.

[116] D. Alonso-Álvarez, D. Ross, and B. S. Richards, “Luminescent down-shifting for CdTe solar cells: A review of dyes and simulation of performance,” in *Conference Record of the IEEE Photovoltaic Specialists Conference*, 2012.

[117] G. C. Glaeser and U. Rau, “Improvement of photon collection in Cu(In,Ga)Se2 solar cells and modules by fluorescent frequency conversion,” *Thin Solid Films*, vol. 515, no. 15, pp. 5964–5967, May 2007.

[118] E. Klampaftis, D. Ross, S. Seyrling, A. N. Tiwari, and B. S. Richards, “Increase in short-wavelength response of encapsulated CIGS devices by doping the encapsulation layer with luminescent material,” *Sol. Energy Mater. Sol. Cells*, vol. 101, pp. 62–67, Jun. 2012.

[119] E. Klampaftis, D. Ross, D. A. Hardy, P. Scanlan, and B. S. Richards, “Adding colour and opening-up graphic design possibilities for photovoltaic modules in the urban landscape,” *28th Eur. Photovolt. Sol. Energy Conf. Exhib.*, pp. 3796–3799, 2013.

[120] D. Timmerman, I. Izeddin, P. Stallinga, I. N. Yassievich, and T. Gregorkiewicz, “Space-separated quantum cutting with silicon nanocrystals for photovoltaic applications,” *Nat. Photonics*, vol. 2, no. 2, pp. 105–109, Jan. 2008.

[121] B. Sadeghimakki, Z. Gao, and S. Sivoththaman, “Proof of Down-Conversion by CdSe/ZnS Quantum Dots on Silicon Solar Cells,” pp. 2262–2266, 2014.

[122] B. Jalali and S. Fathpour, “Silicon Photonics,” *J. Light. Technol.*, vol. 24, no. 12, pp. 4600–4615, 2006.

[123] F. Herman, R. L. Kortum, and C. D. Kuglin, “Energy band structure of diamond, cubic silicon carbide, silicon, and germanium,” *Int. J. Quantum Chem.*, vol. 1, no. S1, pp. 533–566, 1967.

[124] D. J. Lockwood, “Progress in light emission from silicon nanostructures,” in *Spectroscopy of Emerging Materials*, vol. 165, E. C. Faulques, D. L. Perry, and A. V. Yeremenko, Eds. Springer Netherlands, 2005, pp. 97–114.

[125] S. Ossicini, L. Pavesi, and F. Priolo, *Light emitting silicon for microphotonics*. Springer Berlin Heidelberg, 2003.

[126] E. Yablonovitch and T. Gmitter, “Auger recombination in silicon at low carrier densities,” *Appl. Phys. Lett.*, vol. 49, no. 10, pp. 587–589, 1986.

[127] J. Schmidt, M. Kerr, and P. P. Altermatt, “Coulomb-enhanced Auger recombination in crystalline silicon at intermediate and high injection densities,” *J. Appl. Phys.*, vol. 88, no. 3, pp. 1494–1497, 2000.

[128] J. R. Haynes and W. C. Westphal, “Radiation resulting from recombination of holes and electrons in silicon,” *Phys. Rev.*, vol. 101, no. 6, pp. 1676–1678, 1956.

[129] P. J. Dean, J. R. Haynes, and W. F. Flood, “New radiative recombination processes involving neutral donors and acceptors in silicon and germanium,” *Phys. Rev.*, vol. 161, no. 3, pp. 711–729, 1967.

[130] S. Miura, T. Nakamura, M. Fujii, M. Inui, and S. Hayashi, “Size dependence of photoluminescence quantum efficiency of Si nanocrystals,” *Phys. Rev. B*, vol. 73, no. 24, pp. 1–5, 2006.

[131] H. Takagi, H. Ogawa, Y. Yamazaki, A. Ishizaki, and T. Nakagiri, “Quantum size effects on photoluminescence in ultrafine Si particles,” *Appl. Phys. Lett.*, vol. 56, no. 24, pp. 2379–2380, 1990.

[132] L. T. Canham, “Silicon quantum wire array fabrication by electrochemical and chemical dissolution of wafers,” *Appl. Phys. Lett.*, vol. 57, no. 10, pp. 1046–1048, 1990.

[133] L. Brus, “Electronic wave functions in semiconductor clusters: experiment and theory,” *J. Phys. Chem.*, vol. 90, no. 12, pp. 2555–2560, 1986.

[134] F. Iacona, G. Franzò, and C. Spinella, “Correlation between luminescence and structural properties of Si nanocrystals,” *J. Appl. Phys.*, vol. 87, no. 3, p. 1295, 2000.

[135] S. Schuppler, S. L. Friedman, M. A. Marcus, D. L. Adler, Y. H. Xie, F. M. Ross, Y. J. Chabal, T. D. Harris, L. E. Brus, W. L. Brown, E. E. Chaban, P. F. Szajowski, S. B. Christman, and P. H. Citrin, “Size, shape, and composition of luminescent species in oxidized Si nanocrystals and H-passivated porous Si,” *Phys. Rev. B*, vol. 52, no. 7, pp. 4910–4925, 1995.

[136] J. P. Proot, C. Delerue, and G. Allan, “Electronic structure and optical properties of silicon crystallites: Application to porous silicon,” *Appl. Phys. Lett.*, vol. 61, no. 16, pp. 1948–1950, 1992.

[137] T. Shimizu-Iwayama, N. Kurumado, D. E. Hole, and P. D. Townsend, “Optical properties of silicon nanoclusters fabricated by ion implantation,” *J. Appl. Phys.*, vol. 83, no. 11, pp. 6018–6022, 1998.

[138] L. Dinh, L. Chase, M. Balooch, W. Siekhaus, and F. Wooten, “Optical properties of passivated Si nanocrystals and SiO_x nanostructures,” *Phys. Rev. B*, vol. 54, no. 7, pp. 5029–5037, 1996.

[139] M. Wolkin, J. Jorne, P. Fauchet, G. Allan, and C. Delerue, “Electronic States and Luminescence in Porous Silicon Quantum Dots: The Role of Oxygen,” *Phys. Rev. Lett.*, vol. 82, no. 1, pp. 197–200, Jan. 1999.

[140] L. Pavesi, L. Dal Negro, C. Mazzoleni, G. Franzò, and F. Priolo, “Optical gain in silicon nanocrystals.,” *Nature*, vol. 408, no. 6811, pp. 440–4, Nov. 2000.

[141] D. Timmerman, J. Valenta, K. Dohnalová, W. D. A. M. de Boer, and T. Gregorkiewicz, “Step-like enhancement of luminescence quantum yield of silicon nanocrystals,” *Nat. Nanotechnol.*, vol. 6, no. 11, pp. 710–713, 2011.

[142] D. Jurbergs, E. Rogojina, L. Mangolini, and U. Kortshagen, “Silicon nanocrystals with ensemble quantum yields exceeding 60%,” *Appl. Phys. Lett.*, vol. 88, no. 23, pp. 60–63, 2006.

[143] L. Mangolini, D. Jurbergs, E. Rogojina, and U. Kortshagen, “Plasma synthesis and liquid-phase surface passivation of brightly luminescent Si nanocrystals,” *J. Lumin.*, vol. 121, no. 2 SPEC. ISS., pp. 327–334, 2006.

[144] R. Anthony and U. Kortshagen, “Photoluminescence quantum yields of amorphous and crystalline silicon nanoparticles,” *Phys. Rev. B*, vol. 80, no. 11, pp. 1–6, Sep. 2009.

[145] D. C. Hannah, J. Yang, P. Podsiadlo, M. K. Y. Chan, A. Demortière, D. J. Gosztola, V. B. Prakapenka, G. C. Schatz, U. Kortshagen, and R. D. Schaller, “On the origin of

photoluminescence in silicon nanocrystals: Pressure-dependent structural and optical studies,” *Nano Lett.*, vol. 12, no. 8, pp. 4200–4205, 2012.

[146] R. J. Walters, J. Kalkman, A. Polman, H. A. Atwater, and M. J. A. de Dood, “Photoluminescence quantum efficiency of dense silicon nanocrystal ensembles in SiO_2,” *Phys. Rev. B*, vol. 73, no. 13, p. 132302, Apr. 2006.

[147] G. M. Credo, M. D. Mason, and S. K. Buratto, “External quantum efficiency of single porous silicon nanoparticles,” *Appl. Phys. Lett.*, vol. 74, no. 14, p. 1978, 1999.

[148] J. Valenta, R. Juhasz, and J. Linnros, “Photoluminescence from single silicon quantum dots at room temperature,” *J. Lumin.*, vol. 98, no. 1–4, pp. 15–22, 2002.

[149] K. Littau, P. Szajowski, and A. Muller, “A luminescent silicon nanocrystal colloid via a high-temperature aerosol reaction,” *J.*, vol. 97, pp. 1224–1230, 1993.

[150] W. L. Wilson, P. F. Szajowski, and L. E. Brus, “Quantum confinement in size-selected, surface-oxidized silicon nanocrystals.,” *Science*, vol. 262, no. 5137, pp. 1242–1244, 1993.

[151] J. Wilcoxon, G. Samara, and P. Provencio, “Optical and electronic properties of Si nanoclusters synthesized in inverse micelles,” *Phys. Rev. B*, vol. 60, no. 4, pp. 2704–2714, 1999.

[152] M. L. Mastronardi, F. Maier-Flaig, D. Faulkner, E. J. Henderson, C. Kübel, U. Lemmer, and G. A. Ozin, “Size-dependent absolute quantum yields for size-separated colloidally-stable silicon nanocrystals,” *Nano Lett.*, vol. 12, no. 1, pp. 337–342, 2012.

[153] H. Macleod, *Thin-film optical filters*, 4th ed. CRC Press/Taylor & Francis, 2001.

[154] C. C. Katsidis and D. I. Siapkas, “General transfer-matrix method for optical multilayer systems with coherent, partially coherent, and incoherent interference.,” *Appl. Opt.*, vol. 41, no. 19, pp. 3978–3987, 2002.

[155] E. Centurioni, “Generalized matrix method for calculation of internal light energy flux in mixed coherent and incoherent multilayers.,” *Appl. Opt.*, vol. 44, no. 35, pp. 7532–7539, 2005.

[156] A. B. Sproul, M. A. Green, and J. Zhao, “Improved value for the silicon intrinsic carrier concentration at 300 K,” *Appl. Phys. Lett.*, vol. 57, no. 3, pp. 255–257, 1990.

[157] P. P. Altermatt, A. Schenk, F. Geelhaar, and G. Heiser, “Reassessment of the intrinsic carrier density in crystalline silicon in view of band-gap narrowing,” *J. Appl. Phys.*, vol. 93, no. 3, p. 1598, 2003.

[158] A. Schenk, “Finite-temperature full random-phase approximation model of band gap narrowing for silicon device simulation,” *J. Appl. Phys.*, vol. 84, no. 7, p. 3684, 1998.

[159] K. Misiakos and D. Tsamakis, “Accurate measurements of the silicon intrinsic carrier density from 78 to 340 K,” *J. Appl. Phys.*, vol. 74, no. 5, p. 3293, 1993.

[160] Y. P. Varshni, “Temperature dependence of the energy gap in semiconductors,” *Physica*, vol. 34, no. 1, pp. 149–154, 1967.

[161] W. Bludau, A. Onton, and W. Heinke, “Temperature dependence of the band gap of silicon,” *J. Appl. Phys.*, vol. 45, no. 4, p. 1846, 1974.

[162] M. Turcu, I. M. Kötschau, and U. Rau, “Band alignments in the Cu(In,Ga)(S,Se)2 alloy system determined from deep-level defect energies,” *Appl. Phys. A Mater. Sci. Process.*, vol. 73, pp. 769–772, 2001.

[163] S.-H. Wei and A. Zunger, “Band offsets and optical bowings of chalcopyrites and Zn-based II-VI alloys,” *J. Appl. Phys.*, vol. 78, no. 6, p. 3846, 1995.

[164] P. D. Paulson, R. W. Birkmire, and W. N. Shafarman, “Optical characterization of CuIn[sub 1−x]Ga[sub x]Se[sub 2] alloy thin films by spectroscopic ellipsometry,” *J. Appl. Phys.*, vol. 94, no. 2, p. 879, 2003.

[165] H. Neumann, “Optical properties and electronic band structure of CuInSe2,” *Sol. Cells*, vol. 16, pp. 317–333, 1986.

[166] M. A. Green, “Self-consistent optical parameters of intrinsic silicon at 300 K including temperature coefficients,” *Sol. Energy Mater. Sol. Cells*, vol. 92, no. 11, pp. 1305–1310, 2008.

[167] D. B. M. Klaassen, “A unified mobility model for device simulation—I. Model equations and concentration dependence,” *Solid. State. Electron.*, vol. 35, no. 7, pp. 953–959, 1992.

[168] D. J. Schroeder, J. L. Hernandez, G. D. Berry, and A. A. Rockett, “Hole transport and doping states in epitaxial CuIn[sub 1−x]Ga[sub x]Se[sub 2],” *J. Appl. Phys.*, vol. 83, no. 3, p. 1519, 1998.

[169] P. P. Altermatt, J. O. Schumacher, A. Cuevas, M. J. Kerr, S. W. Glunz, R. R. King, G. Heiser, and A. Schenk, “Numerical modeling of highly doped Si:P emitters based on Fermi-Dirac statistics and self-consistent material parameters,” *J. Appl. Phys.*, vol. 92, no. 6, pp. 3187–3197, 2002.

[170] P. P. Altermatt, “Models for numerical device simulations of crystalline silicon solar cells—a review,” *J. Comput. Electron.*, vol. 10, no. 3, pp. 314–330, Jul. 2011.

[171] S. Shirakata and T. Nakada, “Study of Recombination in Cu(In,Ga)Se_2 Solar Cells by Time-Resolved Photoluminescence,” *MRS Proc.*, vol. 1012, pp. 1012–Y04–06, Jan. 2007.

[172] S. Shirakata and T. Nakada, “Time-resolved photoluminescence in Cu(In,Ga)Se_2 thin films and solar cells,” *Thin Solid Films*, vol. 515, no. 15 SPEC. ISS., pp. 6151–6154, 2007.

[173] M. Bhuiyan, M. S. Islam, and A. J. Datta, “Modeling, Simulation and Optimization of High Performance CIGS Solar Cell,” *Int. J. Comput. Appl.*, vol. 57, no. 16, pp. 26–30, 2012.

[174] A. Fell, K. R. Mcintosh, P. P. Altermatt, G. J. M. Janssen, R. Stangl, A. Ho-Baillie, H. Steinkemper, J. Greulich, M. Matthias, B. Min, K. C. Fong, M. Hermle, I. G. Romijn, and M. D. Abbott, “Input Parameters for the Simulation of Silicon Solar Cells in 2014,” *IEEE J. Photovoltaics*, vol. 5, no. 4, pp. 1250–1263, 2015.

[175] “Sun Power.” [Online]. Available: http://us.sunpower.com/solar-panels-technology/.

[176] “Canadian Solar.” [Online]. Available: www.canadiansolar.com.

[177] “Trina Solar.” [Online]. Available: http://www.trinasolar.com/ca/. [Accessed: 16-Dec-2015].

[178] I. Repins, M. A. Contreras, B. Egaas, C. DeHart, J. Scharf, C. L. Perkins, B. To, and R. Noufi, “19.9% efficient ZnO/CdS/CuInGaSe_2 solar cell with 81.2% fill factor,” *Prog. Photovoltaics Res. Appl.*, vol. 16, no. 3, pp. 235–239, May 2008.

[179] P. Jackson, D. Hariskos, E. Lotter, S. Paetel, R. Wuerz, R. Menner, W. Wischmann, and M. Powalla, “New world record efficiency for Cu (In,Ga)Se2 thin-film solar cells beyond 20 %,” *Prog. Photovoltaics Res. Appl.*, vol. 19, pp. 894–897, 2011.

[180] M. a. Green, K. Emery, Y. Hishikawa, W. Warta, and E. D. Dunlop, “Solar cell efficiency tables (version 46),” *Prog. Photovoltaics Res. Appl.*, vol. 23, no. 7, pp. 805–812, 2015.

[181] H. Sugimoto, “High efficiency and large volume production of CIS-based modules,” in *IEEE PVSC 40*, 2014, pp. 3–6.

[182] M. Gloeckler, A. L. Fahrenbruch, and J. R. Sites, “Numerical modeling of CIGS and CdTe solar cells: setting the baseline,” *3rd World Conf. onPhotovoltaic Energy Conversion, 2003. Proc.*, vol. 1, pp. 491–494, 2003.

[183] F. Bouchard, A. W. Walker, Z. Mi, and K. Hinzer, “Modeling a monocrystalline Cu(In,Ga)Se_2 single junction solar cell grown on a GaAs substrate,” in *Proceedings of SPIE*, 2013, vol. 8915, p. 891507.

[184] J. Song, S. S. Li, C. H. Huang, O. D. Crisalle, and T. J. Anderson, “Device modeling and simulation of the performance of $Cu(In_{1-x},Ga_x)Se_2$ solar cells,” *Solid. State. Electron.*, vol. 48, no. 1, pp. 73–79, 2004.

[185] J. Pettersson, C. Platzer-Bjorkman, U. Zimmermann, and M. Edoff, “Baseline model of graded-absorber Cu(In,Ga)Se_2 solar cells applied to cells with $Zn_{1-X}Mg_xO$ buffer layers,” *Thin Solid Films*, vol. 519, no. 21, pp. 7476–7480, 2011.

[186] A. Morales-Acevedo, N. Hernández-Como, and G. Casados-Cruz, “Modeling solar cells: A method for improving their efficiency,” *Mater. Sci. Eng. B*, vol. 177, no. 16, pp. 1430–1435, 2012.

[187] W. N. Shafarman, S. Siebentritt, and L. Stolt, “Cu(InGa)Se2 Solar Cells,” in *Handbook of Photovoltaic Science and Engineering*, vol. 346, no. 2010, 2011, pp. 546–599.

[188] U. Obahiagbon, C. P. Thompson, W. N. Shafarman, and S. S. Hegedus, “The role of the intrinsic zinc oxide layers on the performance of wide-bandgap (AgCu)(InGa)Se2 thin-film solar cells,” in *2015 IEEE 42nd Photovoltaic Specialist Conference (PVSC)*, 2015, pp. 1–4.

[189] P. W. Li, R. A. Anderson, and R. H. Plovnick, “Dielectric constant of $CuInSe_2$ by capacitance measurements,” *J. Phys. Chem. Solids*, vol. 40, no. 4, pp. 333–334, 1979.

[190] I. Repins, S. Glynn, J. Duenow, T. J. Coutts, W. Metzger, and M. A. Contreras, “Required Materials Properties for High-Efficiency CIGS Modules: Preprint,” *Prepr. No. NREL/CP-520-46235. Natl. Renew. Energy Lab.*, 2009.

[191] D. Schmid, M. Ruckh, and H. W. Schock, “A comprehensive characterization of the interfaces in Mo/CIS/CdS/ZnO solar cell structures,” *Sol. Energy Mater. Sol. Cells*, vol. 41–42, pp. 281–294, 1996.

[192] K. A. Neyts, “Simulation of light emission from thin-film microcavities,” *J. Opt. Soc. Am.*, vol. 15, no. 4, pp. 962–971, 1998.

[193] C. E. Valdivia, E. Desfonds, D. Masson, S. Fafard, A. Carlson, J. Cook, and K. Hinzer, “Optimization of antireflection coating design for multijunction solar cells and concentrator systems,” in *Photonics North*, 2008, vol. 2.

[194] J. Sacks, R. M. Savidge, A. M. Gabr, A. Walker, R. Beal, J. Wheeldon, A. P. Knights, P. Mascher, K. Hinzer, and R. N. Kleiman, “Quantum Efficiency Measurements of Down-Shifting Using Silicon Nanocrystals for Photovoltaic Applications,” *PVSC*, 2012.

[195] S. J. Orfanidis, “Electromagnetic Waves and Antennas,” 2014. .

[196] “UQG Ltd.” [Online]. Available: http://www.uqgoptics.com/. [Accessed: 30-Jun-2016].

[197] “Cargille.” [Online]. Available: http://www.cargille.com/refractivestandards.shtml. [Accessed: 28-Jan-2016].

[198] J. Sacks, “Spectral engineering via silicon nanocrystals grown by ECR-PECVD for photovoltaic applications,” McMaster University, 2012.

[199] G. E. Jellison and F. a. Modine, “Parameterization of the optical functions of amorphous materials in the interband region,” *Appl. Phys. Lett.*, vol. 69, no. 3, p. 371, 1996.

Appendix A: Silicon Nanocrystals Growth by PECVD

Fabrication of Si-nC films was part of a collaborative project with McMaster University. The fabrication and characterization of silicon-rich silicon-oxide (SRSO) films were realized by Justin Sack [198]. A Plasma-Enhanced Chemical Vapour Deposition (PECVD) system was used to grow the Si-nC on fused silica substrates followed by annealing using a quartz tube furnace. The fused silica Spectrosil 2000 UV coverslips (CFS-2525) are 0.5 mm thick from UQD Optics [196]. A picture of the PECVD system is shown in Figure A-1 during one of my visits to McMaster University.

Regarding the SRSO deposition, silane (SiH_4) is the source of silicon atoms that when injected in the main chamber of the PECVD leaves free Si atoms to bond with the heated substrate. The plasma source gas in the system is a mixture of Ar and O_2 with varying ratio depending on the specific deposition parameters. The Si:O ratio was controlled by varying the O_2 flow rate rather than varying SiH_4 flow. Varying the SiH_4 flow has shown a large change in the overall deposition rate and thus the O_2 flow was changed to control the Si:O ratio. SRSO films show a decrease in the refractive index, due to less silicon content, when increasing O_2 flow. The Ar flow was varied to compensate for increasing or decreasing amounts of O_2, which is known as argon-compensated deposition.

After the deposition in the PECVD system, the film is an amorphous mix of Si and O with a high number of defects. To remove these defects and form the silicon nanocrystals, high-temperature treatment is required. High-temperature annealing (up to 1200°C) was performed in flowing H_2 (5%) N_2 (95%), which has been shown to improve luminescence intensity due to Si-nC surface passivation [38]. It was noted that higher annealing temperature caused a red-shift in the PL peak. This was due to the formation of larger Si-nC with higher annealing temperatures.

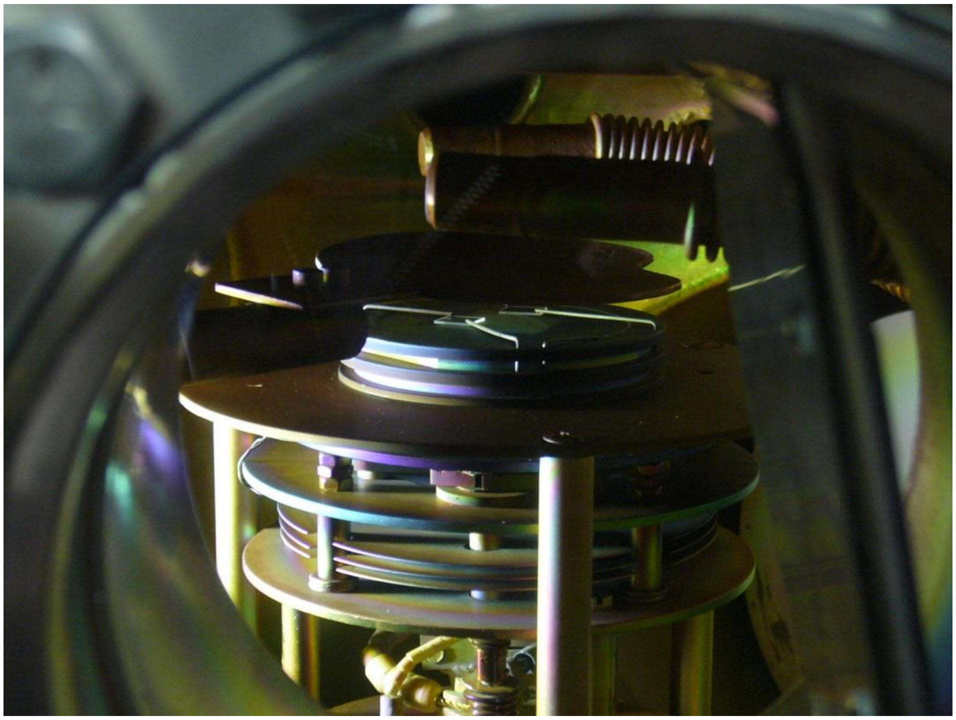

Figure A-1. The PECVD system used in the fabrication of Si-nC. A close-up of the main chamber showing a quartz substrate on the heated sample stage.

Table A-1 shows the deposition parameters for two samples, A and B. Both films were grown on 0.5 mm fused silica substrates at a deposition pressure of 2.1 mTorr while maintaining the temperature at 120°C. The base pressure of the system was on the order of 10^{-7} mTorr range, and magnetron power was set such that the effective forward power was 500 W. Gas flows are maintained constant while deposition time was varied to get different film thicknesses. There is almost a linear relation between deposition time and film thickness. It is expected that on average 65 nm of film is grown every 10 minutes. This relation was confirmed by growing 9 different samples with thicknesses varying from 135 nm up to 528 nm in duration of 20 minutes to 80 minutes, respectively. All films were allowed to cool one hour after deposition before removing them from the PECVD main chamber. Finally films were annealed in a quartz tube furnace at 900°C, 1000°C, 1100°C and 1135°C in flowing H_2 (5%) and N_2 (95%).

Table A-1. Deposition parameters for films A and B with the same gas flows and partial pressures (PP) but different deposition times.

	Ar + SiH_4 flow	Ar + SiH_4 PP	Ar + O_2 flow	Ar + O_2 PP	Ar flow	Ar PP	Deposition time
A	2.50 sccm	0.22 mTorr	5.40 sccm	0.47 mTorr	18.9 sccm	1.41 mTorr	70 min
B	2.50 sccm	0.22 mTorr	5.40 sccm	0.47 mTorr	18.9 sccm	1.41 mTorr	80 min

Although there have been several SRSO films fabricated throughout this project, samples A and B will be used in this work since they are the most efficient ones. The film thickness after growth was determined to be 465 nm and 528 nm for samples A and B, respectively. Both samples were annealed at 1135°C in flowing H_2 (5%) and N_2 (95%). This annealing temperature gave the highest luminescent efficiency, as expected from the literature that annealing should be in the range of 1100-1200°C for efficient luminescence. After annealing the film thicknesses shrinks and is estimated to be 430 nm and 484 nm for samples A and B, respectively. The decrease in thickness after high-temperature annealing is due to the removal of vacancy defects and thus the amorphous film is compressed.

A.1. Transmission Electron Microscopy

The Titan 80-300LB, a High-resolution Transmission Electron Microscopy (HR-TEM), made by FEI and is located at the Canadian Centre for Electron Microscopy, was used to view the Si-nC embedded in a quartz matrix. Figure A-2 shows HR-TEM images of sample B. The image on the left is a dark-field (DF) TEM image and shows the distribution of Si-nC throughout the film represented by white dots. The bright region on the top left is the substrate, while the bottom right region is the edge of the film. The dark region suggests a large Si-nC near the surface of the film. This is suggested to be due to a temperature gradient. In such a thick film, higher temperatures cause larger Si-nC to form near the surface while deeper in the film the temperature is lower and therefore relatively smaller Si-nC are formed. The right image in Figure A-2 is a magnified image showing some Si-nC, a few of which have been circled to indicate the nanocrystal's diameter. The diameter is estimated to be 4 nm on average although the quality of the images does not allow us to confirm this diameter.

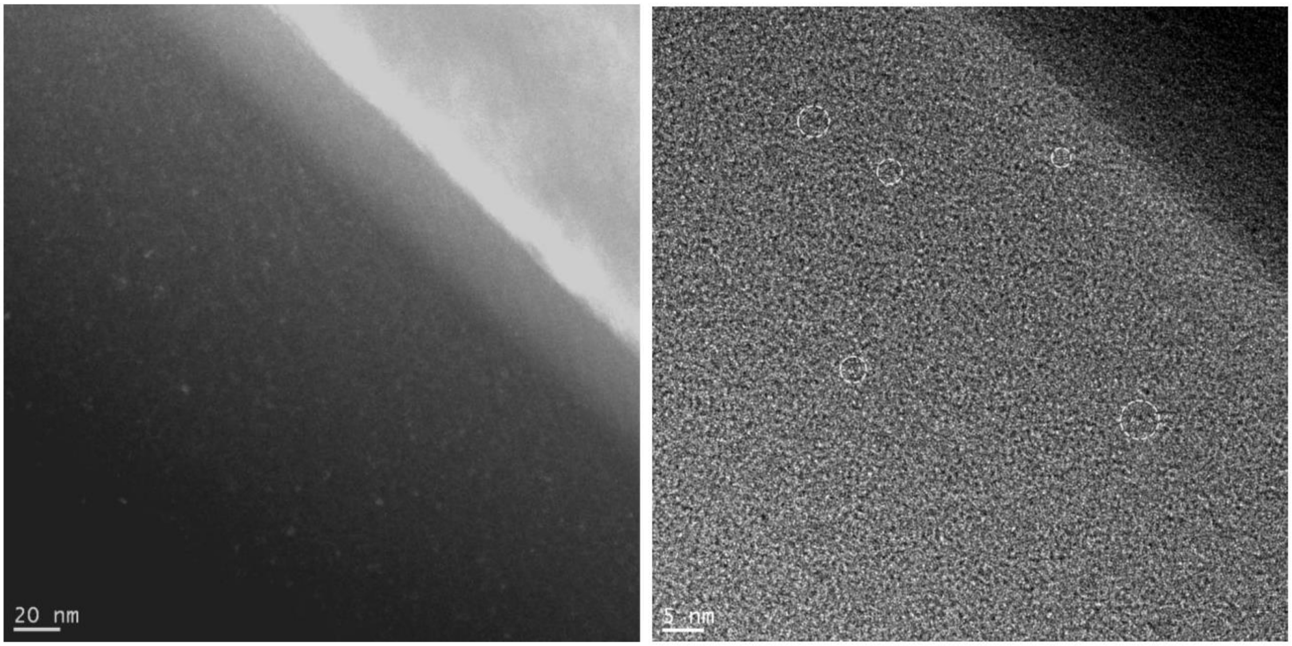

Figure A-2 Dark-field TEM image showing the distribution of Si-nC in the film (left). HR-TEM image of Si-nC showing crystalline regions embedded in SiO2 matrix (right). Both images are for sample B. TEM images after [198].

A.2. Ellipsometry

In order to measure the optical constants and thickness of the Si-nC films, A J.A. Woollam variable angle spectroscopic ellipsometer was used. Ellipsometry is a measure of the change in polarization and is quantified by two angles: the amplitude ratio (Ψ) and phase difference (Δ). Both angles are related to the complex reflectance ratio ρ, as

$$\rho = \frac{r_p}{r_s} = tan\Psi e^{i\Delta} \tag{A.1}$$

where r_p and r_s are the parallel and perpendicular Fresnel reflection coefficients, respectively. The experimental values of Ψ and Δ are then compared with a model in order to get optical constants and film thickness. In this work the Tauc-Lorentz oscillator model was used to fit the measurements [199]. Using an iterative procedure, the optical constants are verified by a Mean Square Error (MSE) value. Low MSE values indicate that the measured values are close to the predicted values.

The measured refractive index and extinction coefficient of films A and B are shown in Figure A-3. Sample B has slightly higher refractive index since it is more silicon rich.

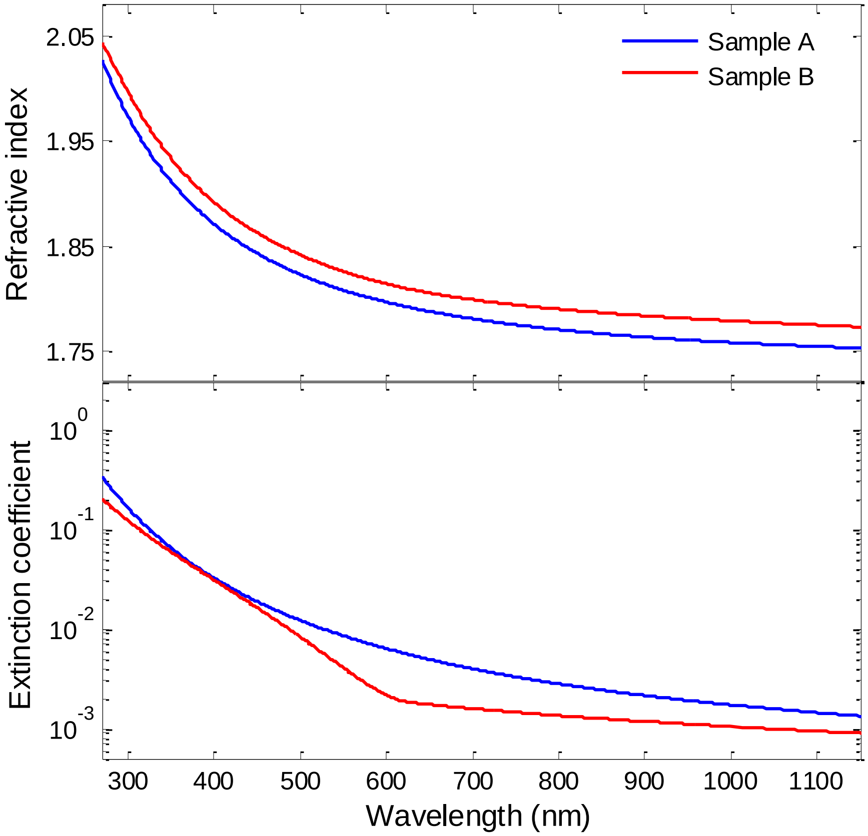

Figure A-3. Optical constants of samples A and B after annealing at 1135°C.

A.3. Photoluminescence Quantum Yield

Photoluminescence (PL) spectroscopy was performed using a continuous-wave 405 nm GaN laser at 21 µW. The beam was focused perpendicular to the sample surface using a 50X long working distance objective lens for spot sizes of ~5 µm. A 7.5 cm convex lens was used as the objective to focus the incident laser beam over a larger area for spot sizes of ~150 µm. PL was collected through the same objective lens using a Yvon-Jobin spectrometer and a liquid nitrogen-cooled CCD detector. Reflected excitation light was filtered out using a 450 nm long-wave pass filter prior to entering the spectrometer. A picture of the calibrated PL measurement setup is shown in Figure A-4.

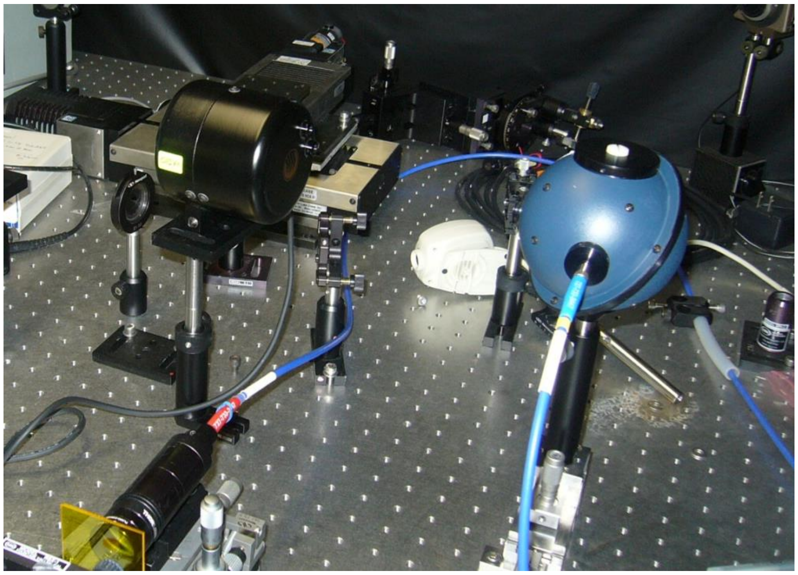

Figure A-4. Photoluminescence quantum efficiency measurement setup at McMaster University showing the 3.3” diameter integrating sphere. The coupled fiber shown is connected to a calibrated spectrometer.

Two quantities were measured using this setup, the photoluminescence external quantum efficiency (*PL_{EQE}*) and the photoluminescence internal quantum efficiency (*PL_{IQE}*). The *PL_{EQE}* is defined as the ratio of the emitted photon flux to the incident photon flux, as

$$PL_{EQE} = \frac{\phi_e}{\phi_i} \tag{A.2}$$

where ϕ_e and ϕ_i are the emitted photon flux and the incident photon flux, respectively. The incident photon flux is calculated by measuring the intensity of the laser source coupled to the integrating sphere with no sample in the integrating sphere. While the emitted photon flux is measured with the sample in the integrating sphere and a low pass filter to block the laser beam from entering the fibre at the output port. On the other hand the *PL_{IQE}* is defined as the ratio of the emitted photon flux (ϕ_e) to the absorbed photon flux (ϕ_a), as

$$PL_{IQE} = \frac{\phi_e}{\phi_a} \tag{A.3}$$

The absorbed photon flux is calculated as follows:

$$\phi_a = \phi_{ref} - \phi_s \tag{A.4}$$

where ϕ_{ref} are ϕ_s the reference and sample photon fluxes, respectively. The reference and sample, Si-nC in this case, are measured by measuring the laser source intensity with the substrate and the sample in the integrating sphere, respectively.

The PL results are shown in Figure A-5 for Si-nC sample with an emission spectrum centered at around 840 nm. As can be seen that the PL intensity is higher for sample B, the thicker film, which is due to more silicon atoms that are present in the film and thus larger number of Si-nCs that are present. This agrees with the higher refractive index for sample B, as was shown in Figure A-3. The red-shift in the PL indicates that thicker films incorporate larger Si-nCs.

The PL_{IQE} of the Si-nCs samples A and B were found to be 0.65% and 0.73%, respectively. While the PL_{EQE} is slightly lower and is were found to be 0.11% and 0.19%, respectively. The PL_{EQE} for sample B is almost double that of sample A since the film is thicker and therefore it emits more photons. However when we compare PL_{IQE} , which is the ratio of emitted photon flux to absorbed photon flux, there is a small difference between the two films and it is within the experimental error. Therefore thicker films will emit more but not necessarily more efficient. The efficiency could be further improved by ensuring oxygen-free growth conditions and passivating the Si-nCs by organic ligands, as suggested in the literature. Although higher conversion efficiency is required in order to observe an enhancement in the solar cell, the objective at this stage of research was to accurately characterize the Si-nC, as indicated in [198].

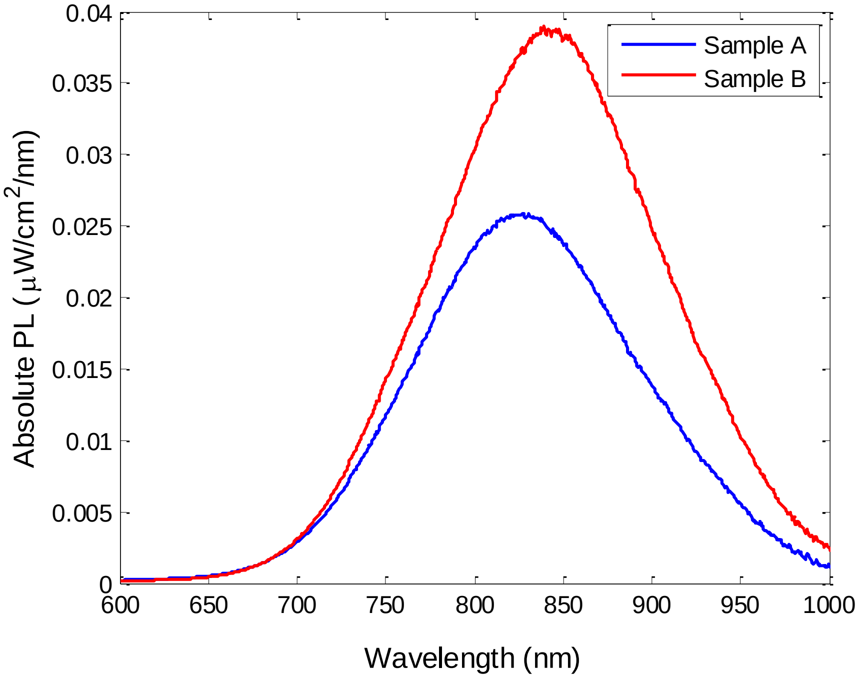

Figure A-5. Calibrated PL spectra of A and B Si-nC films of varying thicknesses deposited on fused silica. PL intensity increased as a function of thickness, and a slight red-shift was seen in the thicker film.